Self-assemblies of Salts and Metal Complexes of 1,8-Naphthalimide Derivatives in Self-recognition and Cation Sensing

A Dissertation Submitted

to the Indian Institute of Technology Guwahati

in Partial Fulfilment of the Requirements for

the Degree of

Doctor of Philosophy in Chemistry

Submitted by

Jagajiban Sendh (Roll No 196122107)

Supervisor: Prof. Jubaraj Bikash Baruah

Department of Chemistry

Indian Institute of Technology Guwahati

Assam, India

Dedicated to
my grandmother
and family members
and well-wishers,
whose unwavering support
and encouragement
have been the cornerstone of
my journey.

Statement of Declaration

I hereby declare that the thesis entitled "***Self-assemblies of Salts and Metal Complexes of 1,8-Naphthalimide Derivatives in Self-recognition and Cation Sensing***" is the result of my original research work conducted under the supervision of Prof. Jubaraj Bikash Baruah, at the Department of Chemistry, Indian Institute of Technology Guwahati, India.

In accordance with standard scientific reporting practices, acknowledgment has been given throughout this thesis whenever the work described is based on the findings of other researchers.

IIT Guwahati — Jagajiban Sendh

February 2025

Prof. Jubaraj Bikash Baruah

Department of Chemistry

Indian Institute of Technology Guwahati

Guwahati, 781039, Assam, India

Phone no. +91-361-258-2311 (O)

Fax no. +91-361-269-0762

Email: juba@iitg.ac.in

Certificate

This is to certify that Mr. Jagajiban Sendh has been working under my supervision as a regularly registered Ph.D. student since December 2019. I am forwarding his thesis entitled "Self-assemblies of Salts and Metal Complexes of 1,8-Naphthalimide Derivatives in Self-recognition and Cation Sensing" for consideration in fulfilment of the requirements for the Ph.D. (Science) degree at this institute.

I certify that Mr. Jagajiban Sendh has fulfilled all the requirements set forth by this institute concerning the research presented in his thesis. Furthermore, this work has not been submitted elsewhere for any degree.

IIT Guwahati

February 2025

Prof. Jubaraj B. Baruah

(Thesis Supervisor)

Acknowledgments

This thesis would not have reached its completion without the support and encouragement of many individuals around me. As I conclude this journey, I would like to express my heartfelt appreciation to those who played a crucial role in making this thesis a reality and an unforgettable experience.

First and foremost, with profound gratitude, I wish to extend my heartfelt thanks to my supervisor, Prof. Jubaraj B. Baruah. His timely and invaluable guidance during the most critical junctures of my career has played a pivotal role in enabling me to achieve this significant milestone. The opportunity to conduct scientific research under his mentorship has been nothing short of transformative. Our numerous discussions and interactions not only deepened my understanding but also opened up new, uncharted territories of scientific exploration. I am deeply indebted to this exceptional individual for all he has offered, particularly his steadfast encouragement and motivation in my pursuit of scientific discovery. My everlasting gratitude is reserved for him.

I would like to extend my sincere thanks to the doctoral committee members, Dr. Kalyan Raidongia (IIT Guwahati), Dr. Dipankar Srimani (IIT Guwahati), and Dr. Akshai Kumar Alape Seetharam (IIT Guwahati) for their insightful advice and valuable suggestions. I am also deeply grateful to the entire faculty and staff of the Department of Chemistry at the Indian Institute of Technology Guwahati for providing a supportive and stimulating work environment throughout this period.

I would like to express my heartfelt thanks to my lab members, specially Dr. Jitendra Nath, Dr. Rinki Brahama, and Mr. Abhaya Pratap Singh, for the opportunity to work alongside them. My gratitude also extends to other group members- Dr. Subhrajyoti Ghosh, Mr. Avijit Rana, Mr. Md Sakir, Mr. Srijan Mukherjee, Mr. Biswamohan Prusty, Mr. Aswin Kumar Sahoo, Mrs. Subhashree Sahu, Mr. Alok Sahu, Mr. Harekrushna Behera, Mr. Kaushik Ghosh, Mr. Arup Kumar Mohapatra, and Mrs. Limashree Sahoo for their timely help, support, and the wonderful time we shared. Words cannot fully convey my appreciation for their companionship, which made our time in the laboratory and beyond both pleasant and memorable. I am also especially grateful to my lab senior, Dr. Munendra Pal Singh Yadav, for his invaluable support at the initial part as a researcher.

I would like to acknowledge with gratitude the financial support provided by the Indian Institute of Technology Guwahati for my research fellowship.

I want to extend my heartfelt gratitude to all my teachers at B.B. Mahavidyalaya Chandikhol, and Ravenshaw University for their love and blessings.

I extend my heartfelt gratitude to my family, whose unconditional love, unwavering support, patience, and blessings have been the foundation of my Ph.D. journey. I am deeply indebted to my parents, Trilochan Sendh and Smitarani Sendh; my uncle and aunt, Satyabrata Prusty and Pushpanjali Sendh; my elder brothers, Shanti Swarup Sendh, Girija Sankar Sendh, Bhabani Shankar Sendh, and Biraja Prashad Sendh; my younger brothers, Subham Saswat Prusty and Sidhartha Sankar Sendh; my elder sisters, Samita Sendh, Sangita Choudhury, Aparajita Priyadarshini, Sushree Sanjita Sendh, and Subradarshini Sendh; and my younger sisters, Swayang Samparna Prusty and Dibyadarshini Sendh. Their unwavering encouragement, guidance, and belief in me have been a constant source of strength and inspiration throughout this journey.

Table of Content

ABBREVIATIONS

Å:	Angstrom
CH_3COOH:	Acetic acid
CV:	Cyclic voltammetry
DLS:	Dynamic light scattering
DMF:	Dimethyl formamide
DMSO:	Dimethyl sulphoxide
DSC:	Differential scanning calorimetry
EDX:	Energy dispersive X-ray
ESR:	Electron spin resonance
FESEM:	Field emission scanning electron microscope
FRET:	Forster resonance energy transfer
H_2O:	Water
IR:	Infrared
ICT:	Isothermal calorimetric titration
MeOH:	Methanol
μM:	Micromolar
nM:	Nanomolar
HNO_3:	Nitric acid
HCl:	Hydrochloric acid
HBr:	Hydrobromic acid
NMR:	Nuclear magnetic resonance
OM:	Optical microscope
PET:	Photo-induced electron transfer
RT:	Room temperature
TGA:	Thermogravimetric analysis
TNP:	Trinitro phenol
UV-visible:	Ultraviolet-visible
XPS:	X-ray photoelectron spectroscopy

Thesis Abstract

The thesis, titled "***Self-assembling of Salts and Metal Complexes of 1,8-Naphthalimide Derivatives in Self-Recognition and Cation Sensing***," presents research focused on the synthesis and characterization of various metal complexes, coordination polymers, and self-assemblies involving naphthalimide derivatives, and their sensing of common metal ions under ordinary conditions.

The self-assemblies studied in the thesis include salts, ionic crystals, polymorphs, and metal complexes. The thesis is structured into five chapters, with each chapter except for the introduction which is comprised of a concise discussion of the relevant literature and references, the rest has experimental details, and references.

Chapter 1: Introduction

The introduction of this thesis explores the diverse applications of 1,8-naphthalimide derivatives, particularly on their photophysical properties and biological relevance. These compounds, known for their fluorescence and ease of functionalization, have been widely used in a variety of sensing applications, including ion detection, biological imaging, and cancer therapy. Their abilities to interact with different ions guide emission properties through mechanisms like photo-electron transfer and Forster resonance energy transfer allowing them to serve as effective sensors for metal ions like Al^{3+}, Hg^{2+}, and Cu^{2+}. They have been incorporated into sensors for detecting fluoride, cyanide, phosphate, and other important ions, utilizing changes in fluorescence intensity upon binding. The versatile nature of these compounds, combined with their environment-sensitive fluorescence behavior, makes them valuable tools in various fields, including drug detection, cell imaging, and environmental monitoring. Additionally, naphthalimides have shown biological activity, including anticancer properties and the ability to target DNA and proteins.

Chapter 2: *Polymorphs, salt, ionic co-crystal, and inclusion complex of N-amino-1,8-naphthalimide.*

This chapter presents the synthesis and characterization of a diverse range of polymorphs, salts, ionic cocrystals, and metal complexes derived from N-amino-1,8-naphthalimide. The compounds were synthesized under varying reaction conditions and were analyzed by using techniques such as single-crystal X-ray diffraction, powder X-ray diffraction, and infrared spectroscopy. The photophysical properties of N-amino-1,8-naphthalimide are also explored, focusing on its transition of fluorescence emission from a quenched state to a fluorescence

"turn-on" state. The study investigates a variety of self-assembly behaviours, particularly the synthons interactions among symmetry-equivalent and symmetry-non-equivalent molecules in the crystal lattice. Additionally, the chapter delves into the formation of ionic cocrystals and salts of N-amino-1,8-naphthalimide. The synthesis of metal complexes, where N-amino-1,8-naphthalimide acts as a coordinated ligand, is further discussed. The key examples include an octahedral copper complex, and a self-inclusion complex with cadmium The dinuclear and trinuclear copper complexes derived 2,6-pyridine dicarboxylic acid, and 3,5-pyrazole dicarboxylic acids, having N-amino-1,8-naphthalimides are presented in this chapter.

Chapter 3: ***Copper and cobalt 2,6-pyridinedicarboxylate complexes having 2-(pyridin-4-ylmethyl)-1H-benzo[de]isoquinoline-1,3(2H)-dione.***

The structural characteristics, thermal stability, and de-solvation processes of one cobalt complex and one copper complex, both incorporating a naphthalimide derivative, 2-(pyridin-4-ylmethyl)-1H-benzo[de]isoquinoline-1,3(2H)-dione, and 2,6-pyridine dicarboxylic acid, were investigated. The study reveals π-π stacking interactions between the naphthalimide rings. The cobalt complex has an octahedral geometry around the cobalt center, while the copper complex exhibits a square pyramidal geometry around the copper center. The copper complex forms a polymeric structure, with the sixth coordination site blocked by the O-atom of the carbonyl group from the naphthalimide ring. The UV-visible, fluorescence emission, and electrochemical properties of both complexes are discussed in detail.

Chapter 4: ***N-(1,3-Dioxo-1H-benzo[de]isoquinolin-2(3H)-yl)isonicotinamide) and 2,6-pyridinedicarboxylic acid as a platform for metal ion sensing***

The study investigates the synthesis and characterization of two iron complexes. Both the complexes were bis-2,6-pyridinedicarboxylate iron(II) complexes having protonated N-(1,3-dioxo-1H-benzo[de]isoquinolin-2(3H)-yl)isonicotinamide while other having diprotonated 7-(isonicotinamido)-1,3,6,8-tetraoxo-N-(pyridin-4-yl)-3,6,7,8-tetrahydrobenzo[lmn][3,8]phenanthroline-2(1H)-carboxamide. In both complexes, the naphydrazide and binaphydrazide groups exist in their protonated forms and act as the cationic components of the structure. The study also highlights the π-π stacking interactions present in the two complexes, which contribute to their structural stability. Additionally, the thermal stability and electrochemical properties of both the complexes and their precursor compounds were thoroughly examined.

Chapter 5: *A zinc coordination polymer of 5-(1,3-dioxo-1H-benzo[de]isoquinolin-2(3H)-yl)isophthalic acid and sensing of cations*

The synthesis and characterization of a zinc coordination polymer derived from the naphthalimide-based ligand 5-(1,3-dioxo-1H-benzo[de]isoquinolin-2(3H)-yl)isophthalic acid (NAPHISO) is reported in this chapter. The asymmetric unit of the coordination polymer comprises a tetra-core Zn_4O unit, contributing to its distinct structural framework. It has two-dimensional structural arrangements with dimethylformamide molecules occupying the voids, further enhancing the material's porosity and stability.

The NAPHISO serves as a fluorescent probe for the detection of Zn^{2+} ions and Ca^{2+} ions, while the coordination polymer demonstrates fluorescence-based sensing capabilities for Fe^{2+} and Cu^{2+} ions, even in the presence of competing metal ions. Furthermore, the thermal stability of the coordination polymer was investigated.

Chapter 1

Introduction

1.1: Introduction

Amide bonds are the constituent of a backbone structure of a protein and they play key roles in the assembling and reactivities of enzymes.[1] Self-assemblies of organic and inorganic amide-based compounds show interesting properties.[2] There is a general interest in studying them due to the ubiquitous nature of the amide-containing compounds. Synthetic polyamide-based compounds with linear or cyclic structures are used as mimics of proteins and have importance as supramolecular materials.[3] They undergo hydrolytic transformations under relatively easier conditions. Hence, amide-based laboratory-synthesized polymeric compounds fall under the category of biodegradable materials.[4] On the other hand, the cyclic imides are a sub-set of

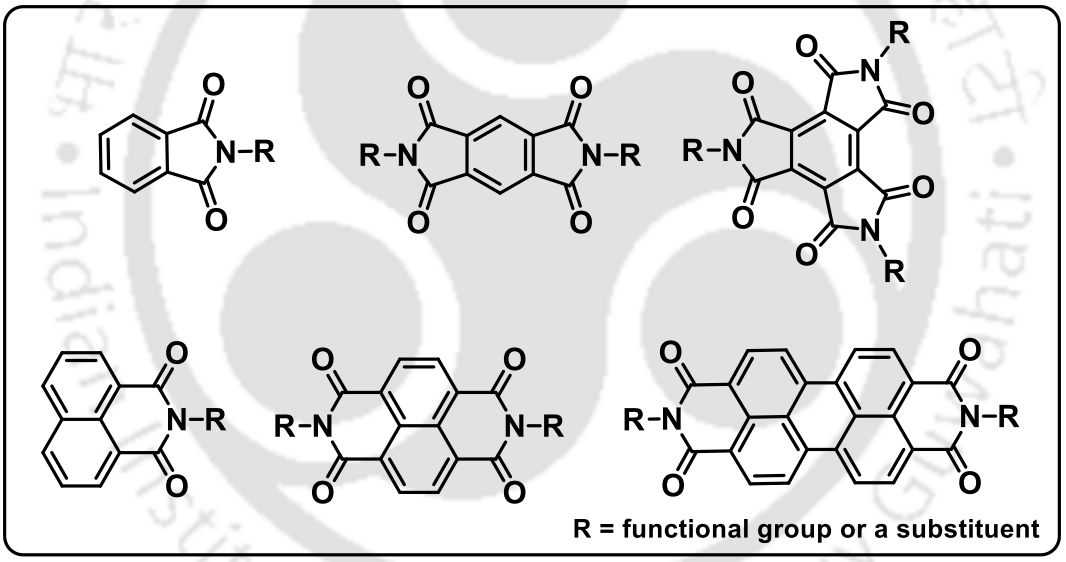

(a)

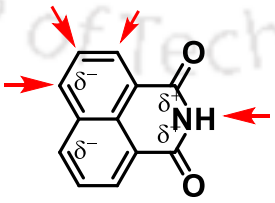

(b)

Figure 1.1: (a) Structural backbone of some aromatic cyclic imides and (b) Arrows showing the sites for functionalization and δ showing the dipolar nature of a 1,8-naphthalimide.

amide-based compounds and they may be derived from aliphatic or aromatic dicarboxylic acids by condensation with amines. There are wide ranges of skeletons of aromatic cyclic amides as illustrated in the Figure 1.1a that are commonly encountered in literature. Each of these classes of compounds has independent electronic properties. Hence, these as functional units of a macromolecular or connected to another unit through flexible tether control the folding and provide control in the directional nature of supramolecular assemblies[5] to modulate properties. They have contributed significantly study as self-assembles or discrete species and contributed in different areas that are listed on the left side of Figure 1.2. On the right side of the figure, are examples of some naphthalimides and naphthalene derived imides. They have applications as synthetic[6] and in biological materials.[7]. In accordance with this, there are extensive studies on aromatic cyclic imides all across the world, which have helped to discover advanced materials properties from these classes of compounds. They are also functionalized at one or more positions of the aromatic ring or the nitrogen atom, which provides diverse functionalized molecules. The common feature among them is that they provide a highly conjugated planar platform, and have a dipolar nature. An illustration is given in Figure 1.1b, it shows the dipolar nature of the 1,8-naphthalimide and

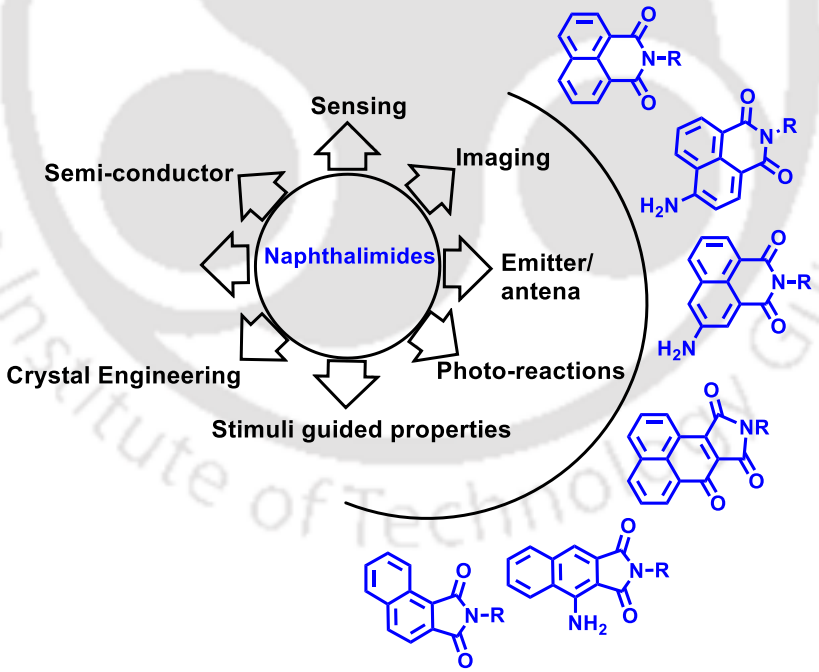

Figure 1.2: A representative scheme showing different naphthalimide-based compounds contributing to different spheres of chemical sciences

It's functionalization sites. Among the cyclic imides, the imides the naphthalimide derivatives find special attention due to their extraordinary abilities to show environment-dependent

fluorescence emissions, reversible redox properties, ability to form varieties of non-covalent assemblies, and binding ability to biological molecules. They form self-assembled metal complexes, ionic cocrystals having diverse possibilities to design applied materials. In the preceding sections of this chapter, selected examples are given to describe the different aspects of 1,8-naphthalimides derivatives.

1.2 Self-Assemblies of 1,8-naphthalimide derivatives

The supramolecular features of 1,8-naphthalimide units in self-assemblies generate different assemblies that can easily modulate the self-assembling properties. The dipolar nature allows it to adopt different stacking arrangements among them or with another aromatic ring. They also assemble by weak interactions such as C–H···π, O–H···π, and N–H···π interactions (~ 0.5-2 kcal/mol), the interplay of these interactions that as subsidiary interactions, improve the stabilities of different assemblies.[8] The strength of the hydrogen bonds varies between 5-15 kcal/mol, whereas dipolar π-interaction is of ~2 kcal/mol. Though the dipolar interactions have

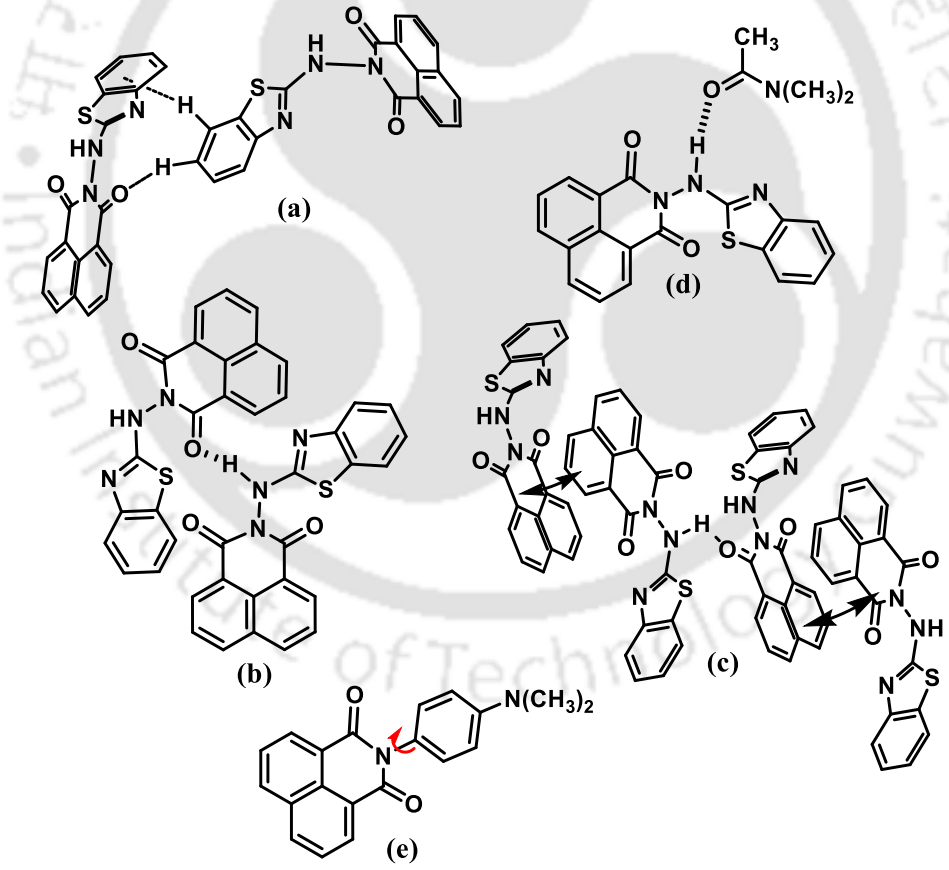

Figure 1.3: (a) and (c) are hydrogen bonded or stacked assemblies of the polymorphs of -(benzo[d]thiazol-2-ylamino)-1H-benzo[de]isoquinoline-1,3(2H)-dione (**1.1**); (d) Its dimethylacetamide solvate and (e) structure of 2-(4-(dimethylamino)phenyl)-1H-benzo[de]isoquinoline-1,3(2H)-dione (**1.2**) (arrow showing the rotatable bond).

smaller interaction energy, they play key roles in deciding a favorable stacking in assemblies of naphthalimide. These interactions are comparable to solute-solvent interactions; the assemblies of naphthalimide derivatives depend on the crystallization conditions, stimuli as well as the nature of the partner molecules.[9] One such example, is the 2-(benzo[d]thiazol-2-ylamino)-1H-benzo[de]isoquinoline-1,3(2H)-dione (**1.1**), which forms polymorphs and solvates depending on crystallization conditions. It provided three polymorphs[10] shown in Figure 1.3 (a)-(c). Each has different packing patterns, as well as schemes of weak interactions; the assemblies of the polymorphs had distinctions in having C-H···π, N-H···O, and π-π interactions in respective assemblies. The dimethylacetamide solvate of the same compound is shown in Figure 1.3(d). This solvate had a clear packing difference with the solvate of the same compound with dimethylformamide. Due to differences in the self-assemblies, each of these forms had characteristic fluorescence emission.

The compound 2-(4-(dimethylamino)phenyl)-1H-benzo[de]isoquinoline-1,3(2H)-dione (**1.2**) shown in Figure 1.3e, has *N*,*N*-(dimethylamino)aniline derived naphthalimide, it had provided two conformational polymorphs. The orientations of the *N*,*N*-dimethylaniline part connected to the naphthalimide were slightly different in the polymorphs, which contributed to differences in weak interaction schemes in respective assembly, making them distinguishable assemblies. The solid-state emission spectra of the two polymorphs were different and also had different lifetime fluorescence emission decay [11], which is shown in Figure 1.4.

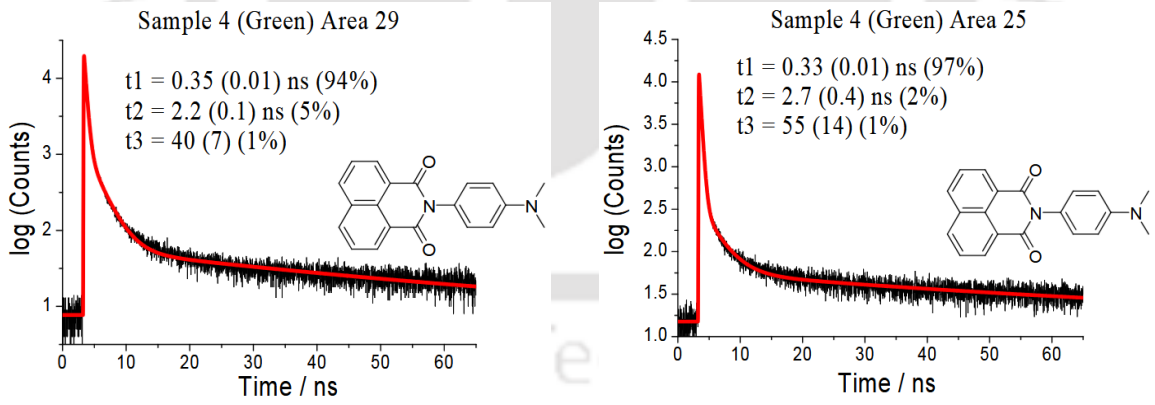

(a) (b)

Figure 1.4: Room temperature emission decay curve and instrument response function recorded for O-DMIM and the least squares fit to a tri-exponential (red line). The insert shows a typical fluorescence lifetime image taken for the crystal sample.

The structural studies on the positional isomers of 2-(pyridin-*n*-ylmethyl)-1H-benzo[de]isoquinoline-1,3(2H)-dione (when n = 2, **1.4**; n= 3, **1.5**; *n* = 4, **1. 6**)[12] and corresponding 8-bromo (**1.6**)[13] or 8-nitro (**1.7a**, **1.7b**)[14] derivatives shown in the Figure 1.4a

had revealed that the location of the nitrogen atom of the respective pyridine ring had influenced their stacking patterns. As shown in the naphthalimide ring as the head and the six-member ring as the tail part of the isomers, **1.4** had the head-to-head arrangements, whereas as shown in Figure 1.4 b-d, the positional isomers **1.5** and **1.6**, had assembling of pairs of respective molecules in head to tail arrangement. In each case, the translation among the naphthalimide rings and centroid to centroid distance between the interacting rings of the self-assembled pairs were distinguishable. Compound **1.3** had no nitrogen atom on the six-membered rings (it had a phenyl group instead of pyridine); the packing pattern of the **1.3**, had dipolar stacking interactions as it had head-to-tail arrangement as shown in Figure 1.4e. The compounds with nitro or bromine groups at the 8-position revealed that the π-stacking patterns were varied with those substitutions and the position of the substituents on the ring. Each of these compounds had characteristic fluorescence emissions and showed aggregation-induced emission. The compound **1.7** formed a cocrystal with 1,4-diiodotetrafluorobenzene, which showed weak phosphorescence. The luminescence properties in the solid state of the positional isomers were dependent on the intermolecular interactions.

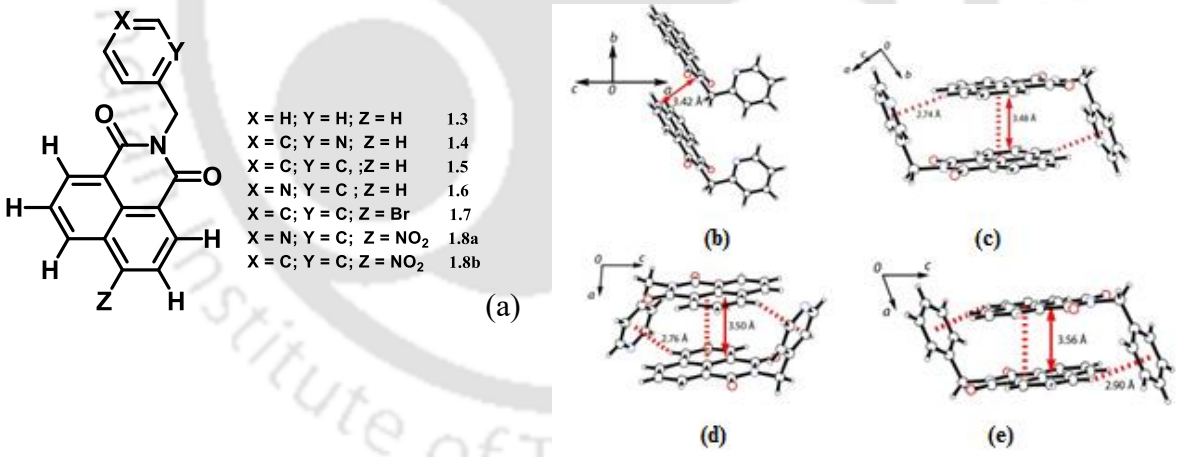

Figure 1.4: (a) The N-benzyl-1,8-naphthalimide and different positional isomers and substituted N-(n-) picolyl-naphthalimides (n =2, 3 or 4). Different stacking arrangements between interacting pairs of molecules (b)-(d) are 2, 3 or N-(4-picolyl)-1,8-naphthalimide, respectively, (e) N-benzylnaphthalimide.

A unit having supramolecular sites once linked to naphthalimide unit provides scopes to generate aggregates with novel optical properties. For example, the unsubstituted compound 2-hexyl-1H-benzo[de]isoquinoline-1,3(2H)-dione (**1.9**) stacks (centroid to centroid distance 3.566 Å) with dipolar interactions but the bromo-derived compound, 2-(6-bromohexyl)-1H-benzo[de]isoquinoline-1,3(2H)-dione (**1.10**) stacks head to head without dipolar interactions,[15] as illustrated in Figure 1.5. Both these forms had distinct differences in respective emission spectrum, the bromo derivative **1.10** showed strong blue emission; whereas, the unsubstituted compound **1.9** had cyan emission with weaker intensity. The compound **1.10** adsorbed chloroform or dichloromethane, upon adsorption there were changes in the emission spectra, and the emissions of the chloroform or dichloromethane adsorbed compound showed emission spectra that were similar to the unsubstituted one (**1.9**). This was due to a reversible change of the stacking patterns caused by chloroform to have or not have dipolar stacking, subsequently affecting the respective emission spectra.

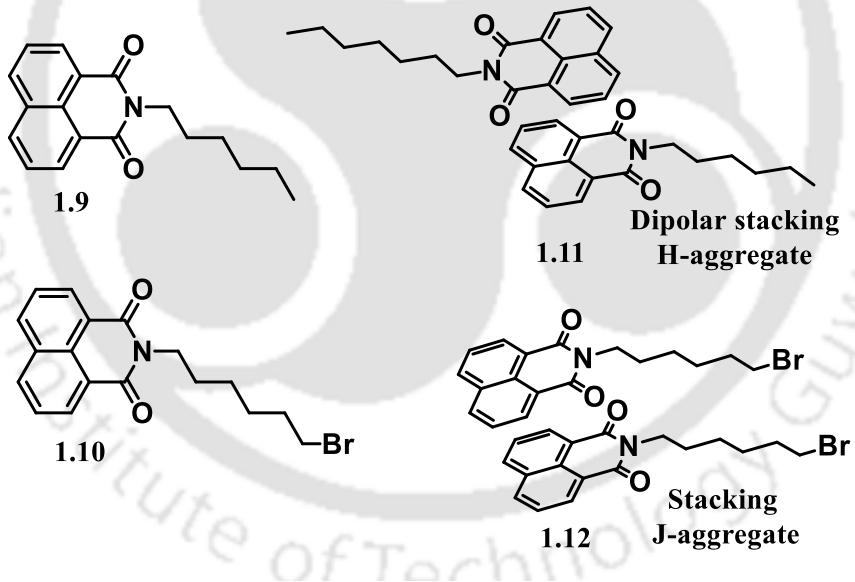

Figure 1.5: 2-Hexyl-1H-benzo[de]isoquinoline-1,3(2H)-dione (**1.9**) and 2-(6-bromohexyl)-1H-benzo[de]isoquinoline-1,3(2H)-dione (**1.10**) and their observed stackings.

The glycine derivative, N-glycidyl-1,8-naphthalimide (**1.13),** formed gels in a mixed solvent comprising water and dimethyl sulphoxide. Imidazole-tethered naphthalimide derivatives (**1.14**) were used to generate various anion-assisted assemblies, for ionic cocrystals and gels. [16] The chiral host N-(2-Imidazol-5-yl-1-carboxyethyl)-1,8-naphthalimide (**1.14**) formed non-

covalent assemblies with different aromatic heterocycles and also with solvent molecules of crystallisations.[17] The **1.14** form self-assembly with quinoline (**1.15**) has the zwitterionic form of the host molecules holding the quinoline through hydrogen bonds and π-stackings. Quinoline molecule encapsulation is shown in Figure 1.6. Channel-like assemblies were formed by interactions between the carboxylate and imidazole units in the self-assemblies. The guest molecules occupied the voids. The guest molecules are held by π-π, C-H···O interactions. The hydrogen-bonded self-assemblies of the cyclic dipeptide tethered naphthalimide, 2-(4-((2S,5S)-5-ethyl-3,6-dioxopiperazin-2-yl)butyl)-1H-benzo[de]isoquinoline-1,3(2H)-dione(**1.16)** shown in Figure 1.6 were investigated.[18] The assembly was formed by the non-covalent interactions of the naphthalimide and dipeptide, they showed aggregation-induced emission. The emission of the compound was affected by selective interactions with phenolic **c**) to

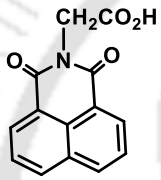

1.13

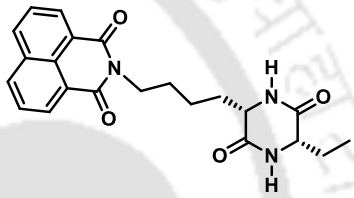

1.16

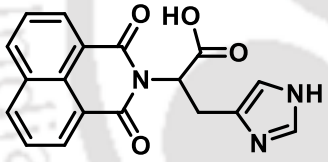

1.14

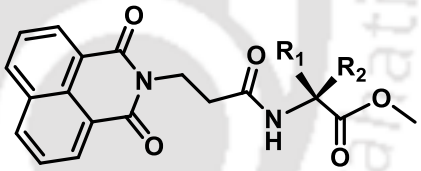

1.17a R_1 = CH-$(CH_3)_2$, R_2 = H
1.17b R_1 = H, R_2= CH-$(CH_3)_2$
1.17c R_1 = CH_3, R_2 = CH_3

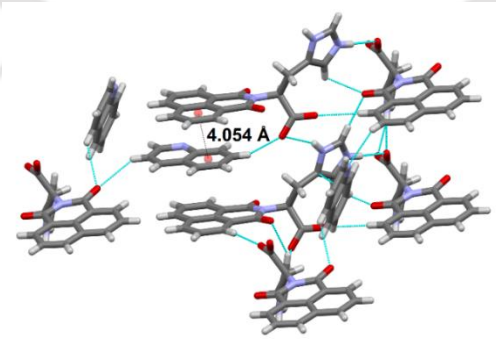

1.15

Figure 1.6: Amino acid-derived N-substituted-1,8-naphthalimides,**1.13** and **1.14;** and **1.5** is the self-assembly of the host-guest complex of **1.4** with quinoline.

drug molecules, doxorubicin, and rifampicin. Those drug molecules could be sensed at nanomolar concentrations. Small chiral peptide units were connected to naphthalimide (**1.17a-**The **1.6** and **1.7** are peptide-derived 1,8-naphthalimide prepared N-functionalized optically active assemblies. The peptides such as naphthalimide-βAla-^{l}Val-OMe and naphthalimide-βAla-^{d}Val-OMe (Ala = alanine, Val = valine, OMe = methoxy group) formed self-supported gels of J-aggregates. Based on optical activity and circular dichroism it was suggested that the self-assembling among the peptide bonds affected the π–π stacking among naphthalimide rings in self-assemblies to regulate the helicity.[19] Benzene carboxylic acid derived naphthalimides serve as hosts for quinoline and pyridine. They provide examples of assemblies in which the host and guest form self-assembled structures to

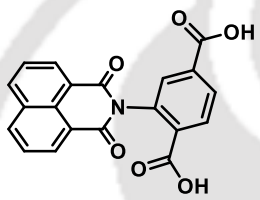

1.18

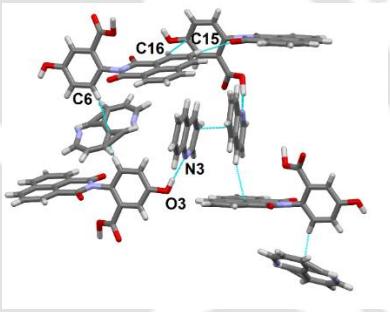

1.19

Figure 1.7: 2-(1,3-Dioxo-1H-benzo[de]isoquinolin-2(3H)-yl)terephthalic acid (**1.18**) and its self-assembly with quinoline molecules (**1.19**).

provide space and recognize another guest of the same or different kind. Hence, they have the scope to prepare multi-component non-covalent assemblies. In such assemblies, the amounts of guest molecules could be incorporated in different amounts concerning the hosts.[20] One such example **1.18,** (1,3-dioxo-1H-benzo[de]isoquinolin-2(3H)-yl)terephthalic acid, provides three different environments to three quinoline molecules **1.19** by forming a 1:3 host-guest complex with quinoline molecules.

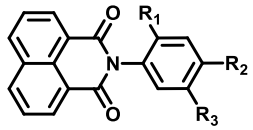

R_1= CO_2H, R_2 = OH, R_3 = H 1.20a

R_1 = OH, R_2 = H, R_3 = CO_2H, 1.20b

R_2 = H, R_2 = CO_2H, R_3 = OH; 1.20c

1.20

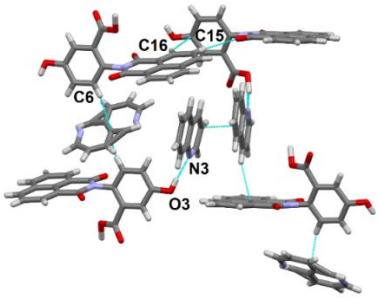

1.21

Figure 1.8: Structures of hydroxycarboxylic acid tethered 1,8-napthalimides **1.20a-c** and **1.21** is the non-covalent assembly of **1.20b** with quinoline.

Each of the cyclic imide hosts **1.20(a)-(c)** shown in Figure 1.8 has hydroxybenzoic acid tethered to 1,8-naphthalimide. These form host-guest complexes with pyridine and quinoline. The assemblies of the host-guest complexes were primarily formed as the consequence of hydrogen bonds involving the carboxylic acid and hydroxyl groups. Whereas, the π- stackings between the 1,8-naphthalimide rings in the assemblies had resulted in the formation of extended supramolecular assemblies.[21] They adopt channel-like structures, and the guest molecules fill up the voids within the channels. One of the assemblies of a host-guest complex of **1.20b** with quinoline **1.21** is shown in Figure 1.8. The host-guest complex retained the quinoline by having C-H···π, O-H···N interactions.

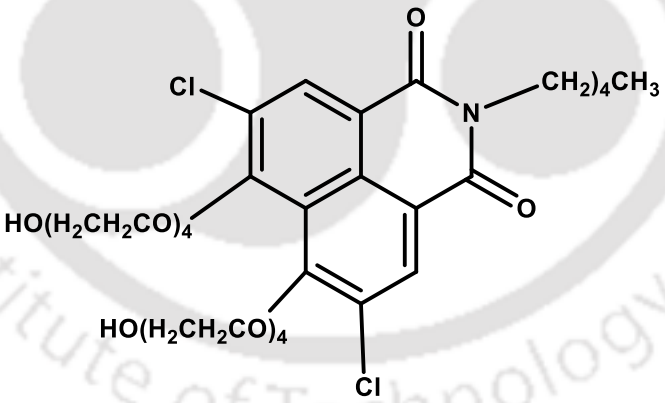

1.22

Figure 1.9: An amphiphilic 1,8-naphthalimide derivative (**1.22**).

The hydrophobic part linked to naphthalimides enhances solubility in non-polar solvents, and having appropriate polyether supramolecular sites, they serve the purpose of crown ether-like bindings. The advantage of such a system is in having the naphthalimide as the signal transduction site. Accordingly, long-chain hydrocarbon molecules of self-assembled N-functionalized naphthalimide derivatives serve as amphiphilic probes. The compound shown

in Figure 1.9 systems having polyethylene glycol parts linked to the 3 and 5 positions of the naphththalimide ring, were described to serve as fluorescence signal reporting units. They assemble to provide assemblies resembling the assemblies of water channels of biological membranes.[22]

From the above discussions, the pertinent points found are that the different types of assemblies of naphthalimides can be generated by stacking the naphthalimide groups differently and the substituents at the naphthalimides not only control the electronic properties but also provide a newer look to assemblies that modulate the optical properties. In guest binding, the weak interactions such as C-H···O, C-H···π interactions of guests with naphthalimide rings have a role in modulating the composition of the host-guest complex.

1.3: Self-assembled metal complexes having 1,8-naphthalimide-derived ligands

The varieties in the stacked structures of naphthalimides provide scopes to form different assemblies, which have been extended to assemblies of different metal complexes derived from naphthalimide-based ligands. The naphthalimide-based pyrazole ligand **1.23** (Figure 1.10) was used for the preparation of the silver complex.[23]

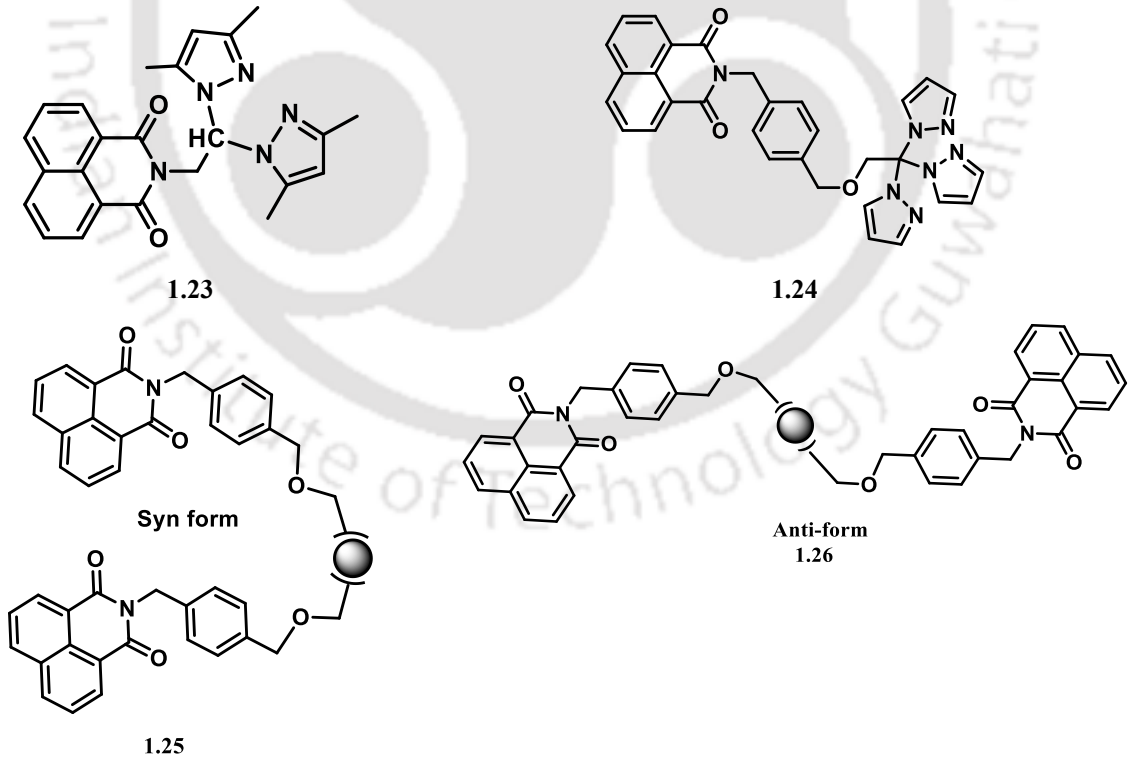

Figure 1.10: Two examples of pyrazole-based naphthalimide tethered ligands; *Syn*- (**1.25**) and *anti*- (**1.26**) forms in copper complexes (balls are copper ions and the concave part is one *tris*-coordinate ligand).

The four-coordinate mononuclear complex [Ag(**1.23**)$_2$]BF_4 is formed by the coordination of nitrogen atoms of the ligands on the pyrazole linker. In this complex the naphthalimide unit did not participate in coordination but provided a supramolecular dipolar π···π stacking among the naphthalimides of each neighboring molecule 1-D chain. The tris(pyrazolyl)methane-based 1,8-naphthalimide ligand (**1.24**) provided two different forms of the hexa-coordinate copper complexes. Both the forms had three nitrogen atoms of three pyrazole rings of the ligand, coordinated to one copper ion. One of the forms had a *syn* (**1.25**) and the other had an *anti* (**1.26**) form as shown in Figure 1.10. The π···stacking interactions between the 1,8-naphthalimide rings guided their supramolecular structures.[24] The pyridyl 4-nitro-1,8-naphthalimide-based ligand **1.27** formed different mononuclear and dinuclear copper complexes, two of which are shown in Figure 1.11. The self-assemblies of the complexes had extensive π-interactions, including π···π, nitro···π, solvent···π, and C=O···π interactions.[25]

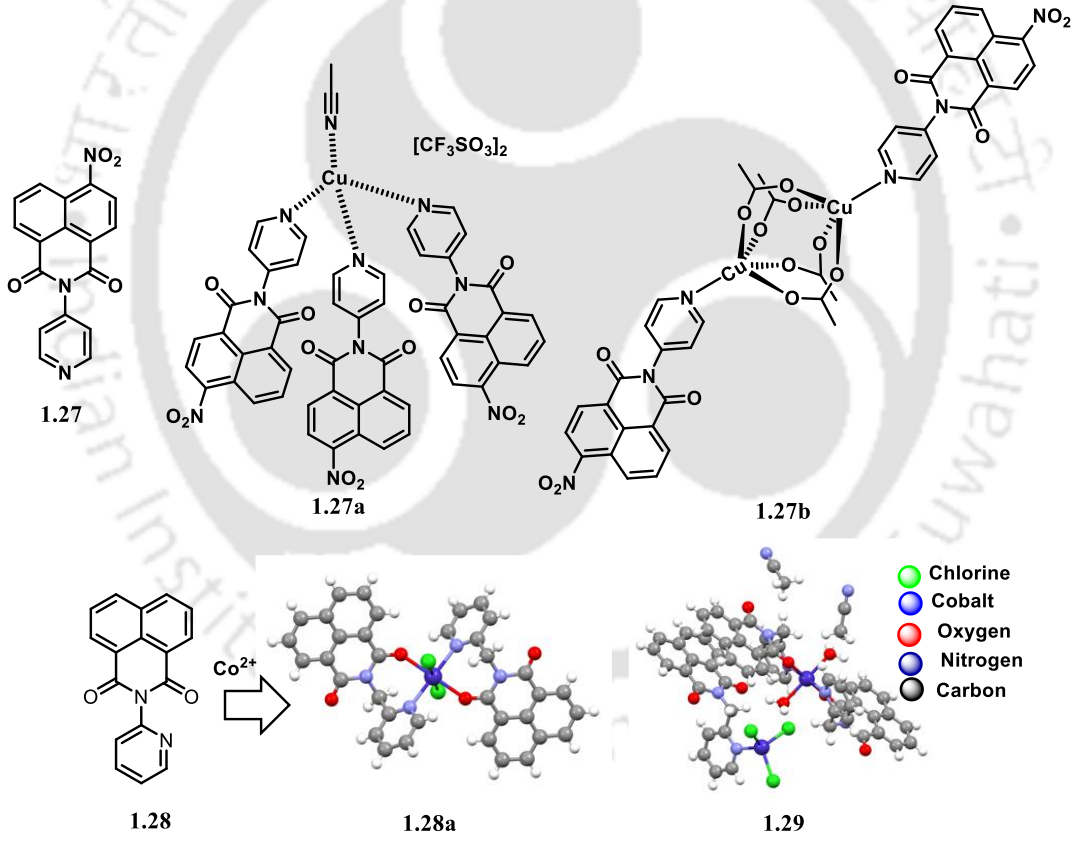

Figure 1.11: Example of a mono-nuclear (**1.27a**) and a bi-nuclear (**1.27b**) copper (II) complex of **1.27**. The **1.28a** and **1.29** are crystal structures of two different copper complexes with **1.28**.

The pyridine-based naphthalimide complexes form a wide range of coordination complexes with d-block metal ions. The coordination mode of the ligand in these complexes was dependent on the projection of the nitrogen atom of the pyridyl unit with respect to one of the

carbonyl groups of 1,8-naphthalimide. The 4-piyridy-1,8-naphthalimide derivatives formed monodentate complexes by coordinating with different metal ions exclusively through the nitrogen atom of the pyridine ring. Among those complexes of the *N*-(3-pyridyl)-4-nitro-1,8-naphthalimide with bivalent manganese or cobalt ions provided metallo-gels. These gels were thermally and chemically reversible. On the other hand, the 2-pyridyl substituted ligand **1.28** formed chelate complexes with Mn, Co, and Zn ions.[26a] In such cases, the pyridyl nitrogen atom and one of the oxygen atoms of the naphthalimide are coordinated to metal ions. Two such cobalt complexes **1.28a** and **1.29** are shown in Figure 1.11 and have interesting features despite originating from the same ligand and metal ion. Complex **1.28** was a bis-chelated complex [Co(**1.28**)$_2$Cl$_2$], it has two 1.28 ligands forming the square planar part of an octahedron arrangement and the other two sites were occupied by chloride ions. Whereas, the complex **1.29** [Co(**1.28**)$_2$(OH$_2$)$_2$][Co (**1.28**) Cl$_3$]$_2$·4MeCN was a complex, that had the cationic part comprised of two ligands and two water molecules coordinating to a cobalt ion. The anionic part had a cobalt ion linked to the ligand in a monodentate fashion with three chloride ions coordinating to a cobalt ion. Two of such anions had neutralized the charge of the cationic part to form the complex. The tetrachlorocuprate salt of 3-picolyl-1,8-naphthalimide was a redox-active compound[26b] showed an electrochemical couple for naphthalimide anion radical formation.

Bis(2-picolyl)amine substituted 1,8-naphthalimide ligand **1.30** formed a tetra coordinate zinc(II) perchlorate complex (**1.31**). This complex was able to recognize pyrophosphate and it formed a diphosphate complex **1.32**. The transformation followed fluorescent changes of the parent ligand in an aqueous solution at two stages (Figure 1.12). The ligand was non-fluorescent, whereas the zinc perchlorate complex with the ligand was strongly fluorescent. Upon interaction with biphosphate, the phosphate complex formed was weakly fluorescent. The recognition of the phosphate binding process was extended to the biological application of the complex to monitor intra-cellular pyrophosphate.[27] and quenched upon the addition of polyphosphate.

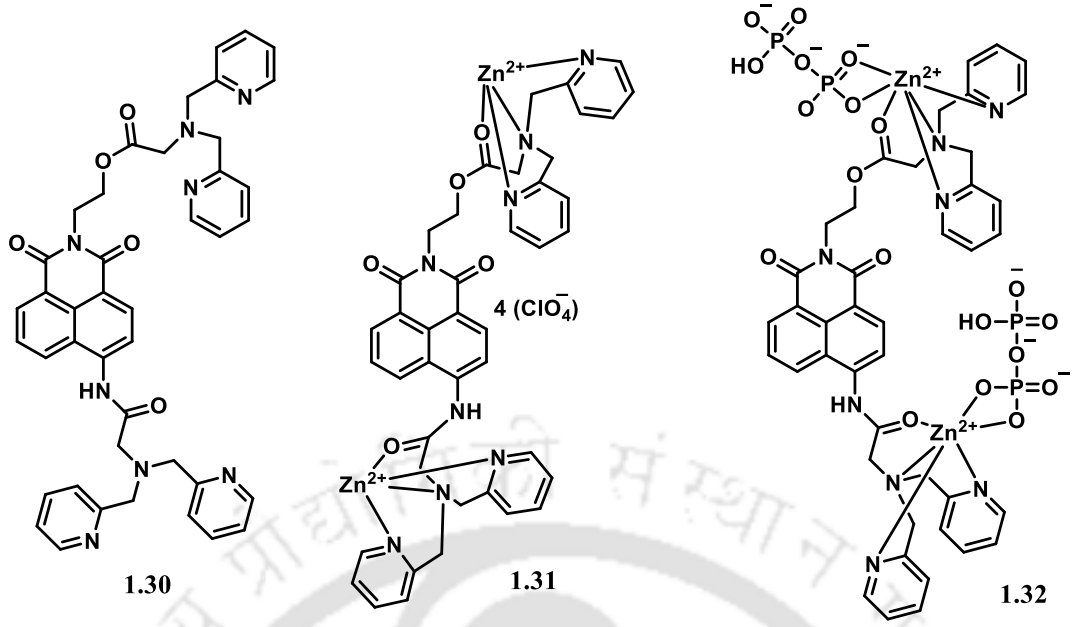

Figure 1.12: Bis-picolylamine based 4-amino 1,8-naphthalilimide derived ligand and the zinc complexes used for phosphate recognitions.

In biological conditions also the fluorescence of the ligand was enhanced by adding Zn^{2+} ions The solvothermal reaction of the (*S*)-2-(1,8-naphthalimido)-3-hydroxypropanoic acid (**1.33**) with cesium hydroxide yielded a cesium complex **1.34.** The crystal structure of the complex showed that its structure had the cesium cations were held together by bridging carboxylates.[28] The cesium ions were at two different ligand environments, one cesium ion had a distorted

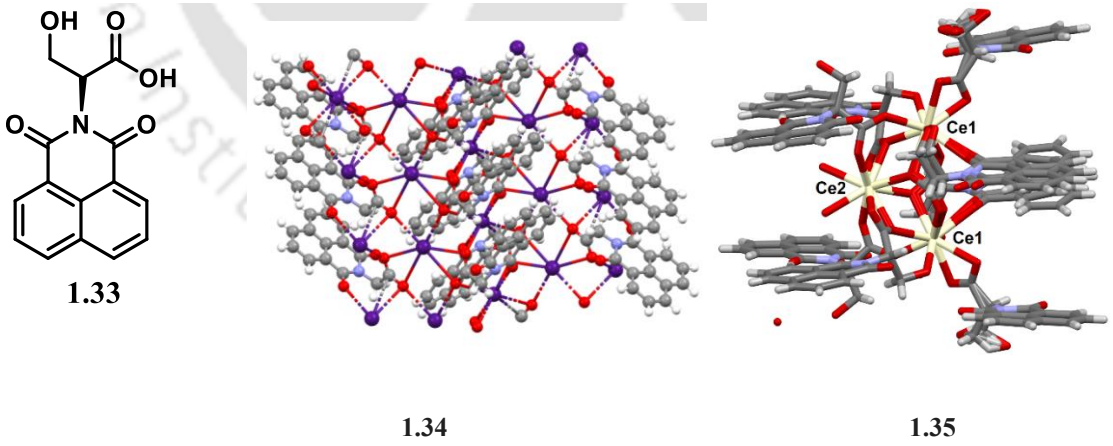

Figure 1.13: The ligand (*S*)-2-(1,8-naphthalimido)-3-hydroxypropanoic acid **1.33**. The binuclear cesium complex **1.34** and trinuclear cerium complex **1.35** of the ligand.

octahedral environment, and it was bound to two carboxylates and had cesium π-interactions. The other cesium ion had adopted a planar geometry (Figure 1.13). The 1,8-naphthalimide rings were assembled to provide sheet-like arrangements by π-stacking interaction.

The optically active lithium salt of (*S*)-2-(1,8-naphthalimido)-3-hydroxypropanoic acid **1.33**, formed octa-coordinate (*S*)-2-(1,8-naphthalimido)-3-hydroxypropanoate (**1.33**$^{-}$) complexes with trivalent La, Ce, Sm, Eu, Gd, Tb, and Dy ions. The structure of the cerium complex **1.35** had two independent types of coordination environment for cesium ions, which is shown in Figure 1.13. The complex underwent isomorphous replacements with Tb or Gd and Tb ions to form non-stoichiometric complexes $[Ce_{2.3}Tb_{0.7}(\mathbf{1.33}^{-})_8(OH)]\cdot(H_2O, EtOH)_x$ and $[Ce_{1.4}Gd_{0.3}Tb_{1.3}(\mathbf{1.33}^{-})_8(OH)]\cdot(H_2O, EtOH)_x$ respectively. The stoichiometric metal complexes were isostructural, each had trinuclear, carboxylate-bonded *intertwined M* helices, with a pitch of 56 Å. These helices were stabilized by π-stackings among the 1,8-naphthalimides. [29]

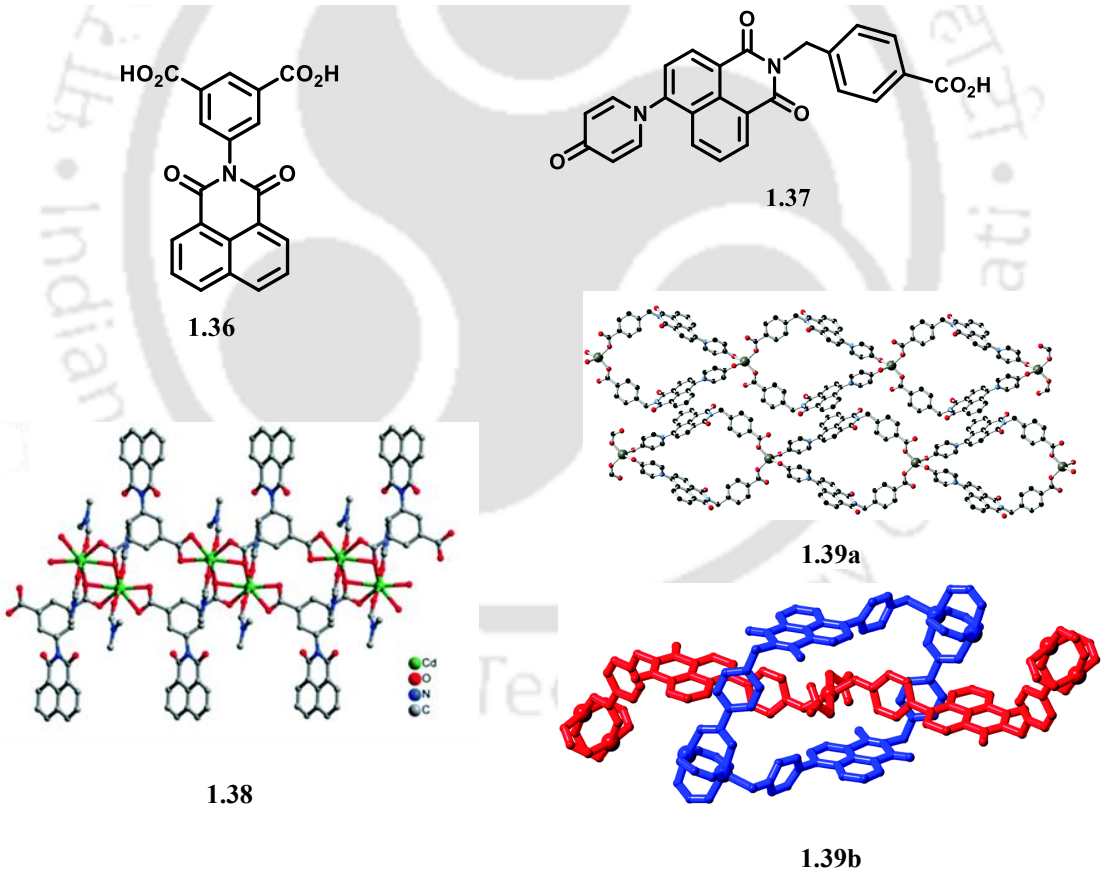

Figure 1.14: The compound **1.36** and its cadmium coordination polymer **1.37**; The compound **1.38**, mononuclear node constructed from it **1.39a**; and a rotaxane-like structure **1.39b** of its coordination polymer.

N-(5-isophthalic acid)-1,8-naphthalimide **1.36** is a versatile ligand to provides different metal complexes with lanthanide, barium, uranyl, calcium, thorium, zinc, and cadmium ions.[30] The **1.36** derived one-dimensional cadmium coordination polymer [Cd(**1.36** dicarboxylate)$(DMF)_2 \cdot DMF$] (**1.37**) had DMF molecules as a ligand as well as solvent of crystallization. It had bidentate chelating carboxylates as well as side-on η^1-oxy-bridged carboxylate binding to form a linear coordination polymer. The coordination polymer showed mechanoresponsive luminescent properties.[31] The powdered and crystalline samples of the coordination polymer had a large difference in π-stackings in their respective packing. As a consequence of the pressure applied while grinding the samples, the stacking patterns were disrupted; hence luminescence intensity of the powdered sample was enhanced. On the other hand, different forms of solvated zinc coordination polymers of the same ligand **1.36** were crystallized from solutions in different solvents. The DMSO or DMF solution provided the respective solvate. The anhydrous form of the coordination polymer had different packing patterns from the solvated ones. Each of these coordination polymers was aggregated differently in different solvents, providing aggregation-induced emission at different wavelengths characteristic of the respective polymer.[32]

The 4-(4-pyridonyl)-1,8-naphthalimide-derived carboxylic acid (**1.38**) provided two independent forms of coordination polymers with copper(II) ions at different crystallization conditions. One coordination polymer was comprised of a linear chain having mononuclear copper nodes **1.39a,** whereas, the other form had binuclear paddle wheel nodes. The second form was permanently porous, it was non-fluorescent, and had polyrotaxane architecture **1.39b** and linear structural features[33] as shown in Figure 1.14.

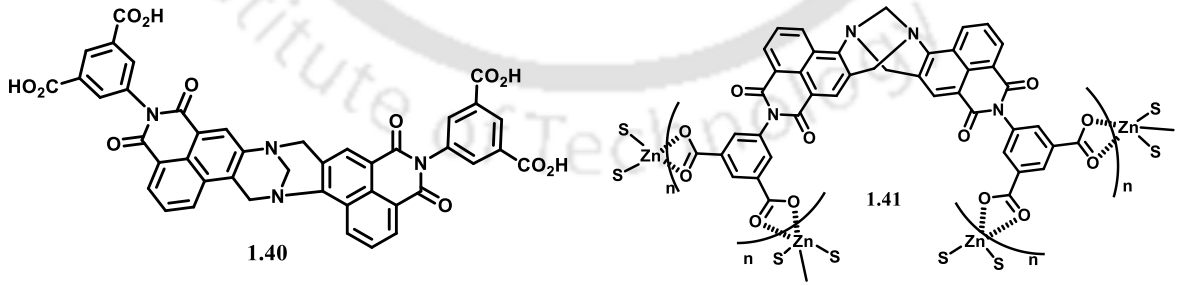

Figure 1.15: Bis-naphthalimide based ligands having diazabicyclo constrained geometry.

The dicarboxylic acid-based bis-naphthalimides having intervening diazabicyclo components such as **1.40** serve as ligands to construct one-dimensional zinc coordination polymers. The **1.40** had a semiflexible part that provided zig-zag structure **1.41** as shown in Figure 1.15. The aqueous suspension of the coordination polymer showed intense green fluorescence emission

at 520 nm. This emission originated from internal charge transfer which was quenched by nitrophenolic compounds such as including 4-nitrophenol, 2,4-dinitrophenol, and picric acid. Hence it had application in detecting those nitro-phenolic compounds in aqueous media.[34]

The metal ion-dependent packings were observed in the self-assemblies of mixed ligand dicarboxylate coordination polymers having 4-picolyl-1,8-naphthalimde (**1.6**) as one of the ligands.[35] In these cases, the flexibility and the geometry of the dicarboxylic acids played a key role. These packing patterns of the complexes are shown in Figure 1.16. The effect of stacking was observed in the single-chain magnet property shown by the cobalt coordination polymer.

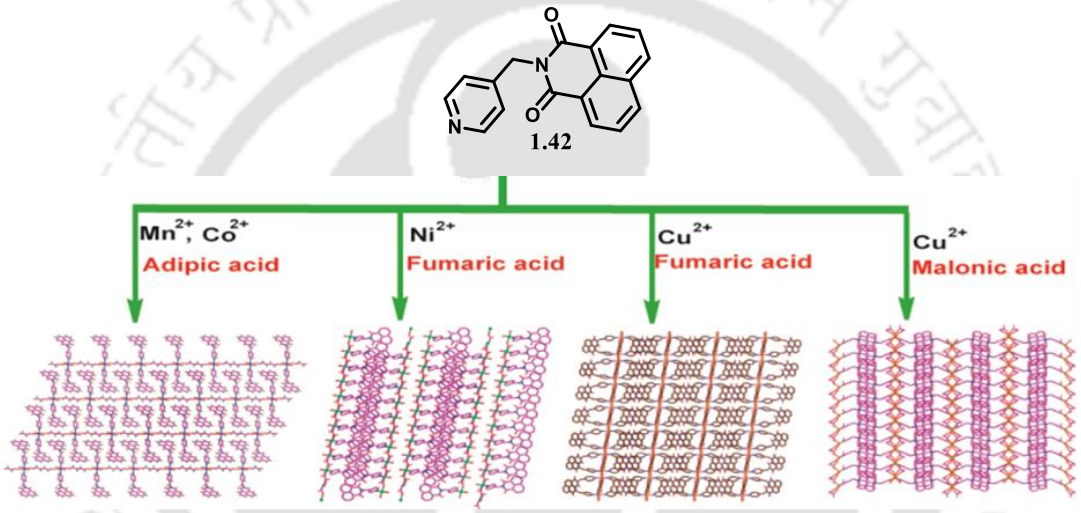

Figure 1.16: Packing patterns of mixed-ligand which coordinated to different metal dicarboxylate complexes of **1.6**.

The coordination numbers and the orientations of the N-(3-imidazol-1-yl-propyl)-1,8-naphthalimide[36a] ligands in various complexes of first-row transition metal ions were different. Hence, introducing the flexible group (propyl group in this case) as an intervening unit to link an imidazole with 1,8-naphthalimide provided avenues to prepare various metal complexes each having different conformation adjustments of the ligand. Depending on the anions, the composition and the coordination numbers were also varied in those complexes. These had influenced the photoluminescence of the complexes. On the other hand, hydroxycarboxylic acid derived naphthalimide for coordination polymer in pyridine that had coordinated pyridine as well as pyridine as guest molecules.[36b]

These examples have suggested diverse openings to modulate structures and compositions of the inorganic complexes having 1,8-naphthalimide based ligands. The electronic, directional,

and coordination properties of the central metal ion vary and the naphthalimide units in such complexes have key roles to affect the photo, electro, magnetic, and thermo-chemical properties.

1.4: Assemblies of naphthalimide derivatives and photo-physical properties

The naphthalimide derivatives are studied to generate donor-acceptor conjugates for use in advanced materials.[37] They are used as dyes, brightening agents, sensors, bioimaging, photovoltaics, and light-emitting diodes. Naphthalimide derivatives with different photophysical and electronic properties are easily prepared in laboratories in cost-effective manners. 1,8-naphthalimide hydrazone derivatives show linear and nonlinear optical (NLO). [38] Chiral 1,2-diaminocyclohexane-based molecules anchored to 1,8-naphthalimide fluorophores show strong circularly polarized luminescence emission.[39] The emission signals were reversed in the aggregated state. The photochemical transformations of naphthalimides result in new compounds with unusual and complicated organic scaffolds. [40] Iodonium salt of naphthalimide derivative (**1.43**) acted as a photo-initiator in the polymerization reactions of methacrylate, epoxide, and vinyl ether. [41]

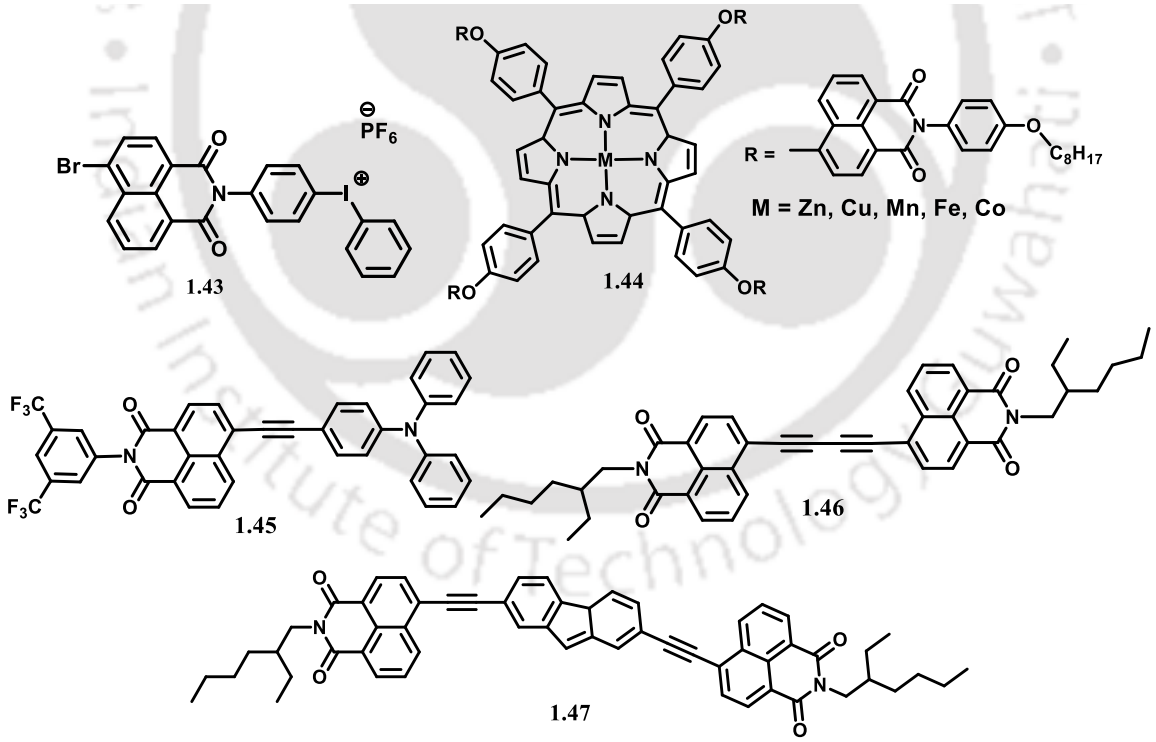

Figure 1.17: Examples of a photo-initiator (**1.43**), porphyrin-based naphthalimides (**1.44**), and naphthalimide-based dyads connected by rigid spacers (**1.46-1.47**).

The naphthalimide-derived porphyrin-based metal complexes **1.44** are shown in Figure 1.17 had showed two characteristic absorption bands. The Soret bands were observed in the range of 380-450 nm and the Q bands in the range of 450–660 nm. The metal complexes serve as light-harvesting antennae. They showed ON and OFF emission properties depending on the central metal complexes bound to the porphyrin.[42]

The naphthalimide-units connected to another chromophore through linear and rigid acetylenic bond **1.46** is an example of donor–π–acceptor showed fluorescence emission through radiative and non-radiative paths. The *bis*-naphthalimdes derivatives **1.46-1.47** have combinations of donor–π–acceptor units. It showed a reversible amorphous-crystalline phase transition with distinguishable colors.[43] They are stimuli-responsive and showed optical waveguiding behavior with low optical loss coefficients. These effects were reflected in the fluorescence lifetime decay measurements for the monomeric and aggregated states. Based on their electrochemical properties they were projected as air-stable n-type semiconductors.[44] The 1,8-naphthalimide conjugate **1.48** has a dipeptide moiety derived from histidine, it forms J-type aggregation in solid, solution as well as in gel state. The hydrogen bonding of the amide group provided a J-type hydrogen bonded π-stacked aggregate of the compound. The emission of the conjugate was quenched by Fe^{3+} and it provided a means for bioimaging of Fe^{3+} inside mammalian cells.[45]

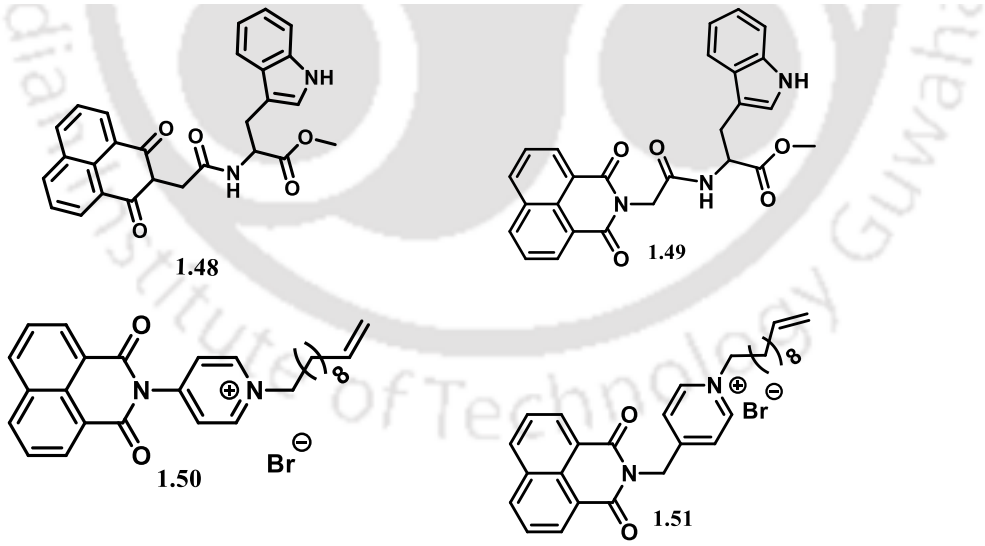

Figure 1.18: Examples of naphthalimide derive with dipeptide or pyridinium salt as linkers.

Reversible fluorescence hydrochromism was observed in the solid state from the 1,8-naphthalimide fluorophore when coupled to amphiphilic pyridinium bromides **1.50** and **1.51**.

Compound **1.51** showed dynamic moisture sorption with a bathochromic shift of 27 nm from blue to green emission. A composite of it with agar-based hygroscopic aerogels had enhanced sensitivity to sense moisture.[46] The 1,8-naphthalimides **1.50** and **1.51** differ in their fluorescence quantum yields due to their molecular flexibilities.[46-47]

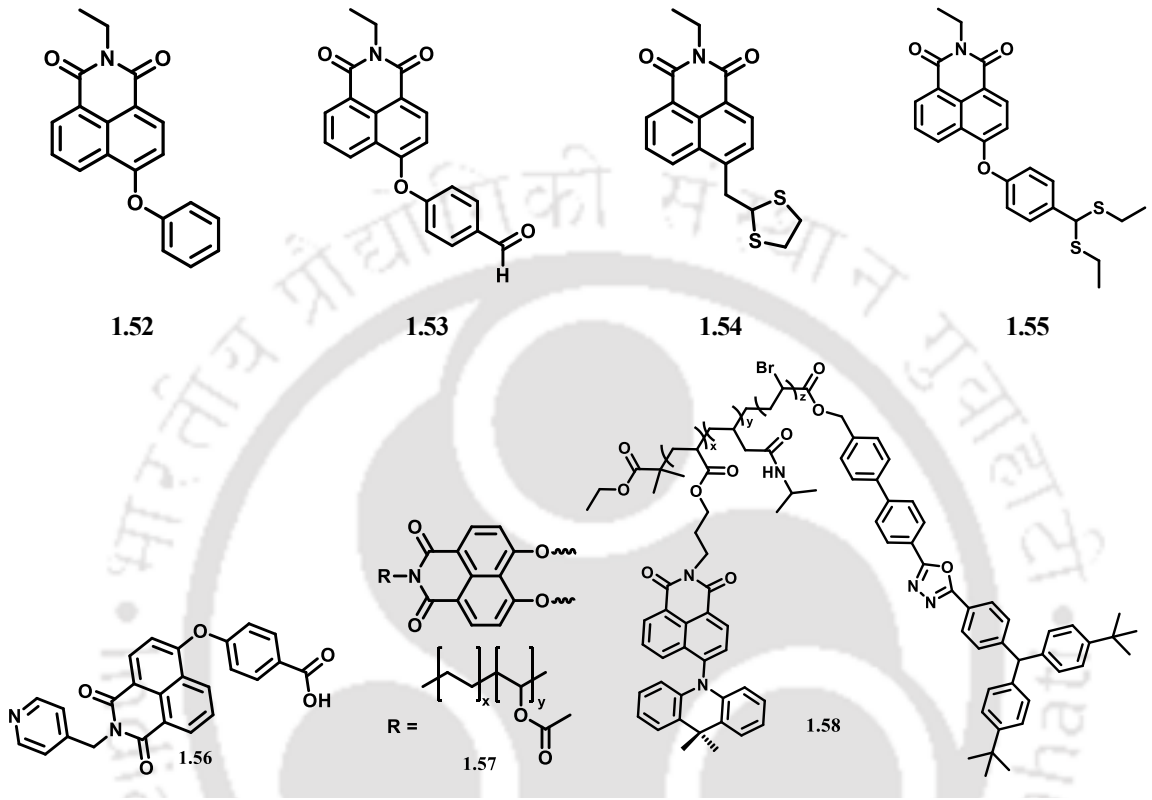

Figure 1.19: Series of 4-functioanlised 1,8-naphthalime derivatives **1.52-1.56**, a polymer linked 1,8-naphthalimide **1.57** and 1.**58**.

A series of N-ethyl 1,8-napthalimides having different functional units at 4-position **1.52-1.55** were designed to elucidate the effect of emission wavelengths. It was found that the presence of electron-withdrawing or donating groups at the 4-positions caused changes in the position of emission wavelengths. On the other hand, the compound *N*-(4-picolyl)-4-(4′-carboxyphenoxy)-1,8-naphthalimide (**1.56**) formed gel in the presence of $\mathbf{K}^+$ ions. The gel could be anchored to silicon support, which had fibrous morphology and was sensitive to thermal, mechanical as well as chemical stimuli[48] which is prepared from the 1,8-naphthalimide derived poly(ethylene-*co*-vinyl acetate) (**1.57** shown in Figure 1.19) served as ultraviolet radiation conversion layer which could absorb UV light and converted to visible light.[49] The polymer **1.58** had exhibited deep-red thermally delayed fluorescence. It had a quantum yield

of approximately 58%. It showed dual emissions at 340 nm and 633 nm, the latter emission peak was attributed to delayed fluorescence from a charge-transfer process.[50]

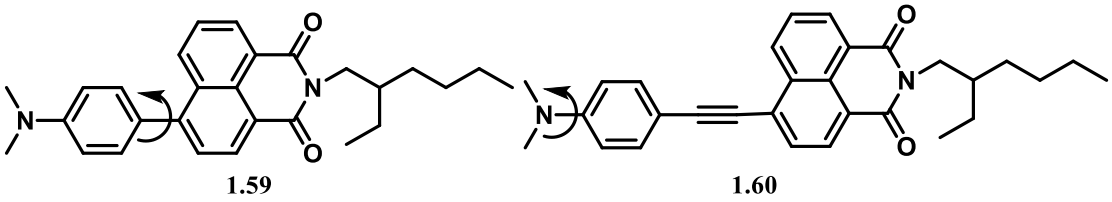

1.59 1.60

Figure 1.20: Examples of compounds showing twisted intramolecular charge transfer emissions.

The compounds **1.59-1.60** showed twisted intramolecular charge transfer (TICT) emissions. Both compounds have electron donor dimethylaniline through different rigid linkers to provide donor-π-acceptor systems. Once either of these compounds was doped in polymer matrixes of different polarities, they showed emission properties that distinguish between the effect of solvation from conformation effects by showing distinct peaks. In non-polar solutions, high fluorescence quantum yields were observed. This property is characteristic of twisted or planar molecules in the excited states. The solvent with higher polarity allowed to tune the Stokes shift but the fluorescence quantum yields of such emissions were low. The low quantum yields from TICT states were due to the twisted state adopted by dimethylaniline by having an orientation of the aryl plane perpendicular to the naphthalimide ring.[51]

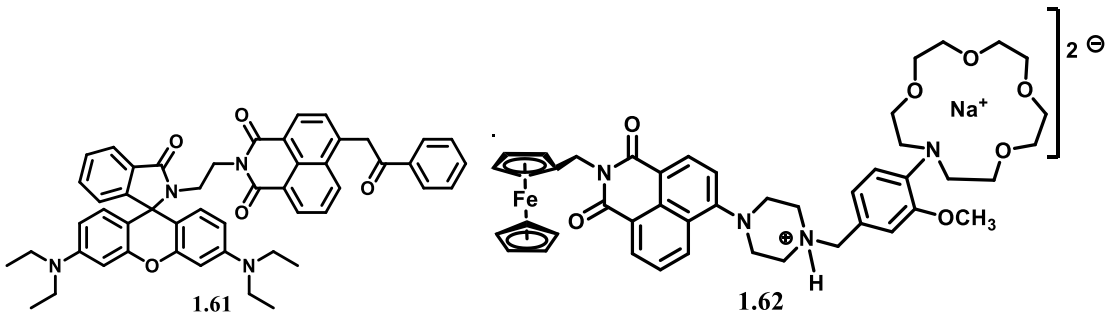

1.61 1.62

Figure 1.21: A rhodamine based and a ferrocene based ionic naphthalimide derivative.

The compound **1.61** is an example trichromophoric system comprised of rhodamine–naphthalimide–benzamide conjugate. The fluorescence emission of it in dimethylsulphoxide was highly affected at a low concentration (<1%) of water in the solution. It also showed pH-dependent emission.[52] The compound **1.62** has an electro-active ferrocene part and a crown ether that binds to sodium ions. The naphthalimide is connected to those units through a cationic tether. This compound undergoes reversible electron transfer in the ferrocene by utilizing ferrocene/ferricenium couple. Furthermore, it has a crown part where the nitrogen atom gets protonated by changing pH. The fluorescence emission of the central naphthalimide

unit could be tuned by adjusting pH or applying appropriate electromotive force.[53] This is an example of a molecular three-input AND logic gate with the naphthalimide fluorophore.

The emission properties change depending on the halogen bond of the bromine atom with the nitrogen atom of an acceptor pyridyl group in self-assemblies of naphthalimide having provision for those interactions. The self-assembly of N-pyridyl 8-bromo naphthalimide had N···Br halogen bonds and dipolar π-stacking and it formed 1D nanowires,[54] it showed green emission. Significant increases in emissions of naphthalimides derivatives were observed upon binding with cucurbituril [7]. Such a cucurbituril [7] supported system was utilized as a displacement assay for the rapid detection of therapeutically relevant drugs.[55] In such detection the cucurbituril [7] formed an inclusion complex by serving as a host for the drugs, that had affected the emission of the naphthalimide bound to the cucurbituril.

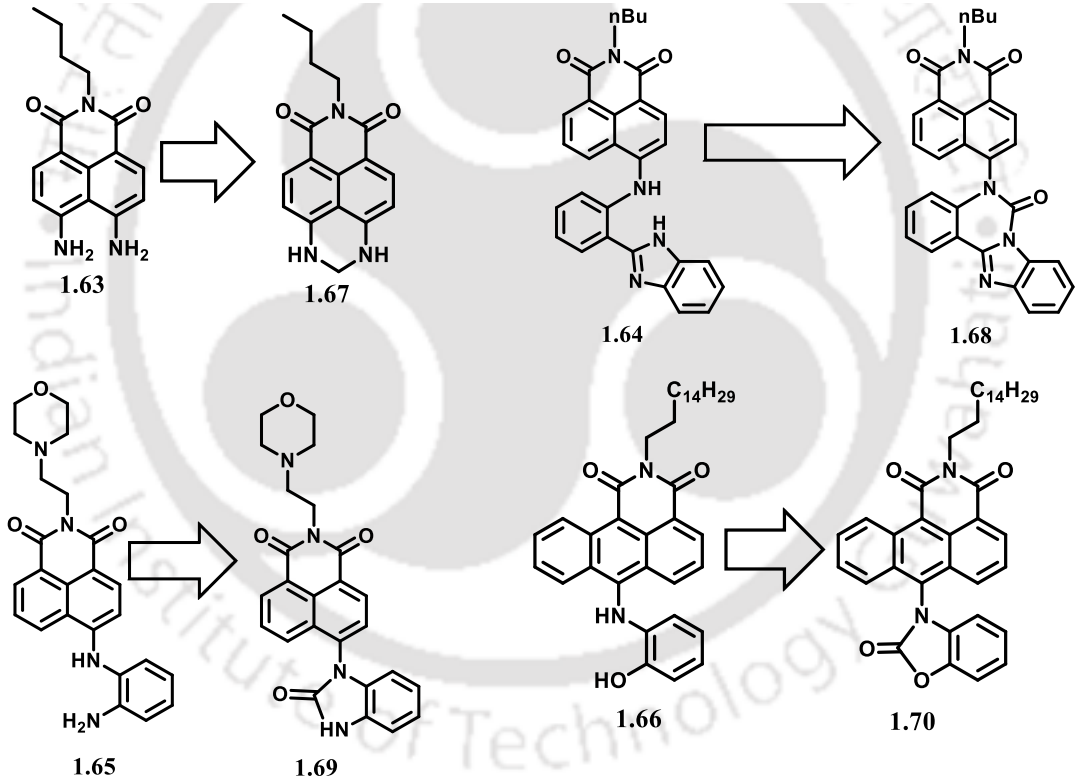

Figure 1.22: Detection of phosgene gas by transforming to **1.67-1.70** to heterocycles after reactions with $COCl_2$.

Phosgene gas is a highly toxic and dangerous chemical warfare agent. Hence its detection is very important. Various naphthalimide based compounds **1.63-1.66** have been used to sense the phosgene gas due to its high reactivity to various functional groups. [56-57] The advantage to for cyclic products by reacting with phosgene by each of these compounds was taken, thereby changing the fluorescence emission of the napthalimide part linked to them. The compounds

underwent cyclisation reactions to form the cyclic products from respective amino-1,8-naphthalimide compounds yielding **1.67-1.70** respectively (Figure 1.21). These probes demonstrated excellent performance in real-world applications, with a detection limit at the nanomolar level.

Picric acid is used as a high-energy compound and as a dye. The picric acid has high acidity, as a consequence it causes protonation of a morpholine containing naphthalimide based receptor **1.71** and converts to salt **1.72** (Figure 1.22). The intramolecular charge transfer emission process of the receptor was affected by the protonation hence the emission of the parent compound was quenched.[58] The morpholine unit had helped to modulate the pH which had enabled an effective cell imaging of picric acid in live cells. The benzamidonaphthalimides show a significant red shift in fluorescence emissions.[59]

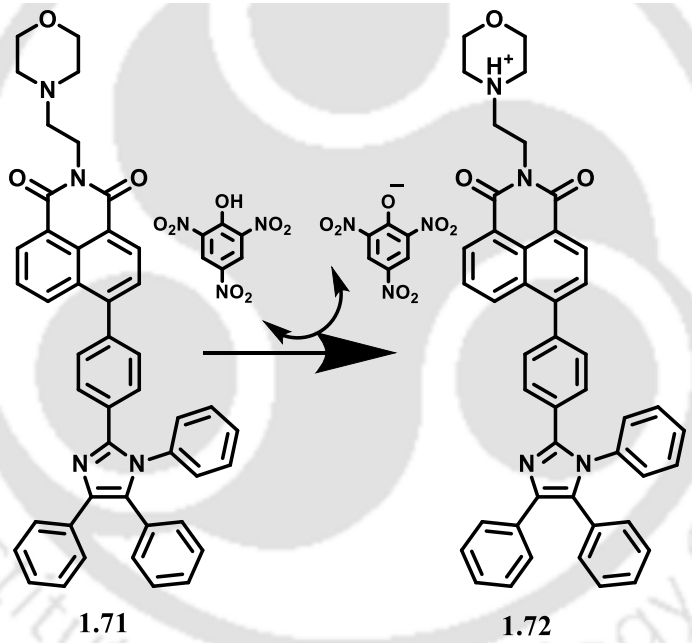

Figure 1.23: A pH responsive napthalimide sensor for binding picric acid.

The applications of naphthalimide unit anchored to another compound effects the properties of another compound in four major ways (a) the properties of the naphthalimide gets influenced, helping in signal transduction, (b) Change the property of another molecule to which naphthalimide is linked, (c) the supramolecular arrangements are modified to collectively get involved in forming new assembly, (d) Overall system behave in a unitary way to provide improved properties.

1.5: 1,8-Naphthalimides in Biological studies

Imide group containing compounds are well known to show antibacterial,[59] antifungal,[60] anti-inflammatory,[61] anti-tumor,[62] anxiolytic,[63] and nerve-conduction-blocking effects[64]. The 1,8-naphthalimide compounds are employed as agents for DNA targeting, [65] in cancer research treatment.[66]

The amino derived bis-naphthalimides derivatives **1.73-1.76** are derived from ethylene diamine, are well known for their anti-cancer activities (Figure 1.24). These compounds have been thoroughly studied and have two common features bidentate ligating portion and other is the intercalating naphthalimide rings. They induce apoptosis by lowering the expression of the Bcl2 protein and releasing cytochrome-c from mitochondria.[67] They interacted with DNA and induced apoptosis in sensitive cells *in vitro* at nanomolar concentrations. Furthermore, substitution on the naphthalimide ring had a significant effect on cytotoxicity.[68] The cleft-like [69] derivatives **1.77-1.78** and related metal complexes such as **1.79-1.80** that are listed in Figure 1.24 were found to show anticancer activity .[70]

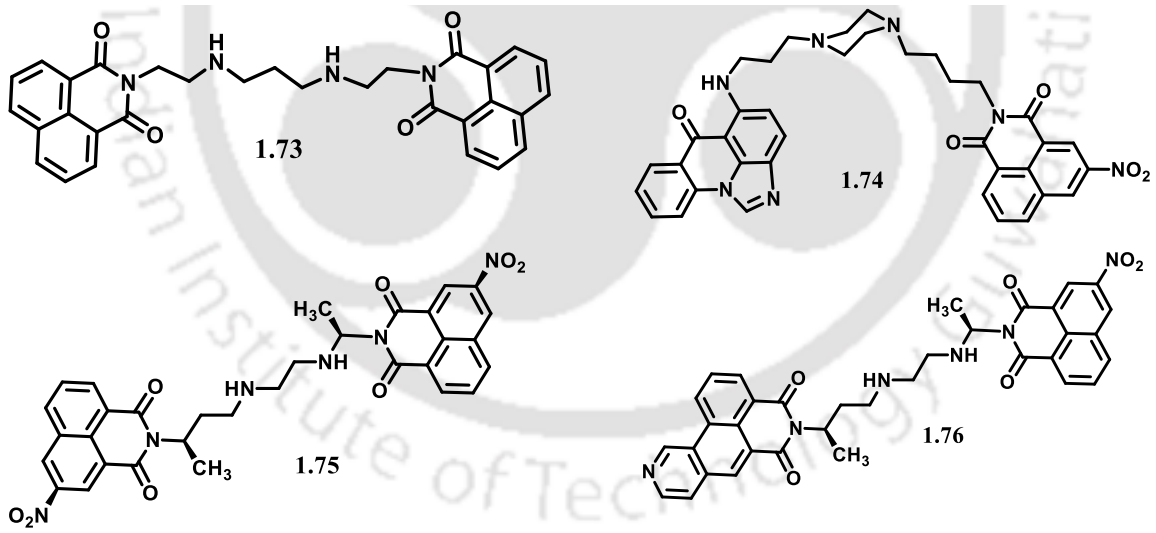

Figure 1.24: Ethylenediamine-derived bis-naphthalimide derivatives that showed anti-cancer activities.

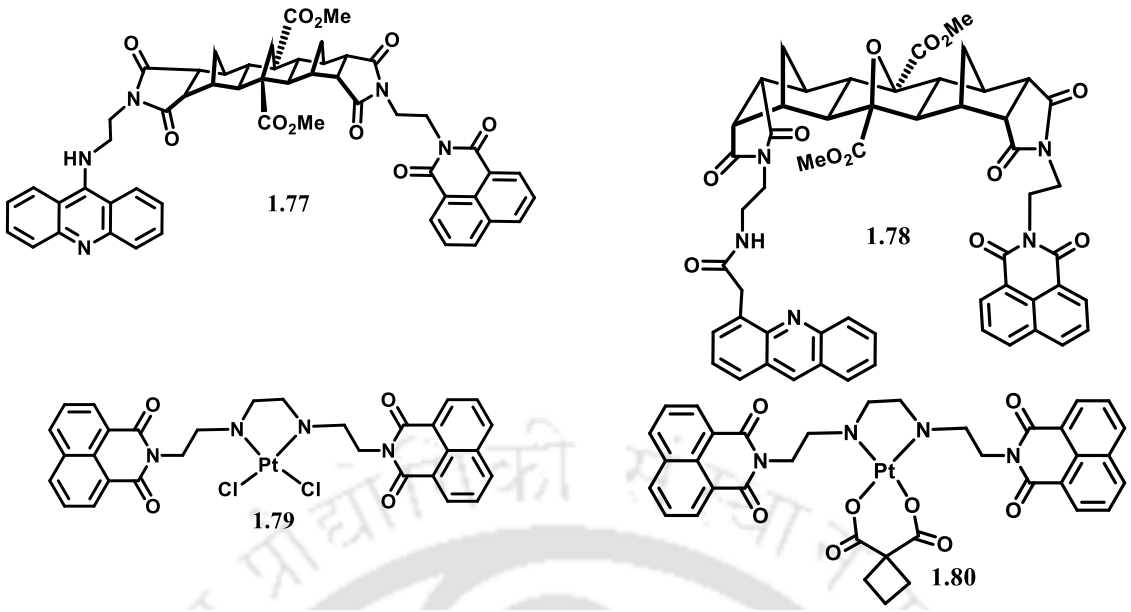

Figure 1.25: Some examples of cleft-like structures of naphthlimides that are studied for anticancer activities.

There also examples of naphthalimides where ionic compounds were tested for enhanced activity and it was found that they show biological activities. The compounds **1.81** and **1.82** of the Figure 1.25 are two such examples. The pH sensitive compound **1.83** also had showed anti-cancer activities. The bis-1,8-naphthalimide containing Tröger's bases **binds** DNA at pH 7.4 and stabilised the DNA helix. Using linear and circular dichroism we further demonstrated that the DNA binding interaction occurs both by intercalation and by groove binding.[71]

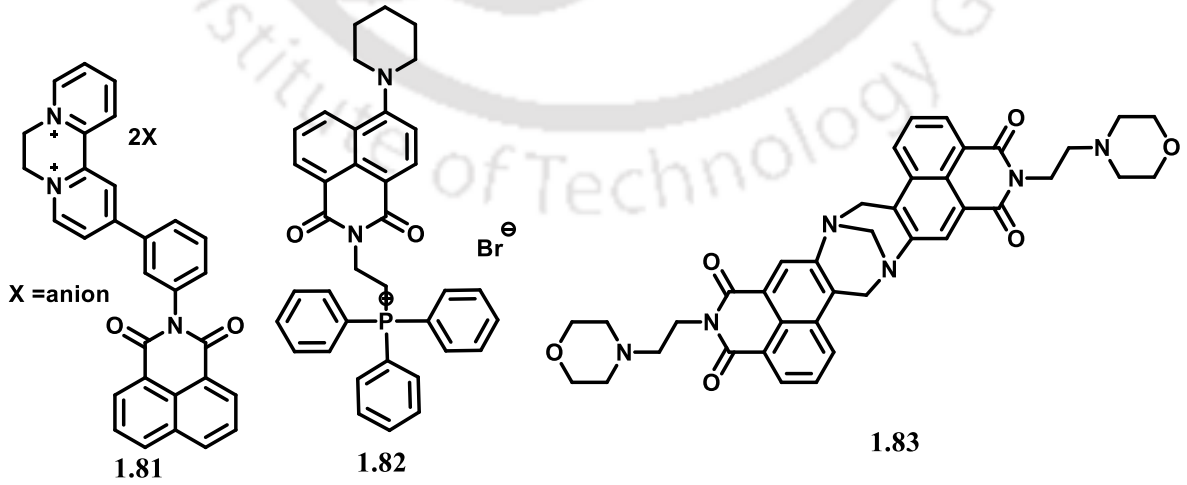

Figure 1.26: Examples of salts and pH-sensitive naphthalimide having anti-cancer activity.

The cobalt complex of 4-picoly 1,8-naphthalimide together with a scorpion-like ligand **1.84** exhibited affinity towards *calf thymus*-DNA (~10^5 M^{-1}). The complex induced DNA cleavage and showed high cytotoxicity against HeLa cervical cancer cells upon UV irradiation.[72] Similar to that tripodal ligands were used to prepare copper complex **1.85** which showed biological activity.[73] It has been further extended to dendrimer-like complex **1.86** showing anti-cancer activity.[74]

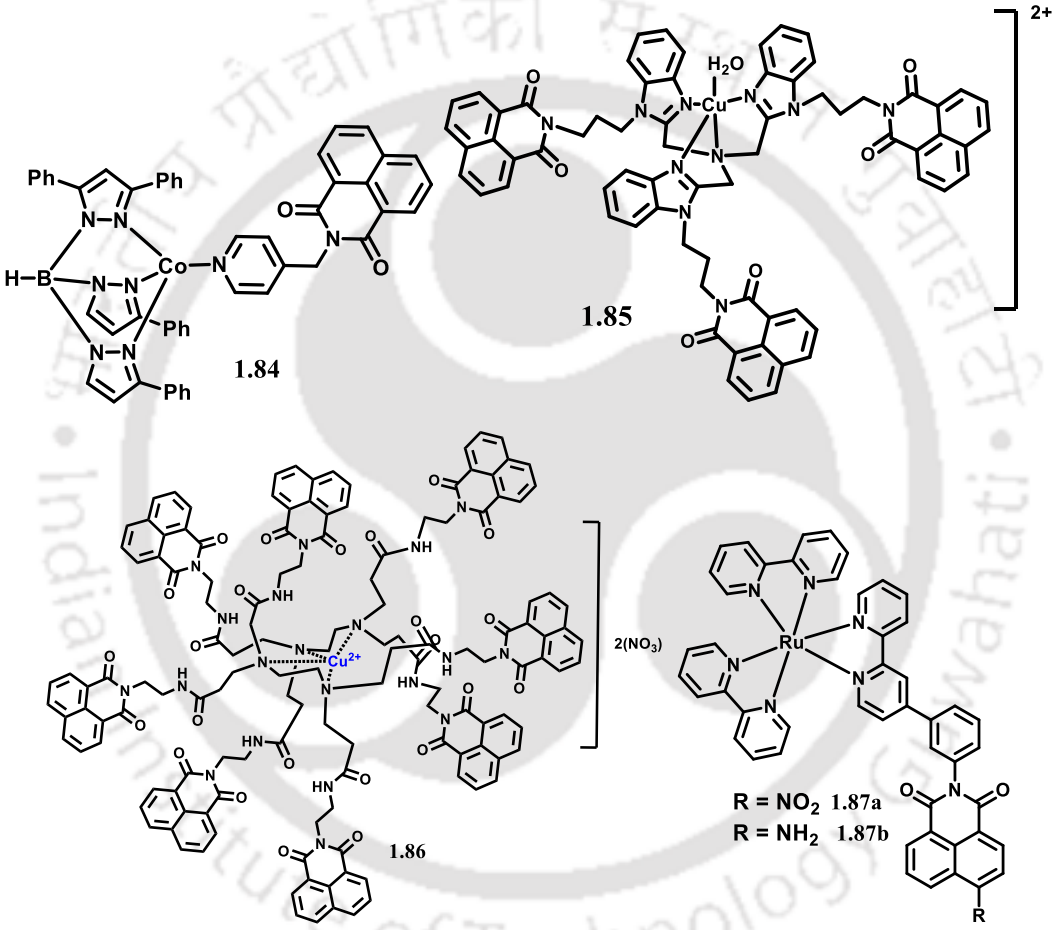

Figure 1.27: Example of scorpion-like ligands in metal complexes 1.84-1.86 and 1.87 is an example of a ruthenium complex with anticancer activity.

Ruthenium(II) complexes **1.87a** and **1.87 b** were found to find DNA.[75] They also caused the photocleaving of DNA under irradiation in an aerated solution (λ_{ex} > 390 nm).[75b] The copper complex of naphthalimide appended tripodal tetradentate ligand binds with ct-DNA. It showed groove binding and also protein binding. It also showed fluorescence quenching of bovine

serum albumin (BSA) involving a static mechanism and affects the conformation of BSA around the tryptophan residues.[76]

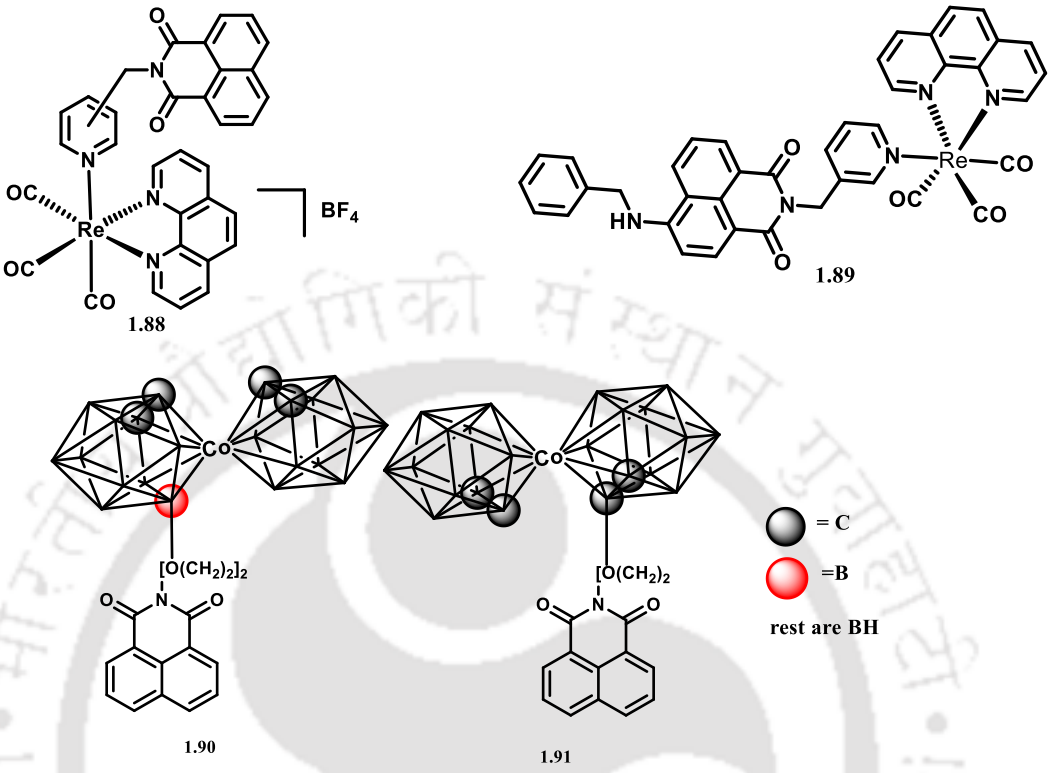

Figure 1.28: Two examples of rhenium complexes **1.88** and **1.89** that showed bioactivities and cobalt carborane complexes, **1.90** and **1.91.**

The rhenium complex *fac*-[Re(1,10-phenanthroline)$(CO)_3$(L)]BF_4 (**1.88**) (L = 3 or 4-picolyl naphthalimide) showed intramolecular charge transfer in the visible region of spectra at 511–534 nm. These complexes also showed ligand-centered and/or ^{3}MLCT emission.[77] The complex had better activity than the drug mebendazole. The rhenium complex **1.89** was useful as a targeting agent for live cell mitochondria. It showed specificity for mitochondrial localization, low cytotoxicity, and a large Stokes shift and was able to perform biological activity in enhanced mitochondrial stress situations.[78] A series of 1,8-naphthalimide–carborane/metallacarborane conjugates were studied for anti-cancer activity and among them the carborane conjugates **1.90**, and **1.91** showed high activity.[79]

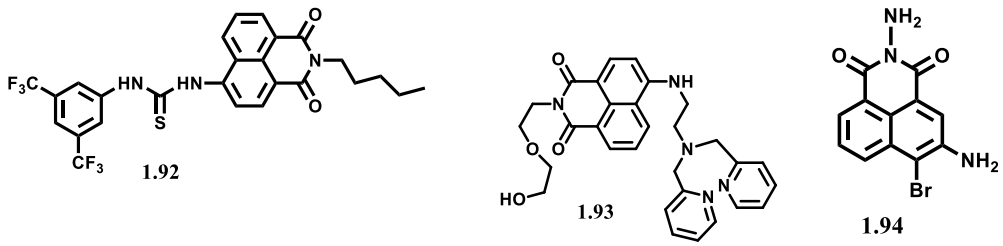

Figure 1.29: Naphthalimides **1.92**, **1.93** used for transport studies, and 1.94 for surface modifications **1.94**.

A mimic of anions transport across phospholipid bilayers in biology was done by using a naphthalimide-based compound **1.92**. The thiourea part had acted as anion-binding sites. Facilitated such anion transfers. Fluorescence studies in cells showed them to cross the plasma membrane and they get localized within the interior of cells.[80] Naphthalimide compounds with Zn^{2+} were also used in imaging in HeLa and HepG2 cells to reveal the penetrability of the sensor.[81] The compound **1.93** showed a fluorescence turn-on response to Zn^{2+}, providing a means to sense the location in zebrafish larvae. The 3-amino-4-bromo-1,8-naphthalimide (**1.94**) is a nuclear imaging agent.[82] It has a strong affinity for salmon sperm DNA with a binding constant of $6.61 \times 10^4\ M^{-1}$. It got intercalated with DNA through the hydrophobic planar naphthalimide, which was confirmed through cyclic voltammetry and circular dichroism. Due to the large Stokes shift and photostability of the compound, it could be used for the imaging of *Legionella pneumophila*,

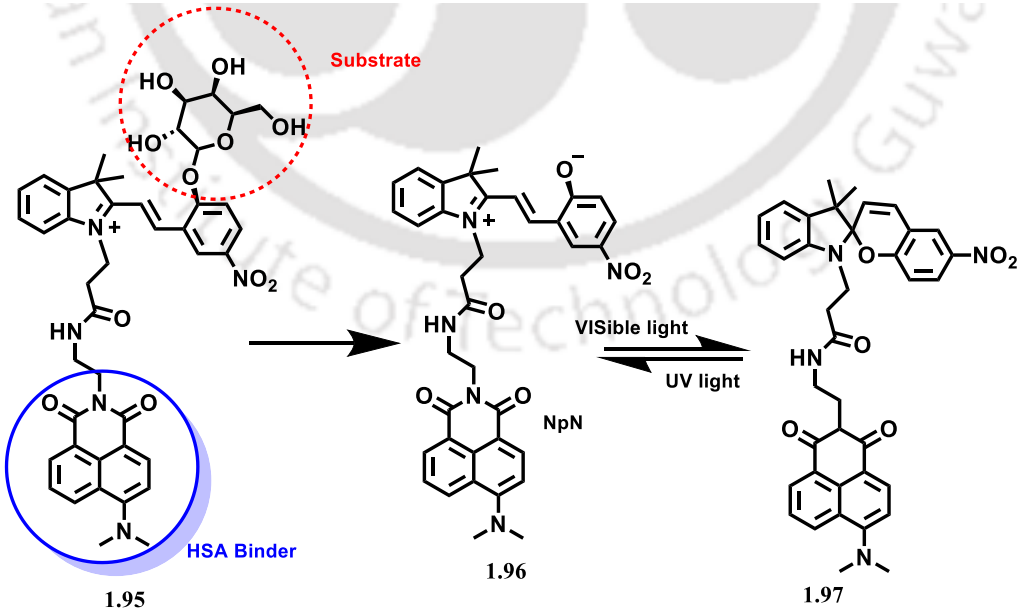

Figure 1.30: Photo-responsive β-galactosidase bound naphthalimide and its different equilibrating forms

The β-galactosidase bound naphthalimide (**1.95**) binds to human serum albumin (HSA). The hybrid 1.95@HSA was used to image ovarian cancer cells.[83] Under biological conditions it releases the glycoside to form **1.96**. The 1.96a is transformed to 1.96b in visible light and could be brought back to **1.96** by radiating with UV light. The parent host had a fluorescence emission at 520 nm, the intensity of it was significantly increased upon binding with HSA, whereas the emission changed while it formed **1.96** or **1.97**.

The naphthalimides not only bind to DNA, but also their environment-sensitive behavior provides large avenues to use them as biological probes. The environment-sensitive nature and higher degrees of ability to make different combinations and also utilize the redox, as well as photoactive properties, make them versatile.

1.6: 1,8-Naphthalimide in the in ion-sensing

The photophysical properties of naphthalimide derivatives are utilized to detect and identify ions. For these purposes, naphthalimides connected to functional units are used to bind an ion, by which the absorption and emission properties of the naphthalimide are influenced. The emissions are affected by various mechanisms, such as photo-electron transfer, twisted intramolecular charge transfer, and Forster resonance energy transfer mechanisms.[84] 4-Amino-1,8-naphthalimide derivatives are widely employed as fluorescent cation sensors for different metal ions due to their ease of functionalization at the 4-position or the imide site. 4-amino-1,8-naphthalimide derivatives possess an amino group with a push-pull effect that enhances the internal charge transfer. This effect originated from the electron-withdrawing ability of the imide unit, which is countered by the electron-donating ability of the amine group. Based on the N- functionalized or naphthalene functionalized groups on the naphthalimide, and also on the design of the binding sites, some examples of the sensing molecules developed by functionalizing the 8-amino position of 1,8-naphthalimides are shown in Figure 1.27. Many of these receptors are selective in detecting different ions and some selected examples of these with detection limits are in Table 1.

Table 1: Specific ion binding by selected 1,8-naphthalimide derivatives and detection limits

Sl. No.	Probe	Ion	Solvent	Detection Limit	Reference
1	**1.98**	Al^{3+}	Methanol	159 nM	85
2	**1.108**	Al^{3+}	Methanol	0.13 μM	94
3	**1.105**	Cu^{2+}	Buffer/DMF	0.32 μM	88
4	**1.93**	Zn^{2+}	Water	57 nM	81
5	**1.117**	Hg^{2+}	Acetonitrile	40 nM	104
6	**1.112**	Hg^{2+}	Buffer/water	0.49 μM	100

7	**1.114**	F^-	THF	0.20 nM	101
8	**1.102**	F^-	Acetonitrile	267 nM	86
9	**1.109**	ClO^-	Buffer/water	0.60 μM	92
10	**1.110**	CN^-	Water	13.8 nM	93
11	**1.107**	HSO_3^-	DMSO/water	61.2 nM	90
12	**1.108**	HSO_3^-	Buffer/DMSO	3.2 nM	91

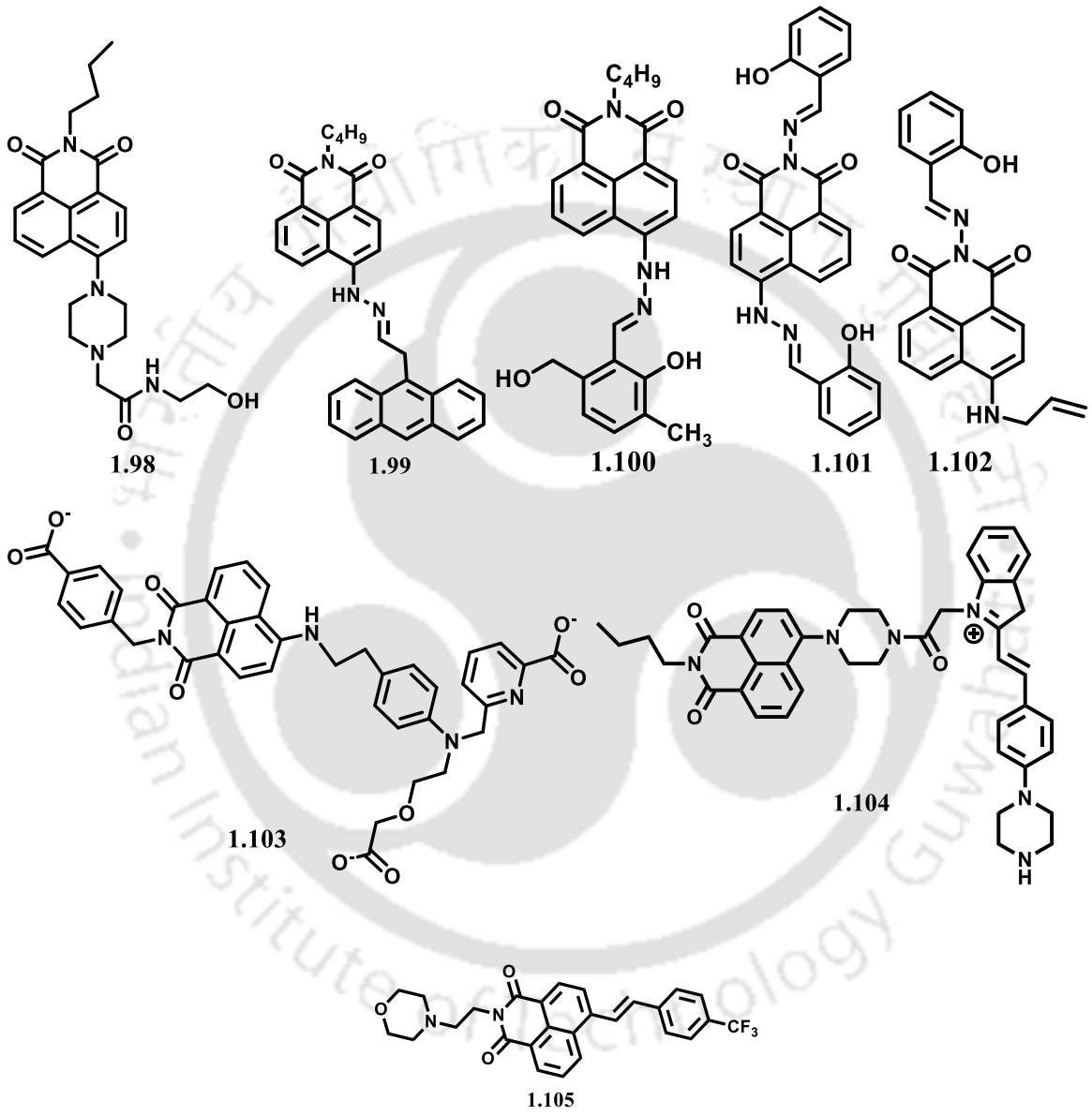

Figure 1.31: The chemosensors of naphthalimides derived from 1,8-naphthalimide by functionalization at the 4-position of the ring.

The naphthalimide-derivative **1.98** was selective to show turn-on fluorescence emission Al^{3+} ions. [85] It formed a 1:1 complex and showed a 60-fold increase in fluorescence intensity due to chelation. The Schiff base derived 1,8-naphthalimide structure 1.99 showed a color change

from yellow to blue and quenching in the fluorescence emission by fluoride. This was due to the deprotonation of the naphthyl hydrazine N-H of the receptor by fluoride ions. Similarly, the gel formed by naphthalimide–pyridoxal[86] compound **1.100**, in DMSO: H_2O (8:1 v/v) mixture, showed a color change from greenish-yellow to deep blue by adding specifically by F^- ions. The gel could discriminate in sensing fluoride ions from acetate ions. The naphthalimide-based Schiff base 1.101 formed a complex with Fe^{3+} ions, which was non-fluorescent.[87] Upon interactions with phosphate the complex had shown emission and serves as a fluorescence turn-on sensor for PO_4^{3-}. The detection limit for PO_4^{3-} was 1.721×10^{-6} M.

4-allylamine-N-(N-salicylidene)-1,8-naphthalimide[88] (**1.102**), with a Schiff base group linked to imide N-atom had showed fluorescence quenching selectively by Cu^{2+} ions over several other metal ions with a detection limit 0.32 μM. Indicating good sensitivity. The coordination of Cu^{2+} to form chelate had affected the intramolecular charge transfer to cause a quenching in emission. The 4-amino-1,8-naphthalimide derivative **1.103** has iminoethoxyacetic acid,[89] The fluorescence emission intensity of this compound was increased by 7-folds at 550 nm upon interactions with Zn^{2+} ions. It could detect zinc ions in aqueous solutions as well as in living cells.

The sensing molecule **1.104**, has two fluorophores naphthalimide and hemocyanin connected through an intervening part. This compound had showed Forster resonance energy transfer which was reflected as a red-emitting fluorescent peak.[90] The compound showed reactivity-based color change by reacting with HSO_3^- ions, and this could be observed by the naked eye. In this example, the conjugated C=C double bonds with indole and 4-(piperazine-1-yl)benzene were the key factors in recognizing the anion. The HSO_3^- ions quenched their fluorescence at 590 nm while there was no effect on the fluorescence at 527 nm. The spectroscopic experiments confirmed that bisulfate reacted with the double bond. This was also able to serve as mitochondria-targeting to monitor exogenous HSO_3^- in living cells. Another example of a reaction-based sensor for bisulfate ions is **1.105**, which showed a high affinity[91] to HSO_3^- due to a nucleophilic addition reaction in aqueous media. It showed dual emission signals from absorption and emission spectra. The N-functionalized naphthalimide **1.106** was used to sense hypochlorite ions. [92] It exhibited selectivity for ClO^- over various competing ions. An aqueous solution of the carboxylic acid **1.107** was fluorescent.[93] This compound had selectively detected cyanide ions in water. The cyanide ions binding had affected the twisted intramolecular charge transfer transition of the compound.

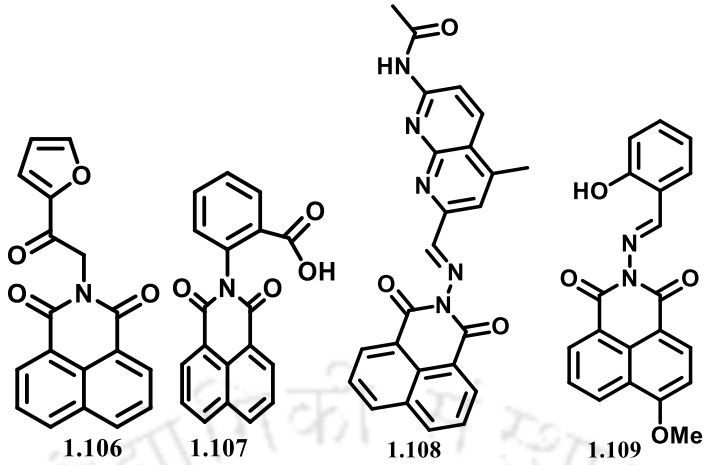

Figure 1.32: Naphthalimide-based compound **1.106** for chlorate ion and **1.107** for cyanide detection and two Schiff-base receptors **1.109** and **1.110** having 1,8-naphthalimide.

The 7-acetamino-4-methyl-1,8-naphthyridine-2-carbaldehyde-(1′,8′-naphthalenedicarbonyl) hydrazone (**1.108**), [94] was highly selective to detect Al^{3+} ions over other common metal ions. The fluorescence intensity of the compound at 414 nm was increased upon interactions with Al^{3+} ions. This was attributed to the suppression of the photoinduced electron transfer process. The aluminum ions bound to the probe could be released from the molecule by treating it with ethylenediamine. The 4-methoxy-1,8-naphthalimide-derived salicylideneamino[95] receptor **1.109** showed emission changes with Zn^{2+} ions.

Linking a naphthalimide unit to a common dye molecule directly or through a spacer provides receptors that have scopes to study a combinatory effect of a dye with a naphththalimide unit. The compound, **1.110** is such an example. It has a 1,8-naphthalimide [96-97] connected to the Rhodamine B unit. It detected Hg^{2+} ions through a Forster resonance energy transfer (FRET) process. It was also used to sense Hg^{2+} ions. These compounds generated OFF-ON signals during the detection of mercury ions followed by the addition of iodide ions. When iodide ions were added to a fluorescence quenched state caused by the Hg^{2+} ions the signal ON took place with increasing concentrations of iodide. Another example of rhodamine-6G-based naphthalimide[98] conjugate is **1.111**. It showed selective binding with Hg^{2+} and Cr^{3+} ions and was sensed by fluorescence emission changes specifically caused by them.

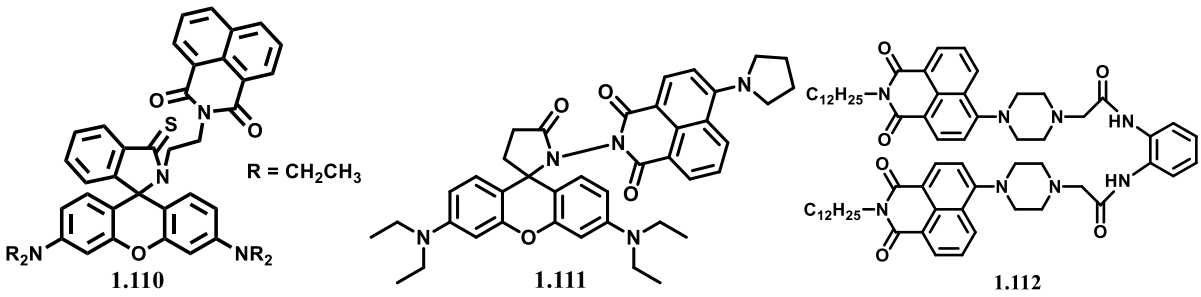

Figure 1.33: Two rhodamine-tethered naphthalimide receptors **1.110** and **1.111**; and **1.112** is a *bis*-naphthalimide receptors with a cleft-like structure.

The compound, **1.112** has a cleft-like structure and is a bis naphthalimide-derived compound. It was used to prepare fluorescent membrane [99] by mixing it with castor oil polyoxyethylene ether and PVC. The membrane was used for the detection of Fe^{3+} ions. The membrane demonstrated excellent reversible sensing and a response time of under 20 seconds with a detection limit of 4.0×10^{-7}. The tris-naphthalimide-based receptor **1.113** was utilized[100] to detect and separate fluoride ions. It is self-assembled in the presence of the fluoride ions and such aggregation causes a strong aggregation-induced emission.

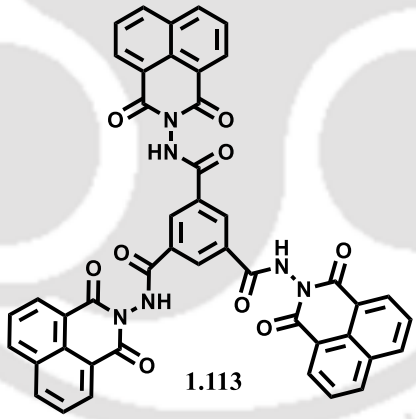

Figure 1.34: A tris-naphththalimide based receptor

Triaryl borane-substituted naphthalimide **1.114** was used to selectively detect fluoride and cyanide ions. In such detection, the chloride, bromide, iodide, and nitrite ions did not interfere. The detections were possible as the fluoride[101] or cyanide reacted with the compound at the boron site. Accordingly, the compound got converted to a salt which caused a red shift in emission spectra. The detection limits for fluoride and cyanide ions were 2.01×10^{-10} M and 3.94×10^{-10} M, respectively.

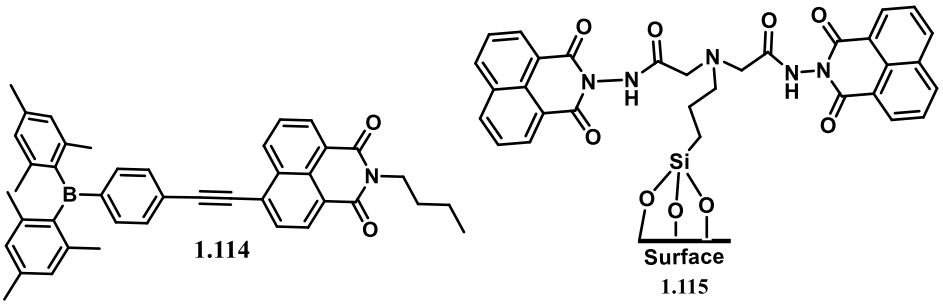

Figure 1.35: A borane-linked naphthalimide **1.114** and a bis-naphthalimide immobilized on a surface **1.115.**

A bis-naphthalimide immobilized on silica **1.115** served as a supported material and exhibited[102] selective sensing of oxyanions and it could remove oxoanions such as CrO_4^{2-}, $Cr_2O_7^{2-}$, and MnO_4^{2-} from a mixture with different anions. The fluorescence of the composite **1.115** was quenched by adding those ions.

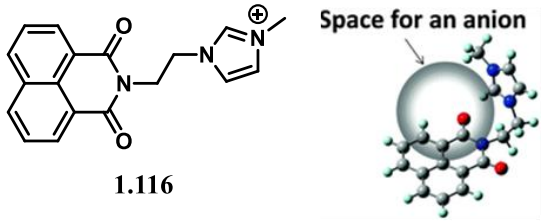

Figure 1.36: A shape-selective anion binding naphthalimide derivative **1.116**

The naphthalimide derivatives also served as a shape-selective receptor for anions to recognize them through their sizes and shape. For example, 1-methyl-3-(*N*-(1,8-naphthalimidyl)ethyl)imidazolium ion **1.116** has a bent shape as shown in Figure 1.36, which binds halide ions. It accommodated the spherical ions in the open space between the

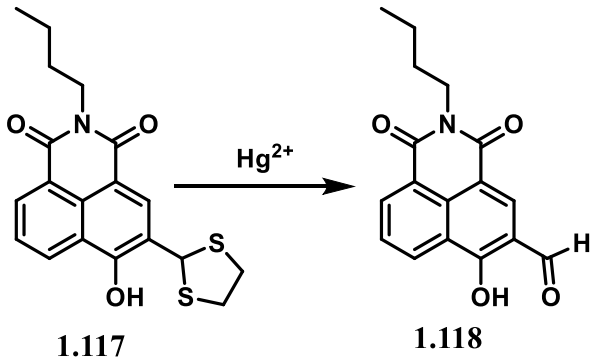

Figure 1.37: A chemical reactivity-based cation sensing by a naphthalimide derivative 1.117.

1,8-naphthalimide group and the imidazolium group.[103] The compound **1.117** is an example of a sensor that performed based on reactivity to sense Hg^{2+} ions. [104] This compound has a carbonyl-protected dithioformyl unit, derived from by reaction of the aldehyde group with ethylenedithiol. This 1,2-dithioformyl group had reacted with Hg^{2+} ions and it transformed the aldehydic form **1.118** of the naphthalimide derived compound. This caused the signal changes in the fluorescence emission to detect specifically mercury ions. The compound showed weak fluorescence emission, while upon interaction without Hg^{2+} ions the color of the emission from the solution of the compound was changed to light yellow. The detection limit for detecting mercury ions was 4.0×10^{-8} M.

These examples have revealed the different ways naphthalimides serve as sensing molecules to detect different ions. The binding site is one of the main factors in these processes, but parallel to this the emission properties of naphthalimide being dependent on the mechanism followed, the detection processes are substrate-specific.

1.7 Scopes of the work:

The naphthalimides serve as one of the small molecules able to generate interesting optical properties[105] and can be functionalized or guided to decipher different optoelectronic properties. Based on these polyimides are utilized in various materials and have been one of the important classes of advanced materials. With the emergence of applications of aggregation-induced emission in biological systems, naphthalimide-based compounds get priority the understanding of these classes of compounds requires higher attention.

A simple extension to a derivative such as N,N′-di-(4-pyridyl)-1,4,5,8-naphthalenediimide (**1.119**)[106] wide scopes to study organic, inorganic, and hybrid assemblies, are eminent. It has a grid like structure in the assembly (**1.120**) that can identify, select, and separate aromatic compounds. [107] It showed excited-state charge transfer interactions between the electron-deficient guests. Accordingly, it had guest-dependent and color-tunable emissions. It is a rigid linker for framework structures and has a wide scope to build ionic assemblies too.

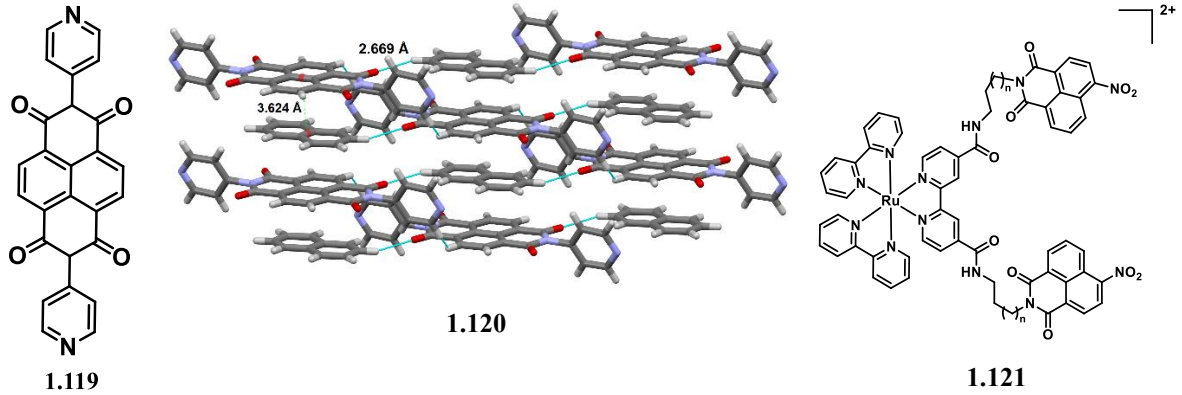

Figure 1.38: Structure of a diimide **1.119** and its self-assembly with naphthalene **1.120**. The **1.121** is an example of a Bis-imide DNA binding switch.

The bis-1,8-naphthalimide 1.121 forms 1.121-Ru(bipyridine)$_3$ complex, which can have a strong binding with DNA and serves as a light switch.[107] The naphthalimides having photo-chemical properties coupled with a metal center or another redox center activate, transform, and degrade organic compounds. The photoactivity of naphthalimide provides great scopes in splitting and energy harvesting.

The challenges remain to get high sensitivity and selectivity in sensing and delivering guest systems. The imides are utilized in generating chiral assemblies. Based on the new possibilities in supramolecular chemistry, medicinal, and utilities as advanced materials we have selected three compounds to study their metal complexes and ability to sense. The ionic cocrystals and various self-assemblies are envisaged to project their utility and the fundamental aspects of self-assembling, specific ion recognitions, and possibilities of self-inclusion by forming metal complexes.

1.8 References:

1 (a) M. Lubberink, W. Finnigan, S. L. Flitsch, Biocatalytic amide bond formation. *Green Chem.* 2023, 25, 2958 - 2970.

(b) A. F. Bradbury, D. G. Smyth, Peptide amidation, *Trends in Biochem. Sci.* 1991, 16, 112 - 115.

2 (a) E. Weyandt, I. A. W. Filot, G. Vantomme, E. W. Meijer, Consequences of amide connectivity in the supramolecular polymerization of porphyrins: spectroscopic observations rationalized by theoretical modelling. *Chem.Eur. J.* 2021, 27, 9700 -

9707. (b) A. Borges, D. Gillespie, A. Nag, Biological applications of amide and amino acid containing synthetic macrocycles. *Supramolecular Chem.* 2019, 31, 575 - 596.

3 (a) Z. Xu, Z. L. Croft, D. Guo, K. Cao, G. Liu, Recent development of polyimides: Synthesis, processing, and application in gas separation. *J. Polymer. Sci.* 2021, 59, 943 - 9625.

(b) Z. T. Li, J. L. Hou, C. Li, H. P. Yi, Shape-persistent aromatic amide oligomers: new tools for supramolecular chemistry. *Chem. Asian J.* 2006, 1, 766 -778.

(c) C. Kim, K. T. Kim, Y. Chang, Supramolecular assembly of amide dendrons. *J. Am. Chem. Soc*. 2001, 123, 5586 - 5587.

4 Z. Meng, J. Yin, F. Zhao, M. Li, Y. Zhang, Y. Liang, Z. Wang, Y. Yang, An efficient chitosan-based naphthalimide-modified fluorescent sensor for rapid detection of 2,4-dinitrophenylhydrazine and its applications in environmental analysis. *Eur. Polymer J.* 2021, 158, 110705.

5 D. Singh, J. B. Baruah, Guest inclusion in cyclic imides containing flexible tethers. *J Incl. Phenom. Macrocycl. Chem.* 2013, 76, 269 - 281.

6 (a) S. Kagatikar, D. Sunil, A systematic review on 1,8-naphthalimide derivatives as emissive materials in organic light-emitting diodes. *J. Mater. Sci.* 2022, 57, 105 - 139.

(b) X. Jia, Y. Yang, Y. Xu, X. Qian, Naphthalimides for labeling and sensing applications *Pure and Applied Chem.* 2014, 86, 1237 - 1246.

(c) M. A. Haidekker, E. A. Theodorakis, Ratiometric mechanosensitive fluorescent dyes: design and applications. *J. Mater. Chem. C*, 2016, 4, 2707 - 2718,

(d) J. Zhang, G. Li, C. Kang, H, Lu, X. Zhao, C. Li, W. Li, Z. Bo, Synthesis of star-shaped small molecules carrying peripheral 1,8-naphthalimide functional groups and their applications in organic solar cells. *Dyes and Pig.* 2015, 115, 181 - 189.

(e) Z. Yulian, M. Mutovska, P. Petrova, R. L. Tomova, P. Ivanov, S. Stoyanov, Dioxin-annulated 1,8-naphthalimides - synthesis, spectral and electrochemical properties, and application in OLED. *Dyes and Pig.* 2021, 184, 108585.

(f) Z. Hanchuang, C. Liu, M. J. Su, X. Rong, Y. Zhang, X. Wang, K. Wang, X. Li, Y. Yu, X. Zhang, B. Zhu, Recent advances in 4-hydroxy-1,8-naphthalimide-based small-molecule fluorescent probes. *Coord. Chem. Rev.* 2021, 448, 214153.

7 (a) W. Nie, L. Hu, Design of 1,8-Naphthalimide-based fluorescent functional molecules for biological application: a review. *ChemistrySelect* 2024, 19, e20230377.

(b) G. Conor, C. Wynne, R. B. P. Elmes, 1,8-Naphthalimide based fluorescent sensors for enzymes. *Coord. Chem. Rev.* 2021, 437, 213713.

(c) H. Yu, Y. Guo, W. Zhu, K. Havener, X. Zheng. Recent advances in 1,8-naphthalimide-based small-molecule fluorescent probes for organelles imaging and tracking in living cells. *Coord. Chemis. Rev.* 2021, 444, 214019.

8 (a) T. K. Park, J. Schroeder, J. R. Jr. New molecular complements to imides. Complexation of thymine derivatives. *J. Am. Chem. Soc*. 1991, 113, 5125 - 5127.

(b) J. K. Nath, J. B. Baruah, Cyclic aromatic imides as a potential class of molecules for supramolecular interactions. *CrystEngComm* 2015, 17, 8575 - 8595.

9 J. K. Nath, A. M. Kirillov, J. B. Baruah. Synthesis, structure, and topological studies of solvates and salts of a chiral zwitterionic host *N*-(2-Imidazol-5-yl-1-carboxyethyl)-1,8-naphthalimide. *Cryst. Growth Des.* 2015, 15, 737 - 751.

10 N. N. Li, W. Liu, N. N. Shi, D. Yang, Z. Zong, X. Zhang, R. X. Wu, C. G. Xu, S. Y. Bi, Y. H. Fan, Multiple naphthalimide dimers polymorphs triggered solvatofluorochromism, solid-state emission and aggregation-induced emission by different interaction and its application in fluorescence ratiometric sensing of dichloromethane and 1,4-dioxane. *Dyes and Pig.* 2021, 188, 109172.

11 X. He, A. C. Benniston, H. Saarenpaa, H. Lemmetyinen, N. V. Tkchenko, U. Baisch, Polymorph crystal packing effects on charge transfer emission in the solid state. *Chem. Sci.* 2015, 6, 3525 - 3532.

12 J. K. Nath and J. B. Baruah, Solvatoemissive dual fluorescence of N-(pyridylmethyl)-3-nitro-1,8-naphthalimides. *J. Fluoresc.* 2014, 24, 649 - 655.

13 B. Ventura, A. Bertocco, D. Braga, L. Catalano, S. d'Agostino, F. Grepioni, P. Taddei, Luminescence properties of 1,8-naphthalimide derivatives in solution, in their crystals, and in co-crystals: toward room-temperature phosphorescence from organic materials. *J. Phys. Chem. C* 2014, *118,* 18646 - 18658.

14 R. J. Sarma, C. Tamuly, N. Barooah, J. B. Baruah, Role of π-interactions in solid state structures of a few 1,8-naphthalimide derivatives, *J. Mol. Struct.* 2007, 829, 29 - 36.

15 Z. Chen, D. Wu, X. Han, Y. Nie, J. Yin, G. A. Yu, S. H. Liu, 1,8-Naphthalimide-based highly blue-emissive fluorophore induced by a bromine atom: reversible thermochromism and vapochromism characteristics. *RSC Adv.* 2014, 4**,** 63985.

16 C. Rizzo, P. Cancemi, L. Mattiello, S. Marullo, F. D'Anna, Naphthalimide imidazolium-based supramolecular hydrogels as bioimaging and theranostic soft materials. *ACS Appl. Mater. Interfaces* 2020**,** *12,* 48442 - 48457.

17 J. Nath, A. Kirillov, J. B. Baruah, Synthesis, structure and topological studies of solvates and salts of a chiral zwitteronic host N-(2-imidazol-5-yl-1-carboxyethyl)-1,8-naphthalimide. *Cryst. Growth Des.* 2015, 15, 737 - 751.

18 C. Balachandra, T. Govindaraju, Cyclic dipeptide-guided aggregation-induced emission of naphthalimide and Its application for the detection of phenolic drugs. *J. Org. Chem.* 2020**,** *85*, 1525 -1536.

19 S. Kuila, A. K. Singh, A. Shrivastava, S. Dey, T. Singha, L. Roy, B. Satpati, J. Nanda. Probing molecular chirality on the self-assembly and gelation of naphthalimide-conjugated dipeptides. *J. Phys. Chem. B* 2023**,** 127*,* 4808 - 4819.

20 D. Singh, P. K. Bhattacharyya, J. B. Baruah. Structural studies on solvates of cyclic imide tethered carboxylic acids with pyridine and quinoline. *Cryst. Growth Des*. 2010, 10, 348 - 356.

21 D. Singh, J. B. Baruah, Solid state assemblies of cyclic imides tethered hydroxy benzoic acids with pyridine and quinoline: toward the formation of channels and cavities. Cryst. Growth Des. 2012, 12*,* 3169 - 3180.

22 V. Petkova, D. Anastasova, S. Dobrev, M. Mutovska, N. Kircheva, V. Nikolova, S. D. Kolev, S. Stoyanov, Y. Zagranyarski, T. Dudev, Naphthalimide-based amphiphiles: synthesis and DFT studies of the aggregation and interaction of a simplified model system with water molecules. *Molecules* 2024, 29*,* 4204.

23 D. L. Reger, R. F. Semeniuc, J. D. Elgin, V. Rassolov, M. D. Smith, 1,8-Naphthalimide synthon in silver coordination chemistry: control of supramolecular arrangement. *Cryst. Growth Des.* 2006, 6*,* 2758 - 2768.

24 D. L. Reger, E. Sirianni, J. J. Horger, M. D. Smith. Supramolecular architectures of metal complexes controlled by a strong π···π Stacking, 1,8-naphthalimide functionalized third generation tris(pyrazolyl)methane ligand. *Cryst. Growth Des*. 2010, 10, 386 - 393.

25 J. A. Kitchen, P. N. Martinho, G. G. Morgan, T. Gunnlaugsson. Synthesis, crystal structure and EPR spectroscopic analysis of novel copper complexes formed from *N*-pyridyl-4-nitro-1,8-naphthalimide ligands. *Dalton Trans.* 2014, 43, 6468 - 6479.

26 (a) J. I. Lovitt, C. S. Hawes, A. D. Lynes, B. Haffner, M. E. Möbius, T. Gunnlaugsson, Coordination chemistry of N-picolyl-1,8-naphthalimides: colourful low molecular weight metallo-gelators and unique chelation behaviours. *Inorg. Chem. Front.* 2017**,** 4**,** 296 - 308.
(b) B. M. P. Beebeejaun-Boodoo, R. Erasmus, M. Rademeyer, Tetrahalometallate salts of N-(4-picolinium)-1,8-naphthalimide: structures and solid-state fluorescence. *CrystEngComm* 2018, 20**,** 4875.
(c) C. Tamuly, N. Barooah, A. S. Batsanov, R. Kataky, J. B. Baruah, Structural and spectroscopic properties of bis-3-picolinium 1,8-naphthalimide tetrachlorocuprate, *Inorg. Chem. Commun.* 2005, 8, 689 - 691.

27 S. Yadav, N. Choudhary, S. Bhai, G. Bhojani, S. Chatterjee, B. Ganguly, A. R. Paital, Recyclable functionalized material for sensitive detection and exceptional sorption of hexavalent chromium and permanganate ions with biosensing applications. *ACS Appl. Bio Mater.* 2021, 4, 6430 - 6440.

28 Daniel L. Reger, Andrew Leitner, Mark D. Smith, Cesium complexes of naphthalimide substituted carboxylate ligands: Unusual geometries and extensive cation-π interactions. *J. Mol. Struct*. 2015, 1091, 31- 36. (Copyrights permission from figure 1.13)

29 D. L. Reger, A. Leitner, M. D. Smith, Homochiral, helical coordination complexes of lanthanides(III) and mixed-metal lanthanides(III): impact of the 1,8-naphthalimide supramolecular tecton on structure, +ic properties, and luminescence. *Cryst. Growth Des.* 2015, 15*,* 5637 - 5644. (Copyrights permission from figure 1.14)

30 D. L. Reger, A. P. Leitner, M. D. Smith, Supramolecular metal–organic Frameworks of s- and f-block metals: impact of 1,8-naphthalimide functional group. *Cryst. Growth Des.* 2016, 16*,* 527 - 536

31 J. J. Liu, S. B. Xia, Q. T. Que, H. Suo, J. Liu, X. Shen, F. X. Cheng, Naphthalimide-containing coordination polymer with mechanoresponsive luminescence and excellent metal Ion sensing properties. *Dalton Trans.* 2020, 49, 3174 - 3180.

32 K. Jin, N. Park, Y. Ahn, D. Seo, D. Moon, J. Sung, J. Park, Solvent-induced structural transformation in a one-dimensional coordination polymer**,** *Nanoscale***,** 2024, 16**,** 4571 -

33 C. S. Hawes, K. Byrne, W. Schmitt, T. Gunnlaugsson, The 4-pyridonyl group as a multifunctional electron donor in 1,8-naphthalimide-based photoluminescent and mechanically interlocked coordination compounds. *Mater. Chem. Front.* 2018, 2, 1366 - 1373.

34 S. Shanmugaraju, C. Dabadie, K. Byrne, A. J. Savyasachi, D. Umadevi, W. Schmitt, J. A. Kitchen, T. Gunnlaugsson, A supramolecular Tröger's base derived coordination zinc polymer for fluorescent sensing of phenolic-nitroaromatic explosives in water. *Chem. Sci.* 2017, 8, 1535 - 1546.

35 J. Nath, A. Mondal, A. Powell, J. B. Baruah, Structures, magnetic properties and photoluminescence of dicarboxylate coordination polymers of Mn, Co, Ni, Cu having N-(4-pyridylmethyl)-1,8-naphthalimide. *Cryst. Growth Des.* 2014, 14, 4735 - 4748. (Copyrights permission from figure 1.16)

36 (a)J. K. Nath, J. B. Baruah, Twisted conformations in complexes of N-(3-imidazol-1-yl-propyl)-1,8-naphthalimide and fluorescence properties. *Inorg. Chem. Frontiers* 2014, 1, 342 - 351.

(b) D. Singh, J. B. Baruah, Hydroxy-carboxylates of manganese, zinc and cadmium, *Inorg. Chim. Acta* 2013, 394, 703 - 709.

37 (a) R. Martín, A. Sánchez-Oliva, A. Benito, I. Torres-Moya, A. M. Garcia, J. Álvarez-Conde, J. Cabanillas-González, P. Prieto and B. Gomez-Lor, Self-assembled D–π–A multifunctional systems with tunable stimuli-responsive emission and optical waveguiding behavior. *J. Mater. Chem. C*, 2024, 12, 2903 - 2910.

(b) M. Poddar, G. Sivakumar, R. Misra, Donor-acceptor substituted 1,8-naphthalimides: design, synthesis, and structure-property relationship. *J. Mater. Chem. C* 2019, **7**, 14798 - 14815.

38 P. Gu, X. Xu, F. Zhou, T. Zhao, G. Ye, G. Liu, Q. Xu, J. Ge, Q. Xu, J. Lu, Study of linear and nonlinear optical properties of four derivatives of substituted aryl hydrazones of 1,8-naphthalimide. *Chinese J. Chem.* 2014, 32, 205 - 211.

39 Y. Sheng, J. Ma, S. Liu, Y. Wang, C. Zhu, Y. Cheng, Strong and reversible circularly polarized luminescence emission of a chiral 1,8-naphthalimide fluorophore induced by excimer emission and orderly aggregation. *Chem. Eur. J.* 2016, 22, 9519 - 9522.

40 M. Oelgemoller, W. H. Kramer, Synthetic photochemistry of naphthalimides and related compounds. *J. Photochem. Photobiol.C: Photochem. Rev.* 2010, 11, 210 - 244.

41 N. Zivic, M. Bouzrati-Zerrelli, S. Villotte, F. Morlet-Savary, C. Dietlin, F. Dumur, D. Gigmes, J. P. Fouassier and J. Lalevée A novel naphthalimide scaffold based iodonium salt as a one-component photoacid/photoinitiator for cationic and radical polymerization under LED exposure. *Polym. Chem.*, 2016, 7, 5873

42 Z. Xu, Q. Mei, J. Weng, W. Huang, Synthesis, characterization and properties of covalently linked porphyrin-naphthalimide pentamer and its metal complexes. *J. Mol. Struct.* 2014, 1074, 687 - 694.

43 S. Misra, P. Singh, A. Das, P. Brandão, P. Sahoo, N. Sepay, G. Bhattacharjee, P. Datta, A. K. Mahapatra, B. Satpati, J. Nanda, Supramolecular assemblies of a 1,8-naphthalimide conjugate and its aggregation-induced emission property. *Mater. Adv.* 2020, 1, 3532 -3538.

44 A. Saini, K. R. J. Thomas, Bis-naphthalimides bridged by electron acceptors: optical and self-assembly characteristics. *RSC Adv.* 2016, 6, 71638 - 71651.

45 D. Sarkar, M. Chowdhury, P. K. Das, Naphthalimide based fluorescent organic nanoparticles in selective sensing of Fe^{3+} and as a diagnostic probe for Fe^{2+}/Fe^{3+} transition. *J. Mater. Chem. B* 2021, 9, 494 - 507.

46 Y. Ni, Z. Sun, Y. Wang, H. F. Nour, A. C. H. Sue, N. S. Finney, K. K. Baldridge, M. A. Olson, Versatile hydrochromic fluorescent materials based on a 1,8-naphthalimide integrated fluorophore-receptor system. *J. Mater. Chem. C*, 2019, 7, 7399 - 7410.

47 S. Mukherjee, P. Thilagar, Molecular flexibility tuned emission in "V" shaped naphthalimides: Hg(II) detection and aggregation-induced emission enhancement (AIEE). *Chem. Commun.* 2013, 49, 7292 - 7294.

48 C. S. Hawes, A. D. Lynes, K. Byrne, W. Schmitt, G. Ryan, M. E. Möbius, T. Gunnlaugsson, A resilient and luminescent stimuli-responsive hydrogel from a heterotopic 1,8-naphthalimide-derived ligand. *Chem. Commun.* 2017, 53, 5989 - 5992.

49 D.M. Han, H. J. Song, C. H. Han, Y. S. Kim, Enhancement of the outdoor stability of dye-sensitized solar cells by a spectrum conversion layer with 1,8-naphthalimide derivatives. *RSC Adv.* 2015, 5, 32588.

50 C. J. Christopherson, D. M. Mayder, J. Poisson, N. R. Paisley, C. M. Tonge, Z. M. Hudson. 1,8-Naphthalimide-based polymers exhibiting deep-red thermally activated delayed fluorescence and their application in ratiometric temperature sensing. *ACS Appl. Mater. Interfaces* 2020, 12, 20000 - 20011.

51 J. Jovaisaite, P. Baronas, G. Jonusauskas, D. Gudeika, A. Gruodis, J. V. Gražulevičius, S.Juršėnas, TICT compounds by design: comparison of two naphthalimide-π-dimethylaniline conjugates of different lengths and ground state geometries. *Phys. Chem. Chem. Phys.* 2023, 25, 2411 - 2419.

52 H. Sharma, K. N. Hearn, A. M. Ranieri, C. Caporale, M. Massi, F. M. Pfeffer, A rhodamine-naphthalimide-benzamide trichromophoric system with solid-state and multiple

solvent dependent aggregate emissive properties. *Mater. Chem. Front.* 2021, 5, 5024 - 5032.

53 G. J. Scerri, J.C. Spiteri, C. J. Mallia, D. C. Magri, A lab-on-a-molecule with an enhanced fluorescent readout on detection of three chemical species. *Chem. Commun.* 2019, 55, 4961 - 4964.

54 A. Jamadar, A. K. Singh, L. Roy, A, Das, Stimuli-responsive luminescent supramolecular assemblies and co-assemblies through orthogonal dipole-dipole interactions and halogen bonding. *J. Mater. Chem. C* 2021, 9, 11893 - 11904.

55 G. H. Aryal, C. H. Battle, T. A. Grusenmeyer, M. Zhu, J. Jayawickramarajah, A naphthalimide derived fluorescent sensor for solid-phase screening of cucurbit[7]uril–guest interactions. *Chem. Commun.* 2016, 52, 2307 - 2310.

56 M. K. Noushija, A. V. Krishna, T. Gunnlaugsson, S. Shanmugaraju, Reactivity-based amino-1,8-naphthalimide fluorescent chemosensors for the detection and monitoring of phosgene. *Sens. Diagn.* 2024, 3, 783 - 798.

57 M. K. Noushija, A. V. Krishna, T. Gunnlaugsson, S. Shanmugaraju, Reactivity-based amino-1,8-naphthalimide fluorescent chemosensors for the detection and monitoring of phosgene. *Sensors Diagn.* 2024, 3, 783 - 798.

58 X. Cao, N. Zhao, H. Lv, Q. Ding, A. Gao, Q. Jing, T. Yi, Strong blue emissive supramolecular self-assembly system based on naphthalimide derivatives and its ability of detection and removal of 2,4,6-trinitrophenol. *Langmuir* 2017, 33, 7788 - 7798.

59 K. N. Hearn, T. D. Nalder, R. P. Cox, H. D. Maynard, T. D. M. Bell, F. M. Pfeffer and T. D. Ashton, Modular synthesis of 4-aminocarbonyl substituted 1,8-naphthalimides and application in single molecule fluorescence detection. *Chem. Commun.* 2017, 53, 12298 - 12301.

60 Y. Y. Zhang, C. H. Zhou, Synthesis and activities of naphthalimide azoles as a new type of antibacterial and antifungal agents. *Bioorg. Med. Chem. Lett*. 2011, 21, 4349 - 4352.

61 F. de Campos, R. Correa, M. M. D. Souza, R. A. Yunes, R. J. Nunes, V. C. Filho, Studies on new cyclic imides obtained from aminophenazone with analgesic properties. *Arzneimittelforschung* 2002, 52, 455 - 461

62 A. Kamal, B. S. N. Reddy, G. S. K Reddy, G. Ramesh, Design and synthesis of C-8 linked pyrrolobenzodiazepine naphthalimide hybrids as anti-tumour agents *Bioorg. Med. Chem. Lett*., 2002, 12, 1933-1935

63 F. Hassanzadeh, M. Rabbani, G. A Khodarahmi, A. Fasihi, G. H. Hakimelahi, M. Mohajeri, Synthesis and evaluation of the anxiolytic activity of some phthalimide derivatives in mice model of anxiety. *Res Pharm Sci*., 2007, 2, 35 - 41.

64 G. J. Kaczorowski, O. B. McManus, B. T. Priest, M. L. Garcia, Ion channels as drug targets: the next GPCRs. *J. Gen. Physiol*. 2008, 131, 399 - 405.

65 (a)S. Banerjee, E. B. Veale, C. M. Phelan, S. A. Murphy, G. M. Tocci, L. J. Gillespie, D. O. Frimannsson, J. M. Kelly, T. Gunnlaugsson, Recent advances in the development of 1,8-naphthalimide based DNA targeting binders, anticancer and fluorescent cellular imaging agents. *Chem. Soc. Rev.* 2013, 42, 1601 - 1618.

(b)M. F. Brana, M. Cacho, A. Gradillas, B. Pascual-Teresa, A. Ramos, Intercalators as anticancer drugs. *Curr. Pharm. Des*. 2001, 7, 1745 - 1780.

(c)M. D. Tomczyk, K. Z. Walczak. 1,8-Naphthalimide based DNA intercalators and anticancer agents. A systematic review from 2007 to 2017. *Eur. J. Med. Chem*. 2018, 159, 393 - 422.

66 (a) S. A. Shaikh, S. S. Bhat, V. K. Revankar, N. S., K. Kumara, N. K. Lokanath, R. J. Butcher, V. Kumbar K. Bhat, Copper(I) complexes with quinolone appended 1,8-naphthalimide conjugates: structural characterization, DNA and protein binding and cytotoxicity studies. *New J. Chem.*, 2022, 46, 16801 - 16812.

(b) S. A. Shaikh, S. S. Bhat, P. L. Hegde, V. K Revankar, A.Kate, D. Kirtani, A. A. Kumbhar, V. Kumbar, K. Bhat, Synthesis, structural characterization, protein binding, DNA cleavage and anticancer activity of fluorophore labelled copper(II) complexes based on 1,8-naphthalimide conjugates. *New J. Chem.* 2021, 45, 16319 - 16332

(c) H. H. Gong, K. Baathulaa, J. S. Lv, G. X. Cai, C.H. Zhou, Synthesis and biological evaluation of Schiff base-linked imidazolyl naphthalimides as novel potential anti-MRSA agents. *Med. Chem. Commun.*, 2016, **7**, 924 - 931.

(d) J. Zhou, C. Fang, Y. Liu, Y. Zhao, N. Zhang, X. Liu, F. Wang, D. Shangguan, Visible-light-induced cleavage of 4-α-amino acid substituted naphthalimides and its application in DNA photocleavage. *Org. Biomol. Chem.* 2015, 13, 3931 - 3935.

67 L. H. Yang, J. Zhao, Y. Q. Zhu, Z. Y. Tian, C. J. Wang, Reactive oxygen species (ROS) accumulation induced by mononaphthalimide-spermidine leads to intrinsic and AIF-mediated apoptosis in HeLa cells. *Oncol. Rep.* 2011, 25**,** 1099 - 1107.

68 K. R. Wang, F. Qian, Q. Sun, C. L. Ma, R. X. Rong, Z. R. Cao, X. M. Wang, X. L .Li, Substituent effects on cytotoxic activity, spectroscopic property, and DNA binding property of naphthalimide derivatives. *Chem. Bio and Drug Des.* 2016, 87, 664 - 672.

69 L. D. Van Vliet, T. Ellis, P. J. Foley, L. Liu, F. M. Pfeffer, R. A. Russell, R. N. Warrener, F. Hollfelder, M. J. Waring, Molecular recognition of DNA by rigid [N]-polynorbornane-derived bifunctional intercalators: synthesis and evaluation of their binding properties. *J. Med. Chem.*, 2007, 50**,** 2326 - 2340.

70 J. M. Pérez , I. Lopez-Solera , E. I. Montero , M. F. Braña, C. Alonso, S. P. Robinson, C. Navarro-Ranninger, Combined effect of platination and intercalation upon DNA binding of novel cytotoxic Pt-bis(naphthalimide) complexes. *J. Med. Chem.*, 1999**,** 42**,** 5482- 5486.

71 S. Murphy, S. A. Bright, F. E. Poynton, T. McCabe, J. A. Kitchen, E. B. Veale, D. C. Williams, T. Gunnlaugsson, Synthesis, photophysical and cytotoxicity evaluations of DNA targeting agents based on 3-amino-1,8-naphthalimide derived Troger's bases. *Org. Biomol. Chem.***,** 2014, 12**,** 6610 - 6623.

72 S. Roy, S. Saha, R. Majumdar, R. R. Dighe, A. R. Chakravarty, Photocytotoxic 3d-metal scorpionates with a 1,8-naphthalimide chromophore showing photoinduced DNA and protein cleavage activity. *Inorg. Chem.* 2009, 48*,* 9501 - 9509.

73 N. Tyagi, M. Viji, S. C. Karunakaran, S. Varughese, S. Ganesan, S. Priya, P. S. S. Babu, A.S. Nair, D. Ramaiah, Enhancement in intramolecular interactions and in vitro biological activity of a tripodal tetradentate system upon complexation. *Dalton Trans.* 2015, 44, 15591 - 15601.

74 I. Grabchev, E. Vasileva-Tonkova, D. Staneva, P. Bosch, R. Kukeva, R. Stoyanova, Impact of Cu(II) and Zn(II) Ions on the Functional Properties of New PAMAM Metallodendrimers. *New J. Chem.* 2018, 42, 7853 - 7862.

75 E. E. L. Jones, N. O. Symonds, S. E. Yates, A. J. Hayes, D. Lloyd, R. Williams, S. J. Coles, P. N. Horton, S. J. A. Pope. Fluorescent Rhenium-Naphthalimide Conjugates as Cellular Imaging Agents. *Inorg. Chem*., 2014, 53, 3788 - 3797.

76 N. Tyagi, M. Viji, S. C. Karunakaran, S. Varughese, S. Ganesan, S. Priya, P. S. S. Babu, A.S. Nair, D. Ramaiah, Enhancement in intramolecular interactions and in vitro biological

activity of a tripodal tetradentate system upon complexation. *Dalton Trans.* 2015, 44, 15591.

77 E. E. Langdon-Jones, N. O. Symonds, S. E. Yates, A. J. Hayes, D. Lloyd, R. Williams. S. J. Coles, P. N. Horton, S. J. Pope, Fluorescent rhenium-naphthalimide conjugates as cellular imaging agents. *Inorg Chem.* 2014. 53. 3788 - 3797.

78 E. E. Langdon-Jones, C. F. Williams, A. J. Hayes, D. Lloyd, S. J. Coles, P. N. Horton, L. M. Groves, S. J. A. Pope, Luminescent 1,8-naphthalimide-derived Re^{I} complexes: syntheses, spectroscopy, X-ray structure and preliminary bioimaging in fission yeast cells. *Eur. J. Inorg. Chem.* 2017, 5279 - 5287.

79 A. Bogucka-Kocka, P. Kołodziej, A. Makuch-Kocka, D. Różycka, S. Rykowski, J. Nekvinda, B. Grüner, A. B. Olejniczak, Nematicidal activity of naphthalimide–boron cluster conjugates. *Chem. Commun.* 2022, 58, 2528 - 2531.

80 S. N. Berry, V. Soto-Cerrato, E. N. W. Howe, H. J. Clarke, I. Mistry, A. Tavassoli, Y.T.Chang, R. Pérez-Tomas, P.A.Gale, Fluorescent trans membrane anion transporters: shedding light on anionophoric activity in cells. *Chem. Sci*. 2016, **7**, 5069 - 5077.

81 C. Zhang, Z. Liu, Y. Li, W. He, X. Gao, Zijian Guo; In vitro and in vivo imaging application of a 1,8-naphthalimide-derived Zn^{2+} fluorescent sensor with nuclear envelope penetrability. *Chem. Commun.* 2013, 49, 11430 - 11432.

82 H. Sharma, J. S. Sidhu, W. M. Hassen, N. Singh, J. J. Dubowski Synthesis of a 3,4-disubstituted 1,8-naphthalimide-based DNA intercalator for direct imaging of legionella pneumophila. *ACS Omega* 2019, *4*, 5829 - 5838.

83 C. Ge, L. Liu, Y. Wang, X. Di, X. Luo, H. Liu, Y. Qian Novel 1,8-naphthalimide derivatives as antitumor agents and potent demethylase, inhibitors. *ACS Medicinal Chem. Lett.* 2023, *14*, 1551 - 1557.

84 D. Wu, A. C. Sedgwick, T. Gunnlaugsson, E. U. Akkaya, J. Yoon, T. D. James, Fluorescent chemosensors: the past, present and future. *Chem. Soc. Rev.* 2017, 46, 7105 - 7123.

85 N. N. Li, S. Zeng, M. Q. Li, Y. Q. Ma, X. J. Sun, Z. Y. Xing, J. L. Li, A highly selective naphthalimide-based chemosensor: ‘‘Naked-eye’’ colorimetric and fluorescent turn-on recognition of Al^{3+} and its application in practical samples, test paper, and logic gate. *J. Fluoresc*. 2018, 28, 347 - 357.

86 C. Pati, K. Ghosh, A 1,8-naphthalimide-pyridoxal conjugate as a supramolecular gelator for colorimetric read out of F^- ions in solution, gel and solid states. *New J. Chem*. 2019, 43, 2718 - 2725.

87 D. Jothi, S. Munusamy, S. Sawminathan, S. K. Iyer, Highly sensitive naphthalimide based Schiff base for the fluorimetric detection of Fe^{3+}. *RSC Adv.* 2021, 11, 11338 - 11346.

88 O. Aderinto, Y. Xu, H. Peng, F. Wang, H. Wu, X. Fan, A highly selective fluorescent sensor for monitoring Cu^{2+} ion: Synthesis, characterization and photophysical properties. *J. Fluoresc.* 2017, 27, 79 - 87.

89 D. Liu, X. Yin, X. Deng, J. Shi, H. Zhu, Z. Shang, J. Chen, G. Yang, H. He, 1,8-Naphthalimide-based fluorescent sensor with highly selective and sensitive detection of Zn^{2+} in aqueous solution and living cells. *Inorg. Chem. Commun.* 2019, 106, 43 - 47.

90 R. Shen, Y. Qian, A mitochondria-oriented fluorescent probe for ultrafast and ratiometric detection of HSO_3^- based on naphthalimide - hemicyanine. *New J. Chem.* 2019, 43, 7606 - 7612.

91 K. R. Everitt, H. C. Schmitz, A. Macke, J. Shan, E. Jang, B.E. Luedtke, K.A. Carlson, H. Cao, Investigation of a sensing strategy based on a nucleophilic addition reaction for quantitative detection of bisulfite (HSO_3^-). *J. Fluoresc.* 2020, 30, 977 - 983.

92 S. C. Lee, C. Kim, Naphthalimide-based probe for the detection of hypochlorite in a near-perfect aqueous solution. *Anal. Sci.* 2019, 35, 1189 - 1193.

93 L. Wang, W.T. Li, W.J. Qu, Y.Q. Fan, H. Yao, Q. Lin, T.B. Wei, Y.M. Zhang, A water soluble naphthalimide-based chemosensor for fluorescent detection CN^- in pure water and its application in practical samples. *J. Brazilian Chem. Soc.* 2018, 29, 1563 - 1569.

94 X.L. Yue, C.R. Li, Z.Y. Yang, A novel Schiff-base fluorescent probe based on 1,8-naphthyridine and naphthalimide for Al^{3+}. *Inorg. Chim. Acta*. 2017, 464 167 - 171.

95 P. A. Panchenko, P. A. Ignatov, M. A. Zakharko, Y. V. Fedorov, O. A. Fedorova, A fluorescent PET chemosensor for Zn^{2+} cations based on 4-methoxy-1,8-naphthalimide derivative containing salicylideneamino receptor group, *Mendeleev Commun.* 2020, 30, 55 - 58.

96 N. Z. Xu, M. M. Liu, M. A. Ye, Y. W. Yao, Y. Zhou, G. Z. Wu, C. Yao, A Rhodaminenaphthalimide conjugated chemosensor for ratiometric detection Hg^{2+} in actual aqueous samples. *J. Lumin.* 2017, 188 135 - 140.

97 Mahato, P.; Saha, S.; Suresh, E.; Di Liddo, R.; Parnigotto, P. P.; Conconi, M. T.; Kesharwani, M. K.; Ganguly, B.; Das, A. ratiometric detection of Cr^{3+} and Hg^{2+} by a naphthalimide-rhodamine based fluorescent probe. *Inorg. Chem.* 2012, 51, 1769 - 1777.

98 Q. Lin, G. F. Gong, Y. Q. Fan, Y. Y. Chen, J. Wang, X. W. Guan, J. Liu, Y. M. Zhang, H. Yao, T. B. Wei, Anion induced supramolecular polymerization: a novel approach for the ultrasensitive detection and separation of F^-. *Chem. Commun.* 2019, 55, 3247 - 3250.

99 W. Fu, X. Guo, L. Jia, Y. Ding, A novel sensing membrane for the determination of ferric ions in aqueous solutions. *Anal. Methods* 2015, 7, 3089 - 3095.

100 C. B. Bai, R. Qiao, J. X. Liao, W. Z. Xiong, J. Zhang, S. S. Chen, S. Yang, A highly selective and reversible fluorescence "off-on-off" chemosensor for Hg^{2+} based on rhodamine-6G dyes derivative and its application as a molecular logic gate. *Spectrochim. Acta A Mol. Biomol. Spectrosc.* 2018, 202, 252 - 259.

101 T. S. Reddy, R. Maragani, R. Misra, Triarylborane substituted naphthalimide as a fluoride and cyanide ion sensor. *Dalt. Trans.* 2016, 45, 2549 - 2553.

102 S. Yadav, N. Choudhary, S. Bhai, G. Bhojani, S. Chatterjee, B. Ganguly, A. R. Paital, Recyclable functionalized material for sensitive detection and exceptional sorption of hexavalent chromium and permanganate ions with biosensing applications. *ACS Appl. Bio Mater.* 2021, 4, 6430 - 6440.

103 H. Izawa, S. Nishino, M. Sumita, M. Akamatsu, K. Morihashi, S. Ifuku, M. Morimoto, H. Saimoto, A novel 1,8-naphthalimide derivative with an open space for an anion: unique fluorescence behaviour depending on the binding anion's electrophilic properties. *Chem. Commun.* 2015, 51, 8596 - 8599.

104 M. Tian, C. Wang, Q. Ma, Y. Bai, J. Sun, C. Ding. A highly selective fluorescent probe for Hg^{2+} based on a 1,8-naphthalimide derivative. *ACS Omega* 2020, 5, 18176 - 18184.

105 T. Kumpulainen, B. H. Bakker, M. Hilbers, A. M. Brouwer, Synthesis and spectroscopic characterization of 1,8-naphthalimide derived "Super" photoacids. J. *Phys. Chem. B* 2015, 119, 2515 - 2524.

106 T. Ono, M. Sugimoto, Y. Hisaeda. Multicomponent molecular puzzles for photofunction design: emission color variation in Lewis acid-base pair crystals coupled with guest-to-host charge transfer excitation. *J. Am. Chem. Soc.* 2015, 30, 9519-9522.

107 G. J. Ryan, T. Gunnlaugsson, S. J. Quinn, Hook, line, and sinker Spectroscopic studies of bi-modular mono- and bis-1,8-naphthalimide-Ru(bpy)$_3$-conjugates as DNA "Light Switches". *Inorg. Chem.* 2022, *61*, 12073 - 12086.

End of introduction

Chapter 2

Polymorphs, salt, ionic co-crystal and inclusion complex of N-amino-1,8-naphthalimide

2.1 Introduction

Various aspects of naphthalimide derivatives with applications in chemical, materials and biological sciences were deliberated in the introductory chapter and have suggested the need for a structure and property correlation of different forms and functionalised naphthalimide derivatives. For instance, the N-amino-1,8-naphthalimide (n = N, 3 or 4) serves as fundamental building units to prepare various derivatives that have utility as drugs, sensors, etc.[1] Among those compounds, the N-amino-1,8-naphthalimide derived compounds have been extensively studied as utility-oriented compounds,[2] but there are limited studies on the parent compound on the supramolecular aspects and its utility as a ligand.[3] The N-amino 1,8-napthalimide molecule has the advantage of not only having a dipolar naphthalimide unit to organise in

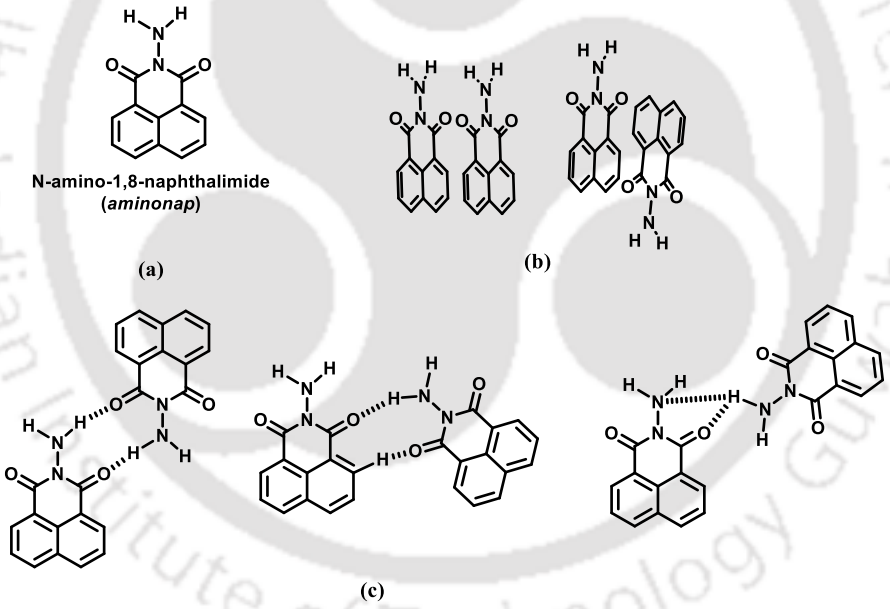

Figure 2.1: (a) The structure of N-amino-1,8-naphthalimide, (b) Head to head and Head to tail stacking arrangements between two molecules of *aminonap*, (c) three examples of homo-synthons.

head to head or head to tail {Figure 2.1 (b)}, as well as the hydrogen bonds between carbonyl and amino groups, can bring diversity in self-assemblies by forming different types of homo- and hetero-synthons.[4] Three such possibilities for the molecules to organize in self-assemblies are shown in Figure 2.1(c). On the other hand, the 1,8-naphthalimide derivatives are redox active, the electrochemical aspects of different assemblies of N-amino 1,8-naphthlimide draw

interest.[5] With the above background, polymorphs, ionic cocrystals, and metal complexes of N-amino-1,8-naphthalimide are described in this chapter.

2.2 Polymorphs of N-amino-1,8-naphthalimide:

The *aminonap* was prepared by reacting 1,8-naphthalenedianhydride with hydrazine hydrate. The compound was characterised by recording its NMR, IR, and mass spectra and by determining the crystal structure. The spectroscopic details are provided in the experimental section.

The crystal structure of the N-amino-1,8-naphthalimide was reported in the literature,[6] and no polymorph of the compound was reported in the literature. As our interest was to search for other polymorphs of *aminonap*, we explored this by attempting crystallization of the *aminonap* from different solvents. However, each crystallization resulted in only one type of crystal that was designated as *Poly-1*. We tried crystallising aminonap from DMF solution, which did not yield suitable crystals as reported earlier in the literature, but serendipitously we obtained crystals of the other form which is designated as *Poly-2*. It was obtained by slow evaporation of an equimolar solution containing *aminonap* and zinc nitrate hexahydrate. The solution had pH 6.3 and was placed in a water-bath at 70 °C for 6 hours, upon cooling and slow evaporation of solvent at room temperature in an open environment for five days, had provided yellow block-like crystals of the *Poly-2*. We have determined both the structures under similar conditions and found that the two polymorphs had similar unit cell volumes, but large differences in the unit cell axes, which are listed in Table 2.1. The crystals of these two polymorphs belong to different space groups and they have three primary features that distinguish them in the packing patterns. The crystal density of the *Poly-1* and *Poly-2* were comparable, the *Poly-1* was 1.523 g/cm^3, whereas *Poly-2* was 1.528 g/cm^3.

Table 2.1: Unit cell parameters of the two polymorphs of *aminonap*

Poly-1	*Poly-2*
Orthorhombic $Pna2_1$	Triclinic P -1
a = 13.296 (2) Å b = 18.408 (4) Å c /Å = 3.781 (11) Å	a = 7.307 (6) Å, b = 9.364 (7) Å, c = 14.655 (10) Å
α = β = γ = 90.00°	α = 81.676(3)◦, β = 80.506(3)◦, γ =69.460(3)◦
V /Å^3 = 925.5 (4)	V /Å^3 = 922.15 (12)

(i) The molecules were arranged head (amine end) to head orientations in pairs, which were one on top of the other in the case of *Poly*-1. The centroid-to-centroid distances of the two eclipsing naphthalimide rings was 3.781 Å. Whereas the stacked pairs of naphthalimide rings were found to be organised in a head to tail (amine of the two

molecules projecting towards opposite sides) parallel manners over each other in the *Poly-2* {Figure 2.2 (c) and (d)}, but there were two distinct centroids to centroid distances among two parallel pairs of the molecules. These distances were 4.030 Å and 3.522 Å. In general, to have an effective π-stacking, the distances between two aromatic planes lie between 3.5 to 4.0 Å.[7]

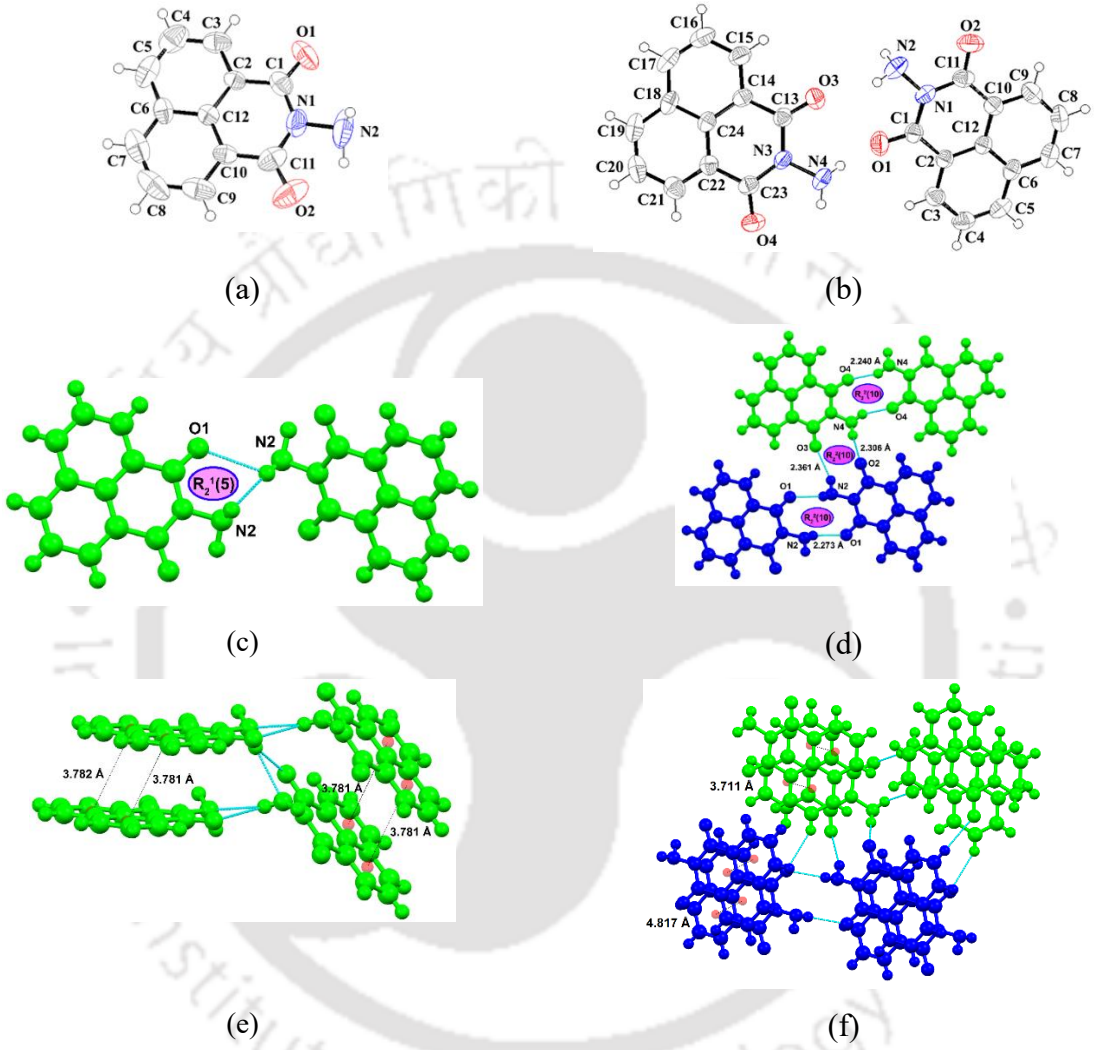

Figure 2.2: (a) and (b) are the ORTEP diagram of the *Poly-1* and *Poly-2* respectively. The hydrogen-bonded dimers in the self-assemblies of (c) Poly-1 and (d) *Poly-2*. (e) and (f) are showing stacking arrangements showing the head to head stacking in *Poly-1* and head to tail arrangement in *Poly-2* (The structures are drawn in different blue and green colours to show the symmetry-independent molecules).

This suggests the presence of stacking interactions among the rings, and possibly due to dipolar arrangements in poly-2 there is a relatively shorter separations between two rings. The

difference in the stacking arises as it has to compete with the intermolecular hydrogen bonds among the neighbouring molecules.

In the former case, the stacking interactions were not dipolar in the latter case the stacking interactions were dipolar. There are other examples of polymorphs of naphthalimide derivatives of the same space group, but with different Z values where the centroid to centroid distance of separations between the staggered stacked rings were between 3.4 to 3.7 Å.[8a]

(ii) The asymmetric unit had one molecule of the *aminonap* in *Poly-1*, whereas the reported polymorph Poly-2 had two symmetry-independent *aminonap* molecules in the unit cell. Symmetry non-equivalence of molecules in a unit cell refers to the phenomenon where multiple molecules exist in the crystallographic unit cell, that are not equivalent by symmetry elements of the crystal. There are many examples of molecules that show polymorphism due to differences in the numbers of molecules in their respective unit cells. For example, N, N-dimethylaniline naphthalimide showed two polymorphs one of which had two symmetry-independent molecules and the other had only one kind of molecule in the respective unit cell. Due to the differences in orientations and the stacking patterns the two polymorphs had distinct fluorescence properties.[8b] Those molecules occupy different orientations, positions, or conformations within the same unit cell, and the differences do not necessarily result from the overall symmetry associated with a crystal. For example, the dihydroxy aromatic compound resorcinol has O-H bonds that adopt different orientations with respect to each other has a polymorph that has two symmetry-independent molecules in the unit cell, and another form has only one molecule in the unit cell.

(iii) In the assembly of the *Poly-1*, one of the N-H bonds of the -NH_2 group hydrogen bonds to the oxygen atom of the carbonyl group of another neighbour molecule. In the solid-state assembly, hydrogen-bonded dimers were formed by N2-H···O1 hydrogen bond formed between the -NH_2 group of one *aminonap* molecule and the -C=O group of another, and N2-H···N2 from N-H bond of the amine of one molecule with N2 atom of amine of the other molecule. This results in a hydrogen-bond cyclic five-membered ring, that is represented by the graph-set notation $R_2^1(5)$. Here, the R represents the cyclic type of arrangement, the subscript denotes the number of acceptor atoms, the superscript indicates the number of donor atoms of the synthon, and the term in brackets specifies the number of atoms involved in the hydrogen-bonded cyclic unit.[9]

In the self-assembly *Poly-2*, hydrogen-bonded dimers were formed by hydrogen bonds between the -NH_2 group of one *aminonap* molecule with the -C=O group of another neighbour

molecule. Two such complementing hydrogen bonds N2-H···O1 in one pair and N4-H···O4 between another pair of molecules had resulted in the formation of two ten-membered hydrogen bonded units, each representative of the graph-set notation $R_2^2(10)$ (Figure 2.2 b). These dimers were connected through N2-H···O3 and N4-H···O2 hydrogen bonds formed between two pairs of self-assembled molecules with equivalent symmetry. The hydrogen bond parameters are listed in the Table 2.2. Thus, extensive hydrogen bonds in both the faces of the *aminonap* molecules, and the hydrogen bonded dimers were linked to each other to provide a sheet-like structure. These sheets appeared as one sheet on the top of another when viewed along the *a*-crystallographic axis. The $R_2^2(10)$ synthons of the dimers formed between two symmetry-related molecules were similar, but the $R_2^2(10)$ synthons formed between two symmetry-independent molecules were relatively weakly held; However, the differences were small yet notable as listed in Table 2.2.

Table 2.2: The bond parameters of the prominent hydrogen bonds in the *Poly-2*.

Hydrogen bond [symmetry]	$d_{D\text{-}H}$ (Å)	$d_{H\cdots A}$ (Å)	$d_{D\cdots A}$ (Å)	∠DHA (°)
N2-H···O1 [1-x, 3-y,- z]	0.86(3)	2.31(3)	3.073(3)	148(2)
N2-H ···O3 [x,1+y, z]	1.00(4)	2.35(4)	3.183 (3)	141(3)
N4 -H···O2 [x,-1+y,z]	0.89(3)	2.27(3)	3.144(3)	165(2)
N4-H…O(4) [1-x, -y, 1-z]	0.90(3)	2.21(3)	3.038(3)	154(2)

These two polymorphs had distinct powder X-ray diffraction (PXRD) patterns. The experimentally determined PXRD patterns of both polymorphs were compared with the one generated from the crystallographic information files. The Miller indices of the diffraction peaks were assigned and patterns were compared, showing that the experimental PXRD peaks were found as anticipated but the experimental peaks were broad and the intensity differed. Specially the peaks of the *Poly-2* were broad, which could be due to the poor crystallinity of the sample. It was difficult to prepare crystals in both cases, but several seeds collected from a series of experiments provided reasonably good matching powder X-ray diffractions of bulk samples enabling us to perform further, transformations, and thermal and spectroscopic studies.

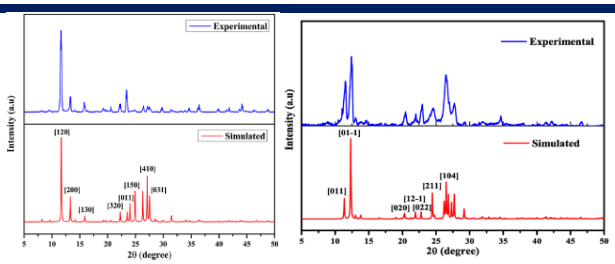

(a) (b)

Figure 2.3: Experimental PXRD patterns shown in blue color of (a) *Poly-1*, and (b) *Poly-2*, the patterns shown in red colour are the ones simulated from respective crystallographic information file.

The IR spectra of the two polymorphs had some distinctions, the N-H region of the spectra of the *Poly-2* had a broad and sharper peak above 3310 cm^{-1} showing the N-H stretch (Figure 2.3a). The carbonyl stretches of Poly-1 was observed at 1711 which was present in Poly-2 at 1692, this showed the better involvement of carbonyl in hydrogen bonding than in the case of the poly-1.

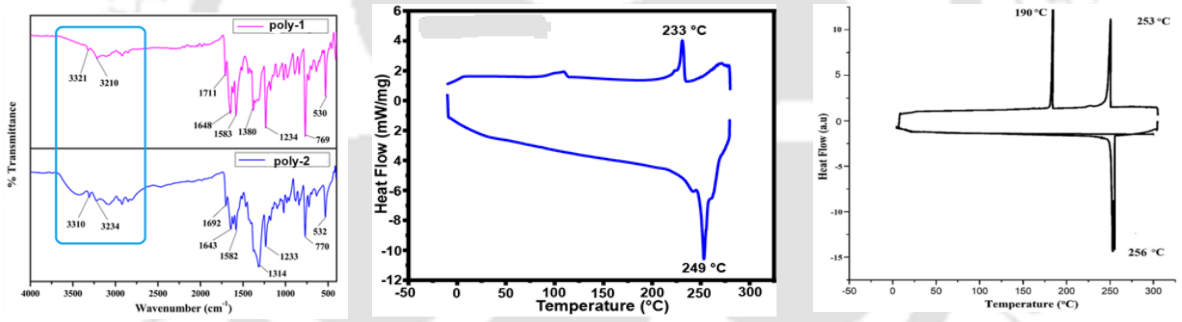

(a) (b) (c)

Figure 2.4: (a) FT-IR spectra of the *Poly-1* (top) and *Poly-2* (bottom). Differential scanning calorimetry of (b) Poly-1 and (c) *Poly-2* (heating and cooling cycle at 10 °C/min performed under N_2 atmosphere).

The polymorphs had distinct melting points that were reflected in the respective differential scanning calorimetry (DSC) shown in Figures 2.3 (b) and (c). The *Poly-1* melted at 249 ◦C, whereas the *Poly-2* was melted at 256 °C. While cooling the Poly-1 crystallised at 233 °C, whereas the *Poly-2* at 253 °C. The Poly-2 underwent a phase transition to an amorphous state while cooling, which was reflected as an exothermic peak at 190 °C and the second cycle of heating the sample showed a flat line from 30 °C until 300 °C, showing that there was no trace of the original form of heating after one heating cycle.

From these results, it was clear that both the head-to-head arrangement and head-to-tail arrangements provided two different packing polymorphs, each of which could be distinguished in the solid state by different spectroscopic tools.

2.3 Nitrate salt and ionic co-crystal of N-amino-1,8-naphthalimide

The -NH_2 group of the N-amino 1,8-naphthalimide has scope to get protonated under acidic conditions and the protonated form would allow specific anion binding. With such anticipation the crystallisations of the salts of the compound with different acids such as hydrochloric, perchloric, and nitric acid was attempted. Among these attempted crystallisations suitable for single crystal diffraction crystals were obtained only when nitric acid was used.

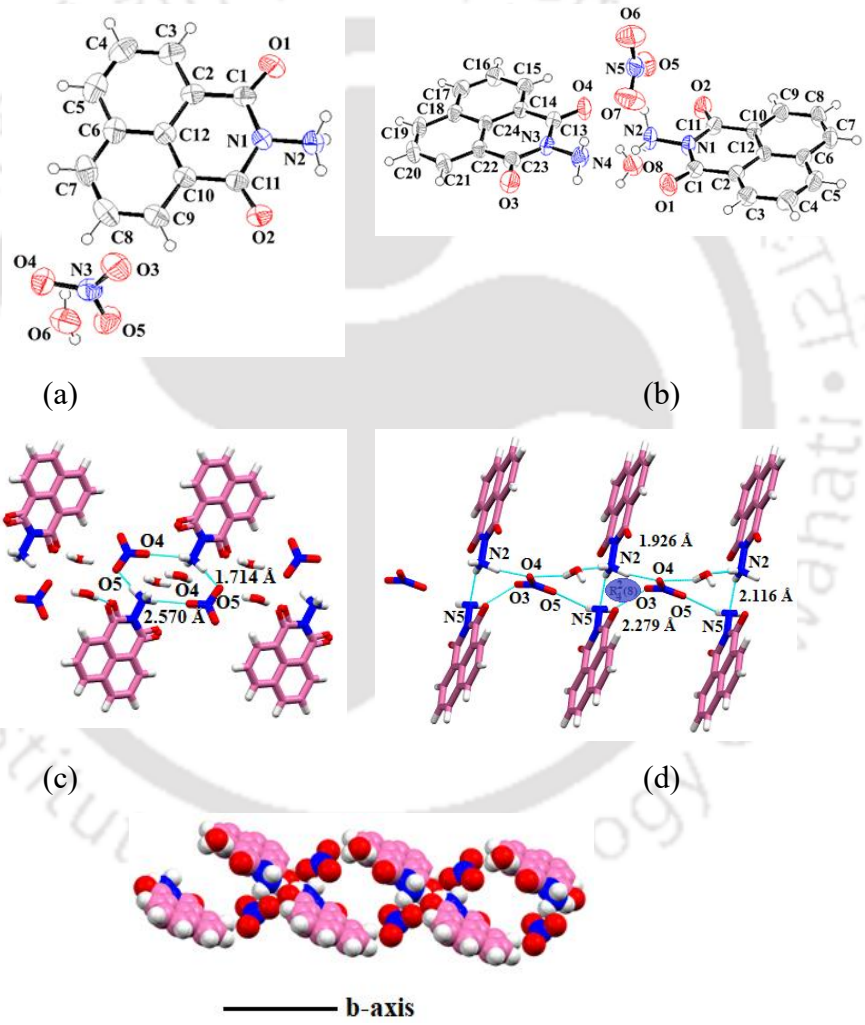

Figure 2.5: ORTEP diagram of the (a) *(Haminonap)NO_3·H_2O* and (b) *(Haminonap)NO_3·aminonap·H_2O* (thermal ellipsoids are with 50% probability), (c) and (d) are respective hydrogen bonded self-assembly of the salt and the ionic cocrystal, and (e) assembling of anions in the ionic cocrystal.

By varying the amounts of nitric acid in solution of the *aminonap*, a hydrated salt *(Haminonap)NO_3·H_2O* and a hydrated ionic co-crystal *(Haminonap)NO_3·aminonap·H_2O* could be crystallised under independent crystallisation room temperature by varying the amounts of nitric acid (salt was formed at pH = 0.3, whereas the ionic cocrystal was formed at pH = 0.56). The asymmetric unit of the hydrated salt has a cation, water molecule and a nitrate ion {Figure 2.4 (a)}, whereas, the ionic cocrystal has these together with a neutral *aminonap* molecule {Figure 2.4(b)}. The crystal parameters are listed in Table 2.1S in the experimental section. The assembly of the salt was comprised of a one-dimensional double helical hydrogen bonded chain-like structure formed by hydrogen bonding of the nitrate ions with the water molecules. The cations were attached to such chains by hydrogen bonds. The chain along the *b*-crystallographic axis is shown in the Figure 2.4(c). Each hydrogen-bonded cyclic units of two neighbouring nitrate ions with the two cations were bridged at two ends by two intervening water molecules, allowing to form extended 1-D chain-like arrangement. The prominent hydrogen bond parameters are listed in Table 2.3. The intervening water molecules holding the hydrogen

Table 2.3: Hydrogen bond parameters of the salt and the ionic co-crystal

Compound	H-bond	d_{D-H} (Å)	$d_{H...A}$ (Å)	$d_{D...A}$ (Å)	∠DHA (°)
(Haminonap)NO_3•H_2O	N2-H ···O6 [x, y, 1+z]	0.86	1.83	2.691(3)	171
	N2-H ···O5[x, y, 1+z]	0.99	1.76	2.745(3)	174
	O6-H ···O3 [x, y, z]	0.85	2.47	3.159(3)	139
	O6-H ···O5 [x, y, z]	0.85	2.04	2.867(3)	164
	O6-H ···O2 [-x 1-y, 1-z.]	0.85	2.12	2.957(3)	171
(Haminonap)NO_3•aminonap•H_2O	N2-H ···O8 [-1+x, y, -1+z]	0.87	1.86	2.726(4)	175
	N2-H ···N5 [x, y, -1+z]	0.87	2.12	2.890(3)	148
	N2-H ··· O4 [1-x, ½+y, -z]	1.04(5)	1.93(5)	2.847(5)	147(4)
	O8-H ···O7 [1-x, -1/2+y, 1-z]	0.85	2.00	2.836(4)	166
	O8-H ···O4 [1-x, ½+y, 1-z]	0.85	2.13	2.915(4)	153
	O8-H ···O5 [1-x, ½+y, 1-z]	0.85	2.32	3.056(5)	145

bonded nitrate-water cyclic moiety independently provided sites to the $^{+}$N-H of the *Haminonap* ions to form hydrogen bonds. Double helical nitrate-water hydrogen bonded double chains were found in the lattice of poly-oxometallate structures.[12] The double helical units of anion-water hydrogen-bonded chains were decorated by π-aromatic cations. The cations were located at parallel positions eclipsing each other, but the distance between the cations of the same chain was 7.41 Å, which was not suitable for π-interactions between the rings. In the overall assembly of the salt, two such chains were assembled such that the dipolar naphthalimide rings of the two chains were in opposite directions. This arrangement provided the naphthalimide rings

were located in parallel positions as pairs, with the dipoles in opposite directions. Each pair has a π-separation 3.64 Å, suggesting the presence of dipolar stacking interaction between them. The salt and ionic cocrystal contain a nitrate ion in their structures, resulting in an N-O stretching frequency observed at 1380 cm^{-1}. This observation is attributed to the presence of free nitrate ions in the compound.

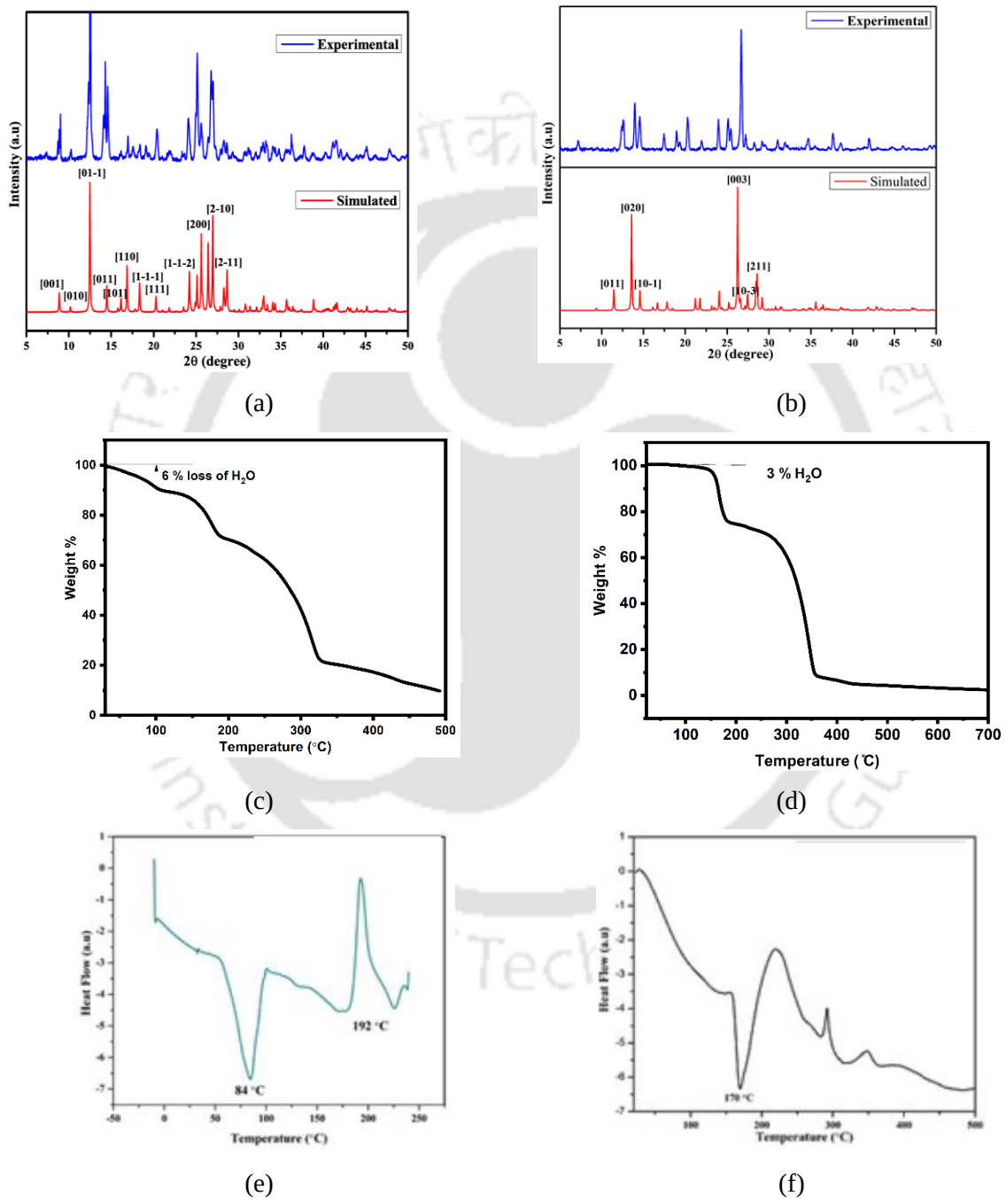

Figure 2.6: PXRD patterns of (a) *(Haminonap)NO_3·H_2O* and (b) *(Haminonap)NO_3 .aminonap·H_2O* (top experimental, bottom simulated from CIF file). Thermogravimetry of the salt (c) *(Haminonap)NO_3·H_2O*,

and (d) *(Haminonap)NO_3·aminonap·H_2O*, DSC of (e)*(Haminonap)NO_3·H_2O*, (f) *(Haminonap)NO_3·aminonap·H_2O* (heating rate 10 °C/min).

In the thermogravimetry of the nitrate salt, there was a weight loss of around 100°C due to the loss of hydrated water molecules (Figure 2.5c). Subsequent weight loss at 170°C was due to the decomposition of the salt, assigned to the loss of nitric acid from the salt, releasing the *aminonap* free. The loss of mineral acids from organic-salts such as picolinium-naphthalimide salts, releasing the parent base is known.[13] Heating above 250°C, the *aminonap* thus released was decomposed. The ionic co-crystal showed weight loss observed around 100°C corresponds to the loss of water molecules. A subsequent loss near 186 °C is associated with the decomposition by release of nitric acid, while the aminonap formed at this stage decomposed at approximately 250-280 °C.

Table 2.4: Distinct characteristics of the polymorphs, salt and ionic cocrystal of aminonap

Polymorph	Space group	Unit cell volume Å^3	Crystal density g/cm^2	Melting point (°C)	Arrangements of naphthalimide rings at parallel positions
Poly-1	Orthorhombic, $Pna2_1$	925.5(4)	1.523	249	Head to head
Poly-2	Triclinic, P-1	922.15(1)	1.528	260	Head to tail
Poly-2 (reported)	Triclinic, P-1	921.2(3)	1.530	-	Head to tail[6]
(Haminonap)NO_3·H_2O	Triclinic, P-1	610.4(6)	1.595	200	Staggered amide parts
(Hamininonap)NO_3· aminonap·H_2O	Monoclinic, $P2_1$	1092.5(1)	1.536	220	Head to head

The average zeta-potentials of the *(Haminonap)NO_3·H_2O* and *(Haminonap)NO_3·aminonap·H_2O* in water were - 4.74 mV and - 4.79 mV respectively (Figure A2.10). The *(Haminonap)NO_3.aminonap·H_2O* showed two types of assemblies one with a small peak for zeta-potential (10 % of the other) at 61.1 mV. The -ve values found in both the cases are reflections of stable assembled species.[14] Whereas, there is about 10 % of a species having positive zeta potential in the zeta potential profile of the ionic-cocrystal, suggesting degradation of the ionic-cocrystal possibly setting part of the neutral species in solution to some extent. The conductance of the salt in water is 0.28 mS/cm for 1 mM solution, whereas the same concentration of the ionic-cocrystal had 0.61 mS/cm. This suggested that the ionic cocrystal had 2.17 times higher conductance than the salt, this could be due to facilitation of hopping of proton to enhance conductance through the Grotthus transport mechanism in its hydrogen-bonded assembly.

The distinct and characteristic features among the polymorphs, salt and ionic-cocrystal of the *aminonap* are listed in Table 2.4. This showed the large differences in their properties and

revealed that the properties of the parent compound **aminonap** can be changed by transforming to different ionic or neutral forms by slight variations of crystallisation conditions.

2.4: Copper and cadmium complexes with aminonap modulating the amounts of aminonap in metal complexes

The metal complexes of 1,8-naphthalimide derivatives generates interest in various supramolecular assemblies, and *aminonap* was a ligand of copper used as a bidentate ligand to prepare copper (II) complex. This bis-chelated complex shown in Figure 2.6(a) has two nitrate groups coordinating with the copper ion, but nitrate anion is also well known to remain as free cations in metal complexes and this fact had provided scope to utilise aminonap to prepare six-coordinated complex *[Cu(aminonap)$_4$](NO$_3$)$_2$* (*2.1*). It was formed when metal salt to aminonap was 1:4 and the reaction was carried out at 70°C for 5 hours.

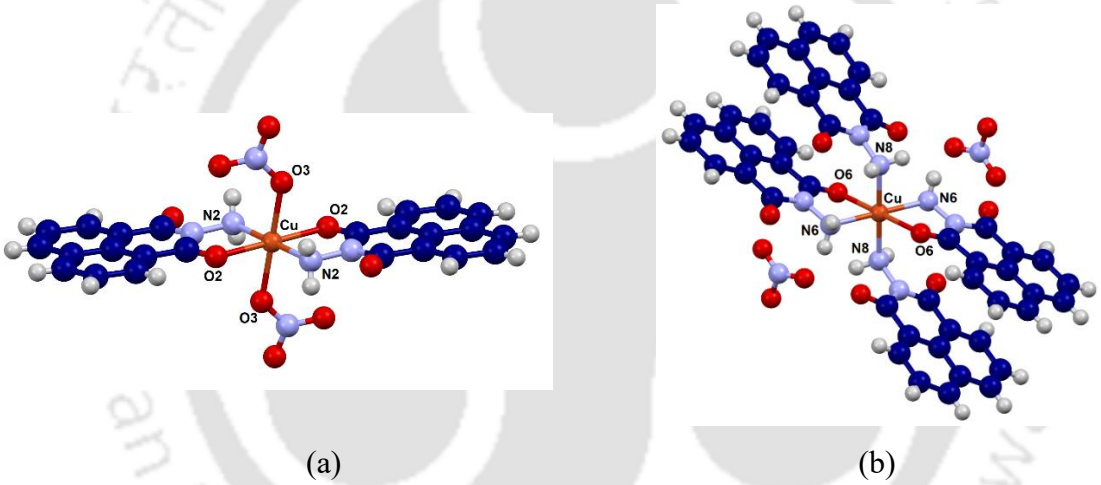

(a) (b)

Figure 2.7 Structure of the (a) *[Cu(aminonap)$_2$(NO$_3$)$_2$]* and (b) *[Cu(aminonap)$_4$](NO$_3$)$_2$* (**2.1**)

The two complexes had differences in compositions, and also the two copper complexes exhibited distinct structural characteristics. The complex *[Cu(aminonap)$_2$(NO$_3$)$_2$]* had a distorted octahedral geometry {(Figure 2.7(a)}. The metal-ligand bond distances were Cu-O(nitrate) 2.163(1) Å, Cu-O(aminonap) 2.131(1) Å, and Cu-N(aminonap) 1.981(1) Å. The longer Cu-O(nitrate) bonds, compared to the other metal-ligand bonds were a consequence of Jahn-Teller distortion of the copper (II) complex (d^9-electronic configuration).

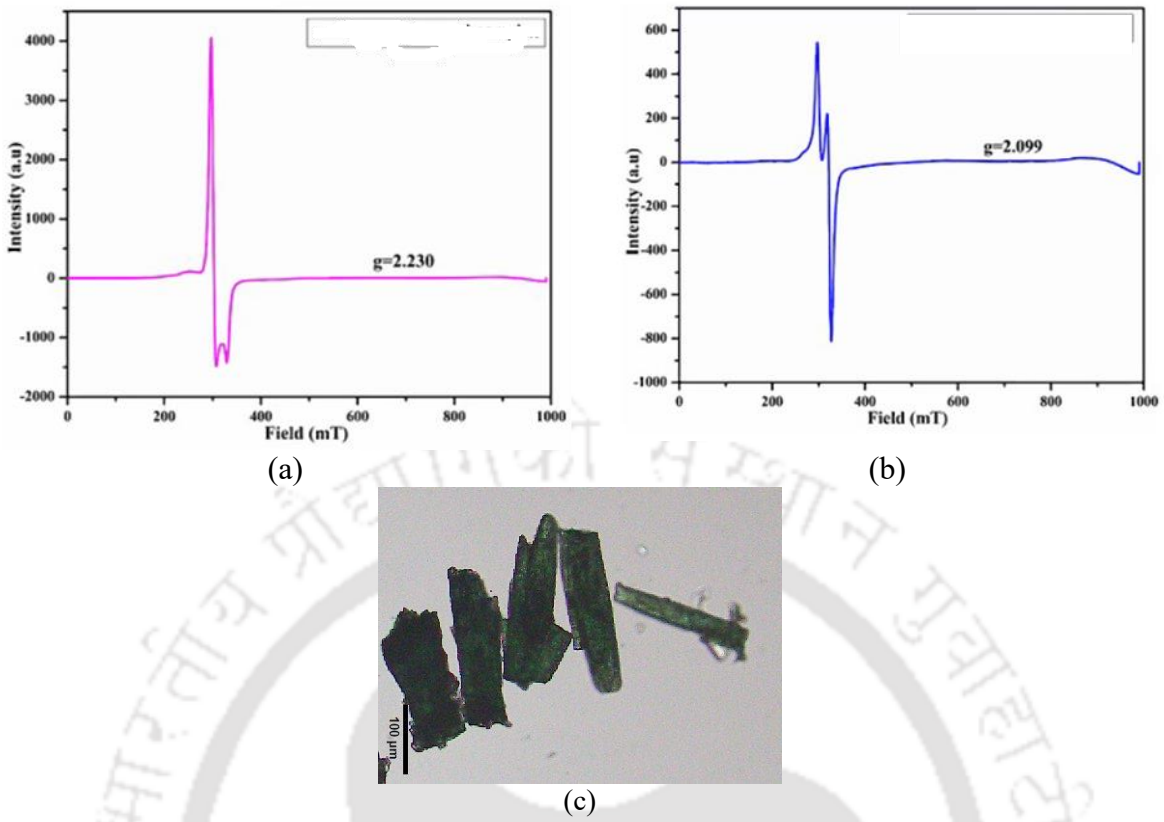

Figure 2.8: Room temperature X-band ESR spectrum of solid samples of (a) $[Cu(aminonap)_2(NO_3)_2]$ complex and (b) $[Cu(aminonap)_4](NO_3)_2$. (DPPH as reference compound). (c) Optical image of complex 2.1.

The structure of the complex *$[Cu(aminonap)_4](NO_3)_2$* (*2.1*) determined by X-ray single crystal diffraction, had the asymmetric unit containing half of the cationic part along with a nitrate ion of the complex. The complex **2.1** features two bis-coordinating ligands and two mono-dentate ligands {Figure 2.7(b)}. The Cu-O and Cu-N bond distances for the bis-coordinating ligands are 2.303(2) Å and 2.046(3) Å, respectively, while the Cu-N distance of the two mono-dentate ligands were equal and it was 2.093(3) Å. In this case, the relative elongation of the Cu-N bond of the mono-dentate ligands was along very less, whereas the $Cu\text{-}O_{(aminonap)}$ bond of the latter.

The complex had a longer bond length than the former, suggesting that the Jahn -Teller axis is along the $Cu\text{-}O_{(aminonap)}$ bond. The complex *$[Cu(aminonap)_2(NO_3)_2]$* displayed three ESR signals with g = 2.230 (Figure 2.8(a)], indicative of rhombic symmetry around the metal ion. While, the ESR spectra of *$[Cu(aminonap)_4](NO_3)_2$* exhibit isotropic symmetry with g = 2.099 (Figure 2.8 (b)]. The thermal stability of the complex was investigated by recording a

thermogram of the complex *[Cu(aminonap)$_4$](NO$_3$)$_2$* (Figure A2.3). The distinctions between the two copper complexes are listed in Table 2.5.

Table 2.5: Comparative distinguishing parameters of the two copper complexes

Complex	Number of aminonap	Ligand environment	Visible absorption (nm)	Decomposition temperature (ºC)
[Cu(aminonap)$_2$(NO$_3$)$_2$]	2	N_2O_4	349	193
[Cu(aminonap)$_4$](NO$_3$)$_2$]	4	N_4O_2	349	200

As mentioned earlier the attempted synthesis to prepare a zinc complex had resulted in the crystallisation of free ligands but we could obtain copper complexes of *aminonap* easily. On the other hand, a cadmium complex with the formula *[Cd(aminonap)$_3$(NO$_3$)](NO$_3$)·2(aminonap)* (*2.2*) was formed from a room temperature reaction of cadmium nitrate with aminonap. This complex was interesting as it had five *aminonap* molecules in the complex; which includes two neutral *aminonap* molecules self-included in the complex and three bidentate *aminonap* ligands. It was an eight-coordinate complex, it featured three neutral bidentate *aminonap* ligands, each coordinating through the nitrogen atom of the amine group and an oxygen atom from one of the carbonyl groups (Figure 2.9).

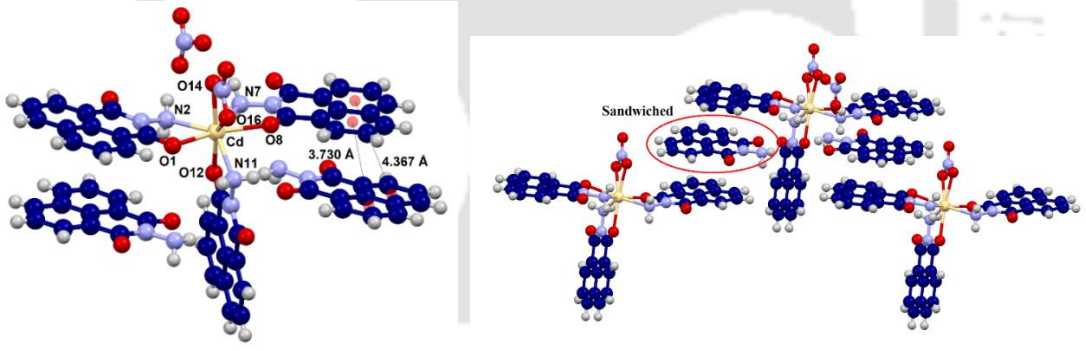

(a) (b)

Figure 2.9: (a) Crystal structure of the cadmium complex *[Cd(aminonap)$_3$(NO$_3$)]NO$_3$ ·2(aminonap)* (*2.2*) {selected bond distances are Cd-O1, 2.364(3)Å; Cd-O14, 2.374(4) Å; Cd-O8, 2.378(3) Å; Cd-N11, 2.378 (3) Å; Cd-O12, 2.385(3) Å; Cd-N7, 2.452(4) Å; Cd-N2, 2.471(4) Å}. (b) The packing of the complex showing the sandwiched *aminonap* in the self-assembly.

In addition to these three aminonap ligands, the complex had a nitrate ion coordinating in a bidentate chelating fashion. It also had another nitrate ion located outside the coordination sphere. The Cd-O bonds were in the range 2.364(3) Å to 2.385(3) Å, whereas the Cd-N bond distances were in the ranges of 2.452(4) Å - 2.471(4) Å These were supportive of the ligands

being coordination with cadmium and comparable to Cd-N and Cd-O bond distances found in cadmium complexes.[15] The coordination environment around the cadmium ion, provided by the three bis-coordinating *aminonap* ligands and the nitrate ligand was N_3O_5.

The two free neutral *aminonap* partner molecules of the complex were located parallel to the bis-ligating ligand on the two sides of the complex. In the crystal lattice, each molecule of the cadmium complex interacted with each neighbour molecule of the complex such that one aminonap ligand from the neighbour molecule was stacking with each other. These stacks sandwiched the free *aminonap* molecules, providing the inclusion complex (Figure 2.9b). In this packing arrangement, the amine and carbonyl groups of the ligands and free aminonap were parallel but located at translated positions, resulting in oblique alignment of the dipoles. The centroid-to-centroid distance between the rings of the ligand and free *aminonap* was 3.730 Å. In the self-assembly, two of the three ligands of each molecule were involved in sandwiching the free *aminonap* molecule, while the third *aminonap* ligand was oriented perpendicularly to the others. These molecules acted as anchors to hold the guest *aminonap* molecules by $O_{(carbonyl)}$-π interactions. Whereas the nitrate outside the coordination sphere provides C-H···O interactions to hold two neighbour molecules together by acting like bridges. Similarly, the non-ligating oxygen atom of the coordinating nitrate group was also involved in C-H···O interactions with C-H of naphthalimide units, contributing to the self-assembled structure.

Comparison of the FT-IR spectra of the aminonap with the cadmium complex (Fig. 2.10a) showed changes in the N–H stretching region in the complex, where the sharp peak at 3324 cm^{-1} of the original parent ligand had broadened in the complex. Additionally, shifts are observed in the C=O stretch and N–H overtone region (1600 - 1700 cm^{-1}), indicating changes due to complexation. The out-of-plane nitrate stretch,[16] had appeared in the coordinated nitrate at 1380 cm^{-1}. The nitrate ions coordinated in bidentate fashions showed N=O stretch in the region of 1630-1788 cm^{-1}, whereas monodentate nitrate shows symmetric and antisymmetric N-O frequencies at approximately 1049 cm^{-1} and 1370 cm^{-1}. The cadmium complex had both ionic and bidentate nitrate, the IR stretching of the complex in the region of 1700 cm^{-1} -1600 cm^{-1} had multiple peaks, hence those binding modes could not be distinguished from the IR spectra. The complex showed sharp weight loss by losing the aminonap in the range of 250 ˚C to 290 ˚C and decomposes by losing the *aminonap* ligands {Figure 2.10(b)}.

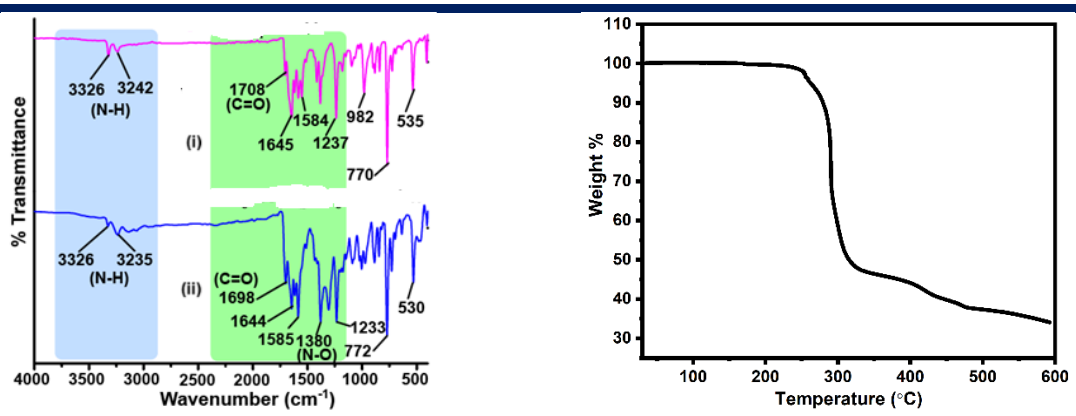

(a) (b)

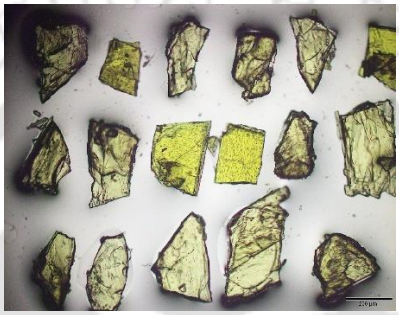

(c)

Figure 2.10: (a) The IR of the (i) *aminonap* and (ii) *[Cd(aminonap)$_3$(NO$_3$)]NO$_3$ ·2(aminonap)*; (b) thermogram of the *[Cd(aminonap)$_3$(NO$_3$)]NO$_3$·2(aminonap)* (heating rate 10 ◦C under argon), (c) optical image of complex 2.2.

Overall, the complex comprises five neutral *aminonap* molecules coordinated by a single cadmium ion, suggesting its potential for removing *aminonap* from solution in higher quantities through the inclusion of complex formation. This method benefits from using the same components as both ligand and guest, contrasting with metal-organic frameworks, where guests typically occupy pre-designed voids. The complex remains thermally stable up to 200 °C, experiencing a 40 % weight loss at this point due to the dissociation of two loosely bound *aminonap* ligands. Similarly, in complex *2.2*, decomposition occurs at 298 °C, resulting from the loss of two uncoordinated *aminonap*, as shown in Figure 2.8.

2.5: Solution study on the complexation of bivalent copper and zinc ions with *aminonap*

As the attempts to obtain a crystalline complex of zinc(II) with the *aminonap* ligand was not successful, two different copper aminonap complexes could be prepared by varying reaction conditions. Hence a solution study was taken up to distinguish the binding constants in different metal ligand equilibria. Isothermal calorimetry is a useful technique to study sequential

bindings of ligands or their sequential dissociations.[17] isothermal calorimetric study was taken up to study the relative binding of this *aminonap* with bivalent copper and zinc(II) ions to understand the complexation behaviour of *aminonap* to these metal ions. An isothermal titration calorimetry (ITC) revealed that zinc(II) nitrate interacted with aminonap (Figure 2.11). The ITC data was fitted to two sequential equilibrium steps of *aminonap* with zinc(II) ions, it yielded association constants $K_1 = (3.29 \pm 0.78) \times 10^3\ M^{-1}$ and $K_2 = (0.71 \pm 0.13) \times 10^3\ M^{-1}$ (Figure 2.11a). K_1 represents the binding constant between an equilibrium metal ion M^{2+} + *aminonap* $\rightleftharpoons$ *aminonnap*, whereas K_2 is for equilibrium between $[M(aminonap)]^+$ + *aminonap* $\rightleftharpoons$ $[M(aminonap)]^{2+}$. The respective entropy change for the first equilibrium was -439 cal/mol/deg, whereas it was -1.14 cal/mol/deg for the second equilibrium. The weak binding of *aminonap* to zinc(II) ions in solution suggested that a complex formed by *aminonap* with zinc ions would easily dissociate. As a consequence of this, the crystallisation of the aminonap took place while compound *aminonap* (0.02mM) with copper(II)nitrate trihydrate (1mM) (each time 2µL addition for 20 times) in milliQ water; and graph fitted to four sequential equilibria.

attempting to prepare its complex with zinc(II) nitrate. Hence, the dissociative equilibrium facilitated the controlled crystallization of the ligand. Isothermal titration calorimetry of the aminonap with copper(II) nitrate trihydrate revealed four sequential equilibria with association constants $K_1 = (12.1 \pm 9.6) \times 10^5\ M^{-1}$, $K_2 = (3.79 \pm 7.4) \times 10^4\ M^{-1}$, $K_3 = (2.43 \pm 4.2) \times 10^6\ M^{-1}$, and $K_4 = (2.88 \pm 1.7) \times 10^3\ M^{-1}$ (Figure 2.11 b). and graph fitted to two sequential equilibrium.

(b) Isothermal calorimetric titration of

The entropy changes for the first equilibrium at 35.9 cal/mol/deg, the second equilibrium at -1.67 cal/mol/deg, the third equilibrium is 47.0 cal/mol/deg, fourth equilibrium is -22.2 cal/mol/deg. The significantly higher magnitude of the third association constant K_3 observed in this titration as compared to the second equilibrium constant K_2, was observed. This complemented the ease of the formation of a bis-chelated complex at room temperature, and the formation of the complex with a 1: 4 metal-ligand ratio was less favoured. This was the reason that the preparation of the copper complex with a 1:4 metal-to-ligand ratio required elevated temperature and more reaction time as compared to that of the corresponding 1: 2 metal-ligand ratio of the complex.

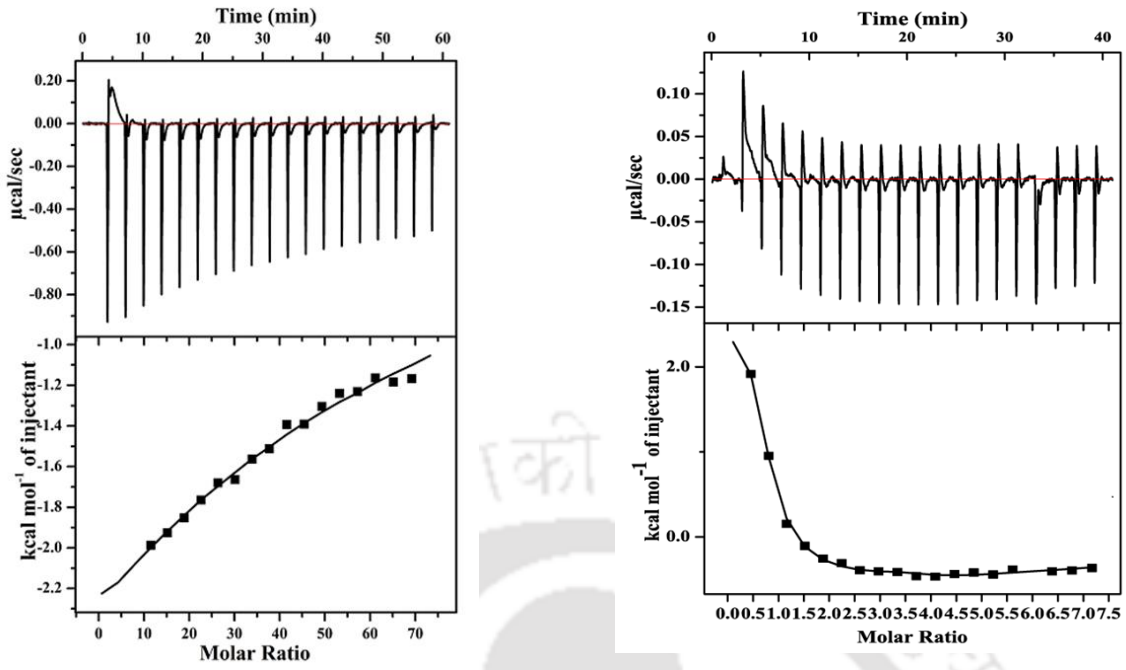

(a) (b)

Figure 2.11 (a): Isothermal calorimetric titration of compound **aminonap** (5×10^{-6} M) with zinc nitrate hexahydrate (2.5×10^{-4} M) (each time 2 µL addition for 20 times) in milliQ water; (b) Isothermal calorimetric titration of compound aminonap (0.02 mM) with copper (II) nitrate trihydrate (1mM) (each time 2 µL addition for 20 times) in milliQ water; and graph fitted to four sequential equilibria.

2.6 Emission spectroscopic studies of *aminonap* with acid and of the cadmium complex

A methanol solution of the *aminonap* was non-fluorescent, this was possibly due to the photo electro transfer of the lone pair of electrons causing an OFF state. Such fluorescence OFF in many naphthalimide compounds is well known.[18] Upon addition of a solution of an inorganic acid such as nitric acid or hydrochloric acid, the solution of the compound in methanol showed a weak emission at 392 nm (λ_{ex} = 335 nm). This emission peak continued to grow to reach a maximum intensity showing the acid-responsive emission by the compound as illustrated in Figure 2.12a and. A similar experiment carried out with acetic acid did not show significant emission (Figure A2.4). Hence, the effective protonation of the amine group was required to cause a fluorescence ON-state of the compound. The fluorescence spectra of the methanol solution of the cadmium complex had an emission peak at 560 nm upon excitation at 334 nm, together with a broad peak at 460 nm. The 560 nm was from aggregation-induced emission of the *aminonap*, as a solution of *aminonap* {Figure 2.12(b)} in dimethylsulphoxide (DMSO) had

showed a weak emission at 560 nm. Such longer wavelength emissions are commonly observed in naphthalimides aggregated by dipolar π-interactions;[19] whereas, the emission at 460 nm is was from intra-ligand transition due to the high stability of the zinc and cadmium d^{10} metal ions charge-transfer transitions are generally not observed [20]The same solution with externally added cadmium nitrate showed slight enhancement in the emission intensity at 560 nm, suggesting the aggregation was not significantly affected by cadmium ions. However, it generated a new emission peak at 460 nm. The change was anion-dependent; cadmium chloride or cadmium acetate did not significantly affect the emission spectra of the *aminonap* in DMSO but the cadmium nitrate anion did. The differences were due to the nitrate anion facilitating the stacks to form the assembled structure as found in the isolated complex which did not happen with the other counter ions.

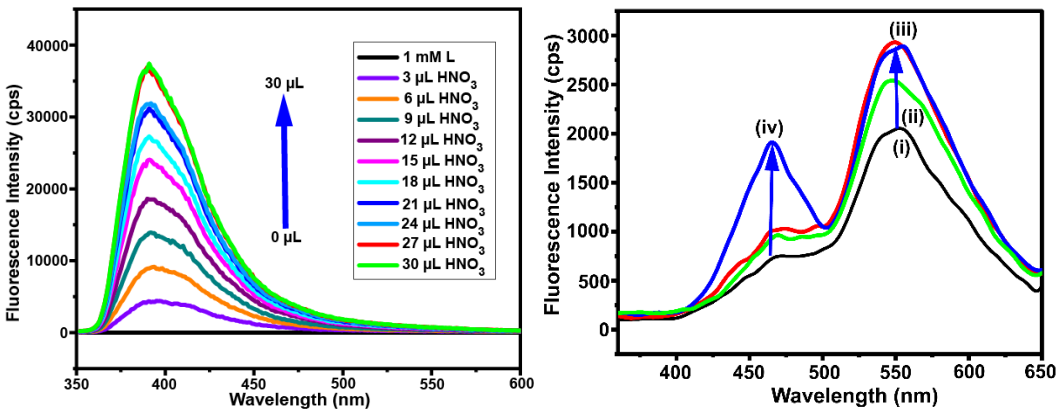

Figure 2.12: (a) The fluorescence titration of *aminonap* in methanol (3mL, 1mM) with the addition of 30 µL of 0.1 mM solution of nitric acid in methanol in each aliquot; λ_{em} = 390 nm. (b) The fluorescence emission spectra of (i) *aminonap* (5×10^{-3} M in dimethylsulphoxide, 3 mL, λ_{ex}, 334 nm) and changes after the addition of (ii) cadmium acetate, (iii) cadmium chloride and (iv) cadmium nitrate (in each case 50 µL of the solution of the corresponding salt 5×10^{-2} M in dimethylsulphoxide was added).

The zeta potentials of the *[Cu(aminonap)$_2$(NO$_3$)$_2$]* and *[Cu(aminonap)$_4$](NO$_3$)$_2$* were -5.08 mV and -5.39 mV showed that the latter had slightly higher –ve value of zeta potential (Figure S 24). These –ve values show that both complexes were stable in solution; The conductance of the 1mM aqueous solution of these two copper complexes was similar. The latter complex should be more ionic due to having two ionic nitrate ions per complex molecule, so it should have higher conductance in solution, the comparable values could be due to the large size of the cation having lower ionic mobility. The cadmium complex had a zeta-potential of -2.94 mV, suggesting it to be a stable complex (Figure A2.8).

2.7 Copper dicarboxylate complexes with amino nap

The ability of nitrogen-containing dicarboxylate ligands to form mixed ligand complexes is well known.[21] Based on such information in hand, two mixed ligands 2,6-pyridine dicarboxylate and 3,5-pyrazoledicarboxylate copper complexes having aminonap ligands listed in Figure 2.13 were synthesised and characterised.

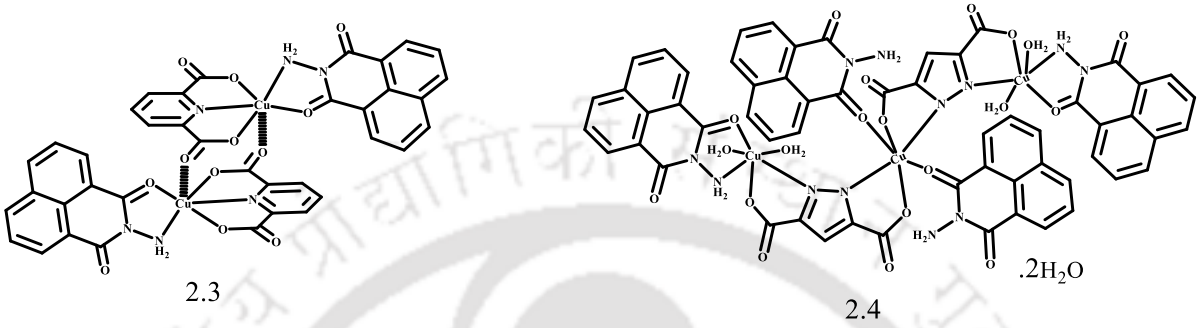

Figure 2.13: The mixed ligand copper(II) dicarboxylate complexes of aminonap

A mixed ligand dinuclear complex *2.3* having the 2,6-pyridinedicarboxylate (*26pdc*) and *aminonap* ligands, was synthesised in a one-pot reaction. The crystal structure of the complex *2.3* showed that the two copper ions of the complex were in similar octahedral geometry as shown in Figure 2.14(a). The *2,6pdc* had served as tridentate ligands, while the *aminonap* ligands were coordinated in a bidentate fashion.

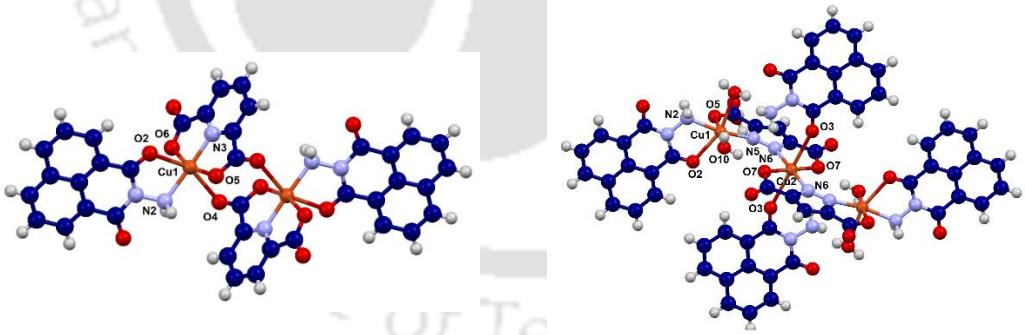

(a) (b)

Figure 2.14: The crystal structures of complexes (a) *2.3,* and (b) *2.4* (ORTEP drawn with 50% probability).

The *26pdc* ligands acted as bridging ligands, linking the two copper centres together. The *26pdc* ligand coordinated conventionally by taking up three coordination sites of each copper ion. The two free carbonyl groups of the *26pdc* acted as bridging units as illustrated in Fig. 3c; which led to the binuclear complex. The Cu-O and Cu-N bond lengths Cu1-N3,1.893(4)Å; Cu1-O6,

2.011(4)Å; Cu1-O5, 2.012(4)Å, showed that *26pdc* was tightly held to copper ions. On the other hand, the bridging Cu1-O4 bond distance was 2.249(2)Å, it was relatively longer than the commonly observed Cu-O bond distance. This showed that the two mononuclear complexes were weakly held together to form the binuclear complex. Whereas, the metal-ligand bonds Cu1-N2 and Cu1-O2 were 2.000(4) Å and 2.373(4) Å showed that weak binding of the carbonyl oxygen of *aminonap* than the coordination of the nitrogen atom of NH_2 to the copper(II) ions. The meal-ligand bond parameters are listed in Table 2.6. The copper···copper distance was 4.89 Å and had shown effective spin only magnetic moment for d^9-complex. The complex may be considered to be a combination of two mononuclear copper complexes formed in a 1:1 ratio of the ligands and the complexes had shared the fifth coordination sites of copper sites of one another. In the visible spectra of the compound, there was a broad absorption at 650 nm due to the $^2T_2$ to ^2E transition.

Table 2.6: Metal-ligands bond-lengths and angles of the complex *2.3*

M-L bond	Bond-length (Å)	< L-M-L	Bond-angle (°)
Cu1-N3	1.893 (4)	N3-Cu1-N2	177.0 (2)
Cu1-N2	2.000 (4)	N3-Cu1-O6	80.90 (17)
Cu1-O6	2.011 (4)	N2-Cu1-O6	98.98 (17)
Cu1-O5	2.012 (4)	N3-Cu1-O5	80.79 (17)
Cu1-O2	2.373 (4)	N2-Cu1-O5	99.38 (16)
Cu1-O4	2.528 (4)	O6-Cu1-O2	87.85 (16)

On the other hand, the reaction of copper acetate with 3,5-pyrazoledicarboxylic acid and aminonap provided a trinuclear complex *2.4* {Figure 2.14(b)}. In this complex, the central copper ion had two mono-dentate aminonap ligands and the coordination environment of the terminal copper centres differs from that of the central copper centre. The terminal copper centres of this complex *$[Cu_3(aminonap)_4(35pza)_2\ (H_2O)_2]$ ·$2H_2O$* exhibited octahedral geometry, with the *aminonap* and two 3,5-pyrazoledicarboxylates (*35pza*) coordinating in bidentate manners. The remaining two sites of the terminal copper ions were occupied by water molecules. The pyrazole N-H was deprotonated and allowed to form chelate with the terminal copper ions. Whereas, the charge of the central copper was neutralized by two carboxylates of two.

Table 2.7: Metal-ligands bond -lengths and bond-angles of the complex *2.4*

Bond	M - L (Å)	< L-M-L	Bond-angle (°)	Bond	M - L (Å)	< L-M-L	Bond-angle (°)

Cu1-O10	1.954 (2)	O10-Cu1-O5	175.99 (10)	Cu2-O7	1.940 (2)	O7Cu2O7	180.0 (7)
Cu1-O5	1.966 (2)	O10-Cu1-N5	100.34 (10)	Cu2-O7	1.940 (2)	O7Cu2N6	84.19 (10)
Cu1-N5	2.019 (3)	O5-Cu1-N5	82.53 (10)	Cu2-N6	1.977 (3)	O7Cu2N6	95.81 (10)
Cu1-N2	2.061 (3)	O10-Cu1-O5	92.19 (11)	Cu2-N6	1.940 (3)	O7Cu2N6	95.81 (10)
Cu1-O2	2.339 (2)	O5-Cu1-N2	85.20 (11)	Cu2-O3	2.662	O7Cu2N6	84.19 (10)
Cu1-O9	2.420 (3)	N5-Cu1-N2	166.56 (11)	Cu2-O3	2.662	N6Cu2N6	180.0 (7)

ligands that served as chelate to the terminal ligands. The *aminonap* served as an ancillary ligand of the complex, *[Cu_3(aminonap)$_4$(35pza)$_2$ (H_2O)$_2$]·2H_2O* (*2.4*). This trinuclear complex had three copper ions linked by two *35pza* tri-anions in a manner shown in Fig 2.14(b). The metal complexes of *35pza* ligand in general provide large structural diversities.[22] Among them the trinuclear,[22a-b] tetranuclear[22c] and metal-organic frameworks[22d] of *35pza* are well known. The trinuclear two-dimensional network of copper 35pza complexes showed anti-ferromagnetic properties.[22f] But discrete units of 2.4 had the distance between the two copper ions in the complex was 4.893 Å. On the other the dinuclear copper complexes of *35pyz* have Cu-Cu distances varying from 3.44 Å to 3.98 Å,[22g,h] they showed magnetic couplings. The Cu-Cu distance in the complex **2.4** was large hence for magnetic coupling. Hence, a conventional paramagnetic susceptibility vs temperature (room temperature to liquid N_2 temp.) profile of discrete copper (II) ions was observed (supporting Figure S6), hence, it was not pursued further. The characteristic features to distinguish this complex were (a) two distinct coordinated water molecules ligating to each of the terminal copper ions; and (b) two distinguishable binding modes of the *aminonap* ligands in the complex. The trinuclear backbone of the complex was comprised of two *35pza* ligands, each acting as a five-membered chelate by coordination of pyrazole nitrogen and oxygen of one carboxylate. The other carboxylate group coordinated to another copper (II) ion to provide the core unit of the trinuclear copper complex. Each terminal copper ion of the core had one *bis*-coordinated *aminonap*. The central copper ion was coordinated to a mono-dentate *aminonap* by using the coordination of an oxygen atom of C=O groups. This *aminonap* had the NH_2 group in free-state. The two *aminonap* ligands that were coordinated to the central copper ion were located at *trans* positions with respect to each other. The Cu···Cu distance was 4.511 Å and was apart enough and not conducive for magnetic interaction. All the copper-nitrogen and copper-oxygen bond distances other than the Cu1-O2 and Cu1-O9 bonds were within 1.9 Å - 2.0 Å, showing strong metal-ligand coordination. The bond parameters are listed in the Table 2.7. In complex *2.4* the Cu1-O2 bond length was 2.339(3) Å; it was a consequence of the weak coordination of the oxygen atom of one of the C=O groups of the naphthalimide to the copper ion. The two water molecules on each terminal

copper ion had different Cu-O bond lengths, one had the Cu1-O9 bond distance 2.420 (3) Å and the other had Cu1-O10 distance 1.954(2) Å. These bonds related the coordinated water molecules; hence, the two coordinated water molecules were distinguishable in the structure. Thermogravimetry of the complex 2.3 showed loss of the *aminonap* ligand at 276°C, followed by the decomposition of 2,6pdc at 306 °C {Figure 2.15(a)}. Complex 2.4 showed a sequential weight loss of six water molecules at 90 °C and 151 °C. This loss was shown as an initial loss of four water molecules at 90°C. This loss was from two weakly coordinated water molecules and two lattice water molecules held by hydrogen bonds. Subsequently, at 151 °C there was loss of weight, for the two tightly bound coordinated water molecules. These observations were consistent with the different Cu-O bond lengths observed in the crystal structure of the complex. The thermal analysis also illuminated the difference in the coordination of *aminonap* ligands in the complex. The monodentate *aminonap* of the complex was released at 253 °C, while the bidentate *aminonap* ligand was lost at 288 °C. Finally, the 3,5-pyrazole dicarboxylate moiety decomposed above 360 °C.

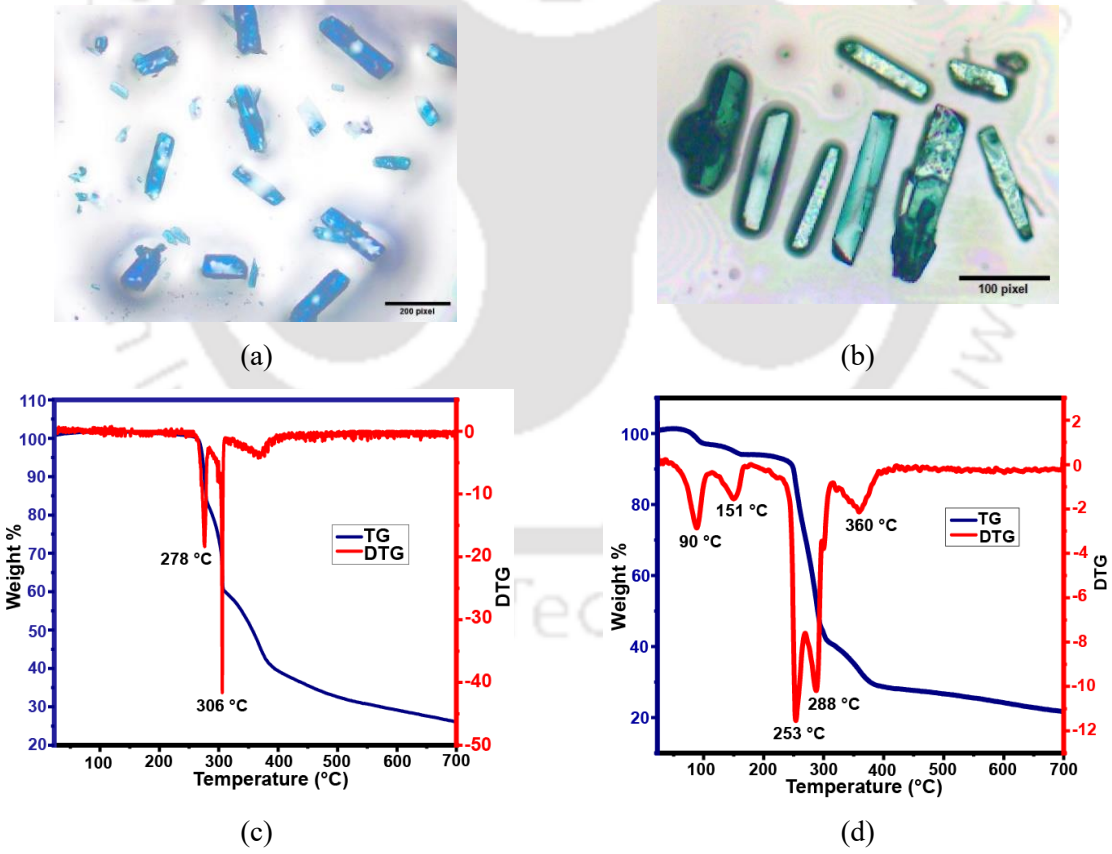

Figure 2.15: Optical image of complex (a) 2.3 (b) 2.4 and Thermogravimetry analysis of complex (c) 2.3 and (d) 2.4 (at a heating rate of 10 °C per minute under an argon atmosphere).

Both of the complex *2.3* and *2.4* had showed magnetic moment of 1.73 BM, which was characteristic of the d^9-electronic configuration of copper (II) ion in an octahedral environment. The complex had a broad visible-absorption at 650 nm due to the $^2T_2$ to ^2E electronic d-d transition.

The photo-electron spectroscopy is useful for establishing the environment of copper ions[23], so, the photo-electron spectra of the copper complexes *2.3* and *2.4* were studied (spectra are shown in supporting figures S5 (a-b) and found that there were two sets of peaks from ionisation of each $2p_{1/2}$(Cu) and $2p_{3/2}$ (Cu), each set of these was doublet. The ionisation peak for $2p_{1/2}$ of copper(II) appeared at 954.4 eV and at 952.4, whereas the $Cu2p_{3/2}$ were at 934.5 eV and 932.5 eV (Figure 2.16a). The copper complex *2.3* also had these two sets of doublet peaks characteristic of copper (II) complexes (Figure S 5a). The two-independent environments of copper (II) ions in the complex *2.4*, were not distinguishable in the X-ray photo-electron spectra. The oxygen O1s ionizations of the three complexes were also very similar. The complexes *2.3* and *2.4* had three peaks, one each from NH_2, imide nitrogen and the nitrogen of the carboxylic acids (Figure A2.5). These made it clear that skeletal differences of the naphthalimide ligands were reflected in the N1s ionization.

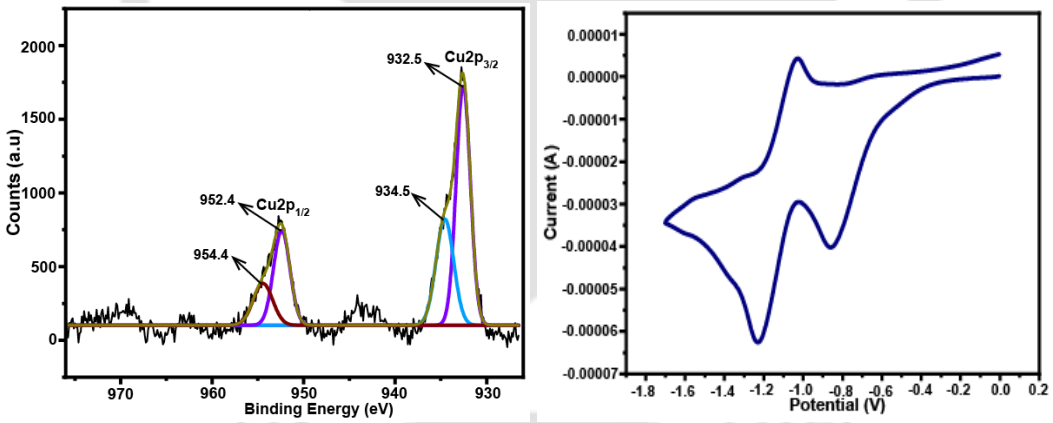

(a) (b)

Figure 2.16: (a) X-ray photo-electron spectra of the complex *2.4* showing the $2p_{1/2}$ (Cu) and $2p_{3/2}$ (Cu) ionizations. (b) Cyclic voltammogram of complex *2.3* (1 mM in DMF; with tetrabutylammonium perchlorate as supporting electrolyte, scan rate 100 mV/sec, + ve scan).

Table 2.8: List of redox potentials of the *aminonap* and the complexes *2.3* and *2.4*

Ligand/ complex	E_{pc}/V	E_{pa}/V	$E_{1/2}$/V
Aminonap	-1.15	-1.27	-1.21
Complex *2.3*	-1.22	-1.59	-1.41
	-0.85	-1.02	-0.94
Complex ***2.4***	-1.71	-1.60	-1.65
	-1.44	-1.20	-1.31

An acetonitrile solution of *aminonap* had the conventional two single-electron redox couple in the negative side of the cyclic voltammogram as found in related naphthalimide.[24] The copper complexes 2.3 and 2.4 showed two redox couples, involving radical anion formation followed by anion formation. The first redox cycle to form the radical anion of the complex *2.4* was a more negative side than the parent ligand. Whereas, the radical anion generated in complex *2.3* was at a much lower EMF ($E_{1/2}$ = -0.94V), and the second redox process of this complex was also relatively easy. These results showed that the dinuclear copper complex *2.3* was easily formed, radical anion {Fig. 2.16 (b)} by electro-reduction, which transformed into an anion (irreversibly). These showed that in each case, the metal complexation had helped to form anions of the naphthalimide part in solution.

2.8: Summary

The polymorphs of *aminonap* having a dipolar stacking arrangement or the dipolar naphthalimide rings in the same direction or opposite directions were demonstrated. The nitrate salt and a nitrate ionic cocrystal having neutral *aminonap* and protonated form could be structurally characterised; they had distinct physical properties. The complexation behaviour of *aminonap* with copper, zinc, and cadmium revealed the weak binding of zinc(II), whereas compositionally different copper complexes could be prepared. The cadmium complex provided a unique example of having three *aminonap* coordinating with the metal ion and making a template for the inclusion of two other molecules of *aminonap* by stacking interactions. The emission spectra showed the selectivity towards cadmium nitrate in changing the emission to a shorter wavelength. Binuclear or trinuclear copper heterocycle-derived dicarboxylate complexes were decorated by *aminonap* in different coordinating modes. The electrochemical aspects revealed the effect of copper coordination to inhibit the anion formation from the anion radical of the ligand that was easily formed in the free ligand under electrochemical conditions.

2.9 Experimental:

Synthesis of N-amino-1,8-Naphthalimide: It was synthesized form a solution of 1,8-naphthalic anhydride (1.0 g, 5 mmol) and hydrazine hydrate (0.24 ml 80 %) in DMF, the solution was placed in an oil-bath at 100°C for 12 hours. The reaction mixture was allowed to cool, and ice-cold water was added to obtain a yellow precipitate, which was filtered and air-dried.

FT-IR (neat, cm^{-1}): 3311(s), 3240(s), 3065(s), 1769 (s), 1706(s), 1651(m), 1583(s), 1435(s), 1379(s),1293 (s),1231(s), 1009(s), 769(s), 529(s). ^{1}HNMR (500MHz, DMSO-d_6, ppm) 8.51 (1H, d, J = 7.2Hz), 8.46 (1H, d, J = 8.1Hz), 7.88(1H, t, J = 7.7Hz). ^{13}C NMR (125 MHz, DMSO-d_6): 160.55, 134.55, 131.30,130.83, 127.33, 126.05,121.70.

Poly-1: It was crystallised from a solution of compound *aminonap* (42.4 mg, 0.2 mmol) in 20 mL of methanol by slow evaporation, which provided yellow needle-like crystals of polymorph *Poly-1* in 60% isolated yield. Melting point, 249 °C. IR (neat, cm^{-1}): 3321 (bw. ν_{N-H}), 3210 (bw, ν_{N-H}), 1711 (s, $\nu_{C=O}$), 1648 (s, ν_{N-H} bend).

Poly-2: To a solution of compound *aminonap* (42.4 mg, 0.2 mmol) in 20 mL of methanol, zinc nitrate hexahydrate (45 mg, 0.2 mmol) was added and stirred to form a homogeneous solution. The pH of the solution was measured and found to be 6.3. The solution was stirred for 30 minutes. Then the resulting solution was placed at 70 °C for 6 h, after which it was cooled to room temperature and filtered. The filtrate was left to stand for 5 days at 18 - 20 °C, which provided yellow block-like crystals. The crystals were hand-picked after decanting the supernatant liquid. The isolated yield of the crystals was 65%. Melting point, 256 °C. IR (cm^{-1}): 3310 (bw, ν_{N-H}), 3234 (bw, ν_{N-H}), 1692 (s, $\nu_{C=O}$), 1643 ($\nu_{N-H\ bending}$).

[Haminonap]NO_3·H_2O: The compound *aminonap* (42.4 mg, 0.2 mmol) was dissolved in 20 mL methanol. To this solution 0.8 ml of concentrated HNO_3 was added and stirred. A transparent solution was obtained whose pH was found to be 0.3. The solution was stirred for half an hour, after which it was kept at 70 °C for 6 h and filtered to obtain a clear filtrate. The filtrate was kept undisturbed at room temperature, which provided yellow block crystals. After decanting the filtrate, the crystals were hand-picked and the amorphous portions was discarded. The crude yield of the precipitate was ~60%. Melting point, 200 °C. IR (cm^{-1}): 3500 - 2500 (bs, ν_{N-H} and ν_{O-H}), 1724 (m, $\nu_{C=O}$), 1686 (s, $\nu_{N-H\ bending}$), 1582 (s, $\nu_{C=C}$), 1330 (s, $\nu_{nitrate}$).

[Haminonap]NO_3·aminonap ·H_2O : The same procedure as for nitrate salt was used but the 0.3 ml nitric acid was used , the pH of the solution was 0.54. Crystallisation had provided yellow needle-like crystals, and good quality crystals were hand-picked from the precipitate. The isolated yield of pure crystals was about 10 %. Melting point, 220 °C. IR (cm^{-1}): 3500-2500 (bs, ν_{N-H} and ν_{O-H}), 1721 (s, $\nu_{C=O}$), 1690 (s, $\nu_{N-H\ bending}$), 1582 ($\nu_{C=C}$), 1330 (s, $\nu_{nitrate}$).

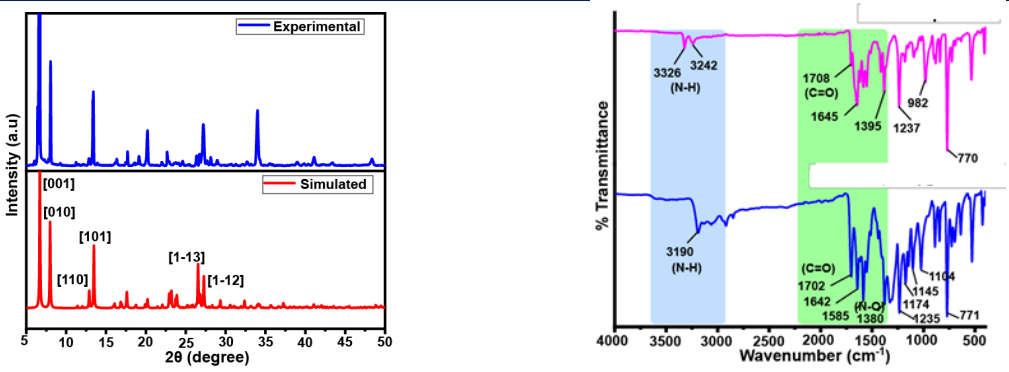

(a) (b)

Figure 2.17: (a) The experimental and simulated PXRD patterns of the complex *2.1*, (b) FT-IR of the (i) *aminonap* (ii) complex *2.1*.

Complex 2.1: A solution of copper nitrate trihydrate (24.2 mg, 0.1 mmol) and *aminonap* (42.4 mg, 0.2 mmol) in 20 mL methanol was stirred at room temperature for 1 hour, then the solution was heated at 70°C for 5 hours. After that the reaction mixture was filtered and left to concentrate by slow evaporation at room temperature. Greenish-blue crystals formed after three days, in which the solid formed was separated by decanting the supernatant liquid, yielding 28% of the product. A reaction with a 1:2 ratio of copper nitrate to ligand aminonap under similar reflux conditions resulted in the crystallisation of *[Cu(aminonap)$_4$](NO$_3$)$_2$* but with a higher isolated yield of approximately 58%. Melting point, 215 °C. FT-IR (cm^{-1}): 3190 (bw, ν_{N-H}), 1702 (s, $\nu_{C=O}$), 1642 (s, ν_{N-H} bending),1332 (s, $\nu_{nitrate}$).

Complex 2.2: A similar reaction as above by using *aminonap* (0.2 mmol, 42.4 mg) with cadmium nitrate tetrahydrate (30.8 mg, 0.1 mmol) provided brown crystals (isolated yield, 15% based on cadmium). Increasing the cadmium-to-ligand ratio to 1:5 improved the yield of the product to ~60 %. Melting point, 255 °C. IR (cm^{-1}): 3326 (bw, ν_{N-H}), 3235 (bw, ν_{N-H}), 1698 (s, $\nu_{C=O}$), 1644 (s, ν_{N-H}, bend), 1313 (s, $\nu_{nitrate}$).

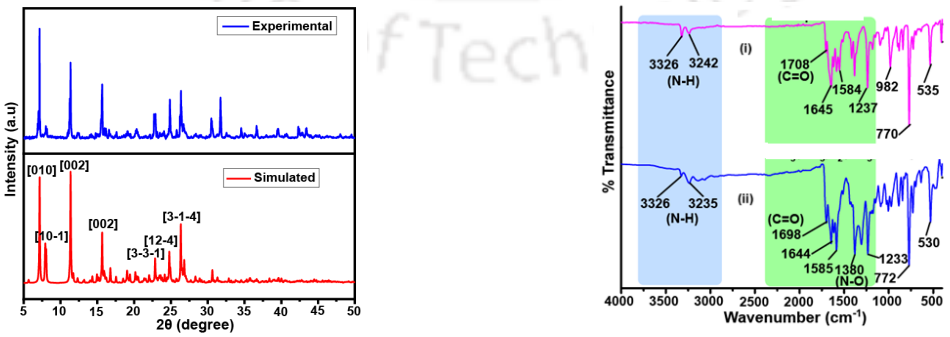

(a) (b)

Figure 2.18: (a) The experimental and simulated powder X-ray diffraction patterns of the complex *2.2*, (b) FT-IR (neat) of the (i) *aminonap* (ii) complex *2.2*.

Complex 2.3: To a warm solution of *aminonap* (42.4 mg, 0.2 mmol) in 20 mL of methanol, copper(II) acetate monohydrate (39.8 mg, 0.2 mmol) was added and it was dissolved by stirring. To this solution, 2,6-pyridinedicarboxylic acid (33.4 mg, 0.2 mmol) was added, and the mixture was stirred for an hour. A blue precipitate was formed was collected and the precipitate was recrystallized by dissolving it in water. 80 %. FTIR: 3190 (s, ν_{N-H}), 3082 (m), 2948 (w), 1724 (s, $\nu_{C=O}$), 1617 (s), 1591 (s), 1348 (s) 1226 (s), 1174 (s), 1137 (s), 1017 (s), 771(s). Elemental Anal. Calcd for $C_{38}H_{22}Cu_2N_6O_{12}$, C, 51.76; H, 2.51; N, 9.53; Found C, 51.72; H, 3.07; N, 9.58. UV-vis (Solid, λ_{max}) 650 nm.

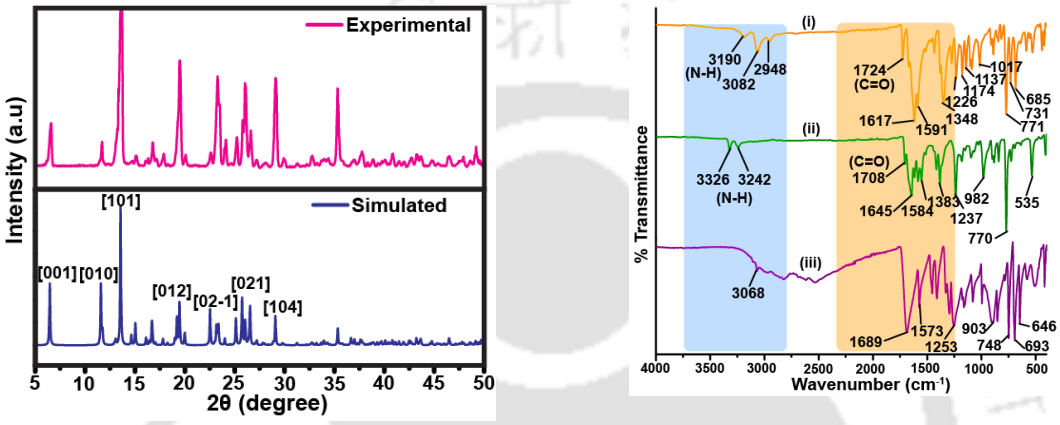

(a) (b)

Figure 2.19: (a) The experimental and simulated powder X-ray diffraction patterns of the complex *2.3,* (ii) FT-IR (neat) of the (i) complex *2.3*, (ii) *aminonap* (iii) 2,6-pyridinedicarboxylic acid.

Complex 2.4: Copper(II) nitrate trihydrate (48.2 mg, 0.2 mmol) and *aminonap* (42.4 mg, 0.2 mmol) was added to 20 mL of warm methanol, and a solution was prepared by stirring it for 30 minutes. Then, 3,5-pyrazoledicarboxylic acid (34.8 mg, 0.2 mmol) was added and the reaction mixture was stirred for an hour. A blue precipitate was formed, which was collected by decantation and dissolved in 5 mL of water and filtered. The filtrate was left undisturbed in an open environment for 2-3 days, and greenish crystals with an isolated yield of 40 % were collected after crystallisation. Elemental anal. calcd for $C_{58}H_{50}Cu_3N_{12}O_{24}$, C, 46.76; H, 3.38; N, 11.28; found C, 46.17; H, 3.70; N, 11.84. IR: 3461(s, νO-H), 3309 (w, νN-H), 1705 (s, ν C=O), 1644 (s, νC=O), 1583 (s), 1332 (s), 1236(s), 991(w), 771(s). UV-vis (solid, λ_{max}) 630 nm.

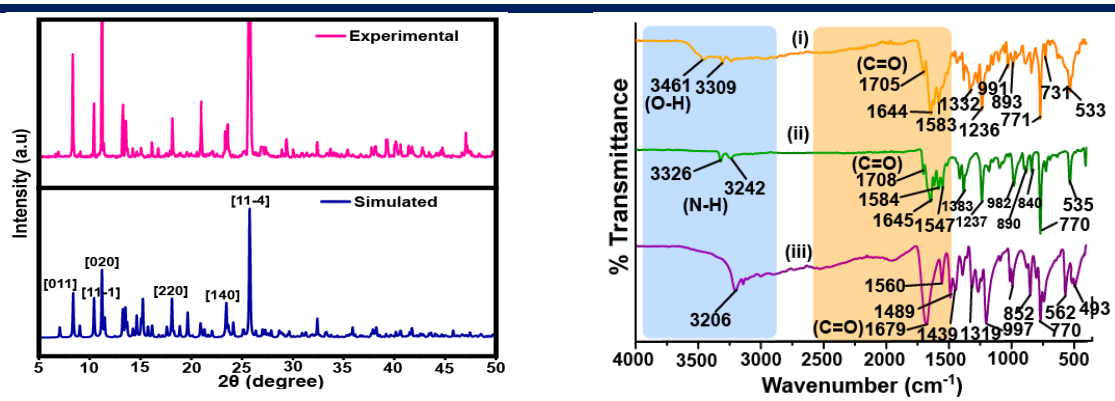

(a) (b)

Figure 2.20: (a) The experimental and simulated powder pattern of complex *2.4*, (b) FT-IR (neat) stacking pattern from (i) complex *2.4*, (ii) *aminonap,* (iii) 3,5-pyrazoledicarboxylic acid.

Fluorescence study:

The fluorescence measurements were carried out using a HORIBA FLUOROMAX 400 instrument. A 2.5 mL solution of 1 mM aminonap in methanol (MeOH) was titrated with an aqueous 0.1 mM hydrochloric acid (HCl) solution, adding 5 µL of HCl incrementally at each step. A similar titration was also conducted using acetic acid instead of HCl.

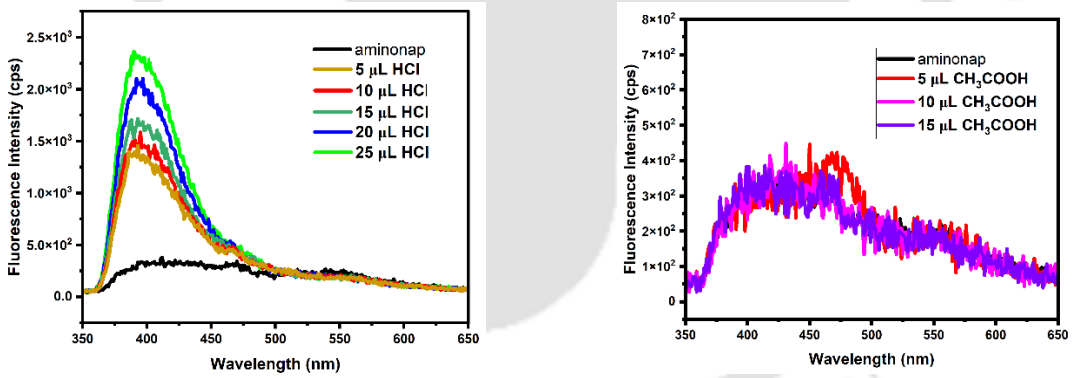

(a) (b)

Figure2.21: The fluorescence titrations of the solutions of the *aminonap* in dimethylformamide (1 mM, 2.5 mL) by adding different aliquots of (a) hydrochloric acid in water (0.1 mM), (b) glacial acetic acid (0.1 mM).

Determination of Zeta-potential

Zeta-potentials of aqueous solutions were recorded on a Malvern ZETASIZER Nano series instrument. Zeta potentials were determined from solutions prepared from aqueous solution of (i) *[Cu(aminonap)$_2$(NO$_3$)$_2$]* (540 µM); (ii) [*Cu(aminonap)$_4$](NO$_3$)$_2$* (225 µM); (iii) *[H aminonap]NO$_3$.H$_2$O* (1360 µM); (iv) [H*aminonap*](NO$_3$)·*aminonap*·*H$_2$O* (330 µM); (v) *[Cd(aminonap)$_3$(NO$_3$)]NO$_3$·2(aminonap)]* (257 µM) in independent experiments.

Structure determination:

Single crystal X-ray diffraction data were collected at 296 K with Mo Kα radiation (λ= 0.71073 Å) by a Bruker Nonius SMART APEX CCD diffractometer equipped with a graphite monochromator and an Apex CCD camera, other than the data for *Poly-1*, *[Haminonap]NO_3·aminonap·H_2O*, *[Cd(aminonap)$_3$(NO_3)]NO_3·2(aminonap)*, *[Cu(aminonap)$_4$](NO_3)$_2$*, [Cu(26pdc)(aminonap)]$_2$,Cu_3(35pza)$_2$(aminonap)$_4$(H_2O)$_4$]•2H_2O were collected on an Oxford SuperNova diffractometer. Data reductions and cell refinement for the Oxford SuperNova diffractometer were performed by CrysAlisPro software and for the Bruker Nonius SMART APEX CCD diffractometer using SAINT and XPREP software. Structures were solved by direct method and were refined by full-matrix least-squares on F^2 using SHELXL-2018 software. All the non-hydrogen atoms were refined anisotropic approximations against F^2 for all the reflections. Hydrogen atoms were placed at their geometric positions by riding and were refined in the isotropic approximation. The crystal and refinement parameters are placed in Table 2.9.

Table 2.9: Crystal and refinement parameters of the polymorphs, salt, ionic co-crystal, and metal complexes.

Parameters	Poly-1	Poly-2	[Haminonap]NO_3.H_2O	[Haminonap] NO_3.aminonap.H_2O
Empirical Formula	$C_{12}H_8N_2O_2$	$C_{24}H_{16}N_4O_4$	$C_{12}H_{11}N_3O_6$	$C_{24}H_{19}N_5O_8$
CCDC No	2168736	2168737	2168738	2168739
Formula wt.	212.20	424.41	293.24	505.44
Crystal system	Orthorhombic	Triclinic	Triclinic	Monoclinic
Space group	$Pna2_1$	P-$1\bar{}$	P-$1\bar{}$	$P2_1$
a/ Å	13.296 (2)	7.307 (6)	6.983 (4)	7.411 (8)
b/ Å	18.408 (4)	9.364 (7)	9.788 (5)	14.018 (13)
c/ Å	3.781 (11)	14.655 (10)	10.103 (6)	10.633 (10)
α/ °	90	81.676 (3)	98.26 (2)	90
β/ °	90	80.506 (3)	94.33 (2)	98.590 (9)
γ/ °	90	69.460 (3)	93.17 (2)	90
V/ Å^3	925.5 (4)	922.15 (12)	610.4 (6)	1092.48 (19)
Z	4	4	2	2
ρ (gcm^{-3})	1.523	1.528	1.595	1.536
μ (mm^{-1})	0.107	0.107	0.131	0.118
F(000)	440.0	440.0	304.0	524.0
Refl collected	2484	28420	6770	4310
Independent reflection	1565	3249	2963	3344
Ranges (h,k,l)	16 ≤ h ≤ 17	-8 ≤ h ≤ 8	-9 ≤ h ≤ 9	-9 ≤ h ≤ 5

	-21 ≤ k ≤ 24 -4 ≤ l ≤ 5	-11 ≤ k ≤ 11 -17 ≤ l ≤ 17	-11 ≤ k≤ 11 -13 ≤ l ≤ 13	-11 ≤ k ≤ 19 -11 ≤ l ≤ 14
Max θ (deg)	25.242	24.998	25.242	25.242
Data/restraints/parameters	2963/0/1943	344/1/339	12076/0/804	3983/0/331
GooF (F^2)	1.057	1.045	1.013	1.078
R indices [I>2σ]	0.0723	0.0523	0.0625	0.0438
WR_2	0.1172	0.1434	0.1790	0.1084

Parameters	**[Cd(aminonap)$_3$(NO$_3$)]NO$_3$•2(aminonap)**	***Cu(aminonap)$_4$](NO$_3$)$_2$***	**[Cu(26pdc)(aminonap)]$_2$**	**Cu$_3$(35pza)$_2$(aminonap)$_4$(H$_2$O)$_4$]•2H$_2$O**
Empirical Formula	$C_{60}H_{40}CdN_{12}O_{16}$	$C_{48}H_{32}CuN_{10}O_{14}$	$C_{38}H_{22}Cu_2N_6O_{12}$	$C_{58}H_{46}Cu_3N_{12}O_{22}$
CCDC No.	2168740	2195313	2255279	2255278
Formula Weight	1297.45	1036.3	881.68	1453.69
Crystal System	Triclinic	Triclinic	Triclinic	Monoclinic
Space group	P-$\bar{1}$	P-$\bar{1}$	P-$\bar{1}$	$P2_1$
a/ Å	13.262(7)	7.578(5)	7.613(13)	12.612(11)
b/ Å	14.348(8)	11.620(8)	7.892(13)	15.770(14)
c/ Å	16.635(10)	13.50	14.140(2)	14.304(12)
α/ °	96.631(5)	77.55(2)	104.569(5)	90
β/ °	104.242(5)	84.28(2)	91.955(5)	97.547(2)
γ/ °	116.913(5)	76.40(2)	91.760(5)	90
V/ Å^3	2640.2(3)	1127.38(13)	821.2(2)	2880.6(4)
Z	2	1	1	2
ρ (gcm^{-3})	1.632	1.526	1.783	1.712
μ (mm^{-1})	0.504	0.568	1.378	1.219
F (000)	1320.0	513.0	446.0	1482.0
Refl collected	21726	35467	20,864	82,817
Independent Refl	12076	-3983	2859	
Ranges (h,k,l)	-17 ≤ h ≤16 -18 ≤ k ≤ 18 -17 ≤ l ≤ 21	-9 ≤ h ≤ 9 -13 ≤ k ≤ 13 -16 ≤ l ≤ 16	-9 ≤ h ≤ 9 -9 ≤ k ≤ 9 -16 ≤ l ≤ 16	-15 ≤ h ≤ 15 -18 ≤ k ≤ 18 -17 ≤ l ≤ 17
Max θ (degree)	25.242	25.077	24.997	25.354
Data/restraints/parameters	565/1/151	3249/0/290	2859/0/262	5164/0/438
Goof (F^2)	1.026	1.050	1.213	1.108
R indices [I>2σ]	0.0662	0.0613	0.9170 0.0650	0.0549 0.0465
WR_2	0.1466	0.1731	0.1299	0.1180

2.10 References:

1. (a) G. Loving, B. Imperiali, A Versatile amino acid analogue of the solvatochromic fluorophore 4-*N,N*-dimethylamino-1,8-naphthalimide: A powerful tool for the study of dynamic protein Interactions. *J. Am. Chem. Soc.*, 2008, 130, 13630 - 13638.

(b) S. Murphy, S. A. Bright, F. E. Poynton, T. McCabe, J. A. Kitchen, E. B. Veale, D. C. Williams and T. Gunnlaugsson, Synthesis, photophysical and cytotoxicity evaluations of DNA targeting agents based on 3-amino-1,8-naphthalimide derived Tröger's bases, *Org. Biomol. Chem.*, 2014, 12, 6610 - 6623.

(c) A. S. Klymchenko, Solvatochromic and fluorogenic dyes as environment-sensitive probes: design and biological applications. *Acc.Chem. Res.*, 2017, *50,* 366 - 375.

(d) J. Zhou, C. Fang, Y. Liu, Y. Zhao, N. Zhang, X. Liu, F. Wang, D. Shangguan, Visible-light-induced cleavage of 4-α-amino acid substituted naphthalimides and its application in DNA photocleavage. *Org. Biomol. Chem.*, 2015, 13, 3931 - 3935.

(e) T. Anand, S. K. A. Kumar, S. K. Sahoo, A new Al^{3+} selective fluorescent turn-on sensor based on hydrazide-naphthalic anhydride conjugate and its application in live cells imaging. *Spectrochim Acta A Mol Biomol Spectrosc*., 2018, 204, 105 - 112.

(f) M. K. Noushija, A. V. Krishna, T. Gunnlaugsson, S. Shanmugaraju, Reactivity-based amino-1,8-naphthalimide fluorescent chemosensors for the detection and monitoring of phosgene. *Sens. Diagn.,* 2024, 3, 783 - 798.

2. M.M. Kumar, P. Venkataramana, P. Y. Swamy, Y. Chityala, *N*-Amino-1,8-naphthalimide is a regenerated protecting group for selective synthesis of mono-N-substituted hydrazines and hydrazides. *Chem. Eur J.,* 27, 2021, 17713 - 17721.

3. P. Raj, A. Singh, A. Singh, N. Singh, Syntheses, crystal structures and photophysical properties of Cu(II) complexes: fine-tuning of a coordination sphere for selective binding of azamethiphos. *Dalton Trans.*, 2017, 46, 985 - 994.

4. G.R. Desiraju, Supramolecular synthons in crystal Engineering-a new organic synthesis. *Angew. Chem. Int. Ed.* 1995, 34, 2311 - 2327.

5. (a) A. D. Johnson, J. A. Buhagiar, D. C. Magri, 4-Amino-1,8-naphthalimide-ferrocene conjugates as potential multi-targeted anticancer and fluorescent cellular imaging agents. *RSC Med. Chem.*, 2021, 12, 2060 - 2064.

(b) D. Chen, X. Yu, Y. Qin, Z. Y. Liao, T. Li, F. F. Guo, K. X. Song, R. L. Yu, Y. M. Xia, W. W. Gao, Electrochemical detection of DNA damage caused by novel potential

2-nitroimidazole naphthalimide-based hypoxia tumor-targeting agent with mimimum side effects. *Microchemical J.,* 2022, 178, 107435.

6. L. P. Grigoreva, L. A. Chetkina, M. G. Neigauz, G. A. Golder, The X-ray structural study of N-aminonaphthalimide. *Kristallografiya*, 1975, 20, 1178 - 1182.

7. T. Chen, M. Li, J. Liu, π–π Stacking interaction: a nondestructive and facile means in material engineering for bio applications. *Cryst. Growth Des.,* 2018**,** *18,* 2765 - 2783.

8. X. He, A. C. Benniston, H. Saarenpää, H. Lemmetyinen, N. V. Tkachenko and U. Baisch, Polymorph crystal packing effects on charge transfer emission in the solid state *Chem. Sci.*, 2015, 6, 3525 - 3532.

9. M. C. Etter, J. C. MacDonald, J. Bernstein, Graph-set analysis of hydrogen-bond patterns in organic crystals. *Acta Crystallogr*., 1990, B46, 256 - 262.

10. S. Jin, R. Sanii, B. Q. Song, M. J. Zaworotko, Crystal engineering of ionic cocrystals sustained by the phenol–phenolate supramolecular heterosynthon. *Cryst. Growth Des.,* 2022, 22, 4582 - 4591.

11. S. L. Childs, L. J. Chyall, J. T. Dunlap, V. N. Smolenskaya, B. C. Stahly, G. P. Stahly, Crystal engineering approach to forming cocrystals of amine hydrochlorides with organic acids. molecular complexes of fluoxetine hydrochloride with benzoic, succinic, and fumaric acids. *J. Am. Chem. Soc.,* 2004, 126, 13335.

12. R. Chatterjee, L. Paul, D. K. Hazra, N. Pal, A. D. Jana, M. Mukherjee, M. Ali, Encapsulation of a double-helical water–nitrate chain inside unique double helical chiral channels formed from Keggin POM and hexa-aqu-cobalt(II) units. *Polyhedron,* 2014, 68, 265 - 271.

13. A. Purkayashtha, J. B. Baruah, Tetrachlorocopper(II) chemistry: delineation of optical, thermal properties. *Thermochimica Acta*, 2002, 390, 187 - 193.

14. A. Serrano-Lotina, R. Portela, P. Baeza, V. Alcolea-Rodriguez, M. Villarroel, P. Ávila, Zeta potential as a tool for functional materials development.*Catal. Today,* 2023, 423, 113862.

15. K. Bania, N. Barooah, J. B. Baruah, Structural variations in self-assembled cadmium benzoate complexes. *Polyhedron.* 2007, 26, 2612 - 2620.

16. M. Y. Mihaylov, V. R. Zdravkova, E. Z. Ivanova, H. A. Aleksandrov, P. S. Petkov, G. N. Vayssilov, K. I. Hadjiivanov, Infrared spectra of surface nitrates: Revision of the current opinions based on the case study of ceria. *J. Catal.,* 2021, 394, 245 - 258.

17. M. Y. Gee, Y. Shen, A.B. Greytak Isothermal titration calorimetry resolves sequential ligand exchange and association reactions in treatment of oleate-capped CdSe quantum dots with alkylphosphonic acid. *J. Phys. Chem. C* 2020, 124, 23964 - 23975.

18. X. Poteau, A. I. Brown, R. G. Brown, C. Holmes, D. Matthew, Fluorescence switching in 4-amino-1,8-naphthalimides: "on–off–on" operation controlled by solvent and cations. *Dyes and Pig.*, 2000, 47, 91 - 105.

19. M. T. Albelda, M. A. Bernardo, E. Garcia-España, M. L. Godino-Salido, S. V. Luis, M. J. Melo, F. Pina, C. Soriano, Thermodynamics and fluorescence emission studies on potential molecular chemosensors for ATP recognition in aqueous solution. *J. Chem. Soc. Perkin Trans.* 2, 1999, 2545 - 2549.

20. K. S. Smirnova, E. V. Lider, T. S. Sukhikh, A. S. Berezin, A. S. Potapov, Cadmium coordination compounds with flexible ligand 1,3-bis(1,2,4-triazol-1-yl)propane: Synthesis, structure and luminescent properties. *Polyhedron*, 2020, 177, 114286.

21. (a) P. King, R. Clérac, C. E. Anson, C. Coulon,A. K. Powell, Antiferromagnetic three-dimensional order induced by carboxylate bridges in a two-dimensional network of $[Cu_3(dcp)_2(H_2O)_4]$ trimers. *Inorg. Chem.*, 2003, 42, 3492 - 3500.

(b) B. Das and J. B. Baruah, Assembling of copper(II) dipicolinate complexes. *Polyhedron*, 2012, 31, 361 - 367.

22. (a) F. M. Nie, Z. Y. Dong, F. Lu, G. X. Li Synthesis, structures, and magnetic properties of two pyrazolato-bridged trinuclear copper(II) complexes. *J. Coord. Chem.,* 2010, 63, 4259 - 4270.

(b) W. L. Driessen, L. Chang, C. Finazzo, S. Gorter, D. Rehorst, J. Reedijk, M. Lutz, A. L. Spek, Two pyrazolato-bridged, linear trinuclear Cu(II) complexes: crystal structures and magnetic properties. *Inorg. Chim. Acta,* 2003, 350, 25 - 31.

(c) D. Selçuk, C. H. Merve, H. Malgorzata, K. Muammer, A tetranuclear copper (II) complex with pyrazole-3,5-dicarboxylate ligands: synthesis, characterization and electrochemical properties. *Zeitschrift für Naturforschung B*, 2016, 71, 305 - 310.

(d) S. Barman, H. Furukawa, O. Blacque, K. Venkatesan, O. M. Yaghi, G. X. Jin, H. Berke, Incorporation of active metal sites in MOFs via in-situ generated ligand deficient metal-linker complexes. *Chem.Commun.*, 2011, 47, 11882 - 11884.

(e) P. King, R. Clérac, C. E. Anson, A. K. Powell, The building block approach to extended solids: 3, 5-pyrazoledicarboxylate coordination compounds of increasing dimensionality. *Dalton Trans.*, 2004, 852 - 861.

(f) P. King, R. Clerac, C. E. Anson, C. Coulon, A. K. Powell, Antiferromagnetic three-dimensional order induced by carboxylate bridges in a two-dimensional network of $[Cu_3(dcp)_2(H_2O)_4]$ trimers. *Inorg. Chem.* 2003, 42, 3492 - 3500.

(g) J. C. Bayon, P. Esteban, G. Net, P. G. Rasmussen, K. N. Baker, C. W. Hahn, M. M. Gumz, Dinuclear Pt(II), Pd(II), Ni(II), and Cu(II) complexes of 3,5-pyrazole carboxylic acid. *Inorg. Chem.,* 1991, 30, 2572 - 2574.

(h) L. Tian, S. P. Yan, D. Z. Liao, Z. H. Jiang, P. Cheng, Syntheses, structures and properties of two one-dimensional chain complexes: $[Mn(Hpdc)(H_2O)_2]n$ and $[Cu_2(Hpdc)_2][4,4'\text{-dpdo}]$ (Hpdc = 3,5-pyrazoledicarboxylic acid group, dpdo = 4,4′-dipyridyl-N,N′-dioxide hydrate). *Inorg. Chem. Commun.,* 2003, 6, 1025 - 1029,

23. (a) H. Rupp, U. Weser, X-ray photoelectron spectroscopy of copper(II), copper(I), and mixed valence systems. *Bioinorg. Chem.,* 1976, 6, 45 - 59.

(b) R. R. Gagne, J. L. Allison, C. A. Koval, W. S. Mialki, T. J. Smith, R. A. Walton, X-ray photoelectron spectra of copper(I) and copper(II) complexes derived from macrocyclic ligands. *J. Am. Chem. Soc.*, 1980, 102, 1905 - 1909.

24. N. Barooah, C. Tamuly, J. B. Baruah, Synthesis, characterisation of few N-substituted 1,8-naphthalimide derivatives and their copper(II) complexes. *J. Chem. Sci.,* 2005, 117, 117 - 122.

Appendix-Chapter 2

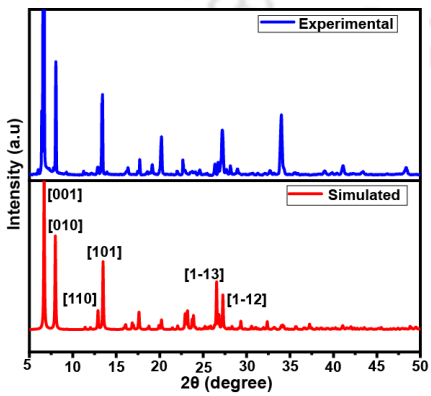

(a)

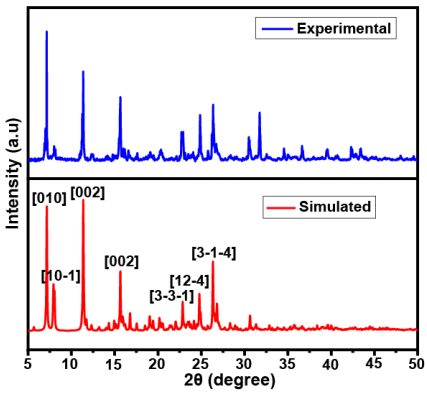

(b)

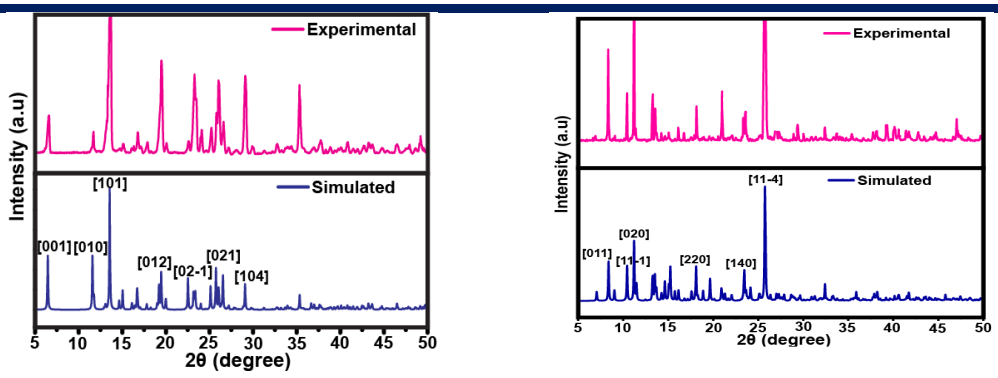

(c) (d)

Figure A 2.1: Powder X-ray diffraction patterns of the (a) 2.1 (b) 2.2 (c) 2.3 (d) 2.4.

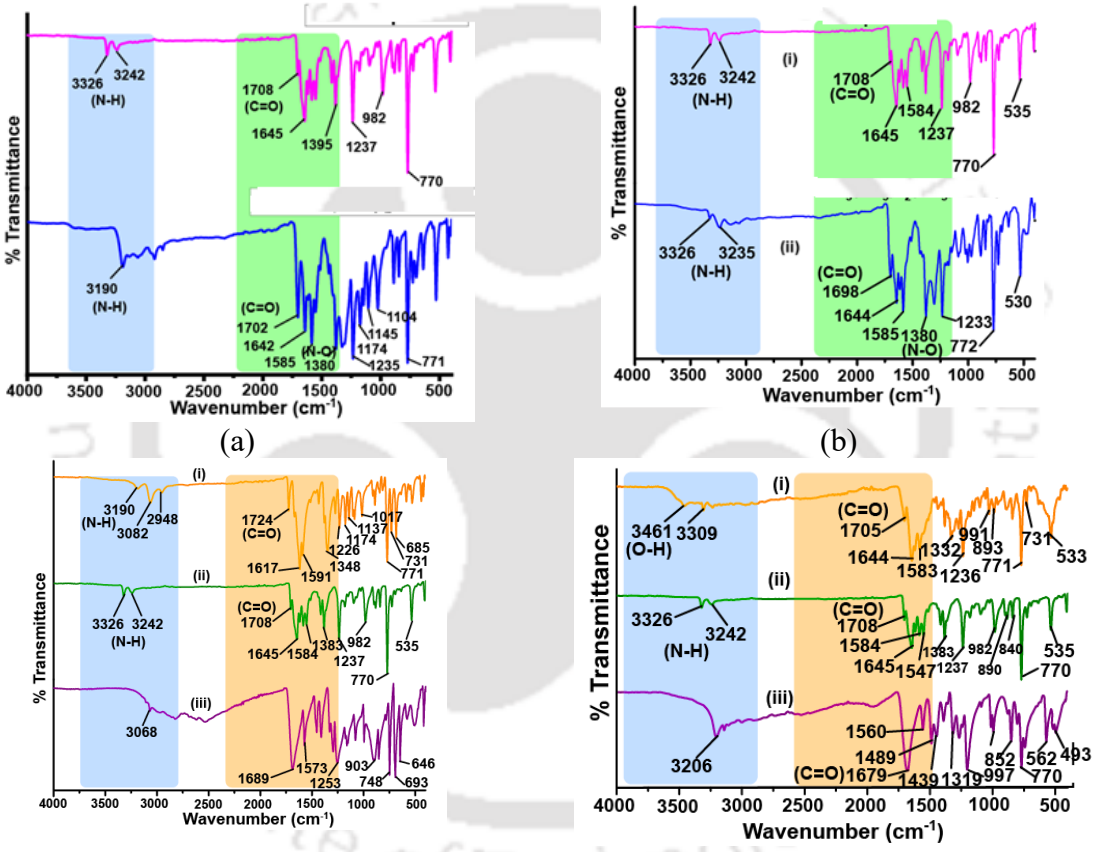

(a) (b)

(c) (d)

Figure A 2.2: FTIR spectra of the (a) 2.1 (b) 2.2 (c) 2.3 (d) 2.4. In each case (i) and (ii) are the respective complexes and aminonap ligands. (iii) in (c) and (d) are for the 2,6-pyridine dicarboxylic acid and 3,5-pyrazole dicarboxylic acid respectively.

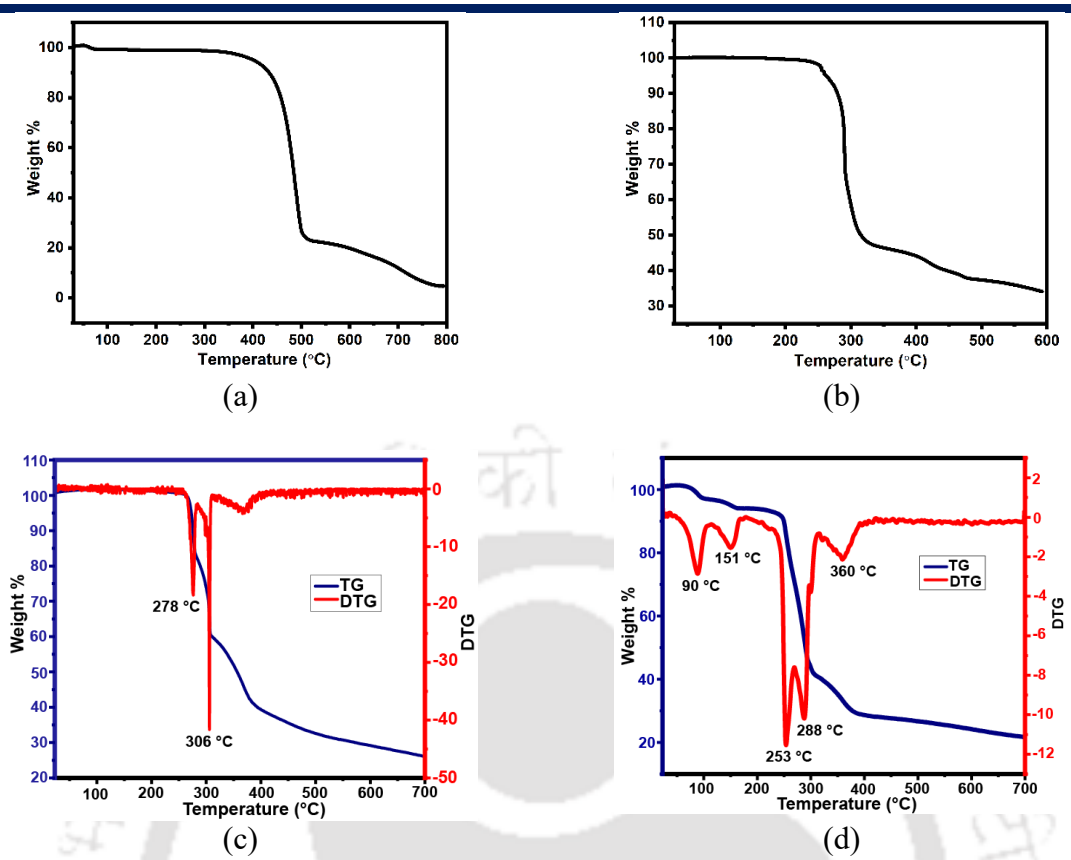

Figure A 2.3: Thermogram of the (a) 2.1 (b) 2.2 (c) 2.3 (d) 2.4 (heating rate 10 °C/min under argon atmosphere).

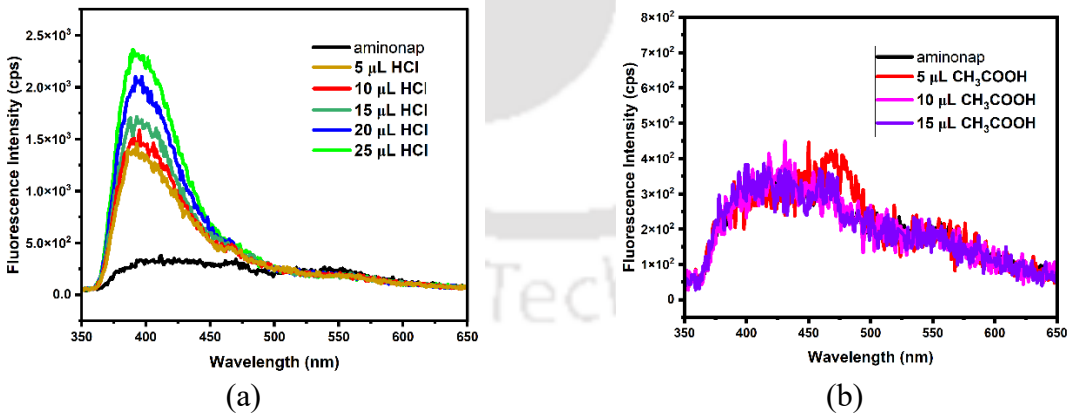

Figure A2.4: The fluorescence titrations of the solutions of the *aminonap* in dimethylformamide (1 mM, 2.5 mL) by adding different aliquots of (a) hydrochloric acid in water (0.1 mM), (b) glacial acetic acid in water (0.1 mM)

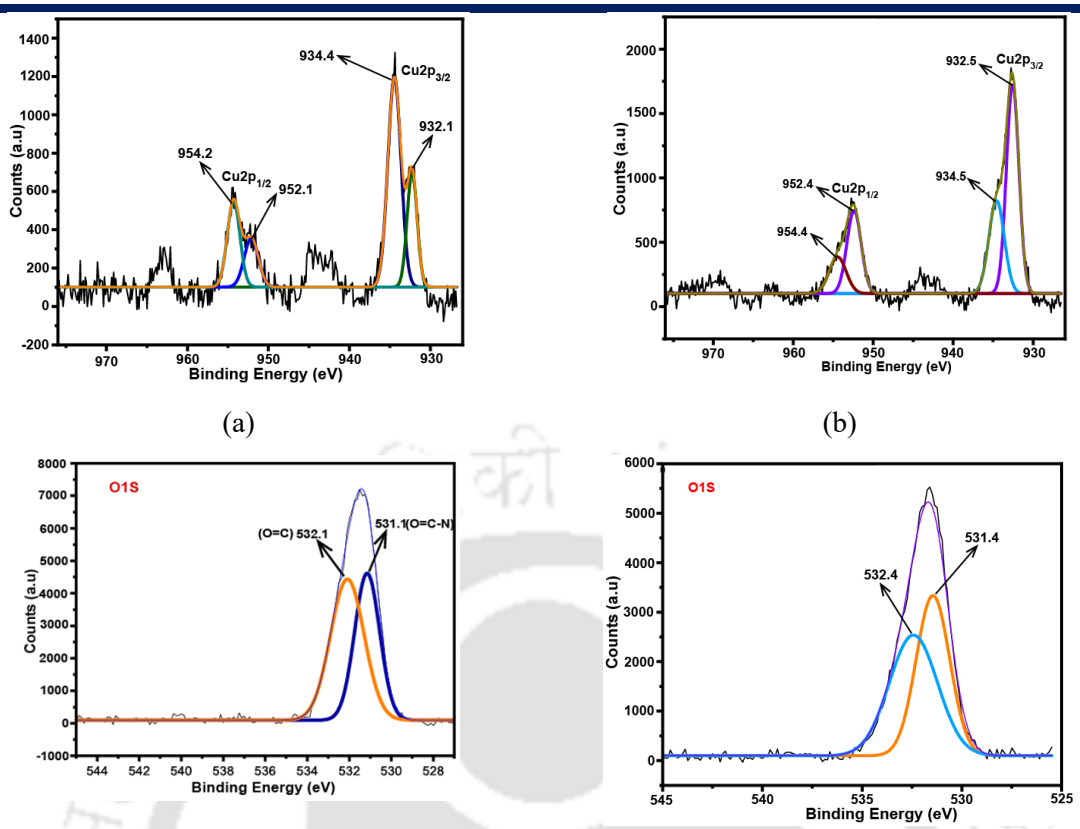

Figure A 2.5: XPS spectrum showing 2p regions of Cu of the complex (a) 2.3 (b) 2.4.

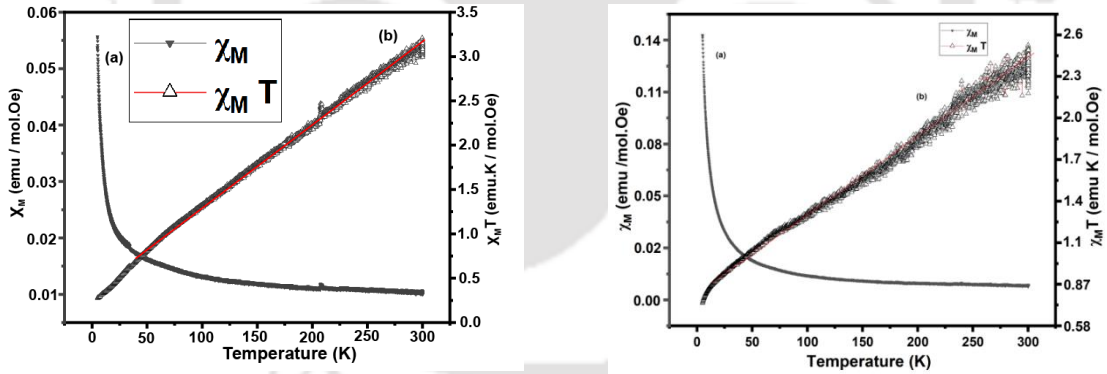

Figure A 2.6: Plots of molar susceptibility (a) and product of molar susceptibility with temperature (b) vs temperature (measured at 0.5 kOe) for the complex (a) 2.3 (b) 2.4.

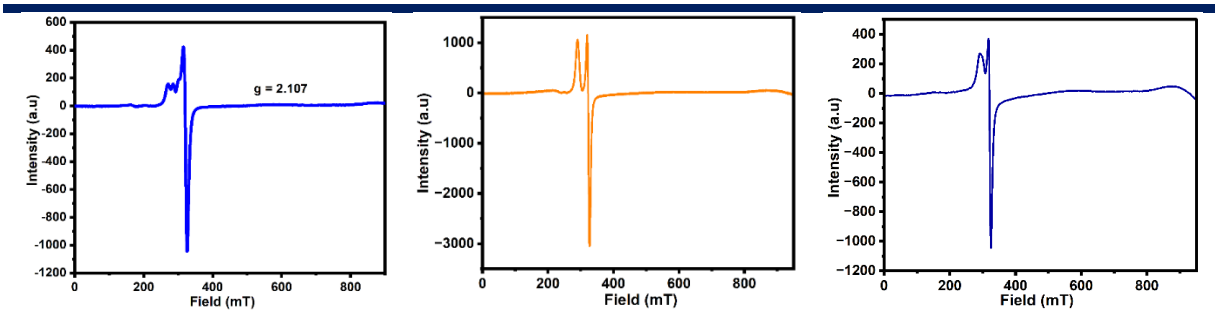

Figure A 2.7: Room temperature X-band ESR spectrum of solid samples of (a) 2.1 (b) 2.3 and (c) 2.4 (DPPH as reference compound).

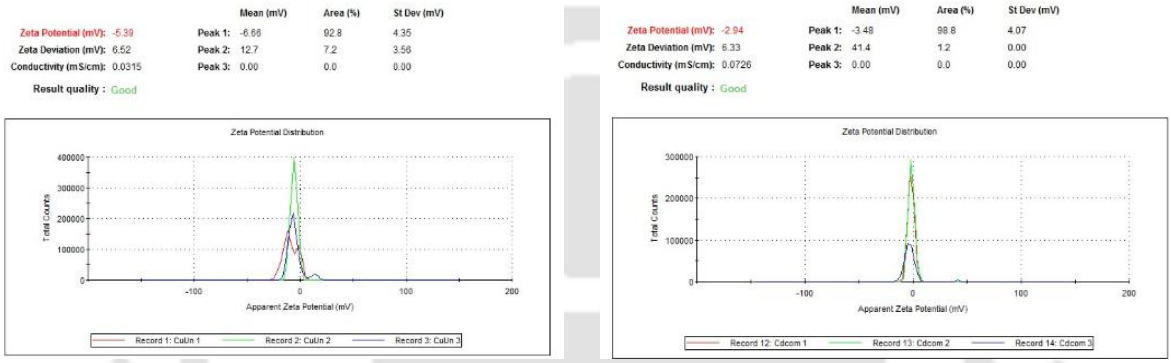

(a) (b)

Figure A 2.8: Zeta-potential plots of aqueous solution of (a) 2.1 (b) 2.2.

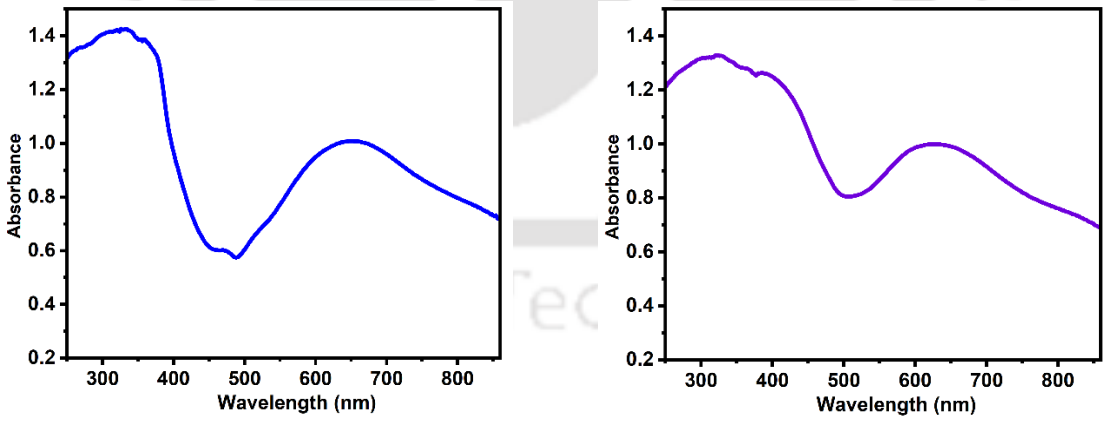

(a) (b)

Figure A 2.9: Solid state UV-visible spectra of (a) 2.3 (b) 2.4.

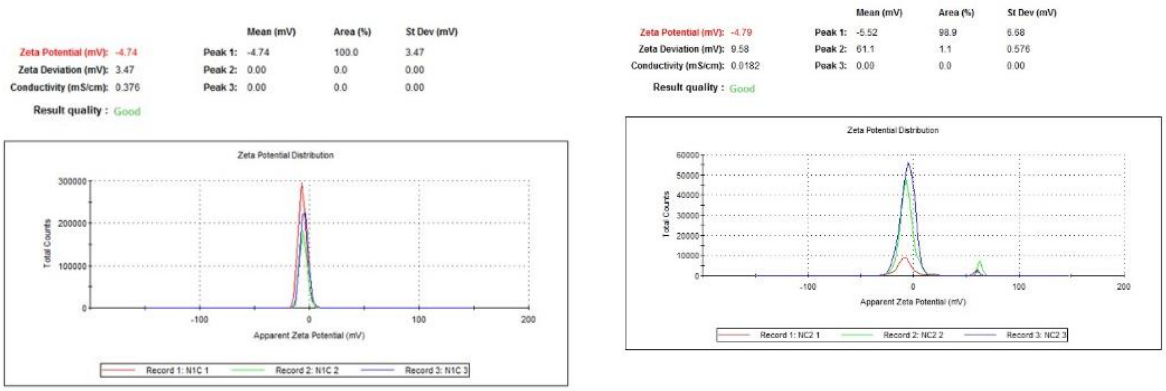

(a) (b)

Figure A 2.10: Conductivity measurements of (a) $[HL]NO_3.H_2O$ (b) $[HL]NO_3.Lf.H_2O$.

Chapter 3

Copper and cobalt 2,6-pyridinedicarboxylate complexes having 2-(pyridin-4-ylmethyl)-1H-benzo[de]isoquinoline-1,3(2H)-dione

3.1 Introduction:

In the last chapter, it was shown that N-amino-1,8-naphthalimide (*aminonap)* forms mixed ligand di- or tri-nuclear copper complexes with nitrogen heterocycle-based dicarboxylates. Based on those results, another naphthalimide-based ligand, namely, 2-(pyridin-4-ylmethyl)-1H-benzo[de]isoquinoline-1,3(2H)-dione (*4pynap*) was selected to study its complexes with cobalt(II) and copper(II). The choice was also based on the ability of the *4pynap* ligand to serve as an ancillary ligand or serve as a protonated species to remain outside the coordination sphere

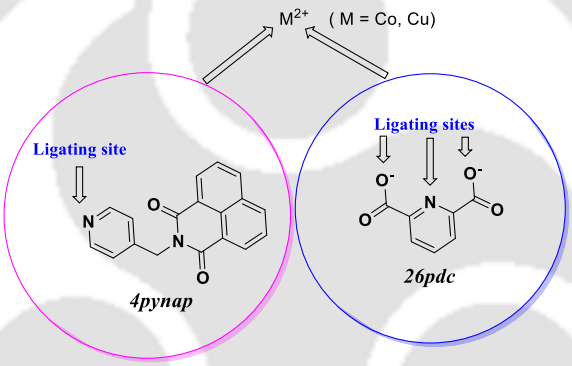

Figure 3.1: The *4pynap* and *26pdc* ligands.

of an anionic complex.[1] 2,6-Pyridinedicarboxylate (*26pdc*) as a ligand conventionally form anionic complexes,[2] and there is interest to explore such complexes ancillary ligands as some of the *26pdc* metal complexes have the abilities for molecular recognitions[3] and show medicinal activities.[4] Thus, there is a necessity to study the competitive binding behaviour of a naphthalimide-based nitrogen-containing ligand such as *4pynap* with *26pdc* as ligands, while binding to a metal ion (Figure 3.1). With this background in this chapter two mixed ligand complexes one with cobalt(II) and the other with copper(II) are described in the following parts.

3.2 Synthesis and characterisation of the complexes

The *4pynap* was prepared by literature reported[5] procedure and characterised it by comparing ^{1}HNMR, FTIR, HRMS spectra reported earlier. One mixed ligand mononuclear copper(II) and another mononuclear cobalt(II) complexes having *4pynap* and *26pdc* ligands were prepared by reacting 2,6-pyrdinedicarboxylic acid and *4pynap* with the respective metal salts. Those reactions provided two complexes *[Co(26pdc)(4pynap)$_2$(H$_2$O)]·H$_2$O* (*3.1*) and

[Cu(26pdc)(4pynap)(H₂O)]·2H₂O (*3.2*) as illustrated in Scheme 3.1. These complexes were characterized by determining structure by single-crystal X-ray diffraction, FT-IR spectroscopy, magnetic moment measurements, and X-ray photoelectron spectroscopy. Their thermal stabilities were evaluated by thermogravimetry.

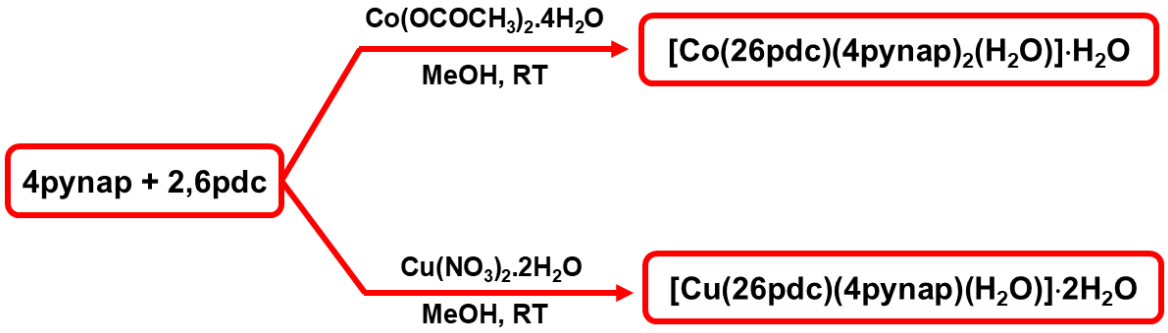

Scheme 3.1: Synthesis of the cobalt(II) and copper(II) complexes.

3.2.1 The structure and characterisation of the cobalt complex

The cobalt(II) complex *[Co(26pdc)(4pynap)₂(H₂O)]·H₂O* (**3.1**) was formed as a monohydrate having one *26pdc,* two *4pynap* and one water as ligands. The complex exhibited a hexa-coordinate distorted octahedral geometry {Figure 3.2 (a)}. The two *4pynap* ligands had occupied the axial positions, these ligands were *trans* to each other, while the equatorial positions were occupied by the nitrogen atom and two oxygen atoms from the *26pdc*, and the oxygen atom of a coordinated water molecule. The cobalt ion was coordinated to two.

1. Bond length distortion:

It measures variation in metal-ligand (M-L) bond lengths

$$\Delta = (1/n)\sum_{i=1}^{n}[(di - dav)/dav]^2$$

Where n = number of M-L bonds (6 for octahedral)
di = individual M-L bond lengths
dav = average M-L bond lengths

Δ = (1/6) * [{(2.012-2.11)/2.11}^{2} + {(2.049-2.11)/2.11}^{2}
+ {(2.146-2.11)/2.11}^{2} + {(2.146-2.11)/2.11}^{2} +
{(2.178-2.11)/2.11}^{2}+{(2.178-2.11)/2.11}^{2}
or Δ = (1/6)* [0.002+0.0008+0.0002+0.0002+0.001+0.001]
or Δ = (1/6) * 0.0052
or Δ = 0.0008

2. Angle variance:

It measures deviation from cis bond angles from 90°.

$\sigma 2 = (1/m\text{-}1)\sum_{j=1}^{m-1}(\theta j - 90°)^2$

where m = number of angles (typically 12 for octahedral)

θj= observed bond angle

= (1/11)* [(90-89.76)^2 + (90-90.24)^2 + (90-88.08)^2 + (90-92.04)^2 + (90-89.76)^2 + (90-90.24)^2 + (90-75.67)^2 + (90-88.08)^2 + (90-92.04)^2 + (90-89.76)^2 + (90-90.27)^2 + (90-88.08)^2]

=(1/11)* [0.0576 + 0.0576 + 3.6864 + 4.1616 + 0.0576 + 0.0576 + 205.3489 + 3.6864 + 4.1616 + 0.0576 + 0.0729 + 3.6864]

=(1/11)*255.0193

= 20.4563

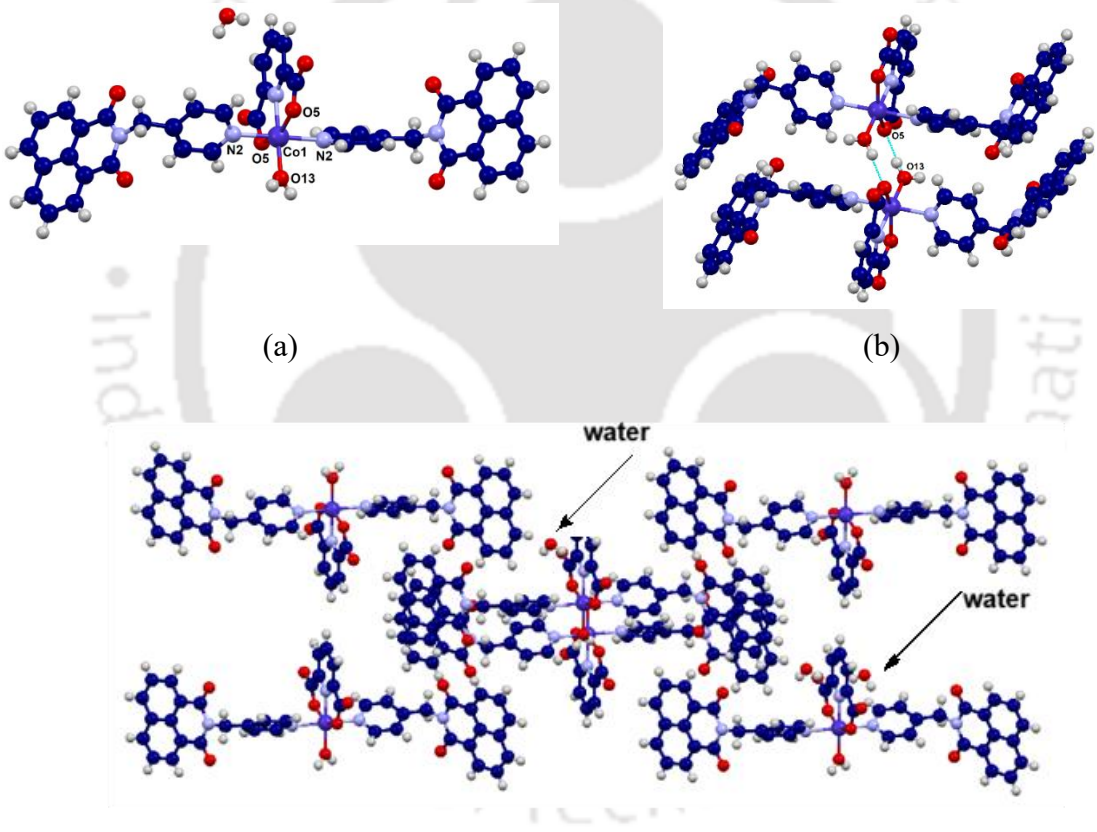

(a) (b)

(c)

Figure 3.2: (a) Ball and stick representation of the crystal structure of the cobalt complex *3.1*. (b) The hydrogen-bonded dimer, (c) Water of crystallization molecules located at the hydrophobic interstitial sites.

Table 3.1: Metal-ligand bond parameters of the complex *3.1*

M-L bond	Bond-length (Å)	∠L-M-L	Bond angle (°)
Co1-O13	2.012 (3)	O3-Co1-N3	180.0
Co1-N3	2.049 (3)	O13-Co1-O5	104.33 (6)
Co1-O5	2.146 (19)	N3-Co1-O5	75.67 (6)
Co1-O5	2.146 (19)	O13-Co1-O5	104.33 (6)
Co1-N2	2.178 (2)	N3-Co1-O5	75.67 (6)
Co1-N2	2.178 (2)	O5-Co1-O5	151.35 (11)
∠L-M-L	Bond angle (°)	O5-Co1-N2	88.08 (8)
O13-Co1-N2	89.76 (6)	O5-Co1-N2	92.04 (8)
N3-Co1-N2	90.24 (6)	O13-Co1-N2	89.76 (6)
O5-Co1-N2	88.08 (8)	N3-Co1-N2	90.24 (6)
O5-Co1-N2	92.04 (8)	O5-Co1-N2	88.08 (8)
O3-Co1-N2	89.76 (6)	N2-Co1-N2	179.53 (12)
N3-Co1-N2	90.24 (6)		

dicarboxylate oxygen atoms and nitrogen atom (N3) of the *26pdc* had a pincer-like arrangement. The two *4pynap* ligands were symmetry-related by a mirror plane bisecting the coordinated water molecule and the *26pdc* plane. The metal-ligand bond parameters are listed in the Table 3.1. Both the ligands displayed identical Co-N bond lengths of 2.177(2) Å. The pyridine nitrogen atom of the *26pdc* ligand was coordinated to the cobalt(II) ion, it had a Co-N bond length of 2.049(3) Å, indicating a strong coordination bond. The metal-ligand Co-O of the carboxylate groups of *26pdc* bonds had same bond distance 2.146(19) Å, which was consistent with typical cobalt(II)-oxygen bonds in carboxylates.[6] Interestingly, the Co-O5 bond to the coordinated water molecule was 2.012(3) Å, this shorter bond distance indicated stronger binding of coordinated water to cobalt ion. Water is a neutral ligand whereas the carboxylates are anionic, but the former Co-O bond was shorter, this difference was likely arising from the electronic effect of central metal ion and hydrogen bonds in the self-assembly. The coordinated water molecule formed intermolecular hydrogen bonds with the carboxylate oxygen atoms of the neighbouring complex by hydrogen bonds (O13-H···O5, $d_{D\cdots A}$ = 2.793 Å; ∠D-H···A = 175.4°), where one of the hydrogen atoms of the coordinated water molecules act as donors {Figure 3.2(b)}. These dimers created a hydrogen-bonded one-dimensional chain along the crystallographic *c*-axis (Figure 3.2). The involvement of the O5 in hydrogen bonding, due to this there was a pull from opposite sides of the metal-ligand bond to form hydrogen-bonded dimers and provide a tight-packed structure, and it resulted in an increase in the Co-O5 bond length.

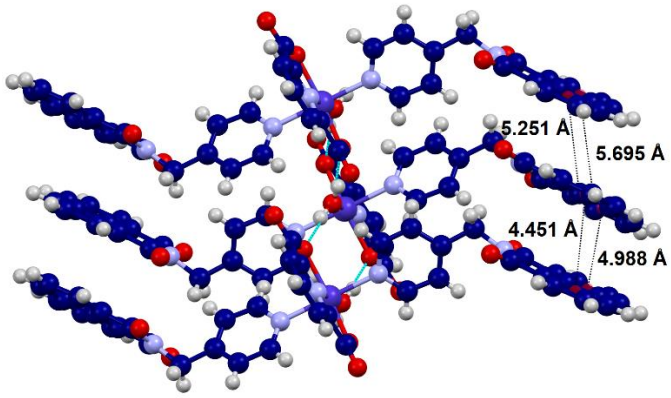

Figure 3.3: Stacking among the naphthalimide rings in the crystal structure of the cobalt complex *3.1*.

The complex had π- stackings among the naphthalimide rings (Figure 3.3). In the crystal lattice of the complex, the parallel rings of the naphthalimide part were placed at translated positions. The centroid-to-centroid distances between the two π-planes were 4.451 Å and 4.988 Å, respectively. These distances were indicative of very weak stacking interactions.[7]

The bulk purity of complex *3.1* (Figure 3.4a) was evaluated by comparing the powder X-ray diffraction (PXRD) pattern of the complex with the experimental PXRD pattern. They matched showing the bulk purity of the crystals of the complex. The FT-IR spectra of the complex (Figure 3.4b) and the ligands showed clear differences from the ligands. In the free *4pynap*, the aromatic and aliphatic C-H stretching vibrations were observed at 3080 cm^{-1} and 2953 cm^{-1}, respectively, and the carbonyl stretch of the imide group appeared at 1692 cm^{-1}. In the complex, the imide C=O stretch was observed at 1704 cm^{-1} and the O-H stretch was at 3383 cm^{-1}. The visible spectra of the complex had a broad peak at 516 nm and it showed an effective magnetic moment of 4.10 BM at 300 K which supported high spin d^7-electronic configuration of the cobalt ion.

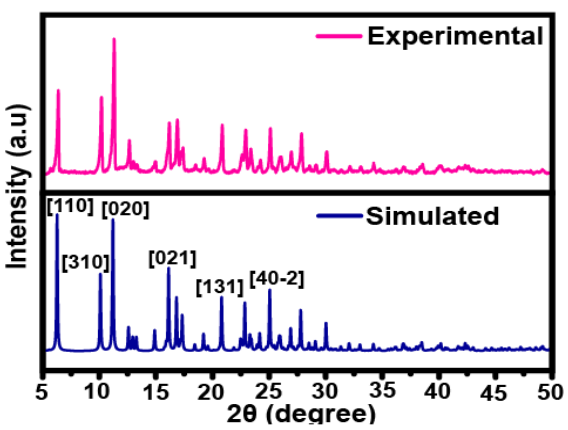

(a)

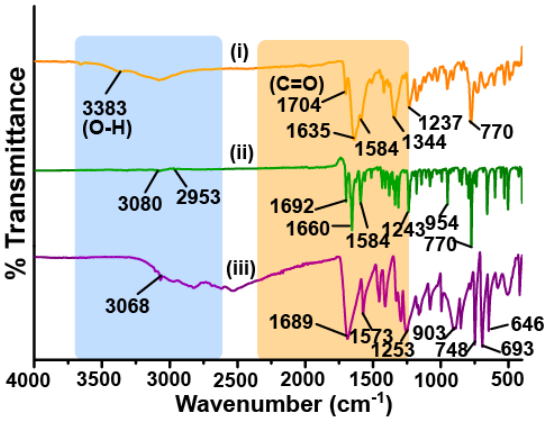

(b)

Figure 3.4: (a) Experimental PXRD pattern (top) and simulated from crystallographic information file by mercury software (bottom,) of complex *3.1,* and (b) FT-IR spectra of the (i) complex *3.1,* (ii) *Naphydrazide,* and (iii) 2,6-pyridine dicarboxylic acid.

The crystal morphology of complex *3.1* was probed by using an optical microscope as well as by scanning electron microscopy (SEM) the images are presented in Figure 3.5 (a) and (b). Each has revealed the rod-like morphology of the crystals and the crystals were of the scale of µm in size. Thermogravimetric analysis of complex *3.1* showed that the complex lost two water molecules one coordinated and one lattice-bound between 100 °C and 125 °C, highlighting a clear distinction between interstitial and coordinated water {Figure 3.5(c)}. It also revealed that it decomposed beyond 378 °C in two steps by the loss of its *4pynap* and *pdc* ligands.

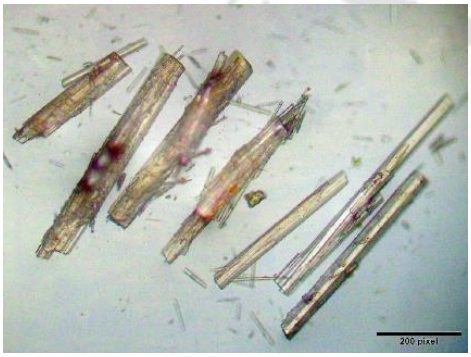

(a)

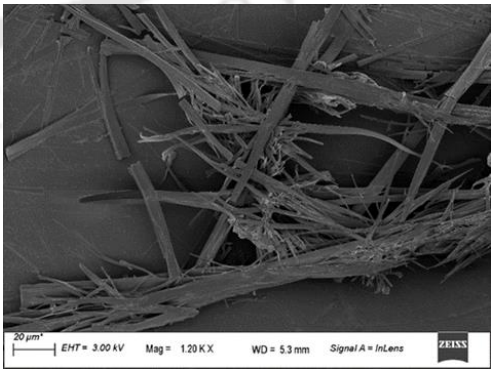

(b)

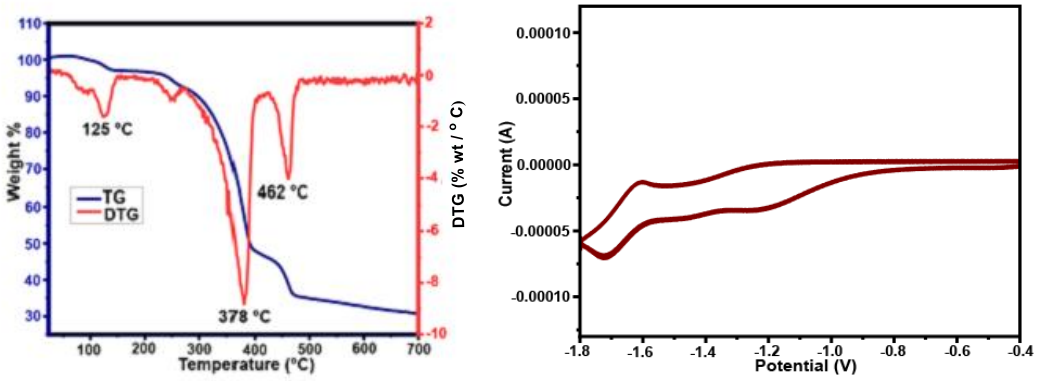

(c) (d)

Figure 3.5: (a) optical image and (b) the scanning electron micrograph of the complex *3.1(Complex 3.1 was finely ground, and dispersed onto a conductive adhesive substrate, and coated with a thin layer of gold to ensure conductivity and minimize charging during imaging.* (c) Thermogravimetry thermogram (red) of the complex *3.1* (red line is differetial curve of the themogram, the thermogram was recorded under argon, heating rate 10^{o} C/min). (d) The cyclic voltammogram of the complex *3.1*, (1 mM in dimethylformamide, tetrabutylammonium perchlorate supporting electrolyte; and Ag/AgCl as reference electrode, scan rate, 100 mV/sec).

Cyclic voltammetry is a valuable tool to understand redox behaviour and electrochemical aspects of naphthalimide derivatives.[8] The electrochemical properties of 4pynap was reported earlier.[8a] The cobalt complex *3.2* (Figure 3.5d) exhibited a ligand based one electron redox peak with $E_{1/2}$ = -1.66 V. The anion formation as a second redox couple was observed at $E_{1/2}$ = -1.21 V, thereby influencing the electrochemical generation of anions in solution.

3.2.2 The structure and characterisation of the copper complex

The complex *[Cu(26pdc)(4pynap)(H_2O)] ·2H_2O (3.2),* one pyridyl group of the *4pynap* coordinates to the copper centre in a monodentate manner and one *26pdc* coordinated in a tridentate fashion. With the fifth site occupied by a water molecule, these dative bonds resulted in a five-coordination environment around the copper ion. The +2 charge of the cobalt centre was balanced by two oxygen atoms from the carboxylate anions in the 2,6-pyridine dicarboxylic acid. The crystal structure of complex *3.2* is shown in Figure 3.6. The single-crystal X-ray diffraction structure of complex *3.2* showed that the complex exhibited a square pyramidal geometry around the copper centre.

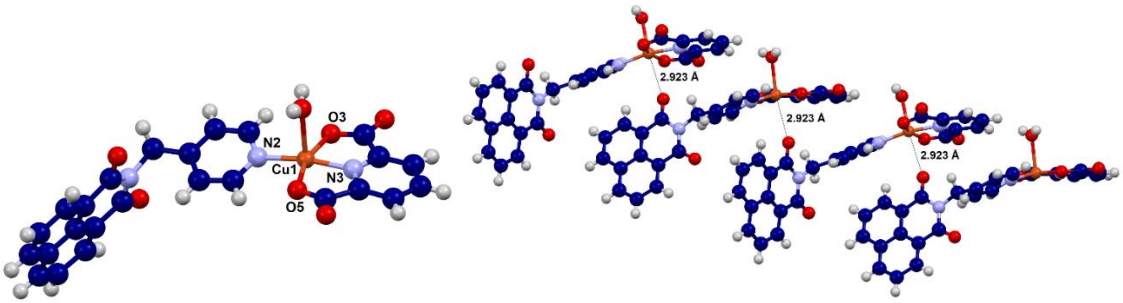

(a) (b)

Figure 3.6: (a) The crystal structures of the mononuclear copper complex *[Cu(26pdc)(4pynap) (H_2O)].2H_2O (3.2)* drawn on ball and stick model using mercury software. (b) One-dimensional chain of the supramolecular coordination polymer formed in the solid-state assembly through weak Cu···O bonds.

The structure of the complex is shown in Figure 3.6(a) had shows that the three coordination sites of the complex were occupied by the ONO donor atoms of *26pdc* ligand, while the fourth and fifth sites of the coordination sphere were occupied by the pyridine nitrogen of one *4pynap* and oxygen atom of a water molecule. The geometry of the complex was analysed by using the τ_5 parameter, which is derived from bond angles to classify five-coordinate geometries. τ_5 is calculated as the difference between the two largest bond angles divided by 60. A τ_5 value close to 1 indicates trigonal bipyramidal geometry, while a value near 0 corresponds to square pyramidal geometry. Based on the largest bond angles, ∠N2-Cu1-N3 (168.92°) and ∠O5-Cu1-O3 (165.93°) of this complex, τ_5 was found to be 0.049. This value confirmed it to have a distorted square pyramidal geometry, with the basal plane comprised of N2O2 ligand atoms environment {Figure 3.6(a)}.

Table 3.2: Metal-ligand bond parameters of the *complex 3.2*

M-L	Bond length (Å)	∠L-M-L	Bond angle (°)
Cu1-N3	1.901 (19)	N3-Cu1-N2	168.91 (8)
Cu1-N2	1.962 (2)	N3-Cu1-O3	80.65 (8)
Cu1-O3	2.022 (18)	N2-Cu1-O3	99.03 (8)
Cu1-O5	2.024 (18)	N3-Cu1-O5	80.41 (8)
Cu1-O7	2.249 (2)	N2-Cu1-O5	99.14 (8)

∠L-M-L	Bond angle (°)	O3-Cu1-O5	160.93 (8)
O3-Cu1-O7	90.39 (8)	N3-Cu1-O7	96.01 (8)
O5-Cu1-O7	93.75 (8)	N2-Cu1-O7	95.08 (8)

The metal-ligand (M-L) bond parameters of the complex are listed in the Table 3.2. The Cu-O and Cu-N bond lengths within the complex range from 1.9 Å to 2.0 Å, excluding the Cu-O bond of the coordinated water molecule. The Cu-O bond length for the coordinated water is 2.249(2) Å, which is noticeably longer than the Cu-O bonds from the 2,6-pyridine dicarboxylate ligand (2.022(18) Å for Cu-O3 and 2.025(18) Å for Cu-O5). This difference indicates weaker binding of the water molecule, consistent with the axial distortion typically observed in copper(II) complexes due to the Jahn-Teller effect of the d^9-electronic configuration. The metal-ligand bond angles (L-M-L) were suiting the distorted square base as listed in Table 3.2. The basal angles were close to 90◦, while the angle with the apical sites were 161 ◦-169 ◦.

A detailed analysis of the structure reveals that the carbonyl group of the naphthalimide moiety in each complex is oriented toward the open face of a neighbouring molecule. This orientation facilitates weak Cu···O=C interactions (Cu-O = 2.923 Å), leading to the formation of a supramolecular coordination polymer in the solid state {Figure 3.6(b)}. Pentacoordinate square pyramidal complex (sqp) of zinc was earlier designed,[9] where the approaching space for the face of a fifth ligand to the central metal ion was blocked by hydrogen bonds of a free benzoate anion with the second coordination sphere. In the current complex, the interactions between the carbonyl group of the naphthalimide ligand and the copper(II) ion of an adjacent molecule effectively blocked the open face of the square pyramidal geometry, preventing the binding of additional ligands. This self-assembly process resulted in chain-like arrangements along the crystallographic c-axis, as illustrated in Figure 3.6(b). The complex showed an effective magnetic moment of 1.90 BM at room temperature corresponding to the d^9 electronic configuration and visible spectra with absorption maxima due to the d-d transition at 683 nm.

The morphology of complex *3.2* was recorded by optical microscopy as well as by scanning electron microscopy (SEM) {Figure 3.7 (a) and (b)}. The SEM and optical microscopic images are presented in Figure 3.11. The bulk purity of the complex *3.2* {Figure 3.7(c)} was assessed by recording the powder X-ray diffraction pattern, in this case also the experimental pattern matched the simulated pattern generated by Mercury software. Additionally, FT-IR spectroscopy was used to compare the stretching frequencies of the free ligands with the metal complex {Figure 3.7(d)}. In the free ligand, the aromatic C-H stretching vibrations were

observed at 3080 cm^{-1}, and the carbonyl stretch of the imide group appeared at 1692 cm^{-1}. In the complex, the O-H stretch was at 3414 cm^{-1}, and the C-H stretches and the carbonyl stretch of imide of the complex were at 3061 cm^{-1} and 1692 cm^{-1} respectively.

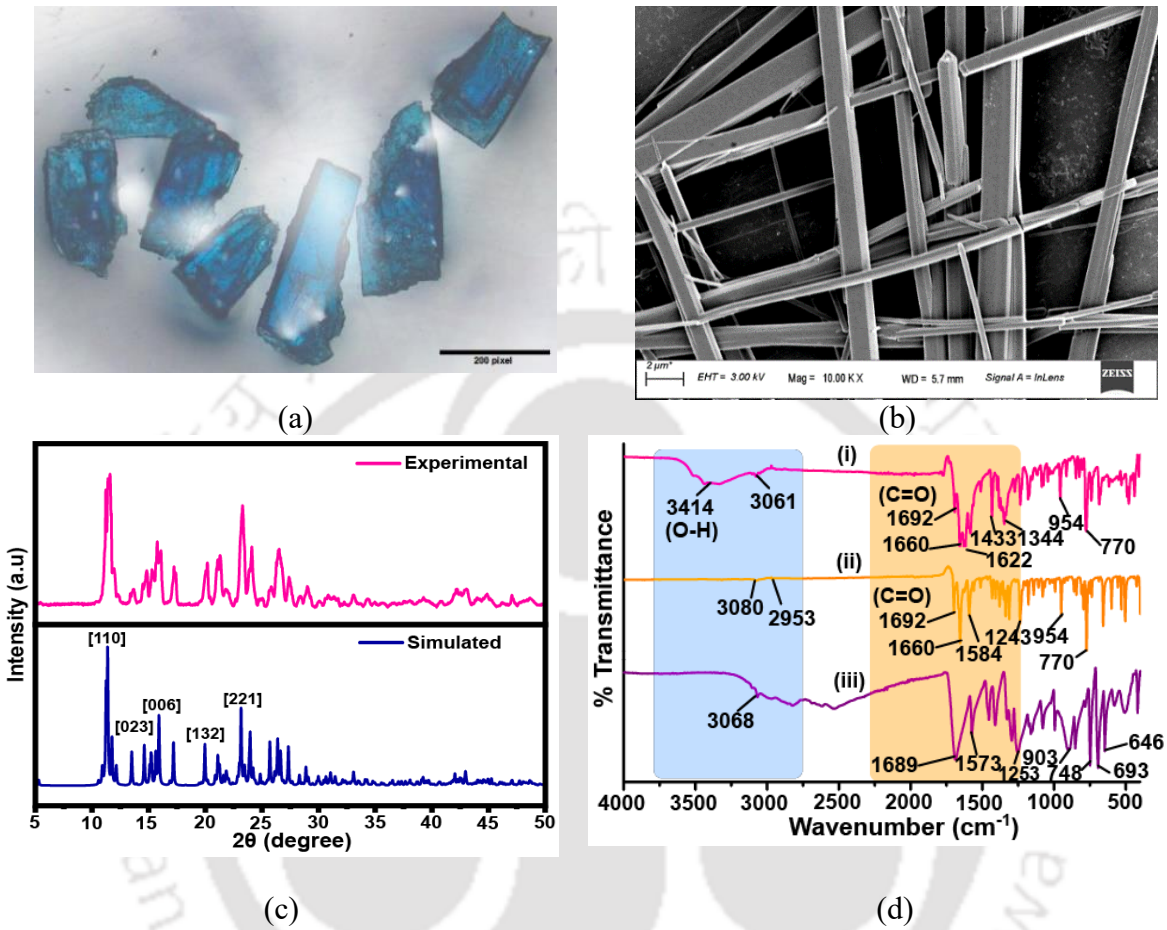

Figure 3.7: (a) The optical microscopic image and (b) scanning electron microscopic image of the crystals of the complex *3.2*. (c) Experimental (top) and Simulated (bottom, obtained from mercury software) PXRD pattern of complex **3.2** and, (d) FTIR spectrum of (i) complex **3.2** (ii) 4-pynap ligand and, (iii) 2,6-pyridine dicarboxylic acid.

The complex *3.2* showed lower thermal stability than the complex *3.1*. It lost the three water molecules between 100 °C and 150 °C (experimental weight loss: 10%; theoretical weight loss: 10.5%). Subsequently, it underwent decomposition in two steps one at 262 °C and the other at 375 °C by losing the *4pynap* and *pdc* ligands (Figure 3.8).

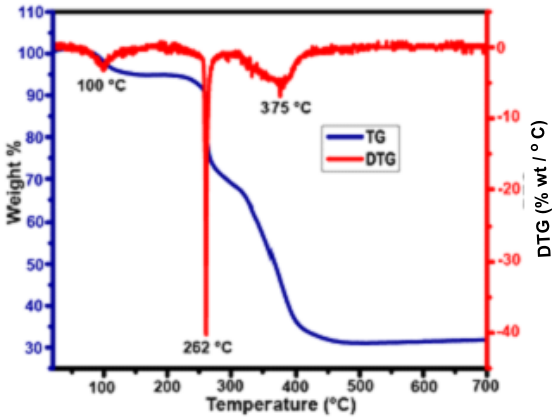

Figure 3.8: Thermogram (blue) and differential (red) of the complex *3.2*, (under argon, heating rate 10° C/min).

3.2.3 Photo-electron spectra and cyclic voltammogram of the copper complex *3.2*

The photo-electron spectra of some of the copper(II) complexes help to depict their structure features, oxidation states as well as electronic properties.[10] The deconvoluted photo-electron spectra of the complex *3.2* in the Cu(2p) peaks displayed two sets of peaks each appearing as doublets, these were due to the ionization of the $2p_{1/2}$ and $2p_{3/2}$ orbitals of copper {Figure 3.9(a)}. For the complex in the copper(II) oxidation state, the ionization peaks for $2p_{1/2}$ had appeared at 954.4 eV and 952.4 eV, while the $2p_{3/2}$ peaks were observed at 934.5 eV and 932.5 eV for complex *3.2*. These values were similar to the copper complexes that were discussed in chapter 2 making no clear distinctions among the different geometries as well as nuclearities of these copper complexes. The X-ray photo-electron spectral peaks for the 1s region of the N atom and 1s region of the O-atom of the complex *3.2* are shown in Figure 3.9 (b) and (c) complement were characteristic of the bonds present in the complex. For example, O(1s) in the complex showed characteristic C=O at 632 eV, O=C-N at 631.04 eV; N(1s) had the characteristic O=C-N-C=O at 400.6 eV and N of pyridine at 399.3 eV.

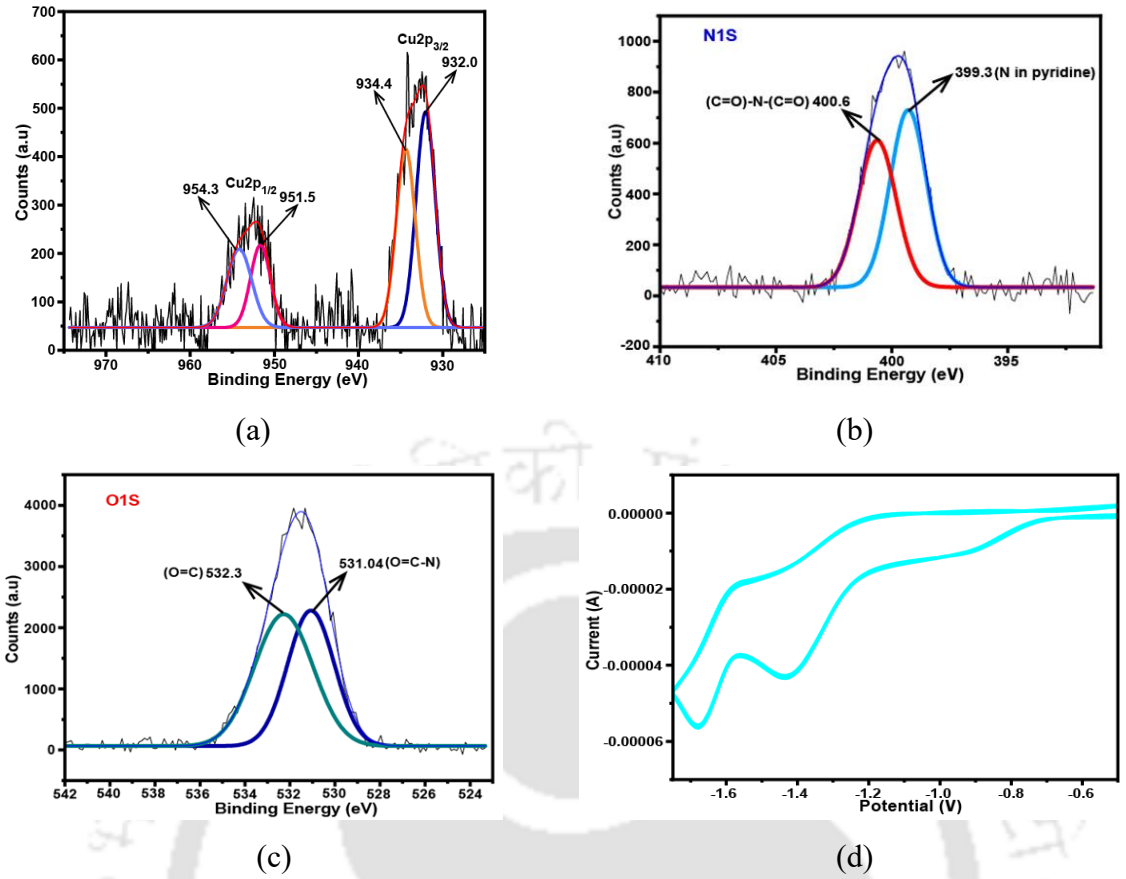

Figure 3.9: X-ray photo-electron spectra of (a) 2p region of Cu, (b) 1s region of N, (c), (1s region of O of the complex *3.2* (in each case deconvoluted spectra of the superimposed peaks observed in the spectra are shown with the original peak). (d) Cyclic voltammogram of the complex *3.2*, (1 mM in DMF; scan-rate 100 mV/sec, + ve scan, tetrabutylammonium perchlorate as supporting electrolyte, Ag/AgCl as reference electrode.

To discern the redox properties, the cyclic voltammogram of the copper complex *3.2* was recorded, it showed two distinct ligand-based redox couples on the -ve side {Figure 3.9 (d)}. The first redox couple corresponded to the formation of a radical anion and the second to the formation of an anion. As compared to the parent ligand, complex *3.2* showed similar redox behaviour for the initial formation of the radical anion but at more negative potentials. Specifically, the radical anion formation in copper complex *3.2* occurred at EMF $E_{1/2}$ = -1.62 V at a higher than the free ligand ($E_{1/2}$ = -1.11 V) for the same redox couple.[8a] Thus, in the complex the ligand oxidation was more difficult.

3.3 Fluorescence Emission Study:

The solvatoemissive properties of *4pynap* and related compounds are well established.[11a] A methanol solution of *4pynap* exhibited very weak emission at 395 nm (λ_{ex} = 335 nm) due to

the photoinduced electron transfer OFF process. This weak emission was due to the participation of the lone pair of electrons on the nitrogen atom of the pyridine ring of *4pynap* in the photo-electron transfer mechanism.[11b] There is a necessity to design fluorescence emission turn-ON sensors for cobalt(II) or copper (II) ions from naphthalimide-based compounds.[12] This interaction influenced the emission pathway from the S_1 to the S_0 transition, leading to the fluorescence OFF state. When a solution of cobalt(II) nitrate was added to a solution of *H₂26pdc* (pKa = 3.24) and naphthalimide derivative *4pynap*, the corresponding metal complex (cobalt or copper) was formed in the solution. While the formation of the metal complex nitric acid was released as a product into the solution. This in-situ generated acid could also protonate the nitrogen atom of the pyridine ring of *4pynap*. As a result, there was an enhancement in the intensity of the emission. A representative plot demonstrating the increase

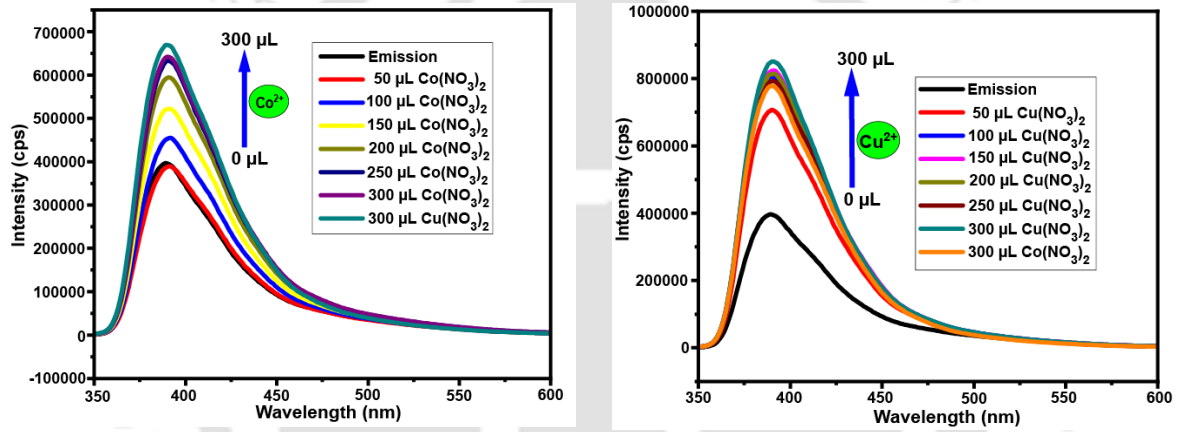

(a) (b)

Figure 3.10: The fluorescence emission titration of (a) *4pynap* + *H₂26pdc* (2 mM in methanol) (b) *4pynap* + *H₂35pza* (2 mM in methanol) with each time addition of 50 µL addition of 20 mM cobalt nitrate solution and 300 µL of 20 mM copper nitrate solution was added.

in emission intensity during the titration of a solution containing *H₂26pdc*, *4pynap*, with cobalt(II) nitrate is shown in Figure 3.10 (a). A similar experiment with a solution of *H₂35pza (3,5-pyrazoledicarboxylic acid)* and *4pynap* solution with copper(II) nitrate solution {Figure 3.10(b)}. This experiment also showed that emission enhancement took place. In general copper(II) or cobalt(II) ions quench the emission of a fluorescent naphthalimide ligand[13] due to their paramagnetic behaviour. But in the present case, the *pdc* or *pza* had masked the cobalt or copper ions so as not to be directly in contact with the fluorophore to feel the paramagnetic effect. Hence, they did not cause quenching but allowed to have a fluorescence ON process through the protonation of *4pynap*. To check the competitive effect of the two metal ions, after the titration of the mixture of pdc and *4pynap* with cobalt metal ions, copper ions were added

once the emission intensity increase reached a maximum value {Figure 3.10(a)}, this had caused no changes. On the other hand, the titration with copper, followed by the addition of cobalt ions also did not cause a change in emission of the highest intensity {Figure 3.10(b)}. This suggested that there was no effect of those metal ions after the maximum intensity was observed in each titration.

3.4 Summary:

Starting from the same set of ligands namely *4pynap* and *26pdc*, two compositionally different mixed ligand complexes of cobalt and copper complexes were prepared in respective one-pot reactions at ambient conditions. The copper complex provided a unique example of a supramolecular coordination polymer that had one very weakly bound Cu-O bond. The stability of the five-coordinated copper complex *3.2* was attributed to supramolecular interactions, specifically from the carbonyl (C=O) groups having suitable projection towards the open faces of the distorted square planar geometry of the complex. Additionally, a fluorescence-ON of a naphthlimide ligand together with a heterocycle-based dicarboxylic acid upon the addition of copper(II) ions was demonstrated. It was depicted that in-situ acid generation could cause the emission-ON process.

3.5 Experimental Section:

Synthesis of *4pynap*: The compound was synthesized from a reaction between 1,8-naphthalic anhydride (1.0 g, 5 mmol) and 4-picolylamine (0.54 g, 5 mmol) in DMF. After refluxing for 12 hours, the reaction mixture was cooled, and ice-cold water was added. A yellow precipitate was formed, filtered, and dried in air. FT-IR (ATR method, cm^{-1}): 3311(s), 3240 (s), 3065 (s), 1769 (s), 1706 (s), 1651(m), 1583 (s), 1435 (s), 1379(s),1293 (s),1231 (s), 1009 (s), 769 (s), 529 (s). ^{1}HNMR (400 MHz, $CDCl_3$, δ) 8.61 (d, 2H, Ar-H J = 8 Hz), 8.51 (d, 2H, Ar-H J = 8 Hz) ,8.23 (d, 2H, Ar-H, J = 8 Hz), 7.8 (t,2H, Ar-H, J = 8 Hz), 7.35 (d, 2H, Ar-H, J = 8 Hz), 5.35 (s,2H, CH_2). ^{13}C NMR ($CDCl_3$, 100 MHz, ppm) 164.2, 150.1, 146.01, 134.6, 131.8, 128.3, 127.2, 123.3, 122.3, 42.3. EI-Mass: 288.

Complex 3.1: To a warm solution of *4-pynap* (115.3 mg, 0.4 mmol) in 20 mL of warm methanol, cobalt(II) acetate (49.8 mg, 0.2 mmol) was added and it was dissolved by stirring. To this reaction mixture, 2,6-pyridinedicarboxylic acid (33.4 mg, 0.2 mmol) was added and stirred for an additional 1 hr. Pink-colored crystals of the cobalt complex were obtained on standing in the solution (yield, 60 % based on cobalt ion). The IR (neat, cm^{-1}) 3383 (s, ν_{O-H}), 1704 (s, $\nu_{C=O}$),

1635 (s), 1584 (s), 1344 (s), 1237 (s), and 770 (s). The UV-vis (solid, λ_{max}) 516 nm. The effective magnetic moment (300 K) is 4.10 BM.

Complex 3.2: The same reaction procedure was followed as described above, but copper(II) nitrate (39.8 mg, 0.2 mmol) was used in place of cobalt(II) salt, and half the amount of *4-pynap* was used. A blue precipitate was obtained, which was collected and recrystallized by dissolving it in water. Isolated yield 50 % (based on copper ion). IR (neat, cm^{-1}) 3414 (br, ν_{OH}), 3061 (s, ν_{C-H}) 1692 (s, $\nu_{C=O}$), 1660 (s), 1622 (s), 1433 (s), 1344 (s), 944 (s), 770 (s). UV-vis (Solid, λ_{max}) 683 nm. Effective magnetic moment (300 K): 1.90 BM.

The powder sample was finely ground to ensure a uniform texture and was mounted onto the XPS sample holder using double-sided conductive tape. To enhance electrical conductivity and minimize charging effects, the sample was securely pressed onto the tape without any additional surface treatments before analysis. Fluorescence titration was performed by taking 2500 µL of 4pynap (2 mM) in a cuvette, followed by the addition of 400 µL of 26pdc (20 mM). The resulting solution was then titrated with 400 µL aliquots of an aqueous metal salt solution (20 mM).

Structure determination:

The structures were determined at room temperature on Bruker D8 Quest Diffractometer equipped with a Photon CMOS detector equipment. The crystal refinement parameters are listed in Table 3.3.

Table 3.3: Crystal and refinement parameters of the complexes *3.1* and *3.2*

Parameters	***[Co(26pdc)(4pynap)$_2$(H$_2$O)]·H$_2$O***	***[Cu(26pdc)(4pynap)(H$_2$O)]·2H$_2$O***
Empirical Formula	$C_{43}H_{33}CoN_5O_{11}$	$C_{32}H_{20}CuN_3O_3$
CCDC No.	2255276	2255277
Formula Weight	854.67	570.99
Crystal System	Monoclinic	Orthorhombic
Space group	P21	$Pna2_1$
a/ Å	31.667 (4)	8.785 (14)
b/ Å	15.709 (18)	16.198 (2)
c/ Å	7.707 (9)	33.405 (5)
α/ °	90	90
β/ °	93.819 (4)	90
γ/ °	90	90
V/ Å^3	3825.7 (8)	4753.9 (12)
Z	4	8
ρ (gcm^{-3})	1.484	1.596

μ (mm^{-1})	0.521	0.981
F (000)	1764.0	2344.0
Refl collected	40154	131,704
Independent Reflections	2010	4482
Ranges (h,k,l)	-38 ≤ h ≤ 38 -18 ≤ k ≤ 18 -9 ≤ l ≤ 9	-10 ≤ h ≤ 10 -19 ≤ k ≤ 19 -40 ≤ l ≤ 40
Max θ (degree)	25.406	25.621
Data/restraints/parameters	3505/0/277	4482/0/349
Goof (F^2)	1.124	1.114
R indices	0.0674	0.0492
[I>2σ]	0.0477	0.0415
WR_2	0.1260	0.1130

3.6 References:

1.(a) S. Blanck, T. Cruchter, A. Vultur, R. Riedel, K. Harms, M. Herlyn, E. Meggers,Organometallic pyridylnaphthalimide complexes as protein kinase Inhibitors, Organometallics, 2011, 30, 4598 - 4606. (b) M. G. Vasquez-Ríos, I. Rojas-León, P. Montes-Tolentino, I. F. Hernández-Ahuactzi, H.Höpfl, Pyridinedicarboxylic acids as versatile building blocks for coordination-driven self-assembly: solvent-induced macrocycle and coordination polymer formation upon combination of 2,5-pyridinedicarboxylate with diorganotin moieties. *Cryst. Growth Des.*, 2018, 18, 7132 - 7149.

(c) C. Tamuly, N. Barooah, A. S. Batsanov, R. Kataky, J. B. Baruah, Structural and spectroscopic properties of bis-3-picolinium 1,8-naphthalimide tetrachlorocuprate, *Inorg. Chem. Commun.,* 2005, 8, 689 - 691.

2. (a) L. C. Nathan, D. C. Zapien, A. M. Mooring, C.A. Doyle, J. A. Brown, Anionic 2,6-pyridinedicarboxylate complexes with some divalent first-row transition metals, *Polyhedron,* 1989, 8, 745 -748.

(b) K. Shankar, A. Kirillov and J. B. Baruah, A modular approach for molecular recognition by zinc dipicolinate complexes. *Dalton Trans.* 2015, 44, 14411 - 14423.

3. (a) L. Yang, L. Wu, H. Zhang, S. Song, L. Liu, M. Li, Synthesis, structure and luminescent recognition properties of cerium(IV) coordination polymers based on pyridine-2,6-dicarboxylic acid. *Dyes and Pig.*, 2013, 99, 257 - 267.

(b) M. P. Singh, J. B. Baruah, Stable host-guest complexes of bis-2,6-pyridinedicarboxylate iron(III) with dihydroxybenzenes. Polyhedron, 2017, 138, 103 - 108.

4. (a) A. Bergeron. K. Kostenkova, H. A. Murakami, E. O. R. Arulanandam. J. S. Diallo, M. Selman, N, Haribabu, D.C. Crans, Enhancement of oncolytic virotherapy by vanadium(V) dipicolinates. Biometals. 2019, 32, 545 - 561.

(b) Z. A. Siddiqi, M. Khalid, S. Kumar, M. Shahid, S. Noor, Antimicrobial and SOD activities of novel transition metal complexes of pyridine-2,6-dicarboxylic acid containing 4-picoline as auxiliary ligand. Eur. J. Med. Chem., 2010, 45, 264 - 269.

5. R. J. Sarma, C. Tamuly, N. Barooah, J. B. Baruah, Role of π-interactions in solid state structures of a few 1,8-naphthalimide derivatives. J. Mol. Struct., 2007, 829, 29 - 36.

6. (a) T.W. Murinzi, E. Hosten, G.M. Watkins, Synthesis and characterization of a cobalt-2,6-pyridinedicarboxylate MOF with potential application in electrochemical sensing. Polyhedron, 2017, 137, 188 - 196.

(b) K. Shankar, M. P. Singh, J. B. Baruah, Extent of protonation of 4,4′-bipyridinium cations and nature of host influences the amount of guest intake by cobalt(II) 2,6-pyridinedicarboxylate. *Inorg. Chim. Acta,* 2018, 469, 440 - 446.

7. (a) T. Chen, M. Li, J. Liu, π–π Stacking interaction: A nondestructive and facile means in material engineering for bioapplications. *Cryst. Growth Des.,* 2018, 18, 2765 - 2783.

(b) D. L. Reger, A. Debreczeni, J. J. Horger, M. D. Smith, Structures of bifunctional molecules containing two very different supramolecular synthons: Carboxylic acid and strong π···π stacking 1,8-naphthalimide ring. *Cryst. Growth Des.,* 2011, 11, 4068 - 4079.

8. (a) N. Barooah, C. Tamuly, J. B. Baruah, Synthesis, characterization of few N-substituted 1,8-naphthalimide derivatives and their copper(II) complexes. *J. Chem. Sci*., 2005, 117, 117 - 122.

(b) H. Izawa, F. Yasufuku, T. Nokami, S. Ifuku, H. Saimoto, T. Matsui, K. Morihashi, M. Sumita, Unique photophysical properties of 1,8-naphthalimide derivatives: generation of semi-stable radical anion species by photo-induced electron transfer from a carboxy group. *ACS Omega*, 2021, 6, 13456 - 13465.

9. A. M. Baruah, R. Sarma, J. B. Baruah, A penta-coordinated bis-(8-aminoquinoline) monobenzoato zinc(II) benzoate complex favored by self-assembly formation. *Inorg. Chem. Commun.* 2008, 11 (1), 121 - 124.

10. (a) D. C. Frost, A. Ishitani, C. A. McDowell, X-ray photoelectron spectroscopy of copper compounds. *Molecular Physics,* 1972, 24, 861 - 877.

(b) S. V. Didziulis, S. L. Cohen, A. A. Gewirth, E. I. Solomon Variable photon energy photoelectron spectroscopic studies of copper chlorides: an experimental probe of metal-ligand bonding and changes in electronic structure on ionization. *J. Am. Chem. Soc.,* 1988, 110, 1, 250 - 268.

11.(a) P. Nandhikonda, M. P. Begaye, Z. Cao, M. D. Heagy, frontier molecular orbital analysis of dual fluorescent dyes: predicting two-color emission in N-aryl-1,8-naphthalimides. *Org. Biomol. Chem.,* 2010, 8, 3195 - 3201.

(b) J. K. Nath, J. B. Baruah, Solvatoemissive dual fluorescence of N-(pyridylmethyl)-3-nitro-1,8-naphthalimides. *J. Fluoresc.,* 2014, 24, 649 - 655.

(c) H. Q. Dong, T. B. Wei, X. Q. Ma, Q. Y. Yang, Y. J. Sun, B. B. Shi, 1,8-Naphthalimide-based fluorescent chemosensors: recent advances and perspectives. *J. Mater. Chem. C,* 2020, 8, 13501 - 13529.

12. S. Thavornpradit, J. Sirirak, N.Wanichacheva, Turn-on naphthalimide fluorescent sensor with high quantum yield and large Stokes shift for the determination of Cu(II), *J. Photochem. and Photobio. A: Chem.,* 2016, 330, 55 - 63.

13.(a) B. Mohan, N. M. Kunhumon, S. Shanmugaraju, Fluorescence sensing and bioimaging of Cu(II) ions using amino-1,8-naphthalimide-based smallmolecule chemosensors *Sens. Diagn.*, 2023, 2, 1158 - 1175

(b) C. Geraghty, C. Wynne, R. B. P. Elmes, 1,8-Naphthalimide based fluorescent sensors for enzymes. *Coord Chem Rev.* 2021, 437, 213713.

Appendix-Chapter 3

2A3.0: Experimental Section

Synthesis of *4pynap*: The compound was synthesized from a reaction between 1,8-naphthalic anhydride (1.0 g, 5 mmol) and 4-picolylamine (0.54 g, 5 mmol) in DMF. After refluxing for 12 hours, the reaction mixture was cooled, and ice-cold water was added. A yellow precipitate was formed, filtered, and dried in air. FT-IR (ATR method, cm^{-1}): 3311(s), 3240 (s), 3065 (s), 1769 (s), 1706 (s), 1651(m), 1583 (s), 1435 (s), 1379(s),1293 (s),1231 (s), 1009 (s), 769 (s), 529 (s). ^{1}HNMR (400 MHz, $CDCl_3$, δ) 8.61 (d, 2H, Ar-H J = 8 Hz), 8.51 (d, 2H, Ar-H J = 8 Hz) ,8.23 (d, 2H, Ar-H, J = 8 Hz), 7.8 (t,2H, Ar-H, J = 8 Hz), 7.35 (d, 2H, Ar-H, J = 8 Hz), 5.35 (s,2H, CH_2). ^{13}C NMR ($CDCl_3$, 100 MHz, ppm) 164.2, 150.1, 146.01, 134.6, 131.8, 128.3, 127.2, 123.3, 122.3, 42.3. EI-Mass: 288.

Complex 3.1: To a warm solution of *4-pynap* (115.3 mg, 0.4 mmol) in 20 mL of warm methanol, cobalt(II) acetate (49.8 mg, 0.2 mmol) was added and it was dissolved by stirring. To this reaction mixture, 2,6-pyridinedicarboxylic acid (33.4 mg, 0.2 mmol) was added and stirred for an additional 1 hr. Pink-colored crystals of the cobalt complex were obtained on standing in the solution (yield, 60 % based on cobalt ion). The IR (neat, cm^{-1}) 3383 (s, ν_{O-H}), 1704 (s, $\nu_{C=O}$), 1635 (s), 1584 (s), 1344 (s), 1237 (s), and 770 (s). The UV-vis (solid, λ_{max}) 516 nm. The effective magnetic moment (300 K) is 4.10 BM.

Complex 3.2: The same reaction procedure was followed as described above, but copper(II) nitrate (39.8 mg, 0.2 mmol) was used in place of cobalt(II) salt, and half the amount of *4-pynap* was used. A blue precipitate was obtained, which was collected and recrystallized by dissolving it in water. Isolated yield 50 % (based on copper ion). IR (neat, cm^{-1}) 3414 (br, ν_{OH}), 3061 (s, ν_{C-H}) 1692 (s, $\nu_{C=O}$), 1660 (s), 1622 (s), 1433 (s), 1344 (s), 944 (s), 770 (s). UV-vis (Solid, λ_{max}) 683 nm. Effective magnetic moment (300 K): 1.90 BM.

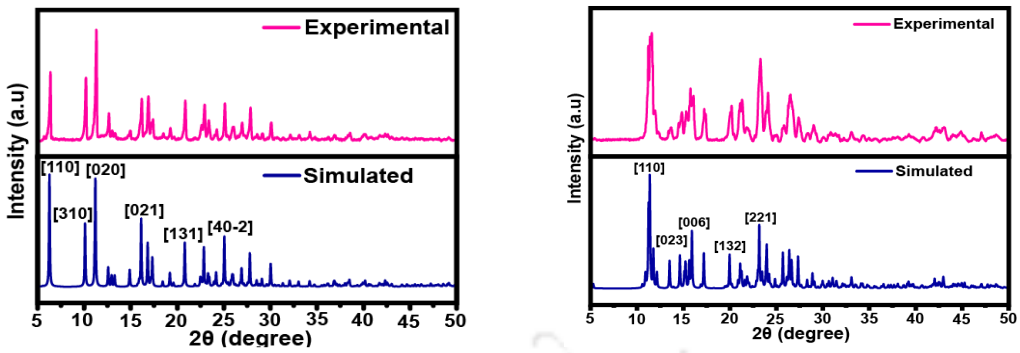

(a) (b)

Figure A3.1: Powder X-ray diffraction pattern of the (a) *3.1* (b) 3.2

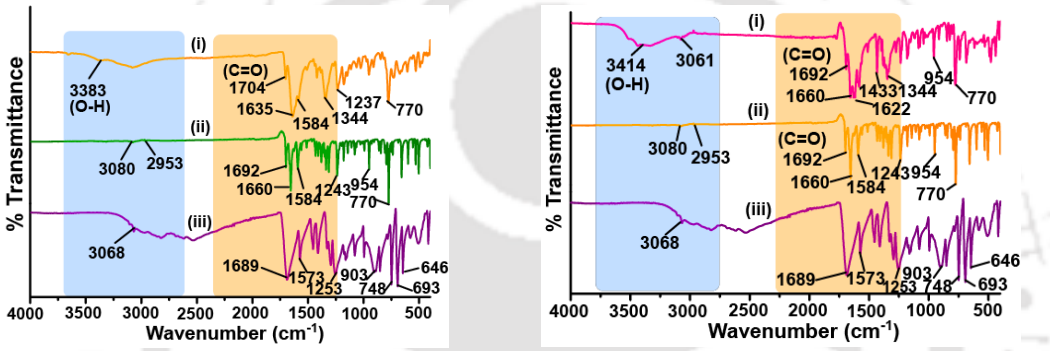

(a) (b)

Figure A3.2: FTIR spectra of powder samples of the (a) *3.1* (b) 3.2.

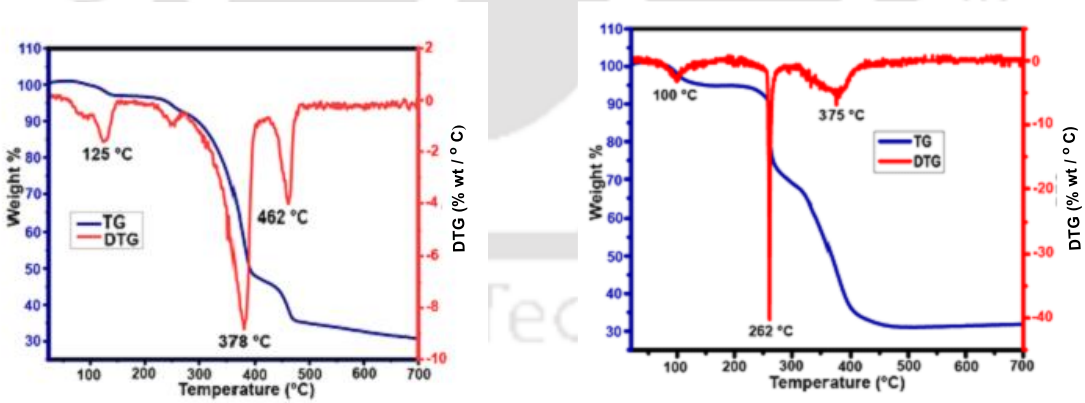

(a) (b)

Figure A3.3: Thermogram of the (a) *4.1* (b) 4.2. (heating rate 10 °C/min under argon atmosphere).

Chapter 4

N-(1,3-Dioxo-1H-benzo[de]isoquinolin-2(3H)-yl)isonicotinamide) and 2,6-pyridinedicarboxylic acid as a platform for metal ion sensing

4.1 Introduction

In the preceding two chapters, it was shown that depending on the nature of the N-substituents on naphthalimide, those ligands could be used as chelating or monodentate ancillary ligands to prepare mixed carboxylate complexes. In this chapter, two N-functionalised amino-naphthalimide compounds, namely N-(1,3-dioxo-1H-benzo[de]isoquinolin-2(3H)-yl)isonicotinamide (*naphydrazide*) and 7-(isonicotinamido)-1,3,6,8-tetraoxo-N-(pyridin-4-yl)-3,6,7,8-tetrahydrobenzo[lmn][3,8]phenanthroline-2(1H)-carboxamide (*binaphydrazide*) shown in the Figure 4.1, are presented. The aim of the investigation was to study them in a free state for the detection of metal ions and also to isolate and characterise their metal complexes to elucidate their abilities in sensing. The chosen compounds have pyridine moiety linked by semi-rigid amide bond, the pyridine part of the compounds will get protonated under mildly acidic conditions or act as a ligand. Depending on pH, these naphthalimide derivatives would have dual abilities to act either as ancillary ligands or as cationic species of a complex. There are many examples of naphthalimide derivatives whose emissions are influenced by metal ions, making some of them suitable for detecting ions at nanomolar concentrations.[1] Furthermore, chelate complexes show chelation induced enhancement of emission[2] and masking effect[3] to modulate optical responses of the central

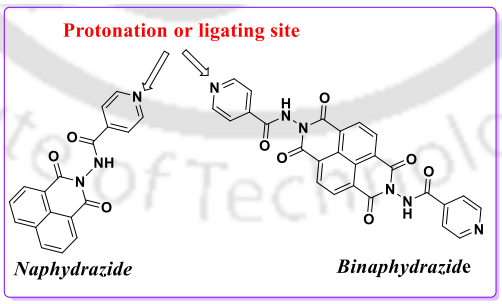

Figure 4.1: The structures of the two naphthalimide functionalised compounds, *naphydrazide, binaphydrazide*

ion useful for metal ion detections. Accordingly, the effect of different metal ions on the UV-visible or fluorescence emission spectra of the compound, *naphydrazide* or *binaphydrazide* together with 2,6-pyridinedicarboxylic acid (H_2*26pdc*) was investigated. The study was performed with the expectation that using a bi-component system of an organic dicarboxylic

acid together with an amine-based naphthalimide derivative would provide a new scheme for detections through competitive bindings to ions, and could also be useful to utilize the in-situ changes of acid-base properties of the media while forming metal-dicarboxylate complex in solution. This bi-component detection approach would offer several advantages: (1) mixed ligand coordination to influence emission properties; (2) reversible non-covalent interactions to modulate spectral responses; (3) masking of metal ions to reduce interference; (4) proton-mediated modulation of photo-electron transfer; and (5) potential for Forster resonance energy transfer. The bi-component systems are useful for topological reactions,[4] and also find utility in sensing[5] and as multi-emission platforms.[6] There are examples in which chelating groups such as ethylenediamine either mask the interference of an ion in the detection of another ion.[7] Hence, there are scopes to identify and utilise new platforms from two components operating concerted manner in detections of metal ions. Such systems will have advantages as there is the possibility to utilise them as multi-component analytes or their competitive binding would help in identifying alternative ratiometric sensing molecules such as the one conventionally used in quantum-dots[8] as well as with small organic molecules.[9]

4.2 Synthesis and Characterization of the Complexes:

The naphydrazide and binaphydrazide ligands were synthesized following a previously reported procedure and were confirmed by comparing their ^{1}HNMR, FT-IR, and HRMS spectra. The two complexes (*Hnaphydrazide*)[*Fe*(*26pdc*)$_2$]·H_2O *(4.1)* and (*H_2binaphydrazide*)[*Fe*(*26pdc*)$_2$]$_2$·*4.5H_2O (4.2)*, as depicted in Scheme 4.1 were prepared

Scheme 4.1: Synthesis of the iron complexes.

by reacting *$H_2$26pdc* with *naphydrazide* or *binaphydrazide* ligands with iron (III) chloride. The complexes were characterized by single-crystal X-ray diffraction, FT-IR spectroscopy, magnetic moment measurements. The thermal stability of both the compounds were studied by thermogravimetric analysis (TGA).

4.2.1 Synthesis and Characterization of (*Hnaphydrazide*)[Fe(*26pdc*)$_2$]·H_2O

The anionic complex 4.1 had the $[Fe(26pdc)_2]^-$ anion and a protonated *naphydrazide* outside the coordination sphere. It had also a water crystallisation molecule. The central Fe^{3+} ion was in a distorted octahedral geometry as found in conventional *bis-pdc* complexes. The two *26pdc* ligands, each coordinated in a tridentate manner, contribute six coordination binding sites of the iron ion. The structure of the complex is shown in Figure 4.2.

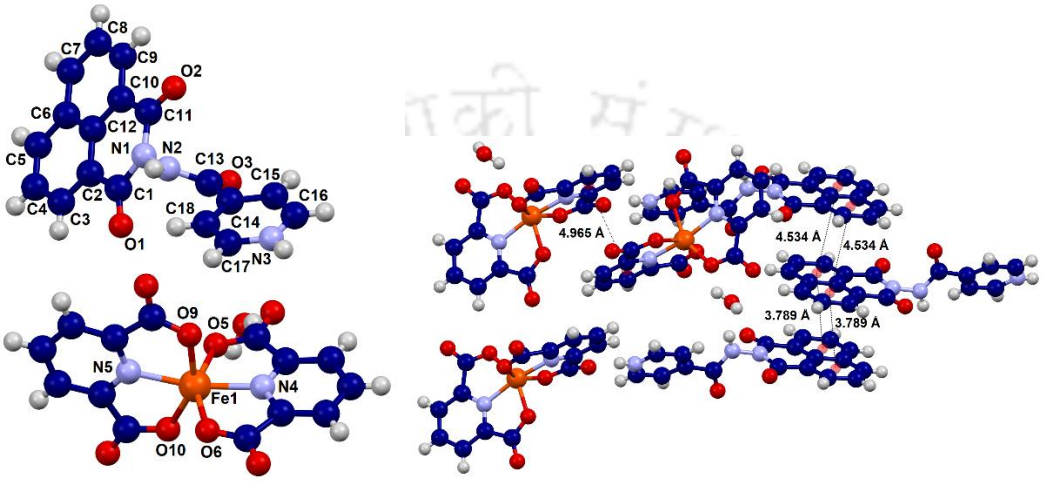

(a) (b)

Figure 4.2: (a) The crystal structure of complex *4.1* (Ball and stick representation) and (b) stacking arrangements among naphthalimide rings in the assembly of the complex (along the c- crystallographic axis).

The Fe-O bond lengths namely Fe1-O5, Fe1-O6, Fe1-O9, and Fe1-O10, were 2.037(2)Å, 2.025(2) Å, 2.015(2) Å, and 1.998(19) Å, respectively. The Fe-N bond distances Fe1-N4 and Fe1-N5 bonds were 2.064(2) Å and 2.071(2) Å. The bond angle O10-Fe1-O5 was 94.14(7)°, O10-Fe1-O6 was 94.68(8)°, and O10-Fe1-N4 was 116.14(8)°. On the other hand, O10-Fe1-N5 bond angle was 75.35(9)° and the O9-Fe1-N5 was 75.38(8)°. These highlighted a distorted octahedron six coordination environment. The angle of N4-Fe1-N5 at 167.94(6)° deviated from 180◦ reflected the deviation from the trans-arrangement of the nitrogen donors, contributing to the overall distortion. further confirm the deviation from perfect octahedral geometry, with subtle variations indicating a distorted spatial arrangement of the ligands. The different metal-ligand bond parameters are listed in the Table 4.1. The complex had extensive stacking among the napthalimide rings, these are shown in Figure 4.2b. The naphthalimide rings were parallel in the c-crystallographic axis and were one on top of the other by having opposite dipoles. There are two different sets of interactions observed assigning A as naphthalimide ring the

arrangement was like .AAA′A′AA… where the distance of separation between two A-rings was 3.789 Å and between the rings A and A′ was 4.534 Å.

Table 4.1: Metal-ligands bond-parameters of the complex *4.1*

M-L bond	Bond-length (Å)	∠L-M-L	Bond angle (°)
Fe1-O10	1.998 (19)	O10-Fe1-O9	150.68 (6)
Fe1-O9	2.015 (2)	O10-Fe1-O6	94.68 (8)
Fe1-O6	2.025 (2)	O9-Fe1-O6	94.36 (8)
Fe1-O5	2.037 (2)	O10-Fe1-O5	94.14 (7)
Fe1-N4	2.064 (2)	O9-Fe1-O5	91.36 (8)
Fe1-N5	2.071 (2)	O6-Fe1-O5	150.87 (7)
∠L-M-L	Bond angle (°)	O10-Fe1-N4	116.14 (8)
O9-Fe1-N5	75.38 (8)	O9-Fe1-N4	93.12 (8)
O6-Fe1-N5	108.09 (7)	O6-Fe1-N4	75.76 (8)
O5-Fe1-N5	100.09 (7)	O5-Fe1-N4	75.43 (8)
N4-Fe1-N5	167.94 (6)	O10-Fe1-N5	75.35 (9)

The bulk purity of complex *4.1* was assessed from the experimentally determined powder X-ray diffraction (PXRD) pattern, and compared with the simulated pattern generated by Mercury software. The complex had an effective magnetic moment of 5.83 BM, which is close to the spin-only value for a high spin d^5 system. It supported the +3 oxidation state of the iron in the complex. FT-IR spectroscopy was also utilized to analyze the changes in stretching frequencies of the ligand and the complex. The N-H stretching vibration of the secondary amide of *naphydrazide* was observed at 3316 cm^{-1}. The carbonyl stretching vibration of secondary 1688 cm^{-1}. The carbonyl stretches of the imide group, of *naphydrazide* appeared at 1718 cm^{-1} which was observed at a shifted position, namely at 1721 cm^{-1} in complex *4.1*. The optical microscopic images as well as scanning electron microscopy (SEM) of the morphology of complex *4.1* were determined, these are shown in Figure 4.3(c) and (d). The SEM showed floral-like arrangements of crystals. Complex *4.1* had thermal stability up to 263 °C and it did not show significant weight loss in thermogravimetry {Figure 4.3 (e)}. The complex was crystallised as hydrate with, no loss below 263 °C, suggesting that the water of crystallisation might have been lost during grinding to prepare the powdered sample. The subsequent weight loss observed from 306 °C continues till 500 °C.

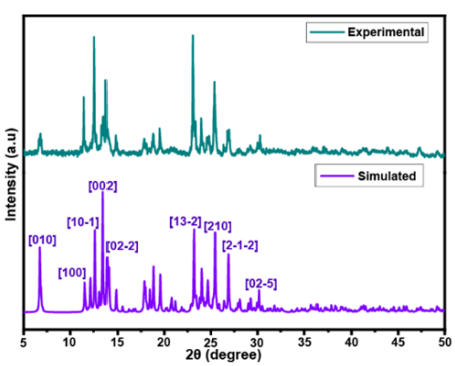

(a)

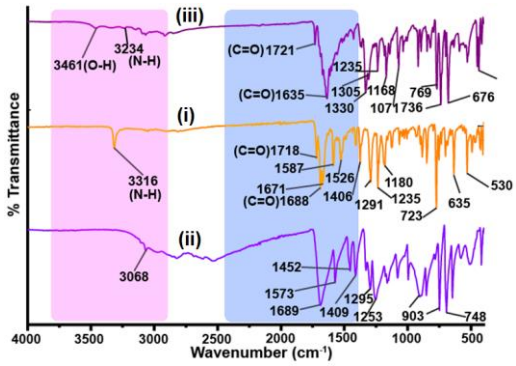

(b)

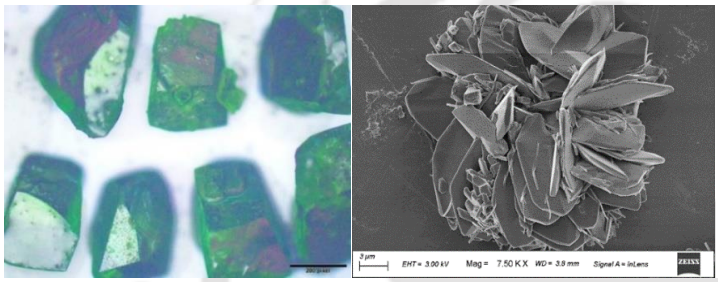

(a) (b)

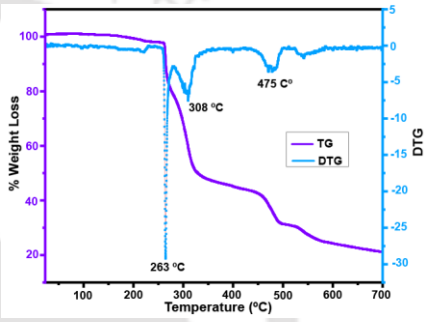

(c)

Figure 4.3: (a) Experimental PXRD pattern (top) and simulated from crystallographic information file by mercury software (bottom,) of complex *4.1*. (b) FT-IR of (i) free ligand (ii) *$H_2$26pdc* and (iii) complex *4.1*. (c) the scanning electron micrograph of complex *4.1* (d) the optical image and (e) the Thermogravimetry thermogram (red) of complex *4.1* (red line is differetial curve of the thermogram, the thermogram was recorded under argon, heating rate 10° C/min).

4.2.2 Synthesis and Characterization of the iron complex (*H_2binaphydrazide*)[Fe(*26pdc*)$_2$]$_2$·4.5H_2O:

The anionic part of complex 4.2 was identical to the one observed in complex 4.1. The asymmetric unit of the crystal structure of this complex had half the molecules of diprotonated *binaphydrazide* and a complex anion $[Fe(pdc)_2]^-$. The complex has two mononuclear $[Fe(pdc)_2]^-$ complex anions with one *H_2binaphydrazide*. The water of crystallisation molecules was highly disordered and could not be resolved in structures. Hence, a solvent mask was calculated and 356 electrons were found in a volume of 1240 **Å^3** in one void per unit cell. This volume was consistent with the presence of nine water molecules shared between two complexes. This accounts for 360 electrons per unit cell. This was further confirmed by thermogravimetry. The structure of the complex is depicted in Figure 4.4.

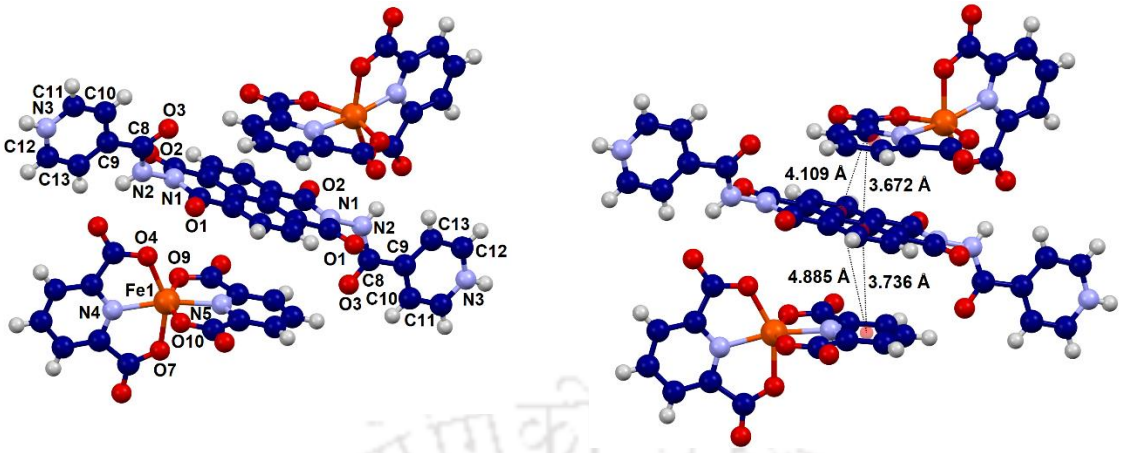

(a) (b)

Figure 4.4: (a) The crystal structure of the iron complex *4.2* (Ball and stick representation) (b) The stacking among the rings of the complex *4.2*.

The metal-ligand bond parameters are listed in Table 4.2. The Fe1-O4, Fe1-O7, Fe1-O9, Fe1-O10, bonds were 2.0123(18) Å, 2.0477(18) Å, 2.0051(18) Å, 1.987(2) Å respectively, While the Fe1-N4 and Fe1-N5 bonds were 2.051(2) Å and 2.049(2) Å, respectively. The bond angles O10-Fe1-N5, 76.32°(9), O10-Fe1-N4, 100.48°(8), and O10-Fe1-O7, 93.36°(8). Additional angles, such as O10-Fe1-O4 at 94.17° (9) and O9-Fe1-N5, 75.97°(8), N5-Fe1-N4, at 168.14° (6) reflected a distorted octahedral geometry. The metal-ligand bond parameters are listed in Table 4.2. Table 4.2: Metal-ligand bond lengths and angles of the complex *4.2*

M-L bond	Bond-length (Å)	∠L-M-L	Bond angle (°)
Fe1-O10	1.987 (2)	O10-Fe1-O9	151.86 (8)
Fe1-O9	2.0051 (18)	O10-Fe1-O4	94.17 (9)
Fe1-O4	2.0123 (18)	O9-Fe1-O4	93.01 (8)
Fe1-O7	2.0477 (18)	O10-Fe1-O7	93.36 (8)
Fe1-N4	2.051 (2)	O9-Fe1-O7	93.08 (8)
Fe1-N5	2.049 (2)	O4-Fe1-O7	151.70 (8)
∠L-M-L	Bond angle (°)	O10-Fe1-N5	76.32 (9)
O9-Fe1-N4	107.65 (8)	O9-Fe1-N5	75.97 (8)
O4-Fe1-N4	76.52 (7)	O4-Fe1-N5	114.91 (8)
O7-Fe1-N4	75.29 (7)	O7-Fe1-N5	93.38 (8)
N5-Fe1-N4	168.14 (8)	O10-Fe1-N4	100.48 (8)

The packing pattern has revealed that the naphthalenediimide ring was trapped in between two chelate rings of the coordinated *pdc*-ligands from two independent anions {Figure 4.4(b)}. Thus, it was included by having two different spacings between the rings. One of the faces of

the naphthalenediimide ring had π-stacking distance of 3.672 Å and the other face had 3.763 Å. These separations were indicative of the naphthalinedimide rings inclusion with charge-transfer. As the water molecules could not be located in crystallography it is not possible to depict the involvement of the pyridinium N-H bond in hydrogen bonds.

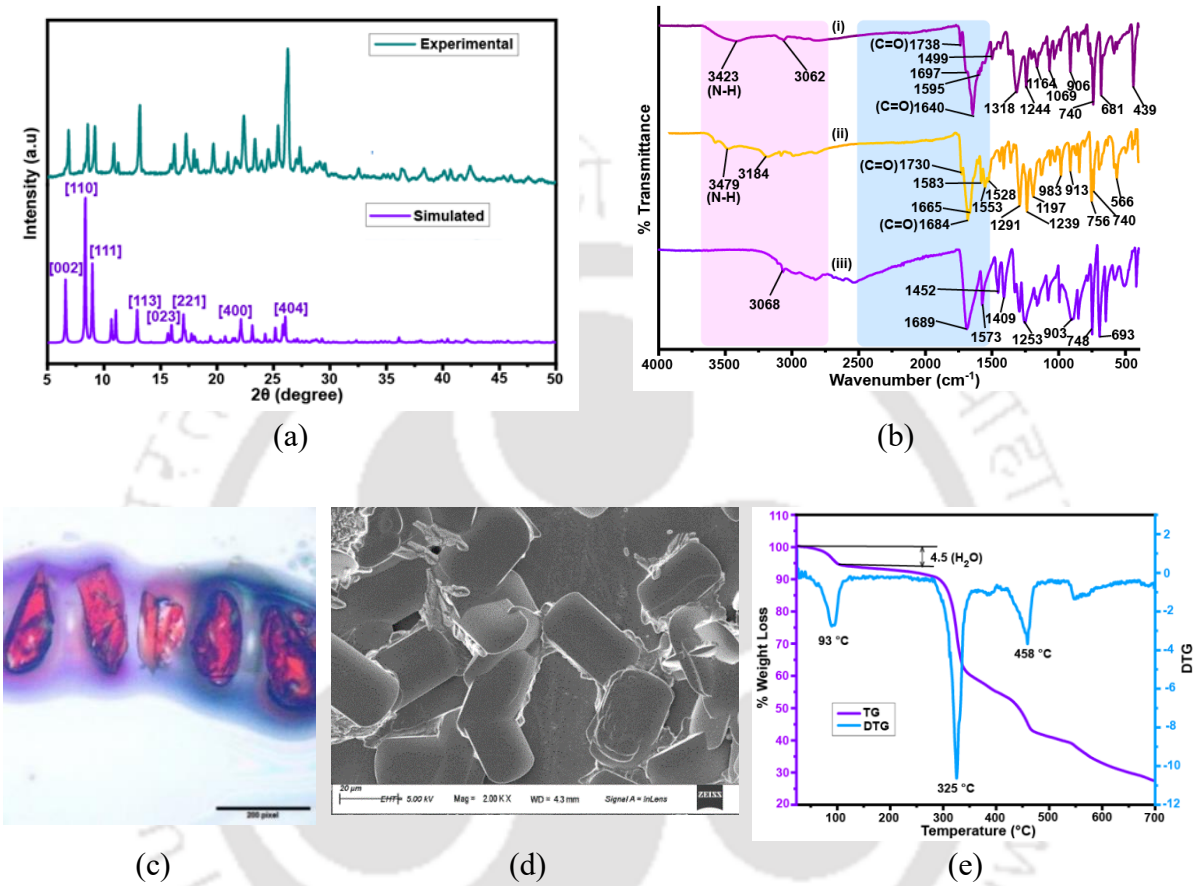

Figure 4.5: (a) Experimental PXRD pattern (top) and simulated from crystallographic information file by mercury software (bottom,) of complex *4.2,* and (b) FT-IR spectra of the (i) complex *4.2,* (ii) *binaphydrazide,* (iii) *$H_2$26pdc*. (c) The optical image and (d) Scanning electron micrograph of the complex *4.2,* (e) Thermogram (violet) of the complex *4.2* (differetial curve is shown in cyan color) under argon, with a heating rate 10° C/min.

The single crystalline phase of the complex *4.2* in bulk, was established by using powder X-ray diffraction. The experimental PXRD pattern of the *4.2* matched with the simulated PXRD pattern generated from the crystallographic information file with the aid of Mercury software {Figure 4.5(a)}. FT-IR spectra of the *binaphydrazide* showed the N-H stretching at 3479 cm^{-1}. The *$H_2$26pdc* had carbonyl stretch at 1689 cm^{-1}. After coordination with the iron center, the

carbonyl stretching vibration was shifted to 1697 cm^{-1}. The carbonyl stretching of the imide group of the free *binaphydrazide* was observed at 1730 cm^{-1} in the free ligand and was shifted to 1738 cm^{-1} upon coordination to the metal center {Figure 4.5(b)}. The effective magnetic moment for the complex was 5.90 BM, which was due to the spin-only value for a high spin Fe^{3+}, d^5 system. The morphology of complex *4.2,* from optical microscopy and scanning electron microscopy is shown in Figure 4.5 (c) and (d). The thermogram of the complex *4.2* had shown loss of water molecules from the crystal lattice at 93 °C {Figure 4.5 (e)}. The weight loss at this temperature corresponded to nine water molecules calculated based on the formula weight. The complex was thermally unstable above 325 °C and it continuously loss mass till 700 ◦C.

The structural studies of complexes *4.1* and *4.2* have shown that their stacking behaviour of them was widely different. In the latter case, the planar part of the cation was embedded by the chelated ligands, showing stacking among the cationic and anionic parts. Whereas, in the case of the *4.1,* the stackings were dipolar and between the cations only.

4.3 UV-visible spectroscopic study:

The pyridine-based naphthalene-derived compounds have been useful for cation detection and the *naphydrazide* was not an exception. As iron(III)-*26pdc* complexes with *naphydrazide* and *binaphydrazide* were obtained, the interactions of these ligands with iron ions were taken up. A solution of *naphydrazide* in dimethylformamide (DMF) exhibited a UV absorption peak at 335 nm ($\varepsilon = 4.51 \times 10^{-3}$ $mol^{-1}m^2$). When an aqueous solution of Fe^{2+} ions was added, the intensity of the absorption at 335 nm increased {Figure 4.6 (a)}. In contrast, the addition of an aqueous solution of Fe^{3+} ions {Figure 4.6 (b)} had caused a blue-shift of the absorption peak to 315 nm, with an increased intensity at this wavelength. Both the Fe^{2+} and Fe^{3+} ions induced a linear increase in the respective absorption intensities with an increasing concentration of the iron ions. However, the sensitivity of *naphydrazide* to Fe^{3+} ions was 7.90 times higher than the sensitivity to Fe^{2+} ions. These sensitivity differences were ascertained from the ratio of the slopes from the respective plots of absorption intensity versus concentration of Fe^{2+} or Fe^{3+} ions {Fig. 4.6(c)}.

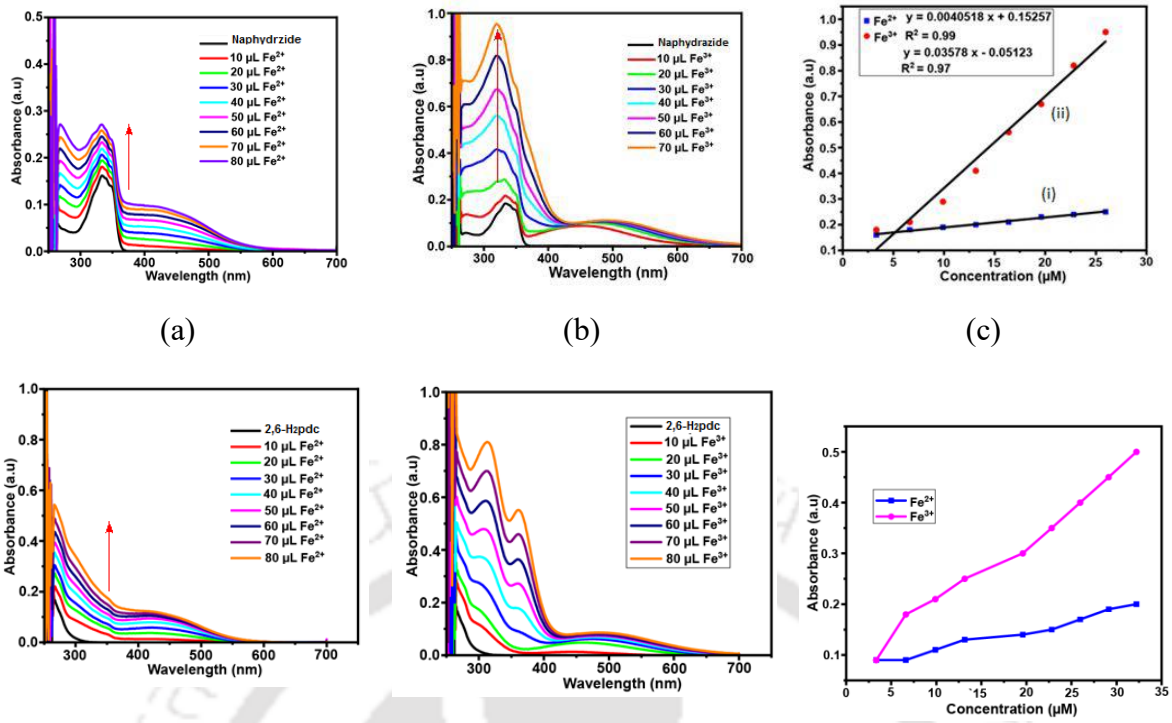

Figure 4.6: UV-visible titration of *naphydrazide* (3.32 µM in DMF, 3 mL) with each aliquot addition of (a) Fe^{3+} ions. (b) with different aliquots of solution of Fe^{3+} ions, (c) Plot of absorbance at of a solution of *naphydrazide* (3 mL) with different aliquots of (i) Fe^{2+} ions at 335 nm and (ii) Fe^{3+} ions at 315 nm. UV-visible titration of *$H_2$26pdc* (3.32 µM in DMF) solution with each time addition of 10 µL solution of 1 mM (d) Fe^{2+} (e) Fe^{3+} ions and (c) is the plot of concentration vs absorbance at 270 nm for Fe^{2+} and at 315 nm for Fe^{3+} of the figures (d) and (e).

In a similar experiment with *$H_2$26pdc*, which has an absorption peak at 270 nm ($\varepsilon = 3.67 \times 10^{-3}$ mol^{-1} m^2), the addition of Fe^{2+} ions resulted in an increased absorption intensity at 270 nm {Figure 4.6(d)}. Similarly, the addition of Fe^{3+} ions to a solution of the $H_2$26pdc led to the appearance of two new absorption peaks at 315 nm and 360 nm, with the intensities of these peaks increasing with the concentration of Fe^{3+} ions {Figure 4.6(e)}. The relative increase in absorption at 315 nm caused by Fe^{3+} ions, compared to the absorption increase at 270 nm caused by Fe^{2+} ions, was determined from the respective slopes of the linear plots of the intensity versus concentration. The slope for the plot with Fe^{3+} ions was 100.46 times higher than that for the slope with Fe^{2+} ions while doing titrations, indicating a much higher sensitivity.

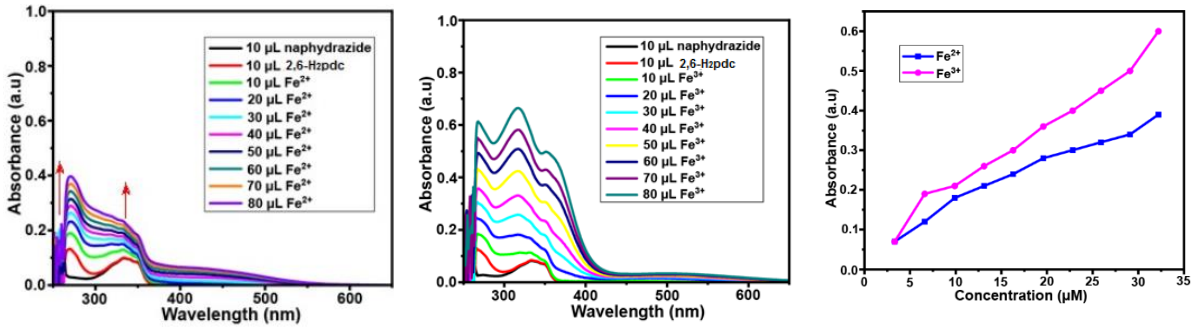

(a) (b) (c)

Figure 4.7: UV-visible titrations of a solution of *naphydrazide* together with *$H_2$26pdc* (both 10 µL from 3.32 µM stock solution in DMF added to 2mL DMF) upon addition of (a) Fe^{2+} (b) Fe^{3+} ions (10 µL in each aliquot from 1 mM stock solution in water in each case) (c) Concentration-dependent absorption at 270 nm from (a) and 315 nm from (b).

of the bi-component system to Fe^{3+} ions. Therefore, based on the absorption peak positions or changes in the intensities, Fe^{2+} and Fe^{3+} ions could be distinguished. The detection of Fe^{2+} and Fe^{3+} independently has inherent difficulties from the interference of each other in detection. The compound 1,10-phenanthroline is commonly used for colorimetric estimation of Fe^{2+}, this detection is known to be interfered with by Fe^{3+} ions.[10] Hence, extra treatment to reduce the Fe^{3+} during estimation is required. A combination of 1,10-phenanthroline with carbon dots has significantly improved Fe^{2+} detection.[11] This improvement was due to the fluorescence resonance energy transfer observed as a consequence of the overlap between the absorption peak of the Fe^{2+}-1,10-phenanthroline complex and the emission spectra of carbon dots. Furthermore, Fe^{2+} ions can selectively disassemble bio-composites of gold nanoparticles, this was useful to detect Fe^{2+} ions without interference from Fe^{3+}.[12] The limit of detection (LOD) for Fe^{3+} ions was 0.45 µM with *naphydrazide* (at 315 nm), 1.28 µM with *$H_2$2,6pdc*, and 0.09 µM with the bi-component system. The LOD values were within the permissible range of 0.3 mg/L to 0.5 mg/L for Fe^{3+} ions in drinking water as recommended by the World Health Organisation.[13] Both, *naphydrazide* alone and the bi-component system was effective in distinguishing Fe^{2+} from Fe^{3+}, detecting Fe^{3+} ions with reasonable LODs. However, the absorptions in the UV-region were used in these methods, which limited their use in practical applications.

4.4 Fluorescence Study:

In chapter 3 it was shown that the in-situ acid liberated in situ from *$H_2$26pdc* while forming a metal complex affects the emission spectra. This observation provided scope to explore the emission changes of the binary mixture of *naphydrazide* with *$H_2$26pdc* with various metal ions. *naphydrazide* in DMF exhibited weak emission at 400 nm (λ_{ex} =335 nm), which was attributed to π* to π transitions. The weak emission was due to quenching of the photo-electron transfer (PET) from the pyridine nitrogen to generate a PET-ON state.[14] There were no notable changes in emission when solution of ions such as NH_4^+, Li^+, Na^+, K^+, Cs^+, Al^{3+}, Sn^{2+}, Fe^{2+}, Cu^{2+} were added to independently prepared solutions *naphydrazide* together with *$H_2$26pdc*. However, a minor increase in the emission intensities was observed with Ag^+ or Zn^{2+} ions, whereas a significant increase in the emission was observed by adding Cd^{2+} ions. The enhancement caused by Cd^{2+} ions was partly quenched by only Mn^{2+} ions, the rest did not interfere, and the bi-component system was identified for selective detection of cadmium ions. These observations have provided an opportunity to find out the detections of cadmium ions by the bi-component system comprising an equimolar amount of *naphydrazide* and *$H_2$26pdc*. So, a series of emission experiments were carried out with the bi-component system with cadmium ions in the presence of various ions which are shown in Figure 4.8 (a)- (k). The emission intensity increase caused by Cd^{2+} ions was approximately eight times greater than that caused by Zn^{2+} ions and 3.2 times greater than the increase caused by Ag^+ ions. The Cd^{2+} ions did not affect the emission of *naphydrazide* in the absence of *$H_2$26pdc*. Optimization studies of the bi-component mixture of *naphydrazide* and *$H_2$26pdc* in the presence of Cd^{2+} ions revealed that a 1:3.2 molar ratio was found to be optimal for studying fluorescence changes induced by cadmium ions.

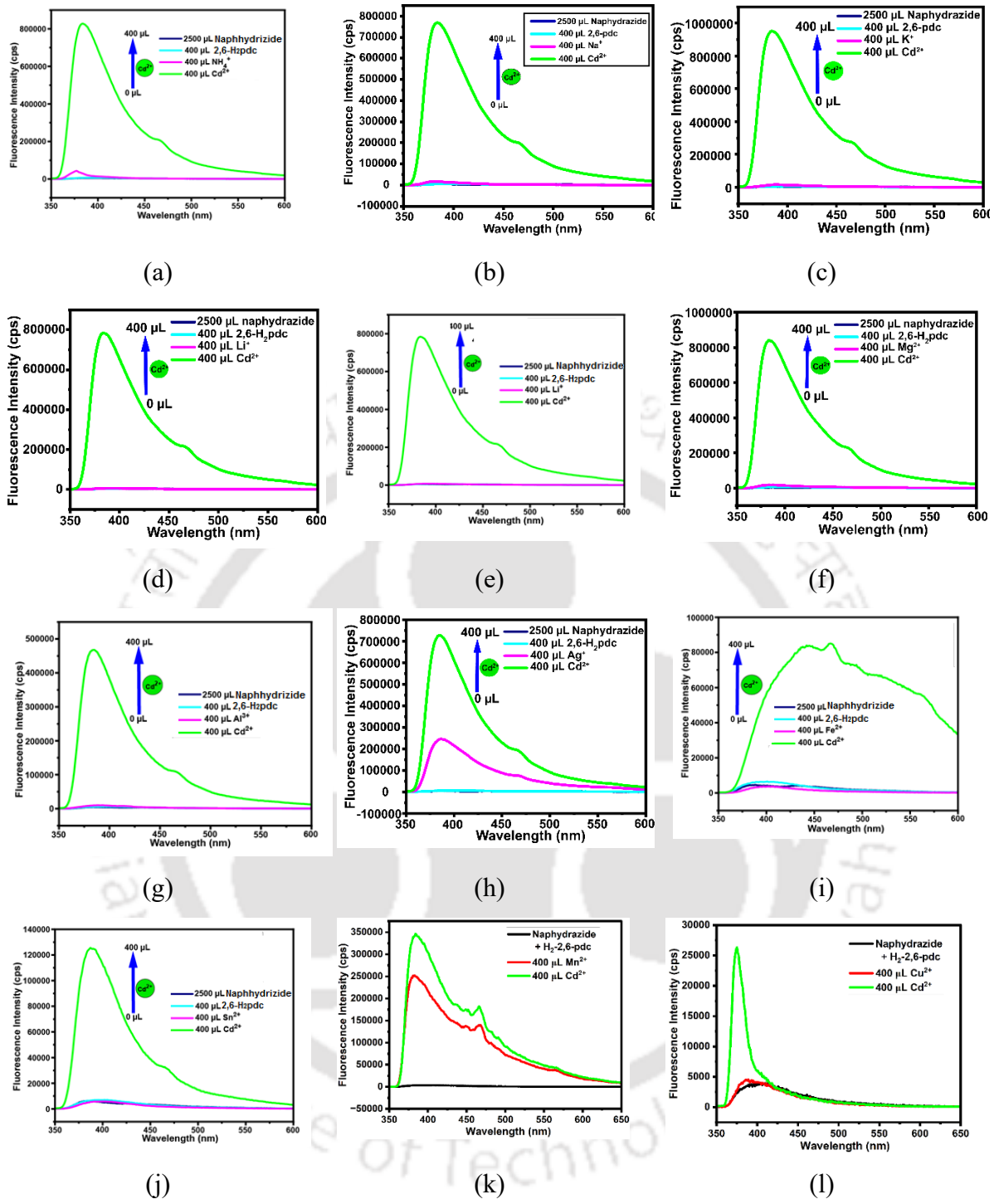

Figure 4.8: Fluorescence turn-on observed in DMF solution of *naphydrazide* together with *H226pdc* in the presence of (a) NH_4^+, (b) Na^+, (c) K^+, (d) Li^+, (e) Cs^+, (f) Mg^{2+}, (g) Al^{3+}, (h) Ag^+, (i) Fe^{2+}, (j) Sn^{2+}, (k) Mn^{2+} and (l) Cu^{2+} ions after addition of solution of Cd^{2+} ions.

In the fluorescence titrations shown in Figure 4.8, in each case, 2.5 mL of *naphaydrazide* dissolved in DMF (2 mM) was taken and its emission was recorded, followed by the

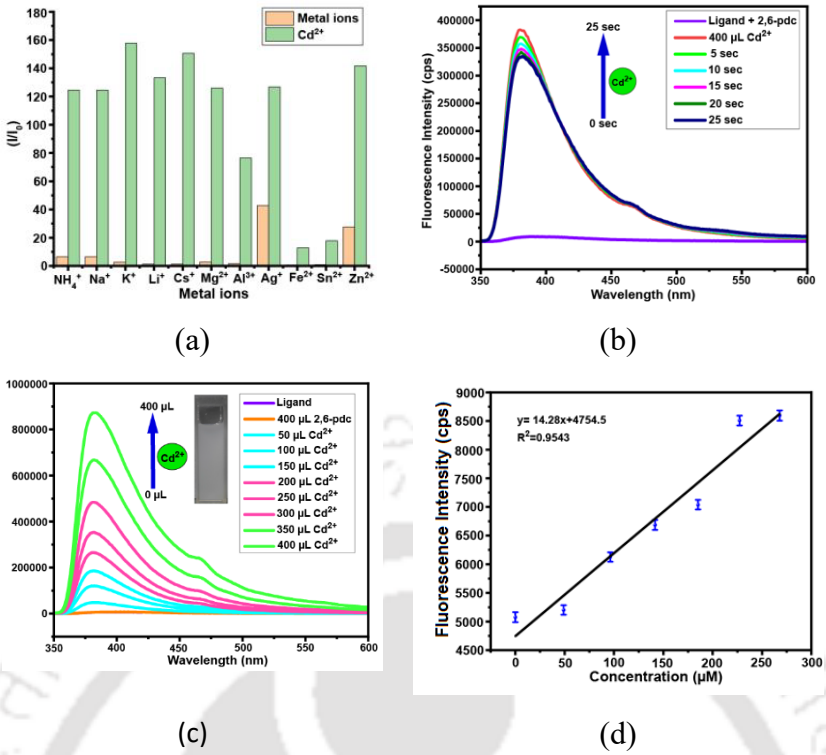

Figure 4.9: (a) Bar-diagram illustrating the relative changes in emission caused on the bi-component system by various metal ions, compared to the Cd^{2+} ions. Emission spectra recorded (b) at different time of the bi-component system with Cd^{2+} ions (400 µL of 20 mM). (c) after adding cadmium ions Cd^{2+} ions (50 µL of 20 mM aliquots), and the (d) Plot of the intensity of fluorescence of a solution of the bi-component solution versus concentration of Cd^{2+} ions. {In each case bi-component system was 2.5 mL of *naphydrazide* + *$H_2$26pdc* (2 mM)}.

addition of H_2-2,6pdc (400 µL of 20 mM) and spectra recorded, and the same spectra of the solution were recorded (shown in green) and titrated with Cd(II)acetate salt solution in each case by adding 50 µL of 20 mM Cd^{2+}. Excess amounts of the *$H_2$26pdc* were required to form a *bis*-chelated complex with cadmium ions and accordingly, the acid liberated during the process had effectively protonated *naphydrazide*. To verify the selectivity for cadmium ions, the competitive effect of the various cations in the presence of cadmium ions was conducted through a series of experiments. To do so, emission spectra of the solution by adding different cations (NH_4^+, Na^+, K^+, Li^+, Cs^+, Mg^{2+}, Al^{3+}, Hg^{2+}, Mn^{2+}, Fe^{2+}, Sn^{2+}; 400 µL of a 20 mM in each case) were recorded. Following this, a solution of Cd^{2+} ions was introduced to each of these solutions and respective emission spectra were recorded (Figure 4.8). The results showed no significant changes from the emission intensity originally caused by the Cd^{2+} ions alone in most of the cases. The effects are listed in the bar diagram {Figure 4.9 (a)} confirmed the selective detection of Cd^{2+} ions by the bi-component system. The stability of the emission peak during

detection after reaching the maxima was checked by recording the emission spectra after different time intervals have showed stability of the peak as shown in Figure 4.9 (b). This time-dependent fluorescence emission showed that the emission intensity reached a maximum spontaneously. The increase in the emission intensity of a solution of the bi-component solution by adding cadmium ions is shown in Figure 4.9 (c), the emission peak enhancement was accompanied by a shift of 13 nm shorter wavelength by showing the peak at 383 nm. As mixed-ligand complexes of *H₂26dc* with Cd^{2+} ions are documented in the literature,[15] the observed change in intensities was likely to be due to the chelation of Cd^{2+} ions with *26pdc*, which led to the released acid to protonate *naphydrazide* causing photo-electron transfer ON-emission, as a consequence of chelation of *26pdc* to cadmium ions. A plot of intensity vs concentration provided a linear plot as depicted in Figure 4.9(d).

On the other hand, the addition of Fe^{3+} ions to the bi-component solution resulted in a complete quenching of the weak emission. In general, Fe^{3+} is known to act as a quencher of fluorescent species.[16] The Fe^{2+} ions have a less significant effect on the emission of the bi-component system, it also did not inhibit the enhancement of emission in the presence of Cd^{2+} but drastically altered the shape of the emission profile {Figure 4.8 (i)} by spreading it across wavelengths from 350 nm to 600 nm, resulting in white-light emission when Fe^{2+} and Cd^{2+} were present together in the solution of the bi-component. The effect of Fe^{2+} ions on the emission was studied at two different ratios of *naphydrazide* to *H₂26pdc* molar ratios, namely with 1:1.25 and 1:2.50. With 1:1.25 molar ratio, broad overlapping emission peaks at 469 nm and 529 nm were observed, their intensities increased with Cd^{2+} concentration and broadening took place to cover the wavelength range from 390 nm to 650 nm. With the molar ratio of 1:2.50 ratio, the broad emission peak 390 nm - 650 nm, was observed but was a skewed peak, showing an emission maximum at 469 nm. Chromaticity index plots (Figure 4.10a and 4.10b) indicated blue emission from the *naphydrazide* and *H₂26pdc* solution in the presence of Cd^{2+} ions. In contrast, the presence of both Fe^{2+} and Cd^{2+} ions resulted in white-light emission. The white-light emission could be attributed to the combined effects of PET-ON and exciplex formation. The lifetime decay profile of the bi-component solution with Cd^{2+} ions was measured, which showed a biexponential decay with very short lifetimes: 0.050 ns (89.58%) and 0.225 ns (10.42%). The short lifetimes are characteristic of exciplex. Without Cd^{2+} ions, the lifetime could not be determined due to weak emission. Upon adding Fe^{2+} ions, the decay profile became biexponential with lifetimes of 0.100 ns (27.03%) and 0.203 ns (72.97%), indicating a new emission path with a relatively longer lifetime was generated by adding

ferrous ions. Hence, the observed white-light emission likely resulted from multiple emission paths, as seen in similar naphthalimide complexes with organic molecules and in two-photon excitation studies.[17] Recent reports also suggest that naphthalimide derivatives can generate white-light emissions.[18]

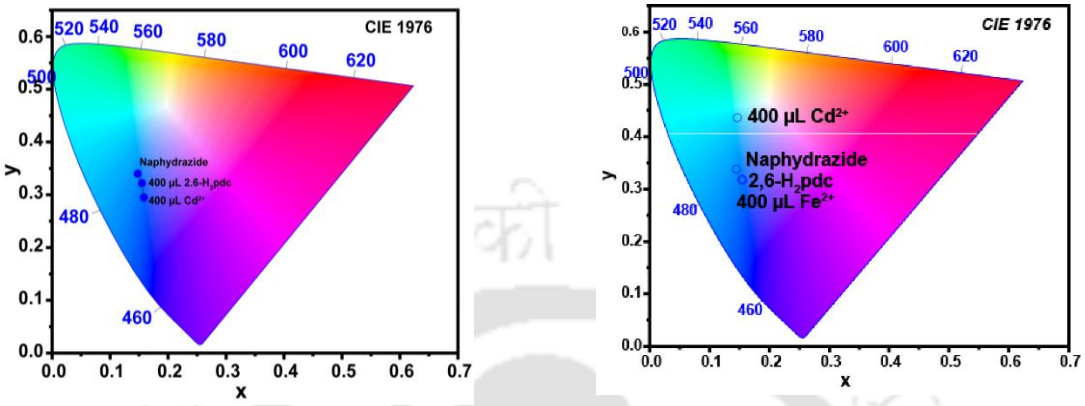

(a) (b)

Figure 4.10: (a) Chromaticity CIE (1976) diagram of a solution of the *naphydrazide* and 2,6-H_2pdc with cadmium ions (2.5 mL of 2 mM, 400 µL of 20 mM 2,6-H_2pdc and 400 µL of 1 mM of Cd^{2+}) and the same solution but with Fe^{2+} ions (400 µL of 1 mM), respectively.

The World Health Organization's maximum permissible limit for Cd^{2+} ions in drinking water is 44 µM (0.005 mg/L).[19] The limit of detection (LOD) for Cd^{2+} ions was found in this study to be 18.31 µM (0.002 mg/L), making it 2.5 times more sensitive than the required limit. This sensitivity is comparable to other sensors reported in the literature but less sensitive than some advanced sensors.[20] Unlike other methods that require specific pH conditions or complex synthetic processes, this system operates efficiently in DMF without the need for buffers. Naphthalimide derivatives functionalized at the 4-position have been noted for selective fluorescence ON with Cd^{2+} ions and OFF with Cu^{2+} ions.[21] Although this sensor demonstrated better sensitivity for Cd^{2+} detection, the simplicity of the current method is an advantage. Other chelation-induced emission enhancements, such as those observed with coumarin-based sensors or hydroxynaphthalene-based Schiff bases, show varying preferences for different ions.[22] Terpyridine-based receptors also distinguish between Cd^{2+} and Zn^{2+}, with detection limits similar to the bi-component sensing platform described here.[23] The current system is notable for its ability to differentiate Cd^{2+} from Zn^{2+}, as well as Fe^{2+} from Fe^{3+} ions, both in colorimetric and fluorescence detections.

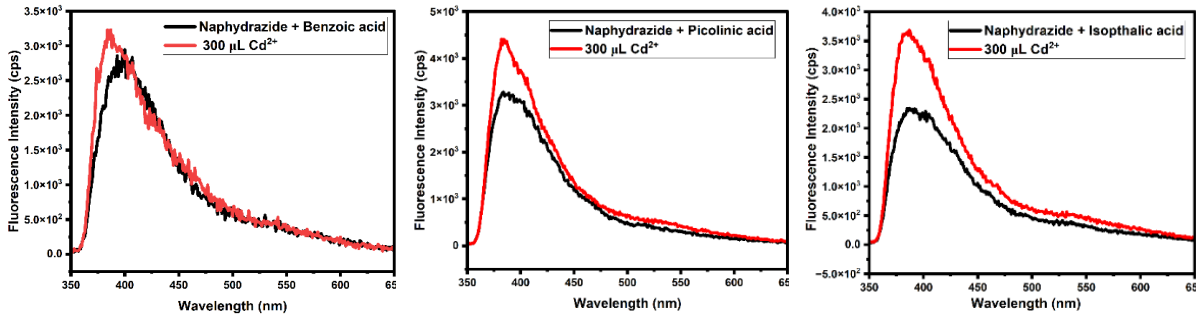

(a) (b) (c)

Figure 4.11: Changes in the fluorescence emission intensity of a solution of *naphydrazide* (2mM) having (a) benzoic acid (20 mM, 300 µL), (b) picolinic acid (20 mM, 300 µL), (c) isophthalic acid ((20 mM, 300 µL), upon addition of Cd^{2+} ions (50 µL of 20 mM) to the respective solution. (λ_{ex} = 335 nm, λ_{em} = 383 nm).

To suggest the specificity of the system, the similar compound Binaphydrzide was not effective for such a study, it was non-emissive in solution. The quenched state was not recovered either by adding *H₂26pdc* or metal salts that were effective for *naphydrazide.* For more comparisons on supercity, emission studies of a series of bi-component systems of *naphydrazide* with various organic acids, including benzoic acid, picolinic acid, or isophthalic acid were investigated. In these cases, the emission sensitivity to cadmium ions was poor as illustrated in Figure 4.11. The effective increase in the emission intensities by the same amount of cadmium ions was 1.12 folds increase in the benzoic acid, 1.34 folds in the picolinic acid, 1.46 folds in the isophthalic acid, and 66.67 folds in the *H₂26pdc* as the partner component of the *naphydrazide*. From the comparisons, the combination of *H₂26pdc* and *naphydrazide* emerged as the suitable bi-component system, demonstrating superior performance compared to the other combinations. This optimized system shows promise for further development and potential applications in relevant areas.

4.5 Cyclic-Voltammetry studies

The iron ions quantification is known to be determined by electrochemical means,[24] hence the ability of the bi-component system having the electroactive naphthalimide unit was investigated. A solution of *naphydrazide* in DMF displayed two quasi-reversible redox couples as in the related compounds[25] at $E_{1/2}$ values of -0.807 V and -1.321 V. These redox couples for *naphydrazide* are illustrated in Figure 4.12 (a). Complex *4.1* in dimethylformamide showed quasi-reversible redox peaks at -0.418 V and -0.697 V, along with an additional peak at -1.02 V {Figure 4.12(b)} The peak at -0.418 V was assigned to the Fe^{2+}/Fe^{3+} couple, while the $E_{1/2}$

at -0.697 V was attributed to the formation of an anion radical from *naphydrazide*. Notably, upon protonatation, the *naphydrazide* in the complex was reduced at a more negative potential compared to the free *naphydrazide*. The dianion formation was irreversible, as indicated by the single reduction peak observed at -1.02 V. A solution of *binaphydrazide* in DMF exhibited two redox couples with midpoint potentials ($E_{1/2}$) at −0.815 V (corresponding to anion radicals) and −1.247 V (corresponding to dianions). In contrast, *complex 4.2* displayed three redox couples with $E_{1/2}$ values at −0.367 V, −0.766 V, and −1.744 V. Among these, the quasi-reversible peak at −0.376 V was attributed to the ferric/ferrous redox couple.

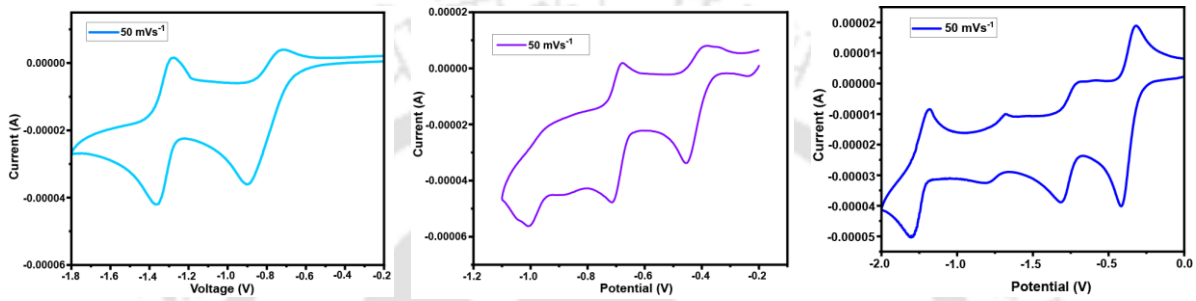

(a) (b) (c)

Figure 4.12: (a) The cyclic-voltammogram of the *naphydrazide,* (b) complex *4.1*, (c) complex *4.2* (1 mM in dimethylformamide, tetrabutylammonium perchlorate supporting electrolyte; scan rate, 50 mV/sec, +ve scan).

A cyclic-voltammetry titration of *naphydrazide* by adding Fe^{2+} and Cd^{2+} ions did not show significant changes, except for a slight variation in the I_{pc} value. But, the cyclic-voltammogram of the bi-component solution of *naphydrazide* with *$H_2$26pdc*, had a notable difference in the anion-radical couple compared to the parent *naphydrazide*. In this case, the radical anion generated was irreversible, while the dianion couple {Fig. 4.13(a)} remained unchanged.

Upon the addition of Fe^{3+} or Fe^{2+} ions to the solution of the bi-components, the reversibility of the anion radical was restored. The irreversibility was imparted by *$H_2$26pdc* to the formation of anion radical of *naphydrazide* {Figure 4.10 (b)} could not be reversed by the addition of Cd^{2+} ions. In the earlier section 4.3, it was shown from UV-vis studies that the bi-component system could effectively differentiate cadmium and ferric ions. However, the competitive binding of cadmium over Fe^{3+} ions toward *$H_2$26pdc* was not the primary factor influencing the electrochemical process. Instead, it was the redox-active ferrous or ferric ions that affected the reconversion of the anion radical to the neutral species.

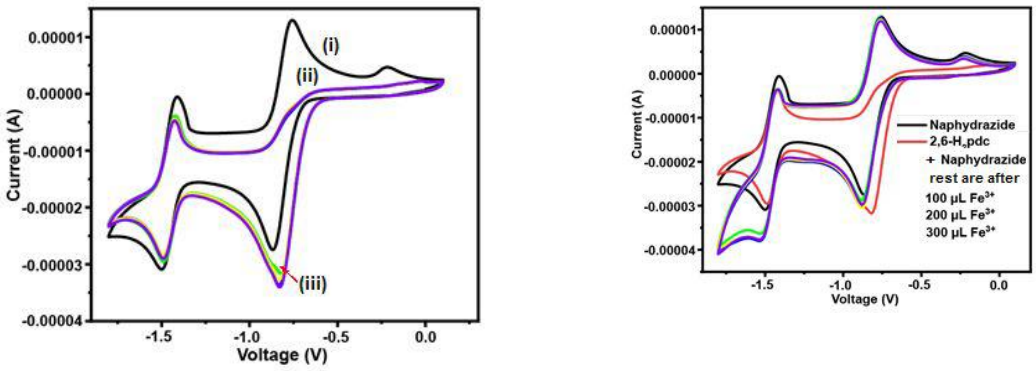

(a) (b)

Figure 4.13: Cyclic-voltamometric titrations: (a) (i) *naphydrazide* (1 mM, 10 mL in DMF) (ii) *naphydrazide* and *H₂26pdc* (1 mM, 5 mL of each) in DMF to which solution of Fe^{3+} ions were added and (b) (i) *naphydrazide* (ii) *naphydrazide* and *H₂26pdc*, (iii) *naphydrazide* + *H₂26pdc* + Cd^{2+} ions (100 µL solution in different aliquots from a 1.0 mM solution of the corresponding stock solution of the metal ion).

4.6 Summary:

Two iron (III) complexes containing *naphhydrazide* and *binaphhydrazide* were structurally characterised. The *naphhydrazide* together with *H₂26pdc* provided a bi-component platform for the differentiation of ferrous from ferric ions by UV-visible spectroscopy, whereas, the fluorescence-spectroscopic study provided on the bi-component system showed a highly sensitive and selective detection methodology for cadmium(II) ions.

4.7 Experimental Section:

The UV-visible absorptions were measured by using a UV Lambda 365+ spectrophotometer. For UV-visible experiments for cation detections, stock solutions (1 mM in water) of corresponding metal (II) acetate except in the case of ferric ion where ferric chloride was prepared. The spectra were recorded after each addition to monitor the changes. The experiments were conducted using 3 mL of UV-grade DMF solvent in a quartz cuvette. To this solvent, 10 µL aliquots of a previously prepared 1 mM stock solution of naphhydrazide and H226pdc in DMF were sequentially added. UV-visible absorption titrations were performed by incrementally adding 10 µL aliquots of an aqueous solution containing the desired metal ion (1 mM). Acetate salts of the metal ions were used, except for Fe(III), where Fe(III) chloride was utilized.

The fluorescence measurements were carried out using a HORIBA FluoroMax spectrofluorometer. For the fluorescence experiments, 2.5 mL of a 2 mM *naphydrazide* solution was taken in a quartz cuvette. Subsequently, 400 µL of a 20 mM solution of *$H_2$26pdc* was added to the cuvette, and emission spectra were recorded. The fluorescence titrations were carried out by placing 2.5 mL of *naphydrazide* (2 mM) in a cuvette, followed by the addition of 400 µL of *$H_2$26pdc* (20 mM) solution. The mixture was then titrated stepwise by adding 100 µL aliquots of a cadmium(II) acetate solution (20 mM) at each interval. 2.5 mL of naphydrazide (2 mM) was added to a cuvette, followed by 400 µL of $H_2$26pdc (20 mM) solution for the competitive fluorescence titrations. Metal acetate solution (400 µL) was introduced by micropipette and emission spectra were recorded, followed by the addition of 400 µL of cadmium acetate solution, and emission spectra were recorded.

The cyclic-voltammograms were recorded using a NOVA cyclic-voltammetry instrument. A stock solution of *naphydrazide* and *$H_2$26pdc* (1 mM, 10 mL) was taken, in a cell comprising of three electrodes (glassy carbon-working electrode, Pt- counter electrode, Ag/AgCl reference electrode) voltammogram. The tetrabutylammonium perchlorate (341.92 mg) was added and the cyclic-voltammogram was recorded at a scan rate of 50 mV per second with a +ve scan. Afterward, 5 mL of the *naphydrazide* solution was replaced with 5 mL of the *$H_2$26pdc* solution. Subsequently, 100 µL of the 1 mM stock solution of the desired analyte was incrementally added, and the voltammograms were recorded after each addition.

SEM Measurements: The respective complex was finely ground, dispersed onto a conductive adhesive substrate, and coated with a thin layer of gold to ensure conductivity and reduce charging during imaging.

Synthesis of *naphydrazide*: It was synthesized by the reported procedure.[26] ^{1}HNMR (600 MHz, DMSO-d_6): 11.71 (s, 1H), 8.88 (s, 2H), 8.60 (t, J = 6 Hz, 4H), 7.97 (t, J = 12 Hz, 2H), 7.93 (d, J = 6 Hz, 2H). IR (KBr, cm^{-1}): 3316 (s), 3250 (w), 2813 (w), 1718 (s), 1688 (s), 1671 (w), 1586 (s), 1526 (s), 1488 (w), 1434 (m), 1406 (s), 1375 (m), 1291 (s), 1235 (s), 1180 (s), 1157 (w), 1124 (s), 1064 (s), 1043 (m), 1025 (m), 1004 (m), 928 (s), 899 (s), 884 (s), 797 (m), 775 (s), 751 (s), 733 (m), 701 (s), 635 (s). ESI mass: calcd 318.0879 [M + H$^+$]; found 318.0880 [M + H$^+$].

Synthesis of *binaphydrazide*: A solution of 1,8-naphthalicdianhydride (670 mg, 2.5 mmol) and isonicotinylhydrazide (685 mg, 5 mmol) in DMF taken in a round bottom flask was placed in oil bath (100°C) and stirred for 12 hours. The reaction mixture was cooled and ice-

cold water was added to the reaction mixture. The resulting wine-colored precipitate was then filtered and air-dried. Yield 90 %. ^{1}HNMR (600 MHz, DMSO-d_6): 11.94 (s, 2H), 7.93(d, J = 6 Hz, 4H), 8.88 (m, 4H), 8.89 (d, J = 6 Hz, 4H). FT-IR (ATR method, cm^{-1}): 3479 (w), 3184 (w),1730 (s), 1583, 1684 (s), 1665 (m), 1553(s), 1528 (m), 1291(s), 1239 (m), 1197 (m), 983 (m), 913 (s), 756 (s), 740 (s), 566 (s).

Complex *4.1*: To a well-stirred warm solution of *naphydrazide* (31.7 mg, 0.1 mmol) and *H₂26pdc* (33.4 mg, 0.2 mmol) in methanol (20 mL), ferric chloride (16.2 mg, 0.1 mmol) was added. The reaction mixture was stirred for 3 hours and provided a brown precipitate, which was collected by decanting the solvent and the precipitate re-dissolved in 10 mL of Millipore water. The solution was filtered and allowed to stand undisturbed for 2-3 days yielding yellow crystals. Isolated yield, 70 % Based on metal. FT-IR (ATR method, cm^{-1}): 3461 (s, $\nu_{O\text{-}H}$), 3324 (s, $\nu_{amide\ N\text{-}H}$), 1721 (s, $\nu_{imide\ C=O}$), 1635 (s, $\nu_{amide\ C=O}$). UV-visible (λ_{max} = 332 nm, € = 0.36 M^{-1}dm^{-1}, Effective magnetic moment (at 25◦C), 5.83 BM.

Complex ***4.2*:** This complex was prepared using a similar procedure to the previous compound but with *binaphydrazide* (50.6 m, 0.1 mmol), *H₂26pdc* (66.8 mg, 0.4 mmol,), and ferric chloride (32.4 mg, 0.2 mmol). Brown crystals were obtained. Yield, 60 % (calculated based on metal. IR (neat, 3636 cm^{-1}): 3423 (s, $\nu_{amideN\text{-}H}$), 1738 (s, $\nu_{imide\ C=O}$), and 1640 (s, $\nu_{amideC=O}$). UV-visible (in DMF) λ_{max} = 378 nm (€ = 0.30 M^{-1}dm^{-1}). Effective magnetic moment (at 25◦C), 5.90 BM.

Structure determination:

The structures of the two iron complexes were determined at room temperature on a Brucker Bruker D8 Quest Diffractometer equipped with a Photon CMOS detector. The crystal and refinement parameters are listed in Table 4.3.

Table 4.3: Crystal and refinement parameters of the complexes *4.1* and *4.2*

Parameters	***[(Hnaphydrazide)[Fe(26pdc)₂]·H₂O***	***[(H₂binaphydrazide)Fe(26pdc)₂]₂·4.5H₂O***
Empirical Formula	$C_{25}H_{21}FeN_5O_{12}$	$C_{54}H_{46}Fe_2N_{10}O_{31}$
CCDC No.	2325870	2325867
Formula Weight	722.38	1442.71
Crystal System	Triclinic	Monoclinic
Space group	P-1	P21
a/ Å	7.808 (6)	16.017 (3)
b/ Å	14.712(11)	14.142(3)
c/ Å	14.844(12)	26.803(6)
α/ °	117.038(16)	90
β/ °	92.27(2)	90.347(9)
γ/ °	98.607(15)	90

V/ Å^3	1490(2)	6071(2)
Z	2	4
ρ (gcm^{-3})	1.610	1.578
μ (mm^{-1})	0.585	0.582
F (000)	738.0	2960.0
Refl collected	35011	71 609
Independent Refl	5296	5567
Ranges (h,k,l)	-9 ≤ h ≤ 9 -17 ≤ k ≤ 17 -17 ≤ l ≤ 17	-19 ≤ h ≤ 19 -16 ≤ k ≤ 17 -32 ≤ l ≤ 32
Max θ (degree)	25.204	25.409
Data/restraints/parameters	5296/0/462	5567/0/397
Goof (F^2)	1.067	1.045
R indices	0.0415	0.0532
[I>2σ]	0.0375	0.0404
WR_2	0.1062	0.1258

4.8 References:

1 (a) H. Q. Dong, T. B. Wei , X. -Q. Ma , Q. Y. Yang , Y. F. Zhang , Y. J. Sun , B. B. Shi, Y. M. Zhang, Q. Lin, 1,8-Naphthalimide-based fluorescent chemosensors: recent advances and perspectives. *Mater. Chem. C*, 2020, 8, 13501-13529. (b) G. Kaur, I. Singh, N. Tandon, R. Tandon, A. A. Bhat, 1,8-Naphthalimide-based chemosensors: a promising strategy for detection of metal ions in environmental and biological systems. *ChemistrySelect*, 2023, 8, e202301661.

2 R. J. Wandell, A. H. Younes, L. Zhu, Metal-coordination-mediated sequential chelation-enhanced fluorescence (CHEF) and fluorescence resonance energy transfer (FRET) in a heteroditopic ligand system. *New J. Chem.*, 2010, 34, 2176 - 2182. (b) A. Roy, M. Nandi, P. Roy, Dual chemosensors for metal ions: a comprehensive review. *TrAC Trends in Anal. Chem.*, 2021,138, 116204. (c) J. W. Nugent, H. Lee, H. S. Lee, J. H. Reibenspies, R. D. Hancock, Mechanism of chelation enhanced fluorescence in complexes of cadmium(II), and a possible new type of anion sensor. *Chem. Commun.*, 2013, 49, 9749 - 9751.

3 (a) M. Elhabiri and A. M. Albrecht-Gary, Supramolecular edifices and switches based on metals. *Coord. Chem. Rev.*, 2008, 252, 1079 - 1092. (b) X. Jiang, Y. Kou, J. Lu, Y. Xue, M. Wang, B. Tian, L. Tan, Fluorescence "on-off-on" assay of copper ions and

EDTA using amino-functionalized graphene quantum dots. *J. Fluoresc.*, 2020, 30, 301 - 308. (c) S. Zhao, X. Lai, F. Liu, L. Chen, Carbon dots combined with masking agent for high selectivity detection of Cr(VI) to overcome interference associated challenges. *Ecotoxicology and Environmental Safety*, 2022, 244, 114069. (d) J. Park, H. Yu, S. H. Park, K. H. Lee, Selective ratiometric red-emission detection of In^{3+} in aqueous solutions and in live cells using a fluorescent peptidyl probe and metal chelating agent. *Analyst*, 2020, 145, 4031 - 4040.

4 B. P. Krishnan, S. Ramakrishnan, K. M. Sureshan, Supramolecular design of a bi-component topochemical reaction between two non-identical molecules, *Chem. Commun*., 2013, 49, 1494 -1496.

5 T. Wakahara, K. Nagaoka, A. Nakagawa, C. Hirata, Y. Matsushita, K. Miyazawa, O. Ito, Y. Wada, M. Takagi, T. Ishimoto, M. Tachikawa, K. Tsukagoshi, One-dimensional fullerene/porphyrin cocrystals: near-infrared light sensing through component interactions. *ACS Appl. Mater. Interfaces*, 2020, 12, 2878 - 2883.

6 X. Lei, Y. Ai, Z. Shu, W. Wang, Y. Li, Precise regulation the multiemission based on soft double salt for Information encryption, *Inorg.Chem.,* 2024, 63, 11354 - 11360.

7 (a) K. Shankar, J. B. Baruah, Modulation of fluorescence emissions of copper (II) 2,2′-biquinoline-4,4′-dicarboxylate. *ChemistrySelect*, 2016, 1, 3038 - 3044. (b) H. Singh, G. Bhargava, S. Kumar, P. Singh, Quadruple-signaling (PET, ICT, ESIPT, -C=N- rotation) mechanism-based dual chemosensor for detection of Cu^{2+} and Zn^{2+} ions: TRANSFER, INH and complimentary OR/NOR logic circuits. *J. Photochem. Photobiol. A,* 2018, 357, 175 - 184.

8 M. H. Lee, J. S. Kim, J. L. Sessler, Small molecule-based ratiometric fluorescence probes for cations, anions, and biomolecules. *Chem. Soc. Rev.,* 2015, 44, 4185 - 4191.

9 P. Wu, X. Hou, J. J. Xu and H. Y. Chen, Ratiometric fluorescence, electrochemiluminescence, and photoelectrochemical chemo/biosensing based on semiconductor quantum dots. *Nanoscale*, 2016, 8, 8427 - 8442.

10 H. Tamura, K. Goto, T. Yotsuyanagi and M. Nagayama, iron(II) with 1,10-phenanthroline in the presence of large amounts of iron(III). *Talanta*, 1974, 21, 314 - 331.

11 X. Sun, J. Zhang, X. Wang, J. Zhao, W. Pan, G. Yu, Y. Qu and J. Wang, Colorimetric and fluorimetric dual mode detection of Fe^{2+} in aqueous solution based on a carbon dots/phenanthroline system, *Arabian J. Chem.*, 2020, 13, 5075 - 5083

12 P. Siyal, A. Nafady, Sirajuddin, R. Memon, S. T. H. Sherazi, J. Nisar, A. A. Siyal, M. R. Shah, S. A. Mahesar, S. Bhagat, Highly selective, sensitive and simpler colorimetric sensor for Fe^{2+} detection based on biosynthesized gold nanoparticles. *Spectrochim. Acta*, *Part A,* 2021, 254, 119645.

13 World Health Organization, Avenue Appia 20, 1211 Geneva 27, Swizerland.

14 (a) W. Sun, S. Guo, C. Hu, J. Fan, X. Peng Recent development of chemosensors based on cyanine platforms. *Chem. Rev.,* 2016, 116, 7768 - 7817. (b) W. *Sun,* M. Li, J. Fan, X. Peng, Activity-based sensing and theranostic probes based on photoinduced electron transfer. *Acc. Chem. Res.,* 2019, 52, 2818 - 2831.

15 (a) A. Sharif, G. R. N. Mahboubeh, Synthesis, structure and characterization of a helical seven-coordinated pyridine-2,6-dicarboxylate-bridged cadmium(II) complex *Acta Chim. Slov.,* 2013, 60, 138 - 143

16 (a) K. W. Cha, K. W. Park, Determination of iron(III) with salicylic acid by the fluorescence quenching method. *Talanta,* 1998, 46, 1567 - 1571. (b) Y. Cheng, M. Wu, Z. Du, Y. Chen, L. Zhao, Z. Zhu, X. Yu, Y. Yang, C. Zeng, Tetra-nuclear cluster-based lanthanide metal-organic frameworks as white phosphor, information encryption, self-calibrating thermometers, and Fe^{2+} sensors. *ACS Appl. Mater. Interfaces,* 2023, 15, 24570 - 24582. (c) Y. Xu, P. Li, X. Hu, H. Chen, Y. Tang, Y. Zhu, X. Zhu, Y. Zhang, M. Liu, S. J. A. A. N. M. Yao, Polyoxometalate nanostructures decorated with CuO nanoparticles for sensing ascorbic acid and Fe^{2+} ions. *ACS Appl. Nano Mater.,* 2021, 4, 8302 - 8313. (d) S. Chakraborty, M. Mandal, S. Rayalu, Detection of iron (III) by chemo and fluoro-sensing technology, *Inorg. Chem. Commun.*, 2020, 121, 108189.

17 Y. Ni, L. Yang, L. Kong, C. Wang, Q. Zhang, J. Yang, Highly efficient dual-state emission and two-photon absorption of novel naphthalimide functionalized cyanostilbene derivatives with finely tuned terminal alkoxyl groups. *Mater. Chem. Front.*, 2022, 6, 3522 - 3530.

18 D. C. Magri, A. A. Camilleri, A white light emitting reconfigurable pyrazoline-naphthalimide logic gate with magnesium, sodium and proton inputs, *Chem. Commun.*, 2023, 59, 4459 - 4462.

19 World Health Organization, Avenue Appia 20, 1211 Geneva 27, Swizerland, http://www.who.int/water_sanitation_health /dwq/chemicals/cadmium/en/

20 (a) D. Y. Liu, J. Qi, X. Y. Liu, Z. G. Cui, H. X. Chang, J. T. Chen, G. M. Yang, 4-Amino-1,8-naphthalimide-based fluorescent Cd^{2+} sensor with high selectivity against Zn^{2+} and its imaging in living cells. *Sens. Actuators, B,* 2014, 204, 655 - 658. (b) Y. Zhang, X. Chen, J. Liu, G. Gao, X. Zhang, S. Hou, H. Wang, A highly selective and sensitive fluorescent chemosensor for distinguishing cadmium(II) from zinc(II) based on amide tautomerization. *New J. Chem.,* 2018, 42, 19245 - 19251. (c) A. Sil, A. Maity, D. Giri, S. K. Patra, A phenylene–vinylene terpyridine conjugate fluorescent probe for distinguishing Cd^{2+} from Zn^{2+} with high sensitivity and selectivity. *Sens. Actuators, B,* 2016, 226, 403 - 411. (d) Y. Dai, K. Yao, J. Fu, K. Xue, L. Yang, K. Xu, A novel 2-(Hydroxymethyl)quinolin-8-ol-based selective and sensitive fluorescence probe for Cd^{2+} ion in water and living cells. *Sens. Actuators, B,* 2017, 251, 877 - 884. (e) S. Goswami, K. Aich, S. Das, A. K. Das, A. Manna, S. Halder, A highly selective and sensitive probe for colorimetric and fluorogenic detection of Cd^{2+} in aqueous media. *Analyst,* 2013, 138, 1903 - 1907. (f) Y. Liu, X. Dong, J. Sun, C. Zhong, B. Li, X. You, B. Liu, Z. Liu, Two-photon fluorescent probe for cadmium imaging in cells. *Analyst,* 2012, 137, 1837 - 18450

21 W. Wang, Q. Wen, Y. Zhang, X. Fei, Y. Li, Q. Yang, X. Xu, Simple naphthalimide-based fluorescent sensor for highly sensitive and selective detection of Cd^{2+} and Cu^{2+} in aqueous solution and living cells. *Dalton Trans.,* 2013, 42, 1827 - 1833.

22 .(a) Shaily, A. Kumar, N. Ahmed, A coumarin–chalcone hybrid used as a selective and sensitive colorimetric and turn-on fluorometric sensor for Cd^{2+} detection. *New J. Chem.,* 2017, 41, 14746 - 14753. (b) Y. Xu, H. Wang, J. Zhao, X. Yang, M. Pei, G. Zhang, Y. Zhang, A dual functional fluorescent sensor for the detection of Al^{3+} and Zn^{2+} in different solvents. *New J. Chem.*, 2017, 41**,** 14746 - 14753.

23 H. Y. Luo, J. H. Jiang, X. B. Zhang, C. Y. Li, G. L. Shen, R. Q. Yu, Synthesis of porphyrin-appended terpyridine as a chemosensor for cadmium based on fluorescent enhancement. *Talanta*, 2007, 72, 575 - 581.

24 M. Lu, N. V. Rees, A. S. Kabakaev, R. G. Compton, Determination of iron: electrochemical methods. *Electroanalysis,* 2012, 8, 1693 - 1702.

25 C. Tamuly, N. Barooah, A. S. Batsanov, R. Kataky, J. B. Baruah, Structural and spectroscopic properties of bis-3-picolinium 1,8-naphthalimide tetrachlorocuprate, *Inorg.Chem.Commun.,* 2005, 8, 689 - 691.

26 A. Tarai, J. B. Baruah, Changing π-interactions and conformational adjustments of N-(isonicotinylhydrazide)-1,8-naphthalimide by hydration and complexation affect photophysical properties. *Cryst. Growth Des.,* 2018, 18, 456 - 465.

Appendix Chapter 4

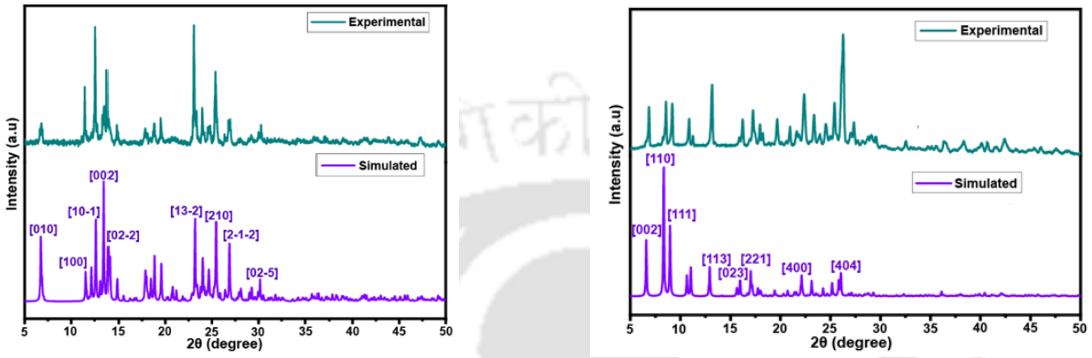

(a) **(b)**

Figure A4.1: Powder X-ray diffraction patterns of the (a) 4.1 (b) 4.2.

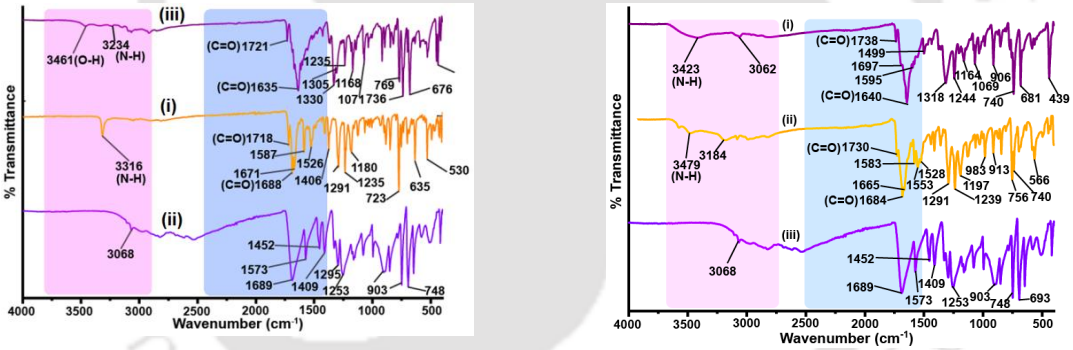

(a) (b)

Figure A4.2: FTIR spectra of powder samples of the (a) *4.1* (b) 4.2.

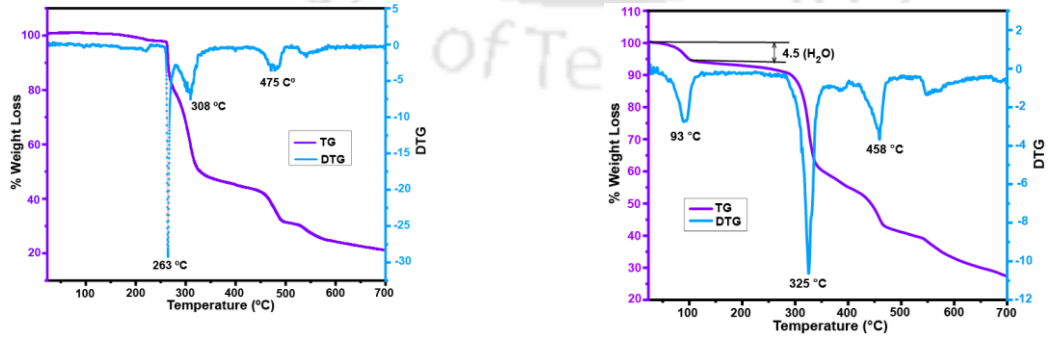

(a) (b)

Figure A4.3: Thermogram of the (a) *4.1* (b) 4.2. (heating rate 10 °C/min under argon atmosphere).

Chapter 5

A zinc coordination polymer of 5-(1,3-dioxo-1H-benzo[de]isoquinolin-2(3H)-yl)isophthalic acid and sensing of cations

5.1 Introduction:

Naphthalimide-derived compounds and their metal-organic frameworks (MOFs) find utility in sensing ions and there is the necessity to compare the fluorescent ligand MOF independently to accrue the advantages of the properties of the free ligand and as a component of a MOF.[1] In the last chapter, the utility of the *naphydrazide* was found to be promising for selective detection of cadmium, as a follow-up to understand coordination behaviour as well as sensing by a carboxylic acid functionalized naphthalimide was studied in this chapter. To do so, the 5-(1,3-dioxo-1H-benzo[de]isoquinolin-2(3H)-yl)isophthalic acid abbreviated as H_2*NAPHISO*

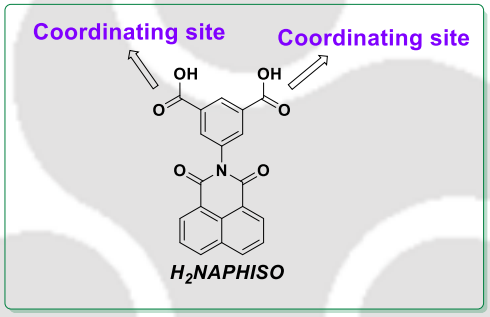

Figure 5.1: The *H*$_2$*NAPHISO* showing the coordinating site for bridging metal ions.

shown in Figure 5.1 was synthesized, characterized, and sensing of commonly available metal ions by it were studied. In literature, it was suggested that the zinc complexes of this ligand were suitable for effective cation detections,[2] but its individual properties in free state for metal ion sensing were not explored. It also is known to form MOF due to the structural feature of 1,3-aromatic dicarboxylic acid which is a common linker[3] for various MOFs useful in sensing cations. The selected ligand has abilities to form gels,[4] inclusion compounds,[5] which provide diverse appeals to understand the ion recognitions through isolation of coordinated complex or its interactions with different substrates/ions in solution. So a coordination polymer of the zinc was prepared and sensing properties were investigated.

5.2 Fluorescence sensing of Zn^{2+} by *H_2NAPHISO*

The compound *H_2NAPHISO* was prepared by the reported procedure and characterized and confirmed its purity before performing the analytical studies. A solution of *H_2NAPHISO* in dimethylformamide (DMF) had a very feeble fluorescence emission at 400 nm (λ_{ex} = 335 nm) as expected from the photo-electron transfer OFF state generally found in many such related compounds.[6] But, its sodium salt was fluorescence and it was used for the Fe^{3+} ions detection through fluorescence emission quenching.[7] The fluorescence intensity of this emission was increased up to 300-fold upon adding a solution of zinc ions. The incremental changes in the emission intensity of a solution of *H_2NAPHISO* with different aliquots of zinc ions are shown in Figure 5.2 (a). The effect of calcium ions was also comparable to zinc ions {Figure 5.2 (b)}. Thus, the compound was not good at detecting zinc ions in the presence of calcium ions. However, the interest of the work was to compare the detection ability of the *H_2NAPHISO* with its coordination polymer, the fluorescence emission spectra of *H_2NAPHISO* solution in DMF with various cations were studied. It was done by adding Mg^{2+}, Ca^{2+}, Al^{3+}, Na^{+}, K^{+}, Li^{+}, Cs^{+}, Mg^{2+}, Hg^{2+}, Mn^{2+}, Fe^{2+}, Ni^{2+}, Cu^{2+}, Sn^{2+}, and Pb^{2+}, and Cd^{2+} individually *H_2NAPHISO* and fluorescence emission of respective solutions were recorded and compared. It was found that the Ca^{2+}, Ag^{+}, $Ni^{2+,}$ and Co^{2+} were able to cause an increase in intensity at 452 nm, and rest of the cases, the quenched state of the parent compound was retained. Subsequently, when the solution of Zn^{2+} ions was added to the solution containing those ions with *H_2NAPHISO*, the emission spectra were recorded {Fig. 5.2 (b)}. The interference in a change in intensity was observed least with magnesium ions. The ratio of fluorescence intensities (I_o/I) is plotted on the y-axis, where I_o represents the fluorescence intensity of the solution of *H_2NAPHISO* after the addition of Zn^{2+}, and the *I* corresponds to the intensity observed with each competing metal ion displayed on the x-axis were plotted in the bar graph. These results also indicated that though there were interferences of the cations in changing the intensity of the zinc ions that would have occurred in their absence, these were not significant to determine the detection of zinc ions in an aqueous solution thereby confirming the selectivity for Zn^{2+}. However, the interfering effect of calcium ions could not be ascertained. It may be noted that excess amounts of zinc ions in biological systems or the environment are a hazard. Hence, developing a low-cost, user-friendly, and easily accessible probe for the selective detection of Zn^{2+} ions presents a significant challenge. It enables selective detection of Zn^{2+} ions using fluorescence sensing, achieving a lower limit of detection.

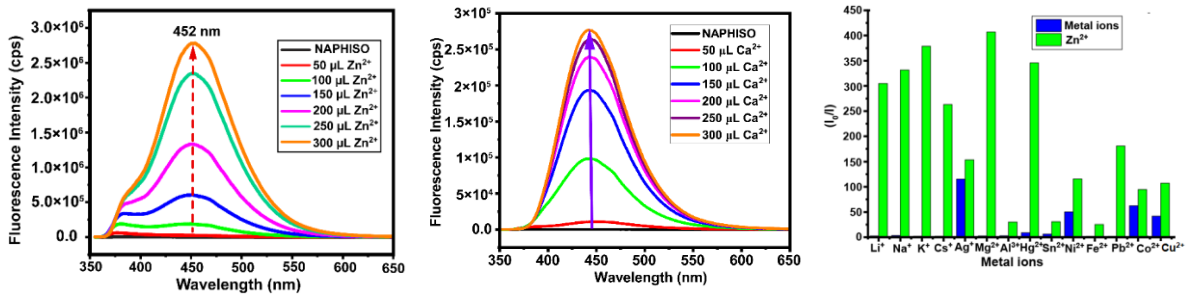

(a) (b) (c)

Figure 5.2: Fluorescence emission spectra of a solution of *H₂NAPHISO* (3 mL, 1 mM in DMF) (λ_{ex} = 333 nm) by adding different aliquots (a) Zn^{2+}, (b) Ca^{2+} solution (50 μL, 10 mM in water). (c) Bar-graph showing relative changes in the fluorescence emission intensities of *H₂NAPHISO* with different ions (50 μL, 10 mM solution of the respective metal salt in water) with respect to the similar solution of *H₂NAPHISO* after adding Zn^{2+} ions to those solutions.

To ascertain the potential influence of water on fluorescence enhancement, additional fluorescence emission titrations were conducted by recording emission spectra of a solution of *H₂NAPHISO* with different amounts of water added externally to the solution. This was required as the naphthalimide derivatives are well known for their aggregation-induced emission enhancements.[8] The results shown in the figure have shown that there was an increase in the emission at 400 nm by water but not significant enough to compare with the zinc ions. In the case of water, a three-fold increase in intensity of emission was observed which was 10 times lower for the zinc ions where it was an increase of 300 folds. This observation enhanced the potential of *H₂NAPHISO* as a robust and selective fluorescent probe for Zn^{2+} detection.

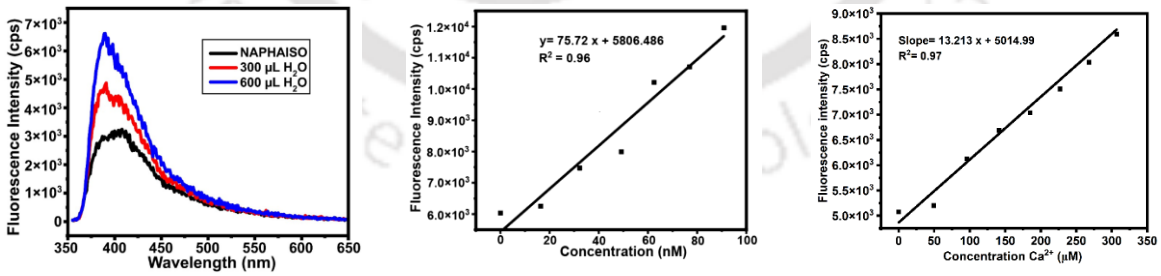

(a) (b) (c)

Figure 5.3: (a) The change in emission spectra of a solution of *H₂NAPHISO* (1 mM in DMF, 2.5 mL) by adding two aliquots of (300 μL). (b) Plots of fluorescence intensity of *H₂NAPHISO* with different concentrations of (b) zinc(II)acetate and (c) calcium acetate.

A series of fluorescence emission spectra was recorded by incrementally diluting the Zn^{2+} concentration and measuring the corresponding fluorescence emission intensities. These data generated a linear plot of the Zn^{2+} concentrations versus fluorescence intensities, with a positive slope, as shown in Figure 5.3(b). The R^2 value for the linear fit was close to unity, indicating the strong linear relation between the analyte concentration and fluorescence enhancement. The effectiveness of the *H_2NAPHISO* was reflected in the limit of detection (LOD) was found to be 3.26 nM. Similarly, a linear plot for the emission intensity of *H_2NAPHISO* with increasing calcium ions was obtained as shown in Figure 5.3 (c). The LOD for calcium ions was 6.18 µM. The *H_2NAPHISO* as a probe is comparable to many other high-performing fluorescence zinc sensors,[9] but the disadvantage is that it cannot be used to detect zinc ions present in hard water due to the same sensitivity of zinc ions to calcium ions.

5.3 Synthesis and Charecterization of Zn_4O coordination polymer:

The zinc coordination polymer designated as *Zn_4O-CP* was prepared by solvothermal method, wherein *H_2NAPHISO* and zinc acetate salt were dissolved in DMF and heated in an autoclave for one day (Scheme 5.1). The solution was then allowed to cool, and the resultant crystals of the coordination polymer *Zn_4O-CP* were collected and characterized. As the same reaction under different conditions was carried out earlier, we checked the preliminary unit cell data obtained from X-ray diffraction of the crystals and found that it was not the form of the zinc MOF that was reported in the literature. The coordination polymer was characterized by X-ray diffraction, FT-IR spectra, and energy dispersive X-ray (EDX) analysis. Its emission properties were investigated to have adequate differences between the selectivity of this and *H_2NAPHISO* for metal ion detections.

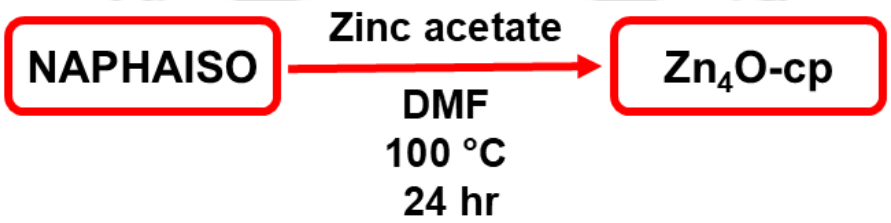

Scheme 5.1: Synthesis of the *Zn_4O-CP*.

5.4 The structure and characterization of the zinc coordination polymer:

The structure of the zinc coordination polymer $[Zn_4O(NAPHISO)_3(DMF)_2]_n$ (*Zn_4O-CP*), was determined by single-crystal X-ray diffraction. The unit cell parameters indicated that the crystals belong to the triclinic space group. A representative node of the coordination polymer

is illustrated in Figure 5.4. It consisted of four zinc ions linked to a central oxide ion via a μ_4-binding mode. The carboxylate groups of each *NAPHISO* ligand coordinate uniformly with the zinc ions through an η^2-bridging mode. The coordination polymer features two symmetry-related chains growing independently and connected through an inversion center, with symmetry operations (i) x, y, z and (ii) -x, -y, -z. Zn_4O cores, commonly found in polynuclear complexes and coordination polymers, are known for their interesting optical properties and are considered structural analogues of zinc oxide.[10] In this coordination polymer, one zinc ion was in an octahedral coordination environment, while the remaining three exhibited tetrahedral geometries. The octahedral zinc ion was coordinated to four oxygen atoms of carboxylates in a square-planar arrangement, each with the oxide oxygen, and a DMF oxygen occupied the trans position. The tetrahedral zinc sites (Zn1 and Zn3) are coordinated by three carboxylate oxygens and one oxide-oxygen, while the third tetrahedral site (Zn4) includes three carboxylate oxygens and one DMF oxygen. Each node of the polymer incorporates two coordinated DMF molecules: one bound to the hexa-coordinate zinc ion (Zn2) and the other to the tetra-coordinate zinc ion (Zn4) {Fig. 5.4(a)}. Metal-organic frameworks with tetranuclear zinc nodes typically exhibit tetrahedral zinc sites coordinated with bridging carboxylates and oxides. However, the *Zn_4O-CP* displayed distinct coordination environments compared to tetranuclear zinc complexes reported in the literature.

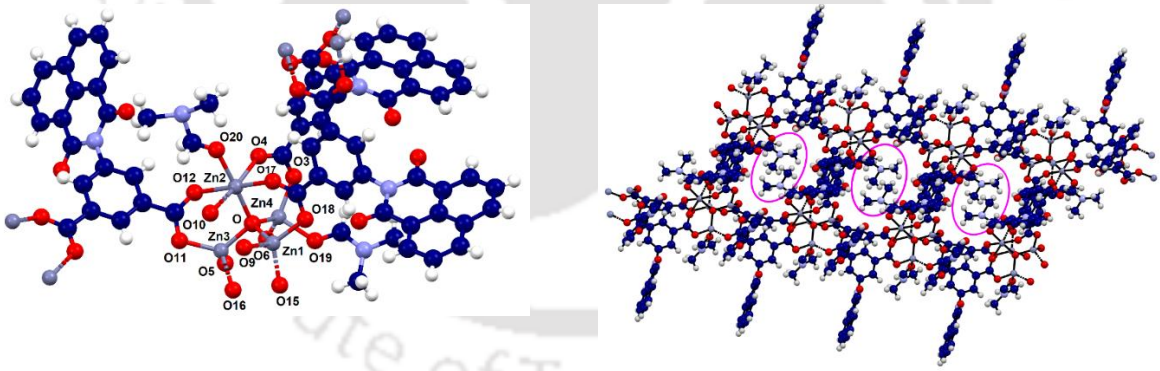

(a) (b)

Figure 5.4: Ball and stick representation of the asymmetric unit of the *Zn_4O-CP* in the crystal structure. (b) 2D structure showing the locations of the coordinated DMF molecules by encircled spaces.

The *Zn_4O-CP* formed a two-dimensional sheet-like arrangement {Fig. 5.4(b)} using the two symmetry-related chains, with enclosures that accommodate the hydrophobic portions of DMF molecules (encircled in the Figure). Strong metal-ligand interactions were reflected by Zn-O bond lengths: Zn4-O19 at 1.994(5) Å and Zn2-O12 at 2.011(4) Å for the coordinated solvent

molecules, and four Zn–O bonds linking zinc ions to the central oxide ion, ranging from 1.905(3) Å to 2.013(3) Å. This showed that solvent molecules were weakly coordinated with zinc ions. Carboxylate Zn-O bonds in the μ_2: η^1 η^1 mode vary between 1.929(4) Å and 2.279(4) Å, demonstrating robust peripheral binding. The shortest distance between parallel naphthalimide planes is 10.36 Å, indicating no π–π interactions within the structure.

Table 5.1: Metal-ligand bond parameters of the coordination polymer *Zn_4O-CP*.

M-L bond	Bond-length (Å)	∠L-M-L	Bond angle (°)
Zn2-O5	2.011 (3)	O5-Zn2-O10	92.17 (12)
Zn2-O10	2.136 (3)	O5-Zn2-O17	94.83 (13)
Zn2-O17	2.140 (3)	O5-Zn2-O4	94.41 (13)
Zn2-O4	2.126 (4)	O5-Zn2-O12	86.89 (13)
Zn2-O12	2.273 (4)	O5-Zn2-O1A	173.3 (4)
Zn2-O1A	2.012 (7)	O5-Zn2-O1B	174.4 (16)
Zn2-O1B	2.045 (15)	O10-Zn2-O17	73.44 (9)
Zn1-O5	1.940 (3)	O10-Zn2-O12	83.78 (13)
Zn1-O18	1.920 (3)	O10-Zn2-O17	93.94 (13)
Zn1-O15	1.947 (3)	O17-Zn2-O12	177.19 (15)
Zn1-O9	1.960 (3)	O4-Zn2-O10	173.42 (14)
Zn3-O5	1.924 (3)	O4-Zn2-O17	85.40 (15)
Zn3-O16	1.992 (3)	O4-Zn2-O12	96.68 (14)
Zn3-O11	1.925 (3)	O1-Zn2-O10	90.3 (5)
Zn3-O5	1.981 (4)	O1-Zn2-O17	91.2 (5)
Zn4-O5	1.907 (3)	O1-Zn2-O4	83.2 (5)
Zn4-O6	1.976 (3)	O1-Zn2-O12	87.2 (5)
Zn4-O3	1.932 (3)	O5-Zn1-O15	109.64 (14)
Zn4-O19	1.993 (4)	O5-Zn1-O9	107.58 (13)
∠L-M-L	Bond angle (°)	O18-Zn1-O5	112.97 (14)
O11-Zn3-O5	107.64 (16)	O18-Zn1-O15	119.30 (14)
O5-Zn4-O3	115.92 (15)	O18-Zn1-O9	105.74 (15)
O5-Zn4-O19	102.58 (16)	O15-Zn1-O9	100.13 (15)
O6-Zn4-O19	99.83 (19)	O5-Zn3-O16	103.94 (13)
O3-Zn4-O6	118.31 (17)	O5-Zn3-O11	120.44 (14)
O3-Zn4-O19	103.54 (19)	O5-Zn3-O5	112.51 (14)
		O11-Zn3-O16	113.80 (15)

The bulk purity of the zinc coordination polymer, Zn4O-CP was assessed using powder X-ray diffraction (PXRD) in Figure 5.5 (a), with the experimental PXRD pattern matching the simulated pattern generated by Mercury software. The FT-IR spectra of solid sample {Figure 5.5(b)} have shown the differences in stretching between the free ligand H2NAPHISO and its

anionic form as coordinated ligands of the coordination polymer. The free ligand had imide C=O stretches at 1667 cm-1 and 1694 cm-1 and the O-H stretch appeared as the broad peak at 3000-2500 cm-1. The C=O stretch of the coordinated and the uncoordinated carboxylate appeared at 1589 cm-1 and 1576 cm-1 respectively.

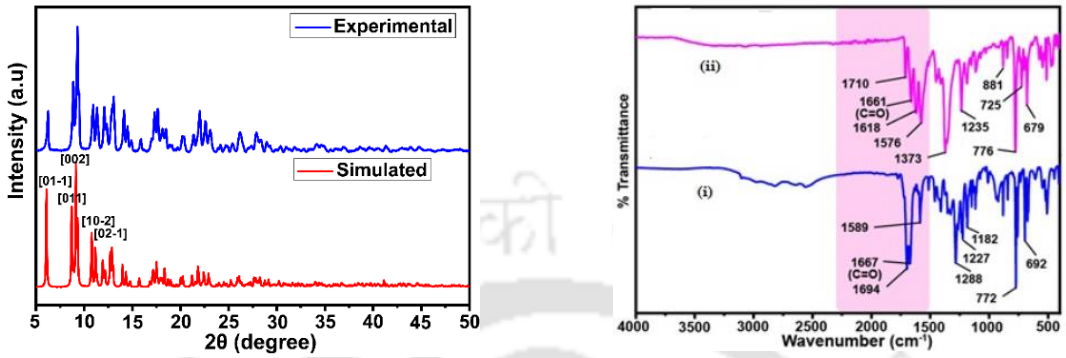

(a) (b)

Figure 5.5: (a) Experimental PXRD pattern (top) and simulated from crystallographic information file by mercury software (bottom) of *Zn_4O-CP,* and (b) FT-IR spectra of the (i) *H_2NAPHISO,* (ii) *Zn_4O-CP.*

The plate-like shape of the crystals was observed through both scanning electron microscopy (SEM) and optical microscopy images (Fig. 5.6a-b). The constituent elements in the material were confirmed by the EDX spectrum (Fig. 5.6c), with the experimental atomic percentages (C, N, O, Zn) matching those obtained from Olex software. To assess the stability of the freshly prepared sample of *Zn_4O-CP*, thermogravimetry under an argon atmosphere was recorded. The coordination polymer loses the coordinated DMF molecules in the range 100◦C - 400◦C (weight loss 2.3%) and undergoes desolvation, showing good thermal stability with had decomposition temperature at 420 °C. At this temperature, 80% of the ligand was lost, leaving behind 20% of the weight, which was attributed to zinc oxide {Figure 5.6(d)}.

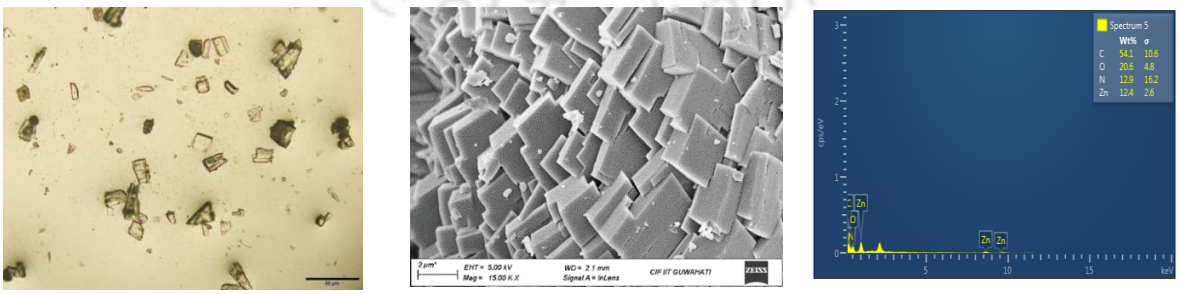

(a) (b) (c)

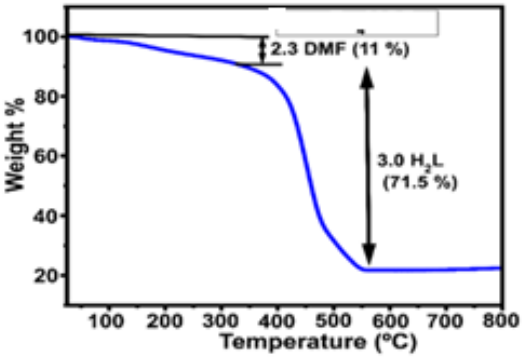

(d)

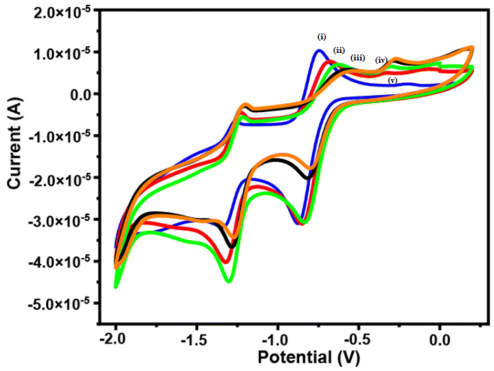

(e)

Figure 5.6: (a) Optical image, (b) scanning electron micrograph, (c) EDX of the powdered sample, (d) Thermogram (blue, under argon, heating rate 10° C/min) the *Zn₄O-CP*. (e) Cyclic voltammogram of (i) *H₂NAPHISO* (1 mM, 10 ml) using tetrabutylammonium perchlorate as supporting electrolyte and the same solution with different amounts of (ii)-(v) Zn^{2+} ions (at each time 100 µL of 1 mM in DMF.

A cyclic voltammetry titration of the *H₂NAPHISO* (1mM, 10 mL) was carried out by adding zinc acetate(1 mM), it was found that with the concentration increased the radical anion was not significantly affected, but the anion formation,[11] became difficult as the second redox cycle in the -ve side of the voltammogram was shifted towards higher potential. The decreased current in each peak of both the cycles on the -ve side, suggested deposition of the ligand on the electrodes

5.5 Fluorescence sensing of Fe^{2+} and Cu^{2+} ions

Various studies have reported paramagnetic ions specially Fe^{2+} ions[12] and Cu^{2+} ions[13] as turn-off fluorescence by using coordination polymer sensors. Many of these approaches have faced challenges in selectivity, sensitivity, detection limits, recyclability, response times, and the choice of sensing medium.[14] The coordination polymer had an emission at 452 nm. To evaluate the sensing of metal ions by the *Zn₄O-CP*, we conducted a fluorescence titration with Fe^{2+}. Stock solutions *Zn₄O-CP* were prepared by sonicating 4 mg of in 10 mL of DMF for 10 minutes. In the experiment, *Zn₄O-CP* suspension (3 ml, DMF/water) was placed in a cuvette, and to this solution, each addition of a solution of aqueous Fe^{2+} ions resulted in a gradual decrease in the fluorescence emission intensity. Saturation of emission intensity decrease occurred after a fluorescence intensity decrease of up to 94.6 % (λ_{ex} = 350 nm, λ_{em} = 435 nm). An identical titration using a solution of Cu^{2+} also showed a similar quenching process {Figure 5.7(b)}.

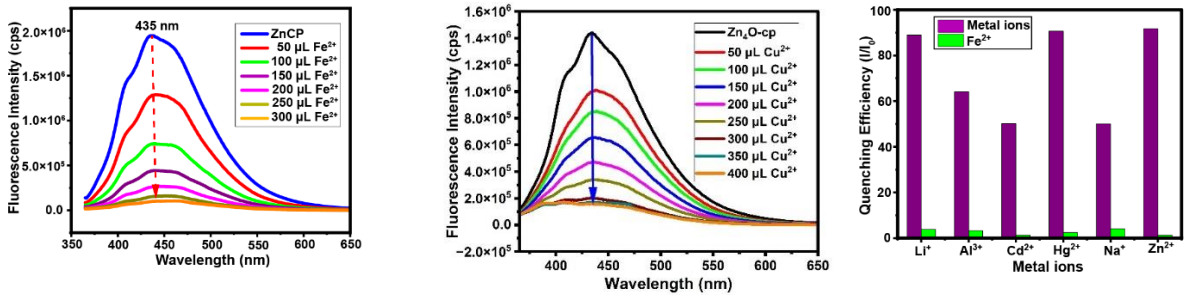

(a) (b) (c)

Figure 5.7: (a) The fluorescence emission of a solution of the *Zn_4O-CP* (3 mL suspension of 4 mg in 10 mL DMF sonicated for 10 min) after each addition of(a) Fe^{2+} ions and (b) Cu^{2+} ions (50 µL of 10 mM aqueous in each aliquot, λ_{ex} = 350 nm). (c) Bar-graph of relative quenching of fluorescence emission intensity caused by Fe^{2+} ions by the presence of various metal ions.

The stability of the response time for sensing was evaluated by a fluorescence experiment carried out at time intervals. The emission spectra of the aqueous *Zn_4O-CP* suspension (100 µL) in DMF (2.9 mL) were recorded five times after one-minute intervals and found that the maximum intensity observed was invariant during this time. The sensing of Fe^{2+} ions by the coordination polymer in the presence of other metal ions namely Li^+, Na^+, Al^{3+}, Hg^{2+}, Cd^{2+}, and Zn^{2+} were investigated. To do so, a series of fluorescence emission experiments with Zn_4O-CP suspension, by initially adding various other ions (in independent experiments, 300 µL of 10 mM in water) followed by adding Fe^{2+} ions (300 µL of 10 mM) to each of those solutions. A comparison of the relative intensities is shown the Figure 5.7(c). It demonstrated that the metal ions under consideration did not influence the quenching of the fluorescence emission intensity caused by Fe^{2+}. The Cu^{2+} ions being another efficient quencher for the emission of the coordination polymer it was not tested together with Fe^{2+} in s solution. Thus, the emission of the *Zn_4O-CP* in DMF was quenched by Fe^{2+} as well as by Cu^{2+} ions. The fluorescence emission intensity of *Zn_4O-CP* was not significantly affected by the other metal ions other than copper ions, indicating that the fluorescence emission was quenched only by the addition of Fe^{2+} ions or Cu^{2+} ions.

The Stern-Volmer plot shown in Figure 5.8(a) supported Fe^{2+} ion quenching. The value Stern-Volmer constant K_{sv} was calculated from the equation $I_0/I = (K_{sv}[Q] + 1)$ (where I_0 and I denote the fluorescence intensity before and after the addition of analytes, respectively and [Q] is the concentration of quencher Fe^{2+}), K_{sv} was found to be $4.343 \times 10^6\ M^{-1}$. The K_{sv} value is M^{-1} was higher than several reported fluorescent sensors for Fe^{2+} ions. The limit of detection of Fe^{2+}

was 42.57 nM. Similarly, copper also showed a linear plot and had a $K_{sv} = 4.4 \times 10^4\ M^{-1}$. The detection limit of copper was 1.27 µM. So, iron detection could be performed at nano-molar concentrations, whereas copper at micromolar concentrations. The quenching is attributed to paramagnetic quenching generally caused by these metal ions at a bivalent state. To establish the structural integrity of the *Zn₄O-CP* in solution, the powder X-ray diffraction pattern of the sample of the CP was compared with the sample prepared after sonication followed by treatment with Fe^{2+} solution. From the comparison of the patterns {Fig. 5.8 (c)}, it was clear that the framework remained intact after the treatment of Fe^{2+}.

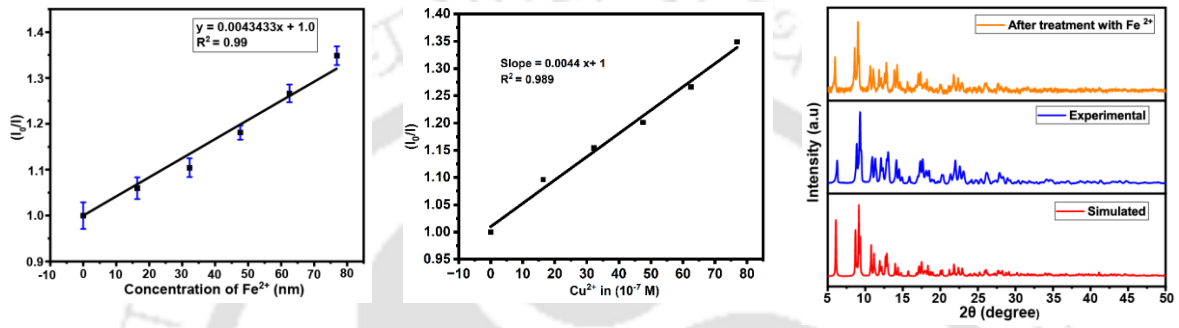

(a) (b) (c)

Figure 5.8: Stern-Volmer plots for the fluorescence emission quenching of the suspension of *Zn₄O-CP* with a solution of (a) Fe^{2+} and (b) Cu^{2+} ions. (c) Comparison of the experimental PXRD of the *Zn₄O-CP* and the PXRD of the same recorded after treatment with Fe^{2+}.

The emission decay profiles of *H₂NAPHISO* with zinc and iron ions as well as of the coordination polymers are depicted in Figure 5.9. The *H₂NAPHISO* with zinc ions *showed* a relatively short average fluorescence lifetime of 11.060 ns.

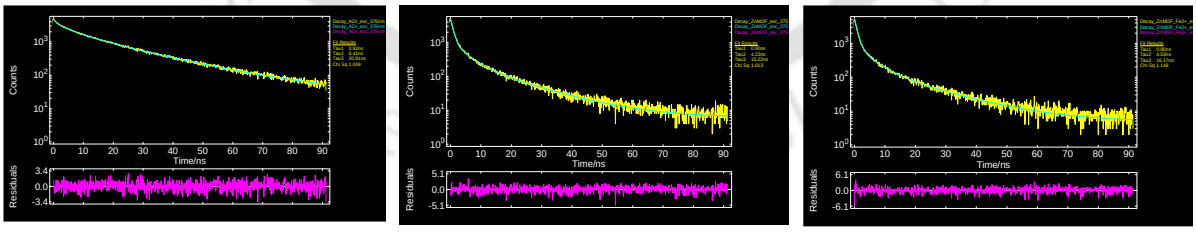

(a) (b) (c)

Figure 5.9: Fluorescence lifetime decay (400 nm) profiles of (a) *H₂NAPHISO* (3 mL, 1 mM DMF) with Zn^{2+} ions (300 µL, 10 mM in DMF). (b) *Zn₄O-CP* (4 mg, sonicated in 3mL DMF); (c) To the suspension (b) with the addition of Fe^{2+} (200 µL, 10 mM in DMF).

Whereas the zinc coordination polymers had 7.219 ns. This showed that complexation had resulted in a decrease in the lifetime, from a free ligand interacting with zinc ions. Whereas,

the *H₂NAPHISO* with Fe^{2+} solution showed an average fluorescence lifetime of 6.639 ns. This reduction in the lifetime

Table 5.2 Lifetime decay data[@]

Substrate	B_1	B_2	B_3	τ_1 (ns)	τ_2 (ns)	τ_3 (ns)	$<\tau>$ (ns)	χ^2
H₂NAPHISO + Zn^{2+}	1234.187	1671.954	2083.249	0.922	15.22	2.16	11.060	1.048
Zn₄O-CP	4340.659	847.915	290.065	0.8959	4.226	15.22	7.219	1.012
Zn₄O-CP + Fe^{2+}	4887.072	719.986	208.383	0.899	4.533	16.17	6.639	1.1482

[@] Tri-exponential fit: $A + B_1\exp(-t/\tau_1) + B_2\exp(-t/\tau_2) + B_3\exp(-t/\tau_3)$
$<\tau> = (B_1\tau_1^2 + B_2\tau_2^2 + B_3\tau_3^2)/(B_1\tau_1 + B_2\tau_2 + B_3\tau_3)$

had indicated an interaction between *H₂NAPHISO* with Fe^{2+}, leading to the fluorescence quenching {5.9 (c)}.

5.6 Summary:

A naphthalimide-derived zinc dicarboxylate two-dimensional coordination polymer was characterised. The fluorescence properties, of the ligand and the coordination polymer for the selective fluorescence detection of commonly available cations were investigated. There were distinct differences in sensing by the two, the ligand was useful for fluorescence sensing of Zn^{2+} and Ca^{2+} ions, whereas the coordination polymer was useful for Cu^{2+} and Fe^{2+} ions. However, the lack of selectivity limits their possible practical applications.

5.7 Experimental Section:

Synthesis of *H₂NAPHISO*: The compound was synthesized from a reaction between 1,8-naphthalic anhydride (1.0 g, 5 mmol) and 5-aminoisopthalic acid (0.907 g, 5 mmol) in DMF (10 mL). After refluxing for 12 hours, the reaction mixture was cooled, and ice-cold water was added. A yellow precipitate was formed, was filtered, and dried in air. The compound was characterised by IR, NMR, and HRMS and compared with an authentic sample.

Synthesis of *Zn₄O-CP:* A mixture of *H₂NAPHISO* (72 mg, 0.2 mmol) and zinc(II) acetate hexahydrate (80 mg, 0.4 mmol) was dissolved in warm DMF (20 mL). This solution was transferred to a Teflon-lined hydrothermal vessel, which was then sealed and heated for 36 hrs in an autoclave at 100 °C. Upon cooling, plate-like crystals formed and settled at the bottom of the vessel. The supernatant was carefully decanted, and the crystals were collected. The structure of a selected single crystal was analyzed using X-ray diffraction, while the composition was verified by EDX analysis, and bulk purity was assessed through powder X-

ray diffraction. The isolated yield: 70 % (calculated based on zinc). FT-IR (Neat) 1661 cm^{-1} (s, $\nu_{C=O\ carboxylate}$) and 1710 cm^{-1} (s, $\nu_{C=O\ imide}$).

Fluorescence measurements: A stock solution of *H_2NAPHISO* (1 mM in DMF) was prepared. For each fluorescence titration 3mL of this solution was placed in a quartz tube and emission spectra were recorded with or without the metal ions. In each case 300 µL of a 10 mM aqueous Zn^{2+} or meta ions were taken and emission spectra were recorded.

The fluorescence emission titration experiments by taking 3 mL of stock solution prepared from Zn_4O-cp were prepared by sonicating 4 mg of Zn_4O-cp in 10 mL of DMF. For the titration, 3 mL of this solution was placed in a quartz cuvette, and incremental additions of different aliquots of a 10 mM Fe(II) acetate solution were performed. At each step, 100 µL of the Fe(II) acetate solution was added, and the fluorescence spectra were recorded to monitor the changes in emission intensities.

Determination of LOD:

From the linear plot of fluorescence emission intensity against concentrations of the slope of the metal ion added. The limit of detection was determined by LOD = k/3σ, where k is the slope of the linear plot. The σ is the standard deviation, It was calculated using the formula:$\sigma = \sqrt{\Sigma(x_i-\mu)^2/N}$. Where x_i represents the fluorescence intensity value, µ is the mean intensity of the measurements, and N is the total number of observations.

Cyclic voltammetry:

Cyclic voltammograms (CVs) were obtained using a NOVA cyclic voltammetry instrument. To a DMF solution of *H_2NAPHISO* (1 mM, 10 mL) in an electrochemical cell equipped with a glassy carbon working electrode, a platinum counter electrode, and an Ag/AgCl reference electrode, tetrabutylammonium perchlorate (341.9 mg, 1 mmol) was added. The CVs were recorded at a scan rate of 50 mV/s with a positive scan. Subsequently, 100 µL aliquots of a 1 mM stock solution of zinc(II) acetate were added incrementally, and after each addition, cyclic voltammograms were recorded.

X-ray single crystal structure determination:

Single-crystal X-ray diffraction for the zinc coordination polymer was carried out using MoKα radiation (λ = 0.71073 Å) at 297 K on a Bruker Nonius SMART APEX CCD diffractometer

equipped with a graphite monochromator and Apex CCD camera. Data processing, including cell refinement, was performed using the SAINT and XPREP software packages. The crystal

Table 5.3: The crystal refinement parameters of Zn_4O-CP

Empirical Formula	CCDC No.	Formula Weight	Crystal System	a/ Å	b/ Å	c/ Å	α/ °	β/ °
$C_{66}H_{48}N_5O_{24}Zn_4$	2377351	1556.57	Triclinic P-1	10.3826(6)	16.2352(10)	33.405(5)	106.864(2)	102.927(2)
γ/ °	V/ Å^3	Z	ρ (gcm^{-3})	μ (mm^{-1})	F (000)	Refl collected	Independent Reflections	Ranges (h,k,l)
102.216 (2)	3188.4(3)	2	1.621	1.575	1582	76522	11228	-12 ≤ h ≤ 12 -19 ≤ k ≤ 19 -25 ≤ l ≤ 25
Max θ(degree)	Data/restraints/ parameters	Goof (F^2)	R indices	[I>2σ]	WR_2			
25	11228/0/869	1.070	0.0507	0.0729	0.1284			

structure was solved via the direct method and refined using full-matrix least squares on F^2 with the SHELXL-2018 program. Hydrogen atoms were placed at geometrically estimated positions and refined isotropically, while non-hydrogen atoms were refined anisotropically against F^2 for all reflections. Crystal and structural parameters are summarized in Table 5.3. The disorder was observed in a naphthalimide ring and a DMF molecule; the disordered components were modeled by splitting the atoms into separate positions and refining them isotropically.

5.8 References:

1.(a) X. Wang, A. Rehman, R. M. Kong, Y. Cheng, X. Tian, M. Liang, L. Zhang, L. Xia, F. Qu, Naphthalimide derivative-functionalized metal-organic framework for highly sensitive and selective determination of adehyde by space confinement-induced sensitivity enhancement effect. *Anal. Chem.,* 2021*,* 93*,* 8219 - 8227. (b) Q. Li, S. Shen, L. Liang, K. Huang, D. Zheng, D. Qin, B. Zhao, Naphthalimide-based multiresponsive copper metal-organic framework for ratiometric detection of ClO^- and turn-on sensing Fe^{3+}, Cr^{3+}, and Al^{3+} in water. *Dyes and Pig.*, 2023, 219,111639. (c) X. Wu, K. Wang, J. Lin, D. Yan, Z. Guo, H. Zhan, A thin film of naphthalenediimide-based metal-organic framework with electrochromic properties. *J. Colloid and Interface Sci.*, 2021, 594, 73 - 79.

2. K. Jin, N. Park, Y. Ahn, D. Seo, D. Moon, J. Sung, J. Park. Solvent-induced structural transformation in a one-dimensional coordination polymer. *Nanoscale*, 2024, 16, 4571 - 4577.

3. (a) M. K. Leszczyński, K. Niepiekło, M. Terlecki, I. Justyniak, J. Lewiński, Chromium (II)-isophthalate 2D MOF with redox-tailorable gas adsorption selectivity. *ACS Appl. Mater.*

Interfaces. 2024, *16*, 45100 - 45106. (b) Y. Pan, W. Liu, D. Liu, Q. Ding, J. Liu, H. Xu, M. Trivedi, A. Kumar, A 3D metal-organic framework with isophthalic acid linker for photocatalytic properties. *Inorg. Chem. Commun.,* 2019, 100, 92 - 96.

4. D. Singh, J. B. Baruah, Solvation controlling reaction paths and gel-formation in imide derivatives, Tetrahedron Letters 2008, 49, 4374 - 4377.

5. (a) D. Singh, J. B. Baruah, Guest inclusion in cyclic imides connected to carboxylic acid by flexible tether. *J. Inclusion Phenomena and Macrocyclic Chem.,* 2013, 76, 269 - 281. (b) D. Singh, J. B. Baruah, Solid state assemblies of cyclic imides tethered hydroxy benzoic acids with pyridine and quinoline: toward the formation of channels and cavities, *Cryst. Growth Des.,* 2012, 12, 3169 - 3180.

6. J. K. Nath and J. B. Baruah, Solvatoemissive dual fluorescence of N-(pyridylmethyl)-3-nitro-1,8-naphthalimides. *Journal of Fluorescence* 2014, 24, 649 - 655.

7. L. Wang, W. T. Li, W. J. Qu, J. X. Su, Q. Lin, T. B. Wei, Y. M. Zhang, A highly selective fluorescent chemosensor for successive detection of Fe^{3+} and CN^{-} in pure water. *Supramol. Chem.* 2017, 29, 489 - 496.

8. (a) C. Felip-León, F. Galindo, J. F. Miravet, Insights into the aggregation-induced emission of 1,8-naphthalimide-based supramolecular hydrogels**.** *Nanoscale***,** 2018, 10**,** 17060 - 17069. (b) S. Misra, P. Singh, A. Das, P. Brandão, P. Sahoo, N. Sepay, G. Bhattacharjee, P. Datta, A. K. Mahapatra, B. Satpati, J. Nanda, Supramolecular assemblies of a 1,8-naphthalimide conjugate and its aggregation-induced emission property**.** *Mater. Adv.***,** 2020**,** 1, 3532 - 3538. (c) Y. Yin, Z. Chen, C. Fan, G. Liu, S. Pu, 1,8-Naphthalimide-based highly emissive luminophors with various mechanofluorochromism and aggregation-induced characteristics. *ACS Omega,* 2019, 4*,* 14324-14332.

9. (a) E. P. S. Pratt, L. J, Damon, K. J. Anson, A. E. Palmer, Tools and techniques for illuminating the cell biology of zinc. *Biochim. Biophys. Acta,* 2021, 1868, 118865. (b) E. M. Nolan, S. J. Lippard, Small-molecule fluorescent sensors for investigating zinc metalloneurochemistry. *Acc. Chem. Res.,* 2009, 42, 193 - 203. (c) L. Ma, G. Liu, S. Pu, C. Zheng, C. Fan, Solvent-dependent selective fluorescence sensor for Zn^{2+} and Al^{3+} based on a new diarylethene with a salicylal schiff base group. *Tetrahedron,* 2017, 73, 1691 - 1697. (d) H. Woo, Y. You, T. Kim, G. J. Jhon, W. Nam, Fluorescence ratiometric zinc sensors based on controlled energy transfer**.** *J. Mater. Chem.***,** 2012, 22**,** 17100 - 17112. (e) D. Yun, J. B. Chae, H. So, H. Lee, K. T. Kim, C. Kim, Sensing of zinc ions and sulfide using a highly practical and water-

soluble fluorescent sensor: applications in test kits and zebrafish. *New J. Chem.*, 2020, 44, 442 - 449.

10. (a) S. S. Kaye, A. Dailly, O. M. Yaghi, J. R. Long, Design and synthesis of an exceptionally stable and highly porous metal-organic framework. *J. Am. Chem. Soc.,* 2007, 129, 14176 - 14177. (b) H. Li, M. Eddaoudi, M. O'Keeffe, O. M. Yaghi, Design and synthesis of an exceptionally stable and highly porous metal-organic framework. *Nature,* 1999, 402, 276 - 279. (c) Y. Zhao, L. Wang, N.N. Fan, M. L. Han, G. P. Yang, L. F. Ma, Porous Zn(II)-based metal–organic frameworks decorated with carboxylate groups exhibiting high gas adsorption and separation of organic dyes. *Cryst. Growth Des.,* 2018, 18, 7114 - 7121.

11. C. Tamuly, N. Barooah, A. S. Batsanov, R. Kataky, J. B. Baruah, Structural and spectroscopic properties of bis-3-picolinium 1,8-naphthalimide tetrachlorocuprate, *Inorg. Chem. Commun.,* 2005, 8, 689 - 691.

12. (a) Y. Cheng, M. Wu, Z. Du, Y. Chen, L. Zhao, Z. Zhu, X. Yu, Y. Yang, C. Zeng, Tetra-nuclear cluster-based lanthanide metal-organic frameworks as white phosphor, information encryption, self-calibrating thermometers, and Fe^{2+} sensors. *ACS Appl. Mater. Interfaces,* 2023, 15, 24570 - 24582. (b) I. David, N. Bhuvanesh, H. Jayaraj, A. Thamilselvan, D. Parimala devi, A. Abiram, J. Prabhu, R. J. A. O. Nandhakumar, Experimental and theoretical studies on a simple S–S-bridged dimeric schiff base: selective chromo-fluorogenic chemosensor for nanomolar detection of Fe^{2+} and Al^{3+} ions and its varied applications. *ACS Omega,* 2020, 5, 3055 - 3072. (c) H. Nawaz, W. Tian, J. Zhang, R. Jia, Z. Chen, J. J. A. Zhang, a. m.; interfaces, Cellulose-based sensor containing phenanthroline for the highly selective and rapid detection of Fe^{2+} ions with naked eye and fluorescent dual modes. *ACS Appl. Mater. Interfaces.,* 2018, 10, 2114 - 2121.

13. H. Asadevi, P. P. Nair, C. Kumari, R. P. Amma, S. A. Khadar, S. C. Sasi, R. Raghunandan ZnO@MOF-5 as a fluorescence "Turn-Off" Ssensor for ultrasensitive detection as well as probing of copper(II) Ions. *ACS Omega,* 2022, 7, 13031 - 13041, (b) F. Ming, J. Hou, D. Huo J. Zhou, M. Yang, C. Shen, S. Zhang, C. Hou, Copper-based metal–organic framework nanoparticles for sensitive fluorescence detection of ferric ions. *Anal. Methods*, 2019, 11, 4382-4389. (c) B. B. Guan, Q. Li, Y. T. Xu, L. H. Chen, Z. S. Wu, Z.L. Fan, W. Zhu, Highly selective and sensitive detection towards cationic Cu^{2+} and Fe^{3+} contaminants via an In-MOF based dual-responsive fluorescence probe. *Inorg. Chem. Commun.*, 2020, 122, 108273.

14. T. Wu, X. J. Gao, F. Ge, H. G. Zheng, Metal-organic frameworks (MOFs) as fluorescence sensors: principles, development and prospects. *CrystEngComm*, 2022, 24, 7881 - 7901.

Appendix-Chapter 5

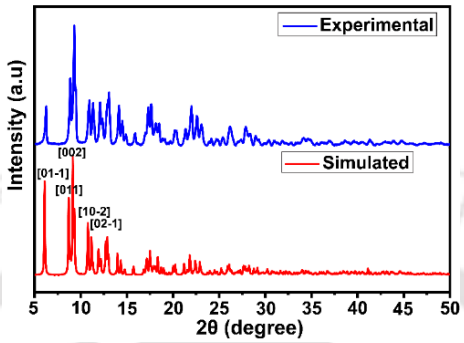

Figure A5.1: Powder X-ray diffraction pattern of the *5.1*.

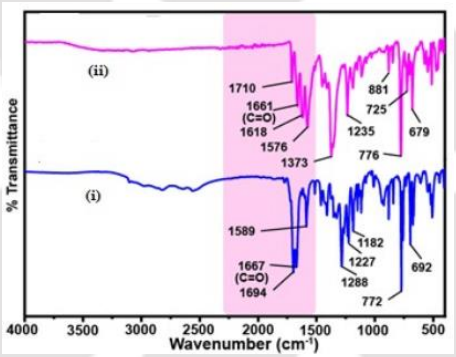

Figure A5.2: FTIR spectra of powder samples of the *5.1*.

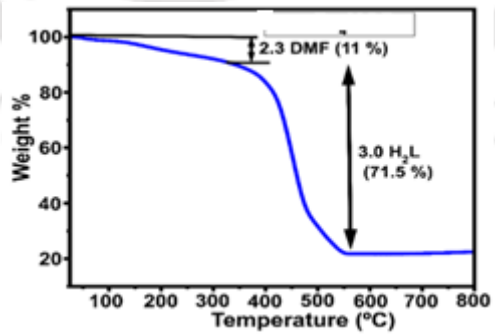

Figure A5.3: Thermogram of the *5.1*. (heating rate 10 °C/min under argon atmosphere)

Thesis Conclusion

The study demonstrated that aminonap forms distinct polymorphic structures with two different stacking arrangements of its naphthalimide rings, which influenced its physical properties. The protonation and formation of nitrate salts and nitrate ionic co-crystals revealed significant structural and property variations, emphasizing the role of protonation in modifying the ligand's coordination capabilities of the ligands. The solution studies have shown the complexation behavior of aminonap with zinc exhibited weak binding, whereas, with copper and cadmium, it had relatively higher binding and enabled to characterization of their stable and versatile complexes. The binuclear and trinuclear copper dicarboxylate complexes with aminonap displayed varying coordination modes, including bidentate and monodentate coordination depending on the nature of the heterocycle on the dicarboxylate portion of the ligands. The cadmium complex had an unusual template structure, where aminonap coordinated in a way that aminonap allowed for stacking interactions to include it as also as a guest, displaying self-inclusion property. Copper, showed paramagnetism but lacked significant magnetic coupling due to large Cu-Cu distances. Additionally, the electrochemical behavior revealed that metal coordination lowered the electrochemical reduction potential, influencing radical anion formation and anion stability in the complexes. The fluorescence properties of the aminonap ligand were also modified upon complexation, with cadmium induced a shift of emission peak to shorter wavelength was observed. Thermogravimetric analysis indicated that the thermal stability of the complexes varied, with distinct decomposition patterns observed for different ligands, further supporting the structural findings. The study has provided valuable insights into the coordination chemistry of aminonap with transition metals, highlighting its potential for designing functional materials and supramolecular systems.

The versatility of naphthalimide-based ligands in coordinating with metal ions to form stable, well-characterized complexes with distinctive optical and electronic properties is demonstrated by characterizing cobalt and copper complexes. The cobalt complex exhibited a stable hexacoordinate distorted octahedral structure, with hydrogen bonding and π-stacking interactions contributing to its solid-state arrangement. The copper complex displayed a unique five-coordinated, square pyramidal geometry, stabilized by supramolecular interactions, particularly weak Cu-O interactions with the naphthalimide moiety. The fluorescence enhancement through in-situ release of acid to protonate ligand illustrated potential applications of such processes in sensing and material design.

The combination of Naphydrazide with $H_2$26-pdc provided a bicomponent platform for the selective detection and differentiation of metal ions. The bi-component system is particularly effective for cadmium ions, through fluorescence spectroscopy. The bi-component platform was also capable of distinguishing Fe^{2+} and Fe^{3+} ions with the help of UV-visible spectroscopy. The simplicity and efficiency of this system, without Buffers or specific pH conditions, make it attractive.

The naphthalimide-derived ligand (H_2NAPHISO) and its zinc coordination polymer (Zn4O-CP) were used for the detection of metal ions. Both the ligand and its zinc coordination polymer display promising properties for fluorescence-based metal ion sensing in a distinct manner. However, challenges related to selectivity and sensitivity, particularly in complex solutions with multiple ions, highlight the need for further optimization of these materials for practical applications in environmental monitoring and biological system.

Details of the analytical equipment

X-Ray Crystallography:

X-ray crystallographic data were collected at 296 K using Mo Kα radiation (λ = 0.71073 Å) with either a Bruker Nonius SMART CCD diffractometer or an Oxford SuperNova diffractometer. Data obtained from the Oxford SuperNova diffractometer were processed using CrysAlisPro software, while SAINT and XPREP software were used for data analysis from the Bruker Nonius SMART APEX CCD diffractometer. Structure determination was performed using direct methods and further refined through full-matrix least-squares calculations with SHELXTL-14 and SHELXTL-97 software.

Non-hydrogen atoms were refined anisotropically against F^2 for all reflections, whereas hydrogen atoms were treated isotropically and positioned using the 'riding' model. The hydrogen atoms of protonated organic molecules were identified through difference Fourier synthesis maps. Similarly, hydrogen atoms associated with water molecules were located via Fourier synthesis, refined with isotropic displacement parameters, and subjected to necessary restraints to optimize their positions. The CIF files for all single-crystal X-ray structures are included in the electronic supplementary material.

Powder X-ray diffraction patterns were recorded using a Rigaku X-ray diffractometer, with Cu Kα radiation (λ = 1.54 Å) as the source, operating at 9 kW power. The measurements were performed on air-dried samples mounted on a glass surface, employing a secondary curved graphite monochromator. Diffraction patterns were acquired over a 2θ range of 5-45º with a step scan rate of 0.02º. Molecular packing diagrams were generated using Mercury 3.7 software.

Cyclic-voltammetry, XPS, ESR, Optical microscopic image, FTIR, Fluorescence, Uv-visible, NMR, lifetime measurements

Fourier transform infrared spectra of the solid samples were recorded using a PerkinElmer Spectrum Two spectrometer in the range of 4000−400 cm^{-1}, employing the attenuated total reflectance method. UV-visible absorption spectra were obtained with a PerkinElmer Lambda 750 spectrophotometer, which features a dual-cell compartment. Fluorescence emission spectra were recorded using a Horiba Jobin Yvon Fluoromax-4 spectrofluorometer, with solutions and powder samples excited at the required wavelengths. Proton nuclear magnetic resonance

spectra were acquired on Varian 400 MHz and BRUKER Ascend 600 MHz NMR spectrometers, using tetramethylsilane as the internal standard.

Electrospray ionization mass spectrometry (ESI-MS) spectra of all compounds were recorded using an Agilent QTOF 6520 mass spectrometer. Fluorescence lifetime decay profiles were measured on an Edinburgh Instruments FSP920 spectrometer, utilizing a 336 nm excitation source. X-ray photoelectron spectroscopy (XPS) analysis was conducted on a PHI5000 Versa Probe III system, employing monochromatic Al Kα radiation (1486.7 eV). Elemental composition analysis was performed using a EuroEA 3000 series elemental analyzer.

Electrochemical measurements were carried out using an Autolab Nova series electrochemical workstation with a three-electrode setup, comprising a glassy carbon working electrode, an Ag/AgCl reference electrode, and a platinum counter electrode. X-band electron spin resonance (ESR) spectra of the powdered samples were recorded at room temperature on a JES-FA200 ESR spectrometer, using a microwave power of 0.995 mW and a frequency of 9.45 GHz, with a modulation amplitude of 10. Magnetic susceptibility measurements for complexes 1 and 2 were conducted using a Sherwood Scientific magnetic susceptibility balance. Temperature-dependent magnetic studies were performed using a Quantum Design Dynacool PPMS (9 T), where samples were cooled at a rate of 5 K/min with liquid nitrogen, and magnetic moments were recorded at different temperatures under a 0.5 kOe field. The obtained data were converted to molar susceptibility and analyzed using Origin software.

All chemicals and solvents were sourced from standard suppliers such as Sigma-Aldrich, E. Merck, and Ranbaxy. Solvents used for spectroscopic studies were of HPLC grade (Aldrich or Merck) and were used without further purification.

Thermal analysis SEM AND EDX measurement:

Thermogravimetric analysis (TGA) was performed using an STA449 F3 Jupiter and SDTQ600 thermal analyzer under an argon atmosphere, maintaining a consistent heating rate of 10 °C min^{-1}. Differential scanning calorimetry was performed using a Mettler Toledo DSC-1, also operated at a heating rate of 10 °C min^{-1}. Elemental compositions were analyzed with a PerkinElmer PE 2400 II CHNS microanalytical analyzer. Field emission scanning electron microscopy (FESEM) was carried out on a Gemini 300 FESEM instrument (Carl Zeiss). Finely ground samples were mounted on carbon tape affixed

to SEM or energy-dispersive X-ray spectroscopy (EDX) sample holders for analysis.

Crystallographic data and refinement parameters of the compounds and complexes.

Parameters	Poly-1	Poly-2	[Haminonap]$NO_3.H_2O$	[Haminonap] NO_3.aminonap.H_2O
Empirical Formula	$C_{12}H_8N_2O_2$	$C_{24}H_{16}N_4O_4$	$C_{12}H_{11}N_3O_6$	$C_{24}H_{19}N_5O_8$
CCDC No	2168736	2168737	2168738	2168739
Formula wt.	212.20	424.41	293.24	505.44
Crystal system	Orthorhombic	Triclinic	Triclinic	Monoclinic
Space group	$Pna2_1$	P-$\bar{1}$	P-$\bar{1}$	$P2_1$
a/ Å	13.296 (2)	7.307 (6)	6.983 (4)	7.411 (8)
b/ Å	18.408 (4)	9.364 (7)	9.788 (5)	14.018 (13)
c/ Å	3.781 (11)	14.655 (10)	10.103 (6)	10.633 (10)
α/ °	90	81.676 (3)	98.26 (2)	90
β/ °	90	80.506 (3)	94.33 (2)	98.590 (9)
γ/ °	90	69.460 (3)	93.17 (2)	90
V/ $Å^3$	925.5 (4)	922.15 (12)	610.4 (6)	1092.48 (19)
Z	4	4	2	2
ρ (gcm^{-3})	1.523	1.528	1.595	1.536
μ (mm^{-1})	0.107	0.107	0.131	0.118
F(000)	440.0	440.0	304.0	524.0
Refl collected	2484	28420	6770	4310
Independent reflection	1565	3249	2963	3344
Ranges (h,k,l)	$16 \le h \le 17$	$-8 \le h \le 8$	$-9 \le h \le 9$	$-9 \le h \le 5$
	$-21 \le k \le 24$	$-11 \le k \le 11$	$-11 \le k \le 11$	$-11 \le k \le 19$
	$-4 \le l \le 5$	$-17 \le l \le 17$	$-13 \le l \le 13$	$-11 \le l \le 14$
Max θ (deg)	25.242	24.998	25.242	25.242
Data/restraints/parameters	2963/0/1943	344/1/339	12076/0/804	3983/0/331
GooF (F^2)	1.057	1.045	1.013	1.078
R indices [I>2σ]	0.0723	0.0523	0.0625	0.0438
WR_2	0.1172	0.1434	0.1790	0.1084

Parameters	**[Cd(aminonap)$_3$(NO_3)]NO_3•2(aminonap)**	***Cu(aminonap)$_4$](NO$_3$)$_2$***	**[Cu(26pdc)(aminonap)]$_2$**	**Cu_3(35pza)$_2$(aminonap)$_4$(H_2O)$_4$]•2H_2O**
Empirical Formula	$C_{60}H_{40}CdN_{12}O_{16}$	$C_{48}H_{32}CuN_{10}O_{14}$	$C_{38}H_{22}Cu_2N_6O_{12}$	$C_{58}H_{46}Cu_3N_{12}O_{22}$
CCDC No.	2168740	2195313	2255279	2255278
Formula Weight	1297.45	1036.3	881.68	1453.69
Crystal System	Triclinic	Triclinic	Triclinic	Monoclinic
Space group	P-$\bar{1}$	P-$\bar{1}$	P-$\bar{1}$	$P2_1$
a/ Å	13.262(7)	7.578(5)	7.613(13)	12.612(11)
b/ Å	14.348(8)	11.620(8)	7.892(13)	15.770(14)
c/ Å	16.635(10)	13.50	14.140(2)	14.304(12)

α/ °	96.631(5)	77.55(2)	104.569(5)	90
β/ °	104.242(5)	84.28(2)	91.955(5)	97.547(2)
γ/ °	116.913(5)	76.40(2)	91.760(5)	90
V/ Å^3	2640.2(3)	1127.38(13)	821.2(2)	2880.6(4)
Z	2	1	1	2
ρ (gcm^{-3})	1.632	1.526	1.783	1.712
μ (mm^{-1})	0.504	0.568	1.378	1.219
F (000)	1320.0	513.0	446.0	1482.0
Refl collected	21726	35467	20,864	82,817
Independent Refl	12076	-3983	2859	
Ranges (h,k,l)	-17 ≤ h ≤16 -18 ≤ k ≤ 18 -17 ≤ l ≤ 21	-9 ≤ h ≤ 9 -13 ≤ k ≤ 13 -16 ≤ l ≤ 16	-9 ≤ h ≤ 9 -9 ≤ k ≤ 9 -16 ≤ l ≤ 16	-15 ≤ h ≤ 15 -18 ≤ k ≤ 18 -17 ≤ l ≤ 17
Max θ (degree)	25.242	25.077	24.997	25.354
Data/restraints/parameters	565/1/151	3249/0/290	2859/0/262	5164/0/438
Goof (F^2)	1.026	1.050	1.213	1.108
R indices		0.0613	0.9170	0.0549
[I>2σ]	0.0662		0.0650	0.0465
WR$_2$	0.1466	0.1731	0.1299	0.1180

Parameters	***[Co(26pdc)(4pynap)$_2$(H$_2$O)]·H$_2$O***	***[Cu(26pdc)(4pynap)(H$_2$O)]·2H$_2$O***
Empirical Formula	$C_{43}H_{33}CoN_5O_{11}$	$C_{32}H_{20}CuN_3O_3$
CCDC No.	2255276	2255277
Formula Weight	854.67	570.99
Crystal System	Monoclinic	Orthorhombic
Space group	$P2_1$	$Pna2_1$
a/ Å	31.667 (4)	8.785 (14)
b/ Å	15.709 (18)	16.198 (2)
c/ Å	7.707 (9)	33.405 (5)
α/ °	90	90
β/ °	93.819 (4)	90
γ/ °	90	90
V/ Å^3	3825.7 (8)	4753.9 (12)
Z	4	8
ρ (gcm^{-3})	1.484	1.596
μ (mm^{-1})	0.521	0.981
F (000)	1764.0	2344.0
Refl collected	40154	131,704
Independent Reflections	2010	4482
Ranges (h,k,l)	-38 ≤ h ≤ 38 -18 ≤ k ≤ 18 -9 ≤ l ≤ 9	-10 ≤ h ≤ 10 -19 ≤ k ≤ 19 -40 ≤ l ≤ 40

Max θ (degree)	25.406	25.621
Data/restraints/parameters	3505/0/277	4482/0/349
Goof (F^2)	1.124	1.114
R indices	0.0674	0.0492
[I>2σ]	0.0477	0.0415
WR_2	0.1260	0.1130

Parameters	***[(Hnaphydrazide)[Fe(26pdc)$_2$]·H$_2$O***	***[(H$_2$binaphydrazide)Fe(26pdc)$_2$]$_2$·4.5H$_2$O***
Empirical Formula	$C_{25}H_{21}FeN_5O_{12}$	$C_{54}H_{46}Fe_2N_{10}O_{31}$
CCDC No.	2325870	2325867
Formula Weight	722.38	1442.71
Crystal System	Triclinic	Monoclinic
Space group	P-1¯	$P2_1$
a/ Å	7.808 (6)	16.017 (3)
b/ Å	14.712(11)	14.142(3)
c/ Å	14.844(12)	26.803(6)
α/ °	117.038(16)	90
β/ °	92.27(2)	90.347(9)
γ/ °	98.607(15)	90
V/ Å^3	1490(2)	6071(2)
Z	2	4
ρ (gcm^{-3})	1.610	1.578
μ (mm^{-1})	0.585	0.582
F (000)	738.0	2960.0
Refl collected	35011	71 609
Independent Refl	5296	5567
Ranges (h,k,l)	-9 ≤ h ≤ 9	-19 ≤ h ≤ 19
	-17 ≤ k ≤ 17	-16 ≤ k ≤ 17
	-17 ≤ l ≤ 17	-32 ≤ l ≤ 32
Max θ (degree)	25.204	25.409
Data/restraints/parameters	5296/0/462	5567/0/397
Goof (F^2)	1.067	1.045
R indices	0.0415	0.0532
[I>2σ]	0.0375	0.0404
WR_2	0.1062	0.1258

Parameters	***Zn4O-cp***
Empirical Formula	$C_{66}H_{48}N_5O_{24}Zn_4$
CCDC No.	2377351
Formula Weight	1556.57
Crystal System	Triclinic
a/ Å	10.3826 (6)

b/ Å	16.2352 (10)
c/ Å	33.405 (5)
α/ °	106.864 (2)
β/ °	102.927 (2)
γ/ °	102.216 (2)
V/ $Å^3$	3188.4 (3)
Z	2
ρ (gcm^{-3})	1.621
μ (mm^{-1})	1.575
F (000)	1582
Refl collected	76522
Independent Reflections	11228
Ranges (h,k,l)	$-12 \le h \le 12$
	$-19 \le k \le 19$
	$-25 \le l \le 25$
Max θ (degree)	25
Data/restraints/parameters	11228/0/869
Goof (F^2)	1.070
R indices	0.0507
[I>2σ]	0.0729
WR_2	0.1284

List of Publications

1. J. Sendh, J. B. Baruah, Polymorphs, ionic cocrystal and inclusion complex of N-amino-1,8-naphthalimide. *CrystEngComm* 2023, 25, 1928 - 1940.

2. J. Sendh, J. B. Baruah, Naphthalimide decorated copper(II), cobalt(II) dicarboxylates and tricking turn-ON emission. *Polyhedron* 2024, 249, 116792.

3. J. Sendh, J. B. Baruah, Bi-component sensing platform for the detection of Cd^{2+}, $Fe^{2+}$and Fe^{3+} Ions. *RSC Adv.* 2024, 14, 27153 - 27161.

4. J. Sendh, J. B. Baruah, Sequential effects of two cations on the fluorescence emission of a coordination polymer with Zn_4O core in node. *RSC Adv.* 2024, 14 (43), 31598 - 31606.

5. J. Sendh, M. P. Singh, J. B. Baruah, 5-[(Pyren-9-Ylmethyl)Amino]Isophthalic acid with nitrogen containing heterocycles: stacking, N-H···π interactions, and photoluminescence. *CrystEngComm* 2021, 23, 6952 - 6966.